UNIVERSITY of CALIFORNIA
Santa Barbara

Luminous and Dark Matter in Early-type Galaxies

A dissertation submitted in partial satisfaction of the
requirements for the degree of

Doctor of Philosophy

in

Physics

by

Alessandro Sonnenfeld

Committee in charge:

Professor Tommaso Treu, Chair
Professor Crystal Martin
Professor Peng Oh

March 2015

The dissertation of Alessandro Sonnenfeld is approved:

_____

Professor Crystal Martin

_____

Professor Peng Oh

_____

Professor Tommaso Treu, Chair

March 2015

Luminous and Dark Matter in Early-type Galaxies

Copyright © 2015

by

Alessandro Sonnenfeld

A mamma e babbo.

Acknowledgments

I came to Santa Barbara to become an astronomer, a dream that has now become reality thanks to the many people that have helped me through this journey.

First and foremost I wish to express the deepest gratitude to my advisor, Prof. Tommaso Treu. He was determinant in my decision to pursue my PhD at UCSB, one of the best decisions I have ever made. Thank you Tommaso, you have always put me in the best possible conditions to do my work and I could not think of a better mentor for my doctoral experience.

What made this experience even better was the many postdocs I had the pleasure to work with. Three of them in particular played a special role by guiding me during my first year at UCSB and teaching me all the tricks of the trade: Matt Auger, Sherry Suyu and Vardha Bennert. Matt, Sherry and Vardha, you are truly wonderful people, when I think of 'Treu Group' I think of you.

Among my fellow students, a special thanks goes to my past officemates Chelsea Harris, Jason Kaufman and the A-Team members for all the engaging conversations and hilarious moments I shared with them.

My parents deserve the warmest thanks. I am sure it was not easy for them to let me move so far away from home, but they always encouraged me and wished for my best. Thank you, mom and dad, I would not have made it without your unconditional support.

A special thanks goes to my brother Michele. Teachers and professors taught me the science, but he taught me how to be curious and how to challenge myself. He shared with me his passion for science and travel, lighting the spark that led me to move across

the ocean and get a PhD. Thank you Michele, you are always in my heart.

Finally, I would like to thank all the friends I have met during my PhD. These years have been the densest of memories in my whole life. It has been an honor to share all these precious moments with you.

Curriculum Vitae

Alessandro Sonnenfeld

Education

2015	Ph.D. in Physics, University of California, Santa Barbara
2010	M.S. in Physics, University of Pisa, Italy, *summa cum laude*
2007	B.S. in Physics, University of Pisa, Italy, *summa cum laude*

Professional Experience

Summer 2014 Teaching Assistant, University of California, Santa Barbara

2010-2014 Graduate Research Assistant, Department of Physics, University of California, Santa Barbara

Summer 2007 Undergraduate student researcher, Stanford Linear Accelerator Center

First Author Publications

Sonnenfeld, A.; Treu, T.; Marshall, P. J.; Suyu S. H.; Gavazzi, R.; Auger, M. W.; Nipoti, C. "The SL2S Galaxy-scale Lens Sample. V. Dark Matter Halos and Stellar IMF of Massive ETGs out to Redshift 0.8" 2015, The Astrophysical Journal, in press.

Sonnenfeld, A.; Nipoti, C.; Treu, T.; "Purely Dry Mergers do not Explain the Observed Evolution of Massive Early-type Galaxies" 2014, The Astrophysical Journal, 786, 89, 8pp.

Sonnenfeld, A.; Treu, T.; Gavazzi, R.; Suyu, S. H.; Marshall, P. J.; Auger, M. W.; Nipoti, C. "The SL2S Galaxy-scale Lens Sample. IV. The dependence of the total mass density profile of early-type galaxies on redshift, stellar mass, and size" 2013, The Astrophysical Journal, 777, 98, 15pp.

Sonnenfeld, A.; Gavazzi, R.; Suyu, S. H.; Treu, T.; Marshall, P. J. "The SL2S Galaxy-scale Lens Sample. III. Lens Models, Surface Photometry and Stellar Masses for the final sample" 2013, The Astrophysical Journal, 777, 97, 13pp.

Sonnenfeld, A.; Treu, T.; Gavazzi, R.; Marshall, P. J.; Auger, M. W.; Suyu, S. H.; Koopmans, L. V. E.; Bolton, A. S. "Evidence for Dark Matter Contraction and a Salpeter Initial Mass Function in a Massive Early-type Galaxy" 2012, The Astrophysical Journal, 752, 163, 17pp.

Sonnenfeld, A.; Bertin, G.; Lombardi, M. "Direct measurement of the magnification produced by galaxy clusters as gravitational lenses" 2011, Astronomy & Astrophysics, 532, A37, 15pp.

Fellowships and Awards

2014	Dr. Pliny A. and Margaret H. Price Prize in Cosmology and AstroParticle Physics. CCAPP, Ohio State University
2013-2014	Dean's Fellowship, University of California, Santa Barbara

Abstract

Luminous and Dark Matter in Early-type Galaxies

by

Alessandro Sonnenfeld

Three open problems in our understanding of early-type galaxies are 1) identifying the process(es) responsible for their rapid size evolution, 2) accurately constraining the stellar IMF and its variations in the population, 3) measuring the density profile of their dark matter halo. We use strong lensing as the main diagnostic tool to address these issues. We first dissected a massive elliptical galaxy in its stellar and dark matter components, measuring both its IMF and the inner slope of the dark matter halo. We then collected a sample of 45 strong lenses in the redshift interval $0.2 < z < 0.8$ and used them, in combination with lenses from other surveys, to measure the slope of the total density profile, the stellar IMF and the dark matter mass in the population of massive early-type galaxies, and their time evolution. Finally, we used our measurements of the evolution of the density slope to test a galaxy growth scenario based on purely dissipationless mergers. Our main results are: the stellar IMF of massive early-type galaxies is significantly heavier than that of the Milky Way and correlates with galaxy mass; the dark matter halo has a steep slope in at least one system; more compact galaxies have less dark matter than their extended counterparts at fixed redshift and stellar mass; early-type galaxies evolve while keeping the slope of their total density profile approximately constant. This last

result cannot be reproduced with purely dissipationless mergers, therefore a little amount of dissipation is required.

Contents

Chapter 1

Introduction

1.1 Early-type galaxies

Early-type galaxies (ETGs) are objects of apparent simplicity, characterized by a smooth stellar distribution, little amounts of gas or dust, and old stellar populations. They constitute a family of objects of remarkable regularity, captured by tight scaling relations such as the fundamental plane (Dressler et al. 1987; Djorgovski & Davis 1987) and the relations between central black hole mass and galaxy properties (Ferrarese & Merritt 2000; Gebhardt et al. 2000; Marconi & Hunt 2003; Häring & Rix 2004). Despite tremendous efforts, it is still unknown what the fundamental source of this regularity is, making ETGs more mysterious objects than their appearance would suggest. Numerical simulations are now able to reproduce some of the key observables of ETGs (Hopkins et al. 2009b; Dubois et al. 2013; Remus et al. 2013; Feldmann & Mayer 2014), but the resolution and statistics that can be reached today are still too low to allow for meaningful quantitative tests. It is still very challenging to obtain realistic simulations of the baryonic component of ETGs, since this is affected by a number of complex physical processes including star formation, feedback from supernovae and the effect of an active

galactic nucleus (AGN).

Understanding the formation and evolution of ETGs is a fundamental piece in the cosmological puzzle. Any model that aims at providing a description of the Universe as a whole must be able to reproduce the observed characteristics of these objects. We can identify four aspects of the structure of ETGs that are posing challenges to our understanding of their formation and evolution: the size evolution of ETGs, the stellar initial mass function (IMF), the properties of the dark matter halo, and the link between the central black hole and the properties of the galaxy as a whole. This Thesis focuses on the first three of these problems, described in the following subsections.

1.1.1 The size evolution

At fixed stellar mass, ETGs at high ($z > 1$) redshift have on average smaller half-light radii than local quiescent galaxies (e.g. Daddi et al. 2005; Trujillo et al. 2006b; van Dokkum et al. 2008; Cassata et al. 2011; Newman et al. 2012a). This evolution in the mass-size relation could be the result of an intrinsic growth, likely as a result of mergers, or of the emergence of new systems with sizes larger than the average of the pre-existing population (progenitor bias). The relative relevance of these two effects is still a matter of debate (Newman et al. 2012a; Carollo et al. 2013; Belli et al. 2013).

Theoretical studies aimed at matching the observed size evolution of quiescent galaxies have focused on dissipationless (dry) mergers (Naab et al. 2009; Nipoti et al. 2009a; van der Wel et al. 2009; Hopkins et al. 2010; Oser et al. 2012; Hilz et al. 2013), as the low star formation rates measured in these galaxies leaves little room for a significant occurrence

of dissipative (wet) mergers. The predicted and observed merger rates in a dry-merger scenario, while still insufficient to reproduce the size growth observed at $z \gtrsim 1.5$, seem to be able to account for the late ($z \lesssim 1.5$) size evolution of quiescent galaxies (Nipoti et al. 2012; Newman et al. 2012a; Posti et al. 2013). In particular, Nipoti et al. (2012) have shown that, on average, the predictions of a purely dry merger model are marginally consistent with the observationally inferred evolution of the $M_* - M_{\rm h}$ and $M_* - R_{\rm e}$ relations in the redshift range $0 \lesssim z \lesssim 1.3$. Dry mergers, however, appear difficult to reconcile with the tightness of the observed scaling relations (Nipoti et al. 2009a, 2012; Shankar et al. 2013). It is not clear then if models based purely on dry mergers can capture the relevant aspects of the evolution of early-type galaxies (ETGs), or if additional physical ingredients are required.

In order to make progress, new observational tests are needed. Size and mass provide a crude description of the structure of a galaxy. More insight can be gained by studying the density profile of ETGs. As will be shown later in this Thesis, observationally constraining the evolution in the slope of the density profile of ETGs can help discriminate between dry or wet merger evolution scenarios.

1.1.2 The stellar initial mass function

In the Milky Way, the stellar IMF is well described by a broken power-law (Kroupa 2001; Chabrier 2003, e.g.). For stellar masses larger than $\sim 0.5 M_\odot$ the power-law slope is very close to the Salpeter (1955) value: $dN(M)/dM \propto M^{-2.35}$. For smaller masses, the IMF turns off to a shallower slope. In recent years there has been growing evidence

that the IMF of massive ETGs differs radically from that of the Milky Way, resulting in a significantly larger mass-to-light ratio (Auger et al. 2010b; Cappellari et al. 2012; Conroy & van Dokkum 2012; Spiniello et al. 2014). While the non-universality of the IMF is still a debated issue (Smith & Lucey 2013), the implications on star formation models of such a discovery, if confirmed, would be very important. A possible explanation for differences in IMF between late-type and massive early-type galaxies is a star formation mechanism based on fragmentation in supersonically turbulent molecular clouds (Padoan et al. 1997; Padoan & Nordlund 2002; Hennebelle & Chabrier 2008; Hopkins 2012, 2013). Different conditions, in particular the Mach number, in the star-forming gas would change the characteristic mass of fragmentation, resulting in different abundances of low-mass stars. New accurate measurements are needed to test this scenario. In the Milky Way, the stellar IMF can be measured simply by counting stars. The same thing is not possible for galaxies outside the local group, let alone for systems at cosmological distances. As we will show in Chapters 2 and 5, gravitational lensing can be used in combination with other dynamical probes to constrain the IMF of massive galaxies out to $z \sim 1$ (Treu et al. 2010; Sonnenfeld et al. 2012; Barnabè et al. 2013; Smith & Lucey 2013; Sonnenfeld et al. 2014; Shetty & Cappellari 2014).

1.1.3 The dark matter halo

On the observational side, most of the efforts in studies of ETGs have been focused on improving our current knowledge of the luminous component of these objects, namely the stellar populations and their cosmic evolution (e.g. Fontana et al. 2004; Cimatti et al.

2006; Pozzetti et al. 2010; Peng et al. 2010b; Choi et al. 2014), while very little is known about the dark matter component. The underlying dark matter distribution is affected by baryonic physics processes: adiabatic contraction of gas can lead to more concentrated dark matter halos (Gnedin et al. 2011) whereas supernova feedback can remove dark matter from the center of a galaxy (Pontzen & Governato 2012). Observational constraints of dark matter halos can be used to test some of the many models for the effects of baryonic physics on the evolution of ETGs. Additionally, measuring the density profile of dark matter in the center of ETGs would help addressing some issues related to the nature of dark matter itself. Dwarf scale galaxies (Oh et al. 2011) and cluster central galaxies (Newman et al. 2013) appear to have cored dark matter profiles. Are dark matter cores ubiquitous? Are they the result of dark matter physics or baryonic physics? What is the contribution of the halos ETGs live in to the dark matter annihilation signal?

Current observational constraints on the dark matter halos of ETGs are scarce and come mostly from the analysis of kinematical tracers data, either alone (see, e.g., Cappellari et al. 2013b; Agnello et al. 2014, for recent results) or in combination with strong gravitational lensing (see, e.g., Sonnenfeld et al. 2012; Newman et al. 2013; Barnabè et al. 2013; Suyu et al. 2014, for recent results). The main advantage of strong lensing is that it allows for accurate and precise measurements of masses out to cosmological distances, making it possible to explore the time dimension and address evolutionary questions (see, e.g., Treu 2010, for a recent review). In Chapters 2 and 5 we show examples of how strong lensing can be used to probe the dark matter halo of ETGs.

1.2 Gravitational lensing

Strong gravitational lensing is the main diagnostic tool used in this Thesis to probe the structure of ETGs. Here we provide a brief overview of the basic equations of strong lensing. For a comprehensive review of the subject we refer to the work by Schneider et al. (1992).

The propagation of light rays in spacetime can be described by making use of the General Relativistic version of *Fermat's principle*:

> *Let S be an event ("source") and l a timelike world line ("observer") in a spacetime ($g_{\alpha\beta}$). Then a smooth null curve γ from S to l is a light ray (null geodesic) if, and only if, its arrival time τ on l is stationary under first-order variations of γ within the set of smooth null curves from S to l.*

For a quasi-Minkowskian spacetime metric, i. e. in the presence of a small gravitational potential $U \ll c^2$, the equations describing the propagation of light rays are formally identical to the classical case if we introduce the following *effective index of refraction:*

$$n \equiv 1 - \frac{2U}{c^2}. \tag{1.1}$$

It can be shown that, in the presence of a point mass M, the deflection angle $\hat{\boldsymbol{\alpha}}$ of a light ray passing in its proximity with impact parameter $\boldsymbol{\xi}$ is

$$\hat{\boldsymbol{\alpha}} = -\frac{4GM}{c^2}\frac{\boldsymbol{\xi}}{|\boldsymbol{\xi}|^2}. \tag{1.2}$$

Cases in which the deflection angle is 1) much smaller than unity and 2) much smaller than the ratio between the typical length over which the transverse component of the gravitational potential varies and the extent of the deflecting mass in the direction of propagation of the light ray, are referred to as *thin lenses*. Condition 1) is equivalent to

non-relativistic conditions (as can be verified from Equation 1.2). Condition 2) excludes mass perturbers for which their transverse size is much smaller than their length in the direction of propagation. These conditions always hold when dealing with lensing from stars or galaxies and are violated only in the presence of black holes. The deflection angle in the presence of a thin lens can be calculated by independently summing the contributions from individual point masses that define the perturber:

$$\hat{\boldsymbol{\alpha}}(\boldsymbol{\xi}) = \frac{4G}{c^2} \int_{\mathbb{R}^2} \frac{(\boldsymbol{\xi} - \boldsymbol{\xi}')\Sigma(\boldsymbol{\xi}')}{|\boldsymbol{\xi} - \boldsymbol{\xi}'|^2} d^2\xi', \tag{1.3}$$

where $\Sigma(\boldsymbol{\xi})$ is the *projected surface mass density*.

We can then write the fundamental equation of gravitational lensing, namely the *lens equation*, relating the angular position of a light source $\boldsymbol{\beta}$ with the position of its image $\boldsymbol{\theta}$ in the presence of a perturber with deflection angle $\hat{\boldsymbol{\alpha}}(\boldsymbol{\theta})$:

$$\boldsymbol{\beta} = \boldsymbol{\theta} - \frac{D_{ds}}{D_s}\hat{\boldsymbol{\alpha}}(\boldsymbol{\theta}), \tag{1.4}$$

where D_s and D_{ds} are the angular diameter distances between observer and source and deflector and source, respectively. The above equation can be easily generalized to multiple lens planes. A schematic representation of a gravitational lens system is shown in Figure 1.1.

The equations presented so far can be used to describe any lensing effect caused by a thin lens. When multiple images of the same source are produced, we are in the *strong lensing* regime. It is useful to introduce the *critical density* Σ_{cr}:

$$\Sigma_{cr} \equiv \frac{c^2 D_s}{4\pi G D_d D_{ds}}, \tag{1.5}$$

where D_d is the angular diameter distance between observer and deflector. The critical
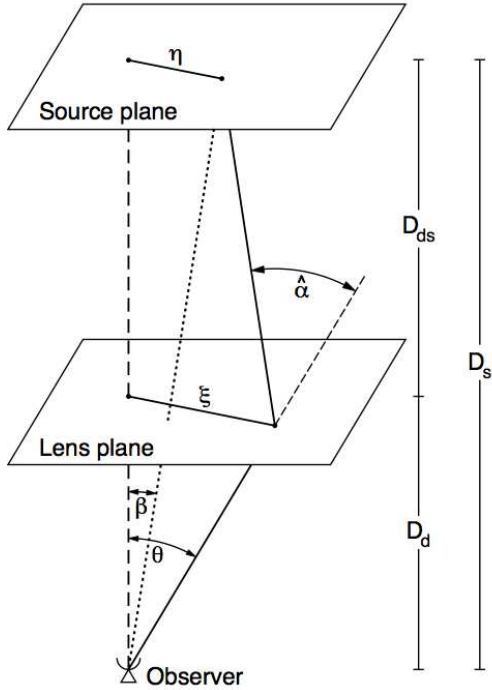
Figure 1.1: Sketch of a typical gravitational lens system (Bartelmann & Schneider 2001).

density depends only on the distances between source, deflector and observer and can be used to define the *dimensionless surface mass density* κ of a lens:

$$\kappa(\boldsymbol{\theta}) \equiv \frac{\Sigma(\boldsymbol{\theta})}{\Sigma_{\mathrm{cr}}}. \tag{1.6}$$

Only lenses with $\kappa(\boldsymbol{\theta}) > 1$ for some value of $\boldsymbol{\theta}$ can act as strong lenses.

The radius of the iso-density contour within which the average surface mass density is equal to the critical density is defined as the *Einstein radius* R_{Ein}:

$$\bar{\kappa}(< R_{\mathrm{Ein}}) = 1. \tag{1.7}$$

The Einstein radius is close in value to the half-separation between multiple images of the same source and can be measured with high precision in typical ETG strong lens systems. Details on how to measure R_{Ein} can be found in Chapter 3. A measurement of the Einstein radius of a lens gives the total projected mass enclosed within R_{Ein}. Mea-

surements of this kind are used in this Thesis to probe the structure of ETGs.

The structure of this Thesis is the following. In Chapter 2 we present a thorough study of a strong gravitational lens elliptical galaxy, through which we measured both the stellar IMF and the inner slope of the dark matter halo of this object. In Chapter 3 we introduce a new strong lensing survey, the Strong Lensing Legacy Survey (SL2S), aimed at extending in redshift space the current number of known lenses. In Chapter 4 we show how the data collected from the SL2S survey can be used to measure the total density profile of the population of massive ETGs and its evolution. In Chapter 5 we use the same sample of lenses to statistically constrain the stellar IMF and dark matter mass of the population of ETGs. In Chapter 6 we use the observations of the evolution in the density profile presented in Chapter 4 to test a theoretical model based on growth of ETGs by purely dry mergers. We summarize our results and discuss future extensions of this work in Chapter 7.

Chapter 2

Stellar and dark matter decomposition in a massive elliptical galaxy

This chapter was published as Sonnenfeld, A., Treu, T., Gav++08, R., Marshall, P. J., Auger, M. W., Suyu, S. H., Koopmans, L. V. E., Bolton, A. S. "Evidence for Dark Matter Contraction and a Salpeter Initial Mass Function in a Massive Early-type Galaxy" 2012, The Astrophysical Journal, 752, 163 and is included here with minor formatting adjustments.

The stellar IMF is the main source of uncertainty in the determination of the stellar mass-to-light ratio in systems with good photometric data. Conversely, if we accurately measure the stellar mass of a system by independent means, it is possible to constrain the IMF by comparing the true stellar mass with the one inferred from photometric fitting. It is possible to measure stellar masses dynamically, granted that the contribution of dark matter to the total mass is taken into account. Determining the stellar IMF and the properties of the dark matter halo are then two aspects of the same problem.

Observationally, the dark matter halo is defined as a mass component that does not follow the light distribution. Typically, stellar and dark matter mass are measured by fitting a bulge and a halo mass component to lensing and stellar kinematics data. The

density profile of the stellar component is known very accurately from photometry, while we must assume a parametrized form for the density profile of the halo. The dark matter halo is believed to have a shallower density profile ($\rho(r) \propto r^{-1}$ in dark matter only simulations Navarro et al. 1997) than the stars, making it possible to disentangle the two components. For typical early-type galaxy strong lenses however, there are residual degeneracies between anistropy, stellar mass to light ratio and inner slope of the dark matter halo and therefore the constraints are weak (Koopmans & Treu 2003; Treu & Koopmans 2004). For this reason, previous studies have adopted theoretically motivated mass density profiles for the dark matter halo (Treu et al. 2010; Auger et al. 2010b), rather than free power laws.

Here we present a detailed study of an early-type galaxy at redshift $z = 0.222$. The galaxy is the strong gravitational lens of the system SDSSJ0946+1006, part of the SLACS sample (Bolton et al. 2004). This ETG is special in that it lenses two sources at different redshifts, creating two nearly complete Einstein rings of different radii. For this reason, the system is also referred to as the "Jackpot". The first lensed source is at redshift $z_{s1} = 0.609$, while there is no spectroscopic measurement of the redshift of the second ring. Thanks to the presence of the two rings, this system provides more information than typical gravitational lenses, despite the lack of the second source redshift. A first study of SDSSJ0946+1006 was carried out by Gavazzi et al. (2008, SLACS Paper VI). An independent lensing analysis of this system was performed by Vegetti et al. (2010), which led to the discovery of a small satellite with no visible counterpart. Here we include new high-quality photometry obtained with the Hubble Space Telescope (hereafter HST) and new deep and spatially resolved spectroscopy obtained at the Keck Telescope. The goal of

our study is to separate the contribution of dark and stellar matter to the total mass of the lens, making as few assumptions as possible about the density profile of the dark matter halo. This task is achieved by combining lensing and dynamics information. Unlike typical early-type galaxy lenses, the wealth of information provided by this system allows us to determine both the mass of the stellar bulge and the inner slope of the dark matter halo. Thanks to the multi-band HST photometry we are able to obtain a photometric redshift of the outer ring, that is necessary for improving the constraints from the lensing data, and to infer stellar masses from stellar population synthesis (SPS) fitting. The comparison between this measurement of the stellar mass and the one obtained through lensing and dynamics allows us to constrain the IMF of the stars in the lens. This is the most robust measurement of the inner slope of the dark matter halo and IMF of an isolated massive ETG.

The structure of this Chapter is the following. In Section 2.1 we describe the new photometric data. Our measurement of the photometric redshift of the outer ring is presented in Section 2.2. In Section 2.3 we present the spectroscopic data and in Section 2.4 we describe measurements of the stellar mass of the lens from stellar population synthesis fitting. Section 2.5 describes a lensing and dynamics model assuming a power-law density profile for the total density profile of the lens, while in Section 2.6 we present the bulge-halo decomposition of the lens. We discuss our results in Section 2.7 and summarize in Section 2.8.

In this Chapter and throughout this Thesis we assume the following values for the cosmological parameters: $H_0 = 70$ km s^{-1}Mpc^{-1}, $\Omega_M = 0.3$, $\Omega_\Lambda = 0.7$. Magnitudes are expressed in the AB system, images are North-up and position angles are in degrees

Table 2.1: Summary of the HST observations.

Instrument	Filter	Exp. time	N_{exp}	Date
WFC3 IR	F160W	2397 s	4	09/12/2009
ACS	F814W	2096 s	4	3/11/2006
WFPC2	F606W	4400 s	4	18/12/2009
WFC3 UVIS	F438W	2520 s	4	20/03/2010
WFC3 UVIS	F336W	5772 s	4	20/03/2010

East of North. In showing our results we display posterior PDFs in multiple projections wherever possible, but when giving a point estimate of an inferred parameter we quote the position of the peak of its one-dimensional marginalised distribution, with uncertainties defined by the 68% credible region.

2.1 Multicolor HST photometry

We present HST images of the lens system SDSSJ0946+1006 in five different bands. In SLACS Paper VI we reported results based on an ACS F814W image only. Images in WFPC2 F606W and WFC3-IR F160W (Cycle 16, Program 11202, PI Koopmans) were available for SLACS Paper IX (Auger et al. 2009). In addition to those data, we now have WFC3 images in F438W and F336W bands (Cycle 17, Program 11701, PI Treu). Table 2.1 summarizes the observations. This section describes the data reduction process (§ 2.1.1) and the photometric properties we derived for the lens galaxy (§ 2.1.2). For conciseness, we sometimes refer to the F160W, F814W, F606W, F438W, F336W bands as H, I, V, B, U respectively. A color composite image of the lens system is shown in Figure 2.1
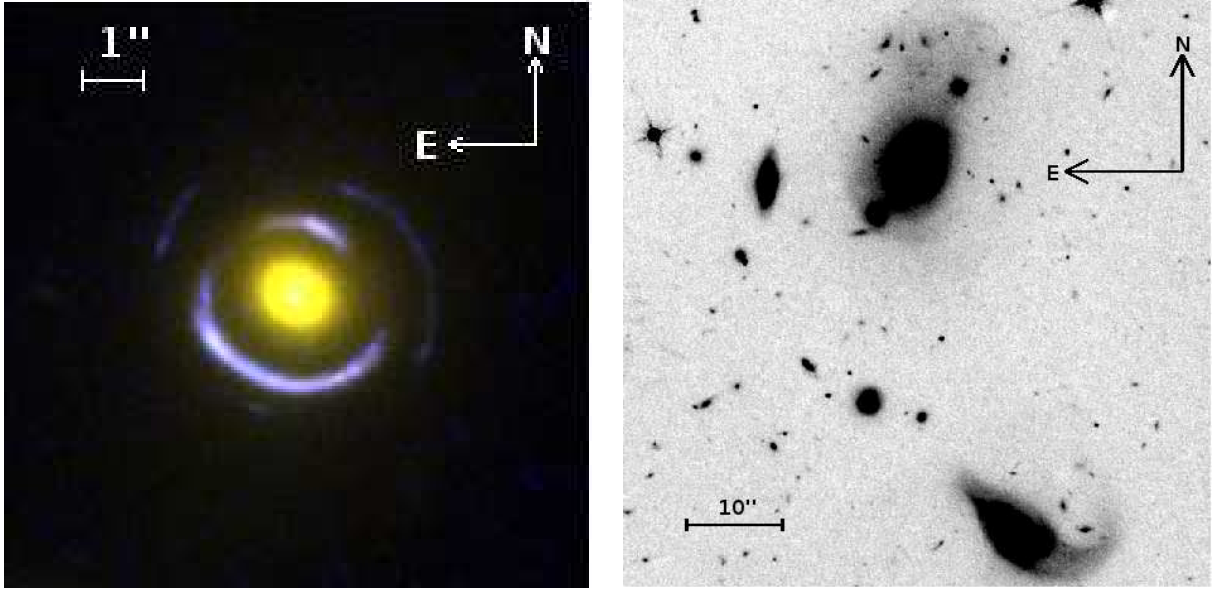
Figure 2.1: *Left panel:* Gravitational lens system SDSSJ0946+1006 in a combination of F814W, F606W and F336W HST images. *Right panel:* WFC3-IR F160W image of the lens system and its surroundings. Note the irregular shape of the faint stellar component at the outskirts of the lens galaxy (top of the image). At the bottom, a neighbor also shows signs of tidal disruption. Both these features may be the result of a close encounter between the two objects.

2.1.1 Data reduction

The data are treated with the standard HST reduction pipeline. For each image, frames are coadded and resampled in a uniform pixel scale using the software MUL-TIDRIZZLE (Fruchter et al. 2009). Pixel sizes are $0.10''$ for the F160W image, $0.050''$ for the F814W and F606W images, and $0.0396''$ for the F438W and F336W images. The images are then brought to the same orientation and $0.050''$ pixel scale by using the software SWARP (Bertin et al. 2002). The PSF of each image is estimated from stars in the field.

2.1.2 Lens galaxy properties

The brightness distribution of the main lens galaxy is first obtained by fitting Sérsic profiles to the data. This task is achieved with the software SPASMOID, developed by M. W. Auger and described by Bennert et al. (2011). SPASMOID fits the data in all the bands simultaneously with a unique model, determining total magnitude and colors of the galaxy at once. By using a single Sérsic component we find a best-fit profile described by a Sérsic index $n = 6.0$, axis ratio $q = 0.95$ and effective radius $r_{eff} = 2.93''$. However, the residuals left by this single-component fit are rather large. Consequently, we add a second component, allowing for the position angle of the major axes of the two profiles to be different but imposing a common centroid. In the fitting process, the light from the rings is masked out manually. This procedure gives robust estimates of the colors of the lens, rather independent from the model adopted to describe the data. Color information will be used in Section 5 to constrain the stellar population. In Fig. 2.2 we show the images of the system in the five bands, before and after subtracting the main lens. Residuals are on the order of a few percent in the F814W band image. Table 2.1.2 reports the best-fit structural parameters of the model, while the best-fit colors are given in Table 2.4. It is worth pointing out that the major axes of the two components are almost perpendicular, and that the mean surface brightness within the effective radius of component 1 is a factor ~ 30 larger than that of component 2. The measured magnitude in the F814W band is consistent with the value reported by Gavazzi et al. (2008) for the same object.

In order to both explore model-dependent systematic errors and obtain a computa-

Component	m_{F814W} (mag)	r_{eff} (arcsec)	n	q	PA (degrees)	$\langle \mathrm{SB} \rangle_{\mathrm{e, F814W}}$ (mag arcsec^{-2})
1	18.38 ± 0.20	0.50 ± 0.10	2.34 ± 0.50	0.79 ± 0.10	63.0 ± 1.0	18.87 ± 0.10
2	17.44 ± 0.10	4.46 ± 0.50	1.60 ± 0.50	0.64 ± 0.10	-23.4 ± 1.0	22.68 ± 0.20

Table 2.2: Best fit parameters for the double-Sérsic model surface brightness profile of the main lens: magnitude in the F814W band, effective radius, Sérsic index (n), axis ratio (q), position angle of the major axis (East of North), effective surface brightness. Each line refers to one of the Sérsic components of the model. The errors represent the typical range of values for the parameters allowed by the model. These errors are correlated: for example, an increase in the value of the Sérsic index n results in a change of the effective radius to fit the observed slope in surface brightness.

tionally more tractable description of the light profile for our lensing analysis, we also model the lens light with the following surface brightness distribution:

$$I(x, y) = I_c r_c \left[\frac{1}{\sqrt{r_c^2 + R^2}} - \frac{1}{\sqrt{r_t^2 + R^2}} \right], \tag{2.1}$$

where $R^2 \equiv x^2/q + qy^2$. This profile corresponds to a truncated pseudoisothermal elliptical mass distribution (tPIEMD) in 3d, with r_c and r_t corresponding to the core radius and truncation radius respectively. Note that the number of parameters of the model is the same as that of a Sérsic profile. Two components are used, as in the Sérsic case. The best-fit parameters are reported in Table 2.1.2. Both the double-Sérsic and the double-tPIEMD profiles fit well the photometry of the lens, with residuals within the outer ring on the order of a few percent in the F814W band (see Figure 2.2).

The inferred total magnitude in the two models is different, but this is due to the different behavior at large radii, where there are no data. In fact, the magnitude within the inner ring is the same for the two models to within 0.01 mags and the inferred colors are consistent within the errors with those reported in Table 2.4.

The infrared F160W data reveal distorsions in the shape of the light distribution at
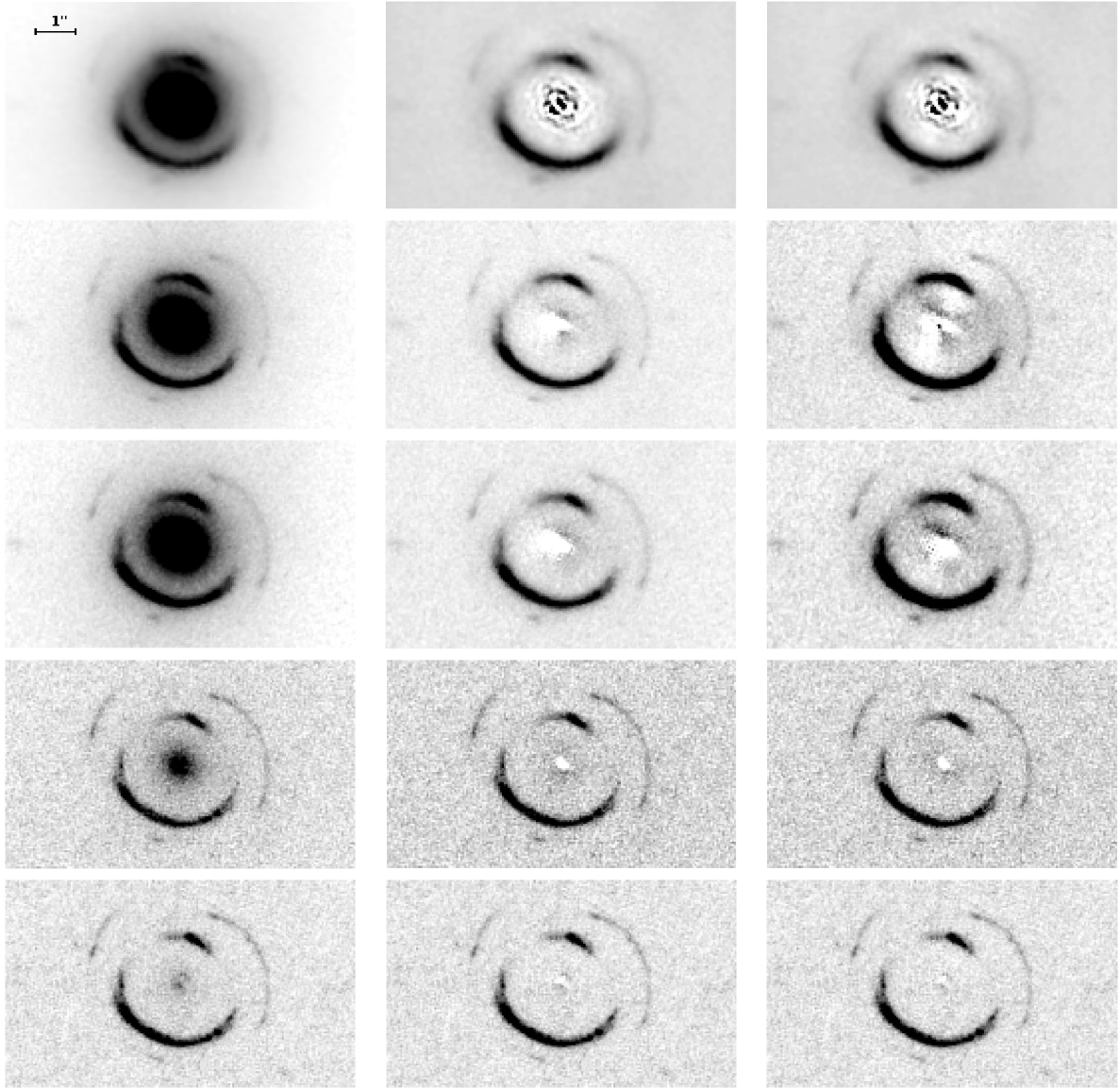
Figure 2.2: From top to bottom: HST F160W, F814W, F606W, F438W and F336W images of the lens system SDSSJ0946+1006 before (left column) and after (middle and right column) light subtraction. *Middle column:* light distribution modeled as a double Sérsic profile, with parameters given in Table 2.1.2. *Right column:* light distribution modeled as a double tPIEMD profile, with parameters given in Table 2.1.2.

Component	m_{F814W} (mag)	r_c (arcsec)	r_t (arcsec)	q	PA (degrees)	$\langle\text{SB}\rangle_{\text{e,F814W}}$ (mag arcsec^{-2})
1	18.75 ± 0.20	0.066 ± 0.010	0.50 ± 0.05	0.66 ± 0.10	63.0 ± 1.0	19.24 ± 0.10
2	17.15 ± 0.10	0.082 ± 0.010	6.05 ± 0.10	0.71 ± 0.10	-24.3 ± 1.0	22.48 ± 0.20

Table 2.3: Best fit parameters for the double-tPIEMD model surface brightness profile of the main lens: magnitude in the F814W band, core radius (r_c), truncation radius (r_t), axis ratio (q), position angle of the major axis (East of North), effective surface brightness.

Table 2.4: Colors of the lens galaxy.

Color	Component 1	Component 2	Global
I - H	1.16 ± 0.05	0.86 ± 0.05	0.96 ± 0.05
V - I	0.81 ± 0.05	0.96 ± 0.05	0.91 ± 0.05
B - V	2.36 ± 0.20	1.52 ± 0.05	1.73 ± 0.05
U - B	2.30 ± 0.30	1.32 ± 0.10	1.44 ± 0.10

large radii (see Figure 2.1), a possible signature of tidal interactions. As previously noted by Gavazzi et al. (2008), a galaxy in the neighborhood of the lens also shows signs of a tidal interaction (see Figure 2.1). It is possible that the two galaxies are undergoing a merger. This deviation from a regular light profile is located far from the probed by our lensing and dynamics measurements and is therefore not a concern for the accuracy of our models. The central part appears smooth to the few percent level and it is unlikely that the ongoing interaction would have an effect on its structure, given its deep potential well. However, as we will discuss in § 2.7.2 this feature provides an interesting clue to the formation mechanism of this galaxy.

Another interesting feature is revealed by the image in the F336W (U) band, as there seems to be some structure in the center of the lens (see Figure 2.2). The fact that this feature is clearly visible only in the U band, where the lens is fainter, may suggest that it is in fact a bluer object distinct from the central galaxy, or blue emission from an active

nucleus. Alternatively, the observed detail could be the result of the presence of a dust lane that separates the light of the lens into two components at shorter wavelengths. In principle it could also be an additional image of the lensed sources.

One way to discriminate between a blue object or a dust lane is to study the position of the centroid of the lens in the different bands. A blue object would shift the centroid towards itself at bluer wavelengths, while a dust lane would remove blue light, causing the apparent centroid to move away from it. When fitting for the centroid of the lens, this latter case is observed: the centroid moves by about one pixel towards the S-E in the F336W and F438W bands with respect to the F814W band. This is a significant effect given the subpixel accuracy of centroniding, and it suggests that dust is most likely the cause of the observed feature in the F336W band. A more detailed discussion of the dust issue is given in Appendix A.

2.2 Photometric redshift of the outer ring

2.2.1 Colors of the ring

One of the main goals of this study is to constrain better the mass distribution in the lens galaxy by obtaining a photo-z of the outer ring. This task requires a measurement of the colors of the ring. A color map of the outer ring is obtained as follows. For each pair of neighboring bands, λ_1, λ_2, we align the corresponding images and then convolve each image with the PSF of the neighboring band. In this way we obtain pairs of images with the same effective PSF, necessary to get an unbiased estimate of the color for each pixel.

Table 2.5: AB colors of the outer ring

I - H	0.61 ± 0.10
V - I	0.21 ± 0.10
B - V	0.15 ± 0.10
U - B	0.53 ± 0.10

Global colors are then measured in the following way. For a given pair of bands, we select individual pixels with flux larger than the background by more than two sigma in both of the bands considered. We make the assumption that the source has spatially uniform colors and estimate them statistically by taking a weighted mean of the individual pixel colors. The measured values of the colors, corrected for galactic extinction, are reported in Table 2.5.

2.2.2 Measuring the photo-z

To estimate the photometric redshift of the outer ring we make use of the software BPZ (Bayesian Photo-z; Benítez 2000). Photo-z analysis consists of fitting synthetic SEDs to the observed colors. BPZ works in a Bayesian framework that allows us to combine the inference with that from other pieces of information: given a prior probability distribution for the source redshift and galaxy type, BPZ calculates the probability of the source being at redshift z_{s2} given its colors $\mathbf{C}$ and magnitude m, $P(z_{s2}|\mathbf{C}, m)$. The stellar templates used for the SED fitting are described by Coe et al. (2006). The F814W magnitude is taken from Gavazzi et al. (2008), where the brightness distribution of the source was reconstructed after a lens modeling. The value adopted is therefore $m_{\mathrm{F814W}} = 27.01 \pm 0.19$

For the redshift distribution we use a prior $P(z|m_{\mathrm{F814W}})$ suggested by Benítez (2000)
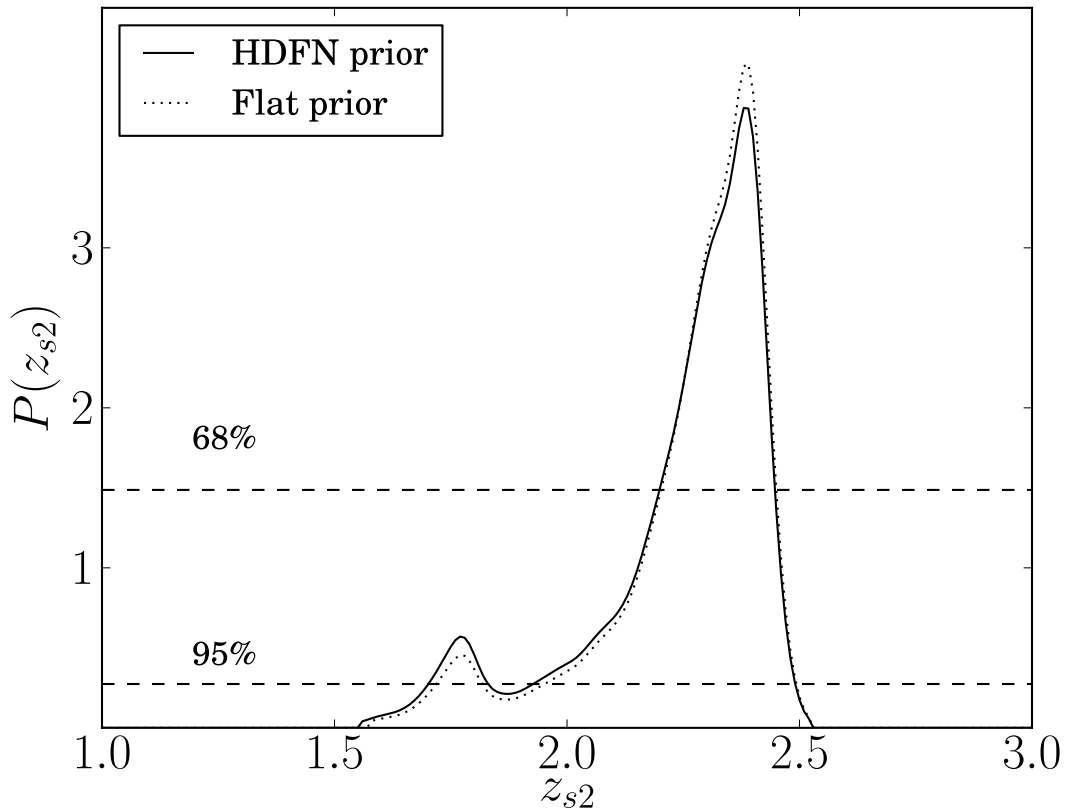
Figure 2.3: *Solid line:* posterior probability distribution function of the source redshift, as calculated with BPZ, assuming a prior on z_{s2} from Hubble Deep Field North number counts. Overplotted are the levels corresponding to 68% and 95% enclosed probability. *Dotted line:* posterior PDF assuming a flat prior on z_{s2}.

and based on number counts from the Hubble Deep Field North (HDFN). Figure 2.3 shows the redshift posterior probability distribution function $P(z_{s2}|\mathbf{C}, m_{\mathrm{F814W}})$. The most likely redshift with 68% confidence interval is $z_{s2} = 2.41^{+0.04}_{-0.21}$. As will be shown later, this information is sufficient to put interesting constraints on the model of the lens system. We also calculated the photo-z assuming a flat prior on z_{s2}, and found a nearly identical result. Colors calculated with a different lens light subtraction, the double-Sérsic model, yield the same photo-z well within the quoted uncertainties.

Table 2.6: Spectroscopic observations: summary

Date	Exp. time	Slit width	Dichroic	Blue grism	Red grating	Red λ_c	Weather	Seeing
12/23/2006	16200	1.0"	560	600/4000	831/8200	6819$\mathring{A}$	Good	0.8"
12/24/2006	12600	1.0"	680	300/5000	831/8200	7886$\mathring{A}$	Good	0.8"

2.3   Keck Spectroscopy

The data were collected during the nights of 2006 December 23 and 24 with the LRIS instrument at the Keck Telescope I. The original goals of the observations were to measure a velocity dispersion profile of the foreground deflector and to measure the redshift of the outer ring. The first goal was succesfully achieved, while we were not able to detect any spectroscopic signature from the farthest source.

Because of the dual scope of our study, two different instrumental setups were used. The first setup, used during the first night, was optimized for a better measurement of the velocity dispersion of the deflector. The wavelength range in the red detector, the one used for the measurement of σ, was $\sim 5700 - 7600\mathring{A}$, bracketing important absorption features in the rest frame of the lens at $z = 0.222$. During the second night we centered the slit on the longest arc of the outer ring, and used a setup with a broader wavelength range, up to $\sim 8600\mathring{A}$. A summary of the observations, with specifications on the setups used, is provided in Table 2.6. The spectrum of the system is shown in Fig. 2.4. There is no evidence for the presence of emission lines from objects other than the foreground lens and the inner ring. Given our measurement of the photo-z of the outer ring, we would expect Ly-α emission to fall around $\sim 4150\mathring{A}$, but it cannot be identified in our spectrum. We can put an upper limit of $\sim 5 \times 10^{-18}$ erg cm^{-2} s^{-1} to the flux in Ly-α
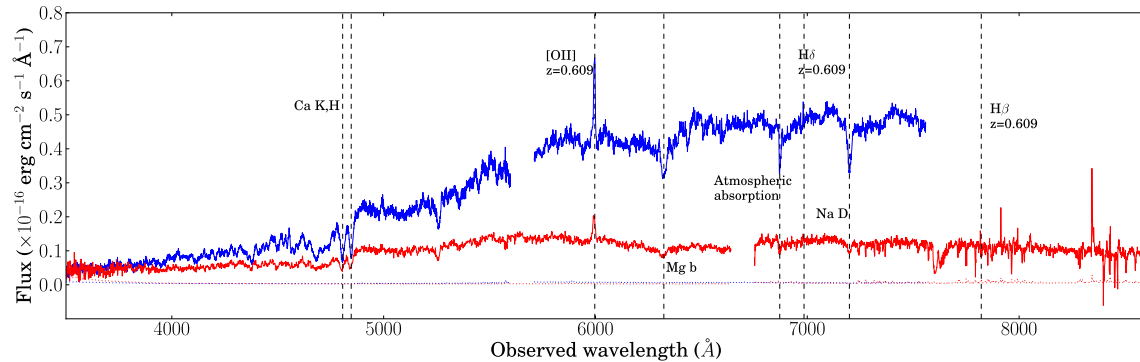
Figure 2.4: LRIS spectra of the Jackpot. *Blue:* data from the first night. *Red:* data from the second night. The two spectra are extracted from rectangular apertures $1'' \times 3.36''$. Dotted line: noise level.

from the source.

2.3.1 Velocity dispersion

The velocity dispersion of the main lens is measured by fitting stellar templates convolved with a Gaussian velocity distribution to the observed spectrum. This operation is carried out with a Monte Carlo Markov Chain approach, using a code developed by M. W. Auger, and described by Suyu et al. (2010). The rest frame wavelength range used for the fit is $5100 - 5850\text{Å}$. For the stellar templates we used linear combinations of nine spectra from the INDO-US library, corresponding to K,G,F and A stars. The most prominent absorption feature in the wavelength range considered is Mgb (5175Å). However, we experienced difficulty in finding a good fit to both Mgb and the rest of the spectrum. It is known that some galaxies have enhanced magnesium features in the spectrum that are not well reproduced in standard stellar templates (Barth et al. 2002). For this reason we decided to mask the Mgb absorption line out of the fitted spectrum.

With the aim of obtaining a velocity dispersion profile, we measured σ in a set of

Slit offset	$\langle v \rangle$	σ
(arcsec)	(km s^{-1})	(km s^{-1})
-1.05	101 ± 21	252 ± 25
-0.84	85 ± 16	273 ± 18
-0.63	62 ± 11	263 ± 14
-0.42	30 ± 10	278 ± 12
-0.21	20 ± 10	287 ± 11
0.00	0 ± 9	287 ± 11
0.21	-22 ± 11	286 ± 11
0.42	-55 ± 12	299 ± 13
0.63	-67 ± 13	274 ± 15
0.84	-63 ± 15	272 ± 19
1.05	-94 ± 24	301 ± 25

Table 2.7: Mean velocity and velocity dispersion profile. Apertures are $1.00 \times 0.21''$ rectangles.

apertures. The spatial position of the apertures was determined by fitting the centroid of the trace of the lens in the twodimensional spectra and it is accurate to $\sim 0.02''$. In Table 2.3.1 and Fig. 2.5 we report the measured values of σ and of the mean velocity in each aperture, while in Fig. 2.5 we show the fit in the central $0.42''$ as an example. There is evidence for some rotation, with $v_{\rm rot}^2 \ll \sigma^2$.

2.4 Stellar masses

Here we present a measurement of the stellar mass of the foreground lens galaxy. The procedure adopted is the following: we fit stellar population synthesis models to the observed spectral energy distribution (SED) of the galaxy. A measurement of this kind was already performed by Grillo et al. (2009) and Auger et al. (2009, SLACS Paper IX) for the same object. Their results agree within the errors. Grillo et al. (2009) used SDSS multiband photometry (u, g, r, i, z bands) as their observed SED. In SLACS Paper IX,
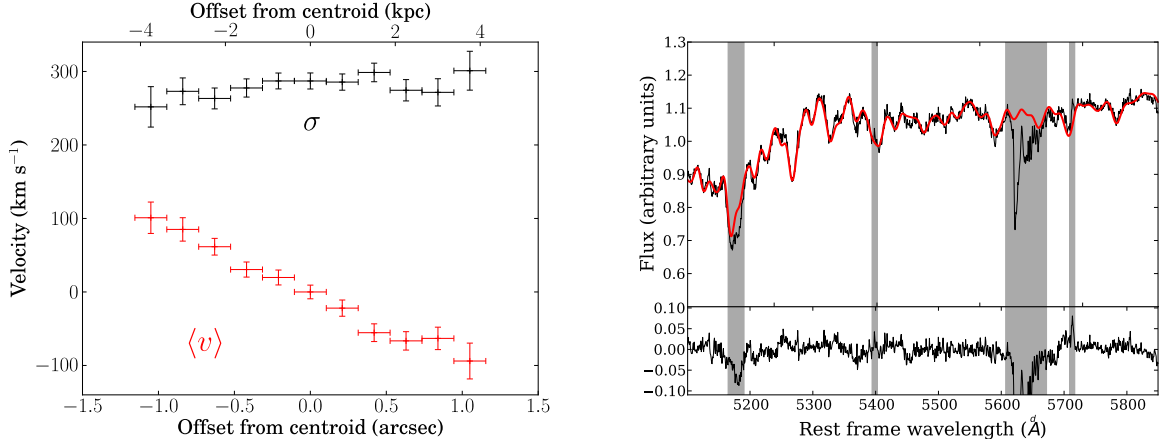
Figure 2.5: *Left panel:* Mean velocity and velocity dispersion profiles of the main lens within 1.15″ from the centroid. *Right panel:* Fit of the velocity dispersion of the lens. *Top:* The red curve is the best fit synthetic spectrum. Shaded regions are masked and not used for the fit. *Bottom:* Residuals of the fit in fractions of the total flux.

high resolution HST data was used, but only in two bands (F814W and F606W). Auger et al. (2009) also introduced a powerful statistical analysis method, based on Bayesian statistics that allows for physically meaningful priors on the model parameters as well as a full exploration of uncertainties and correlation between the inferred parameters. With five band HST photometry we can now extend the analysis of SLACS Paper IX, to obtain a more robust estimate of the stellar mass.

The fitting method is the same as that developed by Auger et al. (2009), and can be summarized as follows. Composite stellar population models are created from Bruzual & Charlot (2003) stellar templates. The star formation history is modeled with a single exponentially decaying burst. The parameters of the model are age, metallicity, exponential burst timescale, dust reddening and stellar mass. The parameter space is explored using a Monte Carlo Markov Chain (MCMC) routine, through which the posterior PDF is characterized. The stellar templates used are based on either a Salpeter or a Chabrier IMF. For the description of the photometry of the lens we use the double tPIEMD model

Table 2.8: Stellar mass of the foreground lens, from SPS models

IMF	Chabrier $\log(M_*/M_\odot)$	Salpeter $\log(M_*/M_\odot)$	
Comp. 1	$10.85^{+0.09}_{-0.06}$	$11.13^{+0.05}_{-0.11}$	This work
Comp. 2	$11.27^{+0.05}_{-0.08}$	$11.52^{+0.06}_{-0.08}$	This work
Total	11.40 ± 0.06	11.66 ± 0.06	This work
	$11.38^{+0.04}_{-0.12}$	$11.61^{+0.02}_{-0.08}$	Grillo et al. (2009)
	11.34 ± 0.12	11.59 ± 0.12	Auger et al. (2009)

described in Sect. 2.1.2, that is consistent with the analyses presented in the following Sections. The stellar masses of the two components are fitted independently. Results are listed in Table 2.8, together with the values previously found by Grillo et al. (2009) and Auger et al. (2009).

The analysis reveals the presence of dust for component 1, coherently with our previous findings. Repeating the fit with the dust-corrected magnitudes yields indistinguishable stellar masses. The logarithm of the stellar masses changes by 0.06 if we use the description of the light profile with Sérsic components instead of tPIEMDs. This is due to the different behavior at large radii of the two profiles. Differences in the mass within the outer Einstein radius for the two models are instead well within the measurement errors.

2.5 A single component model: measuring the average slope

In this Section we present a single-component lensing and dynamics study of the foreground galaxy, where the total density distribution of the lens is described with a

power-law. The goal is to obtain a measurement of the slope of the total mass profile and also to test the accuracy allowed by our data in constraining mass models. The system, with its two Einstein rings, offers more constraints than typical single-source lenses. However, the analysis is complicated by the presence of two different lenses along the line of sight. Light rays from the second source are first deflected by the object corresponding to the inner ring and then by the foreground lens, with the result that, unlike the single lens case, the relation between the size of the outer Einstein ring and the enclosed projected mass of the lens is nontrivial. Nevertheless, this can be properly accounted for as described below.

A first lens modeling of the system was carried out in SLACS Paper VI. The procedure adopted there was a conjugate points method: multiply imaged spots in the lensed features are identified, and the lens model is determined by minimizing the distance between the corresponding points in the source plane. This is a conservative approach, since it does not make use of all of the information from the surface brightness of the rings. The main lens was modeled as a power law ellipsoid, with dimensionless surface mass density $\kappa \equiv \Sigma/\Sigma_{cr}$ given by:

$$\kappa(\vec{r}, z_s) = \frac{b_\infty^{\gamma'-1}}{2}(x^2 + y^2/q^2)^{(1-\gamma')/2}\frac{D_{\mathrm{ls}}}{D_{\mathrm{os}}}, \tag{2.2}$$

where $b_\infty = 4\pi(\sigma_{\mathrm{SIE}}/c)^2$ and D_{ls} (D_{os}) is the angular diameter distance of the source relative to the lens (observer). The second lens (first source corresponding to the brighter arc) was modeled as a singular isothermal sphere (SIS). The model parameter space was explored via a MCMC. The results showed that two types of solution are possible: a model with larger σ_{SIE}, shallower slope γ' and less massive second lens, or a model with

a more massive second lens and steeper main lens slope (see Figure 9 of SLACS Paper VI, or black contours of Figure 2.6). Part of this degeneracy was due to our ignorance of the redshift of the outer ring.

In this Chapter we use the lens model of SLACS Paper VI described above and improve it by incorporating 1) our measurement of photo-z of the outer ring and 2) a stellar dynamics analysis.

2.5.1 Stellar dynamics modeling

We wish to use our measurements of the velocity dispersion profile of the lens to constrain our lens models. This is done with a procedure similar to that adopted by Suyu et al. (2010), which can be described as follows. For a given model provided by the lensing analysis, we compute a model velocity dispersion profile and compare it to the observed one. The model velocity dispersion is obtained by solving the spherical Jeans equation

$$\frac{1}{\rho_*}\frac{d\rho_*\sigma_r^2}{dr} + 2\frac{\sigma_\theta^2}{r} = -\frac{GM(r)}{r^2}, \tag{2.3}$$

where $\rho_*(r)$ is the density distribution of the light, σ_r and σ_θ are the radial and tangential components of the velocity dispersion tensor, $M(r)$ is the total mass enclosed within the spherical shell of radius r. We impose spherical symmetry in the mass model by adopting a spheroidal mass distribution

$$\rho(r) \propto r^{-\gamma'} \tag{2.4}$$

with normalization chosen such that the total projected mass enclosed within the Einstein radius equals that of the corresponding circularized lens model. The light distribution is

described as the sum of two tPIEMD profiles, with the same parametrization described in Section 2.1.2 (best-fit parameters are in table 2.1.2). The 3d stellar distribution corresponding to the surface brightness profile (2.1) used to fit the photometry is

$$\rho(r) = \rho_c r_c^2 \left[\frac{1}{r_c^2 + r^2} - \frac{1}{r_t^2 + r^2} \right], \tag{2.5}$$

with $r \equiv x^2/q_* + q_* y^2 + z^2$. Here we set the axes ratios q_* to one, as we are assuming spherical symmetry.

We then assume a Osipkov-Merritt model for the velocity dispersion tensor (Osipkov 1979; Merritt 1985):

$$\frac{\sigma_\theta^2}{\sigma_r^2} = 1 - \frac{r^2}{r_a^2 + r^2}, \tag{2.6}$$

where r_a is the anisotropy radius (orbits are radially anisotropic beyond r_a). Finally, we simulate the line-of-sight velocity dispersion measured in our apertures. Rotation is neglected. Although the lens is seen to be rotating, its mean velocity is small compared to the velocity dispersion and should not contribute much to the dynamics of the object. The effect of this approximation will be discussed further below.

2.5.2   Combining the constraints

The models of the lens are defined by the set of parameters $\boldsymbol{\eta} \equiv \{\sigma_{\mathrm{SIE,lens}}, \gamma', \sigma_{\mathrm{SIS,s1}}, z_{s2}\}$: the strength and power-law index of the foreground lens, the strength of the background lens and the redshift of the outer ring, respectively. Each model gives a prediction of the velocity dispersion in each aperture, $\sigma_{\mathrm{ap},i}^{\mathrm{(mod)}}$. The new posterior probability distribution for the model is obtained via importance sampling: the MCMC sample corresponding to the lens modeling of SLACS Paper VI is weighted by the likelihood of the measurements

$\mathbf{d} \equiv \{z_{s2}, \sigma_{\mathrm{ap},i}^{\mathrm{(meas)}}\}$ given the model parameters $\boldsymbol{\eta}$. The following likelihood function is used:

$$L(\mathbf{d}|\boldsymbol{\eta}) = P_z(z_{s2}) \prod_i G_i(\sigma_{\mathrm{ap},i}^{\mathrm{(meas)}}|\boldsymbol{\eta}) \tag{2.7}$$

where $P_z(z_{s2})$ is the PDF in Figure 2.3 and

$$G_i(\sigma_{\mathrm{ap},i}^{\mathrm{(meas)}}|\boldsymbol{\eta}) = \frac{1}{\sqrt{2\pi\Delta_{\sigma,i}^2}} \exp -\frac{(\sigma_{\mathrm{ap},i}^{\mathrm{(meas)}} - \sigma_{\mathrm{ap},i}^{\mathrm{(mod)}})}{2\Delta_{\sigma,i}^2}, \tag{2.8}$$

and $\sigma_{\mathrm{ap},i}$ and $\Delta_{\sigma,i}$ are the zeroth and second moment of the posterior PDF of the measured velocity dispersion in aperture i, respectively.

In Fig. 2.6 we show the updated Posterior PDF obtained by importance sampling with the photo-z and dynamics measurements, both separately and jointly. It is clear that although photo-z and stellar kinematics alone leave some degeneracies, the posterior pdfs are almost perpendicular in this space, and therefore the combination of the two is particularly effective. The estimate of the slope obtained by marginalizing over the other parameters is

$$\gamma' = 1.98 \pm 0.02. \tag{2.9}$$

We stress that our uncertainty on this parameter is a factor of four smaller than the typical error on γ' from studies of single-source gravitational lenses with SDSS spectroscopy (Auger et al. 2010a, see Figure 2.13). Comparable precision was reached by Barth et al. (2011) for a sample of lens systems with two dimensional kinematics constraints from integral field spectroscopy.

In order to better understand the significance of these results, we try to quantify the error introduced by our simplified model for the stellar dynamics. Two of our assumptions are potential sources of bias: spherical symmetry and the non-rotating approximation.
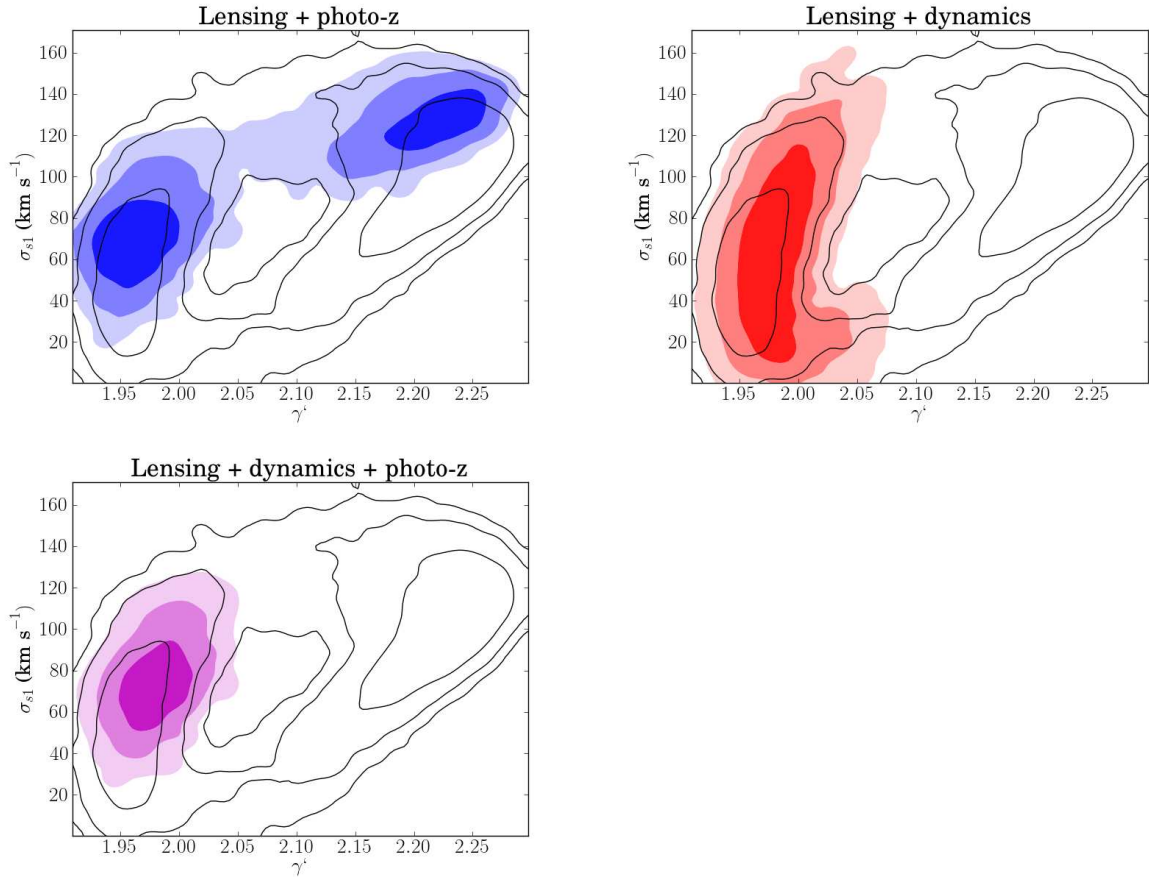
Figure 2.6: Posterior PDF of γ' and σ_{s1} of the updated (filled contours) lens model, together with the old model of SLACS Paper VI (empty contours). The updated model includes only the photo-z measurement of the outer ring in the top left panel, only the velocity dispersion profile of the lens in the top right panel, and both the photo-z and velocity dispersion profile in the bottom panel. The levels correspond to 68%, 95% and 99.7% enclosed probability.

The uncertainty in the mass determination from kinematics data is of order $\delta\sigma^2/\sigma^2 \sim$ 10%. Biases on the order of this uncertainty or smaller are unlikely to bring significant changes to the results of our analysis. By considering only the velocity dispersion and neglecting rotation, we underestimate the mass of the galaxy by a factor $\sim (v_{\rm rot}/\sigma)^2$, which is within 10% in all apertures but one. To gauge the importance of this effect we perform the following test. We fit the model velocity dispersion profiles to the following "effective velocity dispersion": $\sigma_{\rm eff} \equiv \sqrt{\sigma^2 + v_{\rm rot}^2})$. We then apply the same importance sampling procedure described above to get a new constraint on the density slope γ'. The new estimate with 1σ uncertainty is:

$$\gamma' = 1.97 \pm 0.02, \tag{2.10}$$

which is consistent with the original estimate given by (2.9). On the basis of this result, we can conclude that our approximation of non-rotating halo introduces a systematic error of order 0.01 on the inferred value of the slope γ'.

Quantifying the systematics introduced by the spherical symmetry assumption is more complicated. In a previous work, Barth et al. (2011) performed a robust dynamical modelling of 12 SLACS lenses previously analysed with a spherical Jeans equation approach by Auger et al. (2010a). The slopes γ' inferred by Auger et al. (2010a) are consistent with the more accurate measurements of Barth et al. (2011), with a bias on γ' of 0.05 ± 0.04. However, the uncertainty on γ' that we achieve in our work is smaller than that and an estimate of the bias requires additional work. Two distinct effects come into play. First, the lens has a non-circular projected shape in both its mass and light distribution. Second, the galaxy may even have asymmetries along the line of sight. The

importance of these effects on our analysis is quantified in Appendix B. By relaxing the assumption of spherical symmetry the additional uncertainty on the velocity dispersion is about $\delta\sigma^2/\sigma^2 \sim 10\%$. It follows that none of our results change appreciably.

An independent analysis of the system was carried out by Vegetti et al. (2010). The method adopted by them is more complex than the one used in SLACS Paper VI: they made use of information from all the pixels of the lensed features to reconstruct the source surface brightness as a whole. Using data from the inner ring only, they obtained the following estimate for the density slope:

$$\gamma' = 2.20 \pm 0.03^{\text{(stat)}}. \tag{2.11}$$

This is a local estimate of the slope γ', obtained by measuring the magnification of the arc in the radial direction. Our measurement is instead an average slope, obtained by fitting a single power-law halo to data spanning the lens from the center (dynamics) to the outer lensed ring. This difference may suggest that the actual mass distribution of the lens is different from a simple power-law halo. It is also for this reason that we proceeded to model the system with a more complex model.

2.6 A two-component analysis: dissecting luminous and dark matter

We perform a two-component lensing and dynamics study where the mass distribution is composed of a dark matter halo and a bulge of stars.

2.6.1 Lensing and dynamics modeling

We use a power-law ellipsoid for the dark matter, while the stars are described with the double tPIEMD model found from the photometry analysis. The second lens is again modeled as a SIS. The parameters of the stellar distribution are fixed to the best-fit values reported in Table 2.1.2. The global mass-to-light ratio is left as a free parameter, but the relative contribution of the two components is fixed according to the results of the stellar population synthesis analysis presented in Section 2.4. For a unit F814W-band magnitude, component 1 is measured to be a factor of 1.73 (1.77) heavier than component 2 assuming a Salpeter (Chabrier) IMF. In our lensing model, the mass-to-light ratio of component 1 is set to be 1.75 times larger than for component 2.

We also allow for constant external shear γ_{ext} with position angle $\mathrm{PA}_{\mathrm{ext}}$ and constant external convergence κ_{ext} in the lens plane. Issues related to the external convergence are discussed below in a dedicated subsection. Compared to the lensing study presented in the previous section, this model has two additional free parameters: the stellar mass M_*^{LD} and the external convergence κ_{ext}. Given the very tight constraint on the average slope γ' from the single component analysis, we expect to be able to determine both the slope of the dark matter halo γ_{DM} and the stellar mass M_*^{LD} with sufficient accuracy. The range of values of the slope of the dark matter halo explored in this analysis is $1.0 < \gamma_{\mathrm{DM}} < 3.0$.

The technique adopted to fit the model to the lensing data is the same used for SLACS Paper VI: a conjugate points method implemented with a MCMC. The dynamics analysis is carried out with a procedure very similar to the one described in § 2.5.1: we solve the

spherical Jeans equation for our model and obtain a synthetic velocity dispersion profile to be compared to the measured one. The (spherically symmetric) model mass distribution is obtained by circularizing the projected mass distribution of the lens model, setting q_{DM} and q_* to one, and by taking the corresponding spherical deprojections. The light distribution is set by circularizing the double tPIEMD profile specified in Table 2.1.2.

We then proceed to incorporate information on stellar dynamics and on the redshift of the background source. This is done by importance sampling, with the same method described in § 2.5.2.

2.6.2 External convergence

Objects other than the main lens can contribute to the surface mass density κ. This external convergence is hard to detect and is degenerate with the total mass of the lens galaxy. Ignoring the contribution to κ from perturbers can lead in principle to a bias in the measurement of the key parameters of the lens. In order to take into account the effect of external convergence on our error budget, we include it in our model by generating random values of κ_{ext} drawn from a plausible distribution. This procedure allows us to propagate correctly this uncertainty to the other model parameters. Kinematics information can also help to constrain κ_{ext} to some extent, as it is only sensitive to the mass dynamically associated with the galaxy, in contrast to lensing that is sensitive to all mass structures along the line of sight to the source.

Insight on the actual value of κ_{ext} can be gained by studying the lens environment. According to Treu et al. (2009), this is found to be marginally underdense with respect

to average lines of sight, therefore there is no evidence for the presence of a group in the lens neighborhood. The closest cluster known to the NASA/IPAC Extragalactic Database (NED) is MaxBCGJ146.87912+10.07800, at redshift $z = 0.151$ and projected distance 8.70 arcmin from our lens (Treu et al. 2009). If we assume a SIS profile for the cluster with a typical value for its velocity dispersion $\sigma = 1000$ km s^{-1} we obtain a contribution to the convergence $\kappa_{\mathrm{cl}} < 0.01$. We also scanned the Sloan Digital Sky Survey archive looking for massive red galaxies within 5' of the lens. Only one early-type galaxy was found, at a redshift $z = 0.218$ and angular distance 2.6'. If we assume that this object is the brightest galaxy of a group and associate it with a SIS halo of $\sigma = 500$ km s^{-1} the corresponding convergence at the location of the lens is $\kappa = 0.02$. Finally, the lensing analysis of Gavazzi et al. (2008) quantified the external shear as $\gamma_{\mathrm{ext}} = 0.07$ directed -31 degrees East of North. The HST images show two objects with the same alignment relative to the lens (see Fig. 2.1). If we make the assumption that those objects are responsible for the shear and assume again a SIS profile we obtain $\kappa_{\mathrm{ext}} = |\gamma_{\mathrm{ext}}| = 0.07$.

Hilbert et al. (2007) studied the external convergence associated with strong lensing systems in cosmological simulations. They found that for a source at redshift $z_s = 5.7$ the distribution of κ_{ext} is skewed with a peak at -0.04, has zero mean and a scatter of 0.05. A slightly smaller scatter and a peak at -0.02 is found by Suyu et al. (2010) for sources at $z_s = 1.39$.

Taking all these aspects into account, we adopt as prior for κ_{ext} in our analysis a Gaussian distribution peaked at 0.05, with dispersion $\sigma_\kappa = 0.05$ and truncated to values in the interval $-0.05 < \kappa_{\mathrm{ext}} < 0.15$. This range should capture the indication of a positive contribution from the object responsible for the shear and take into account the effect

of random mass clumps along the line of sight. Priors with a broader range of allowed values of κ_{ext} lead to larger uncertainties on the other model parameters, but none of the conclusions of our study is altered.

2.6.3   Results

Contour plots of the posterior PDF for the model parameters are shown in Figures 2.7 and 2.8. The best-fit velocity dispersion profile is plotted in Figure 2.10. The inference on the two key parameters M_* and γ_{DM} is shown in better detail in Figure 2.9. By marginalazing over the remaining parameters, our model constrains the stellar mass to

$$M_* = 5.5^{+0.4}_{-1.3} \times 10^{11} M_\odot. \tag{2.12}$$

This estimate comes from lensing and dynamics data, and does not rely on assumptions on the mass-to-light ratio of the stars. This value will be compared with the measurement of the stellar mass obtained independently from photometry.

Another important result is the constraint that we obtain on the slope of the dark matter halo:

$$\gamma_{\mathrm{DM}} = 1.7 \pm 0.2 \tag{2.13}$$

This result shows strong evidence for a contraction of the dark matter distribution relative to the r^{-1} inner slopes typical of dark matter only simulations (Navarro et al. 1997). Figure 2.11 shows the mean density profile of each mass component compared to the mean single power-law fit from Sect. 2.5.

Our inference for the anisotropy radius constrains $r_a > 13$ kpc, meaning that radial anisotropy is ruled out in the region probed by our data. This is consistent with previous
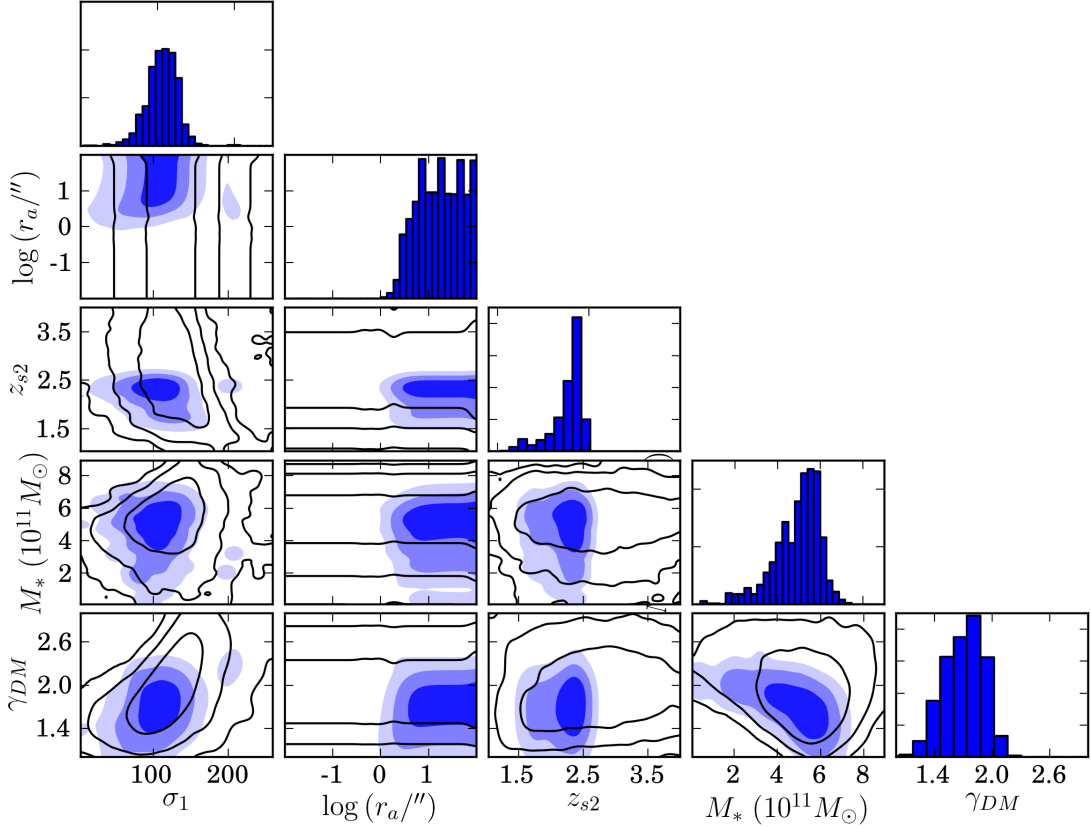
Figure 2.7: Posterior PDF in the multidimensional space spanned by the stellar mass M_*^{LD}, slope of the dark matter halo γ_{DM}, radial anisotropy scale radius r_a, strength of the second lens σ_{s1} and redshift of the second source z_{s2}. The levels correspond to 68%, 95%, 99.7% enclosed probability. *Solid contours:* constraints from lensing only. *Shaded regions:* constraints from lensing, dynamics, and photo-z.
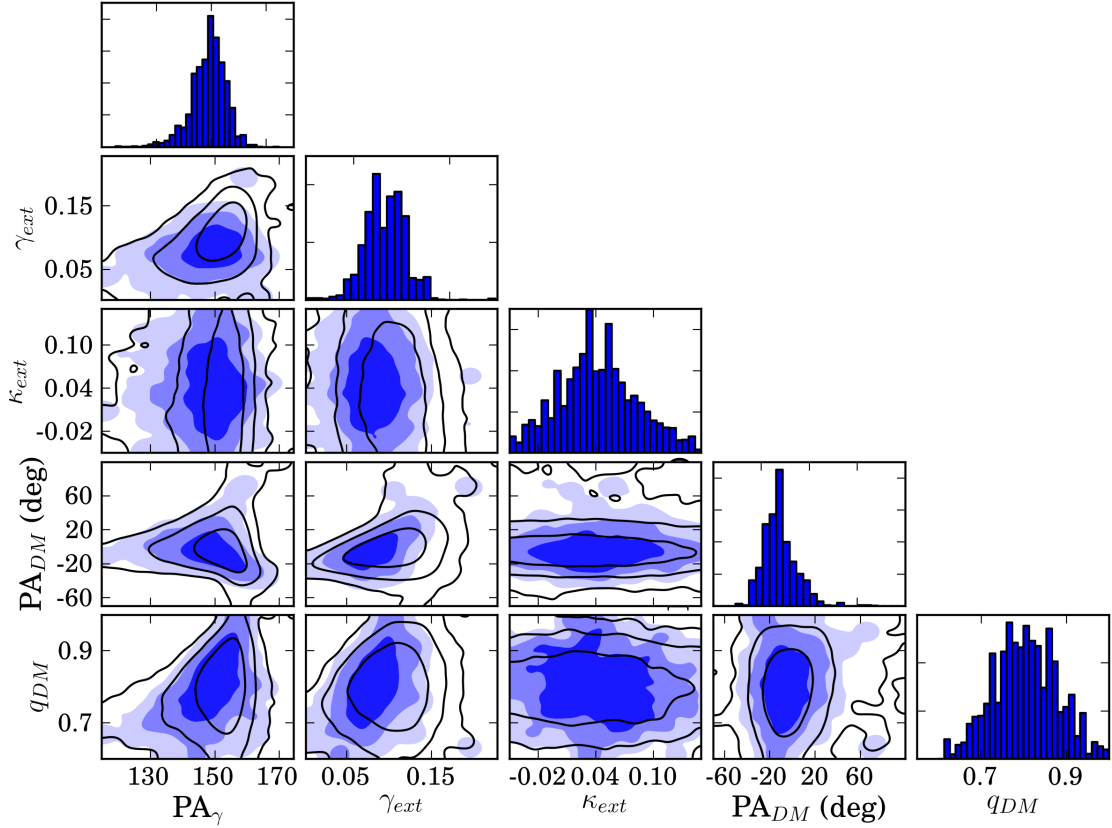
Figure 2.8: Posterior PDF in the multidimensional space spanned by external convergence κ_{ext}, strength and position angle of the external shear, γ_{ext}, PA_{ext}, axis ratio of the dark matter halo q_{DM}, position angle of the major axis of the dark matter halo, PA_{DM}. The levels correspond to 68%, 95%, 99.7% enclosed probability. *Solid contours:* constraints from lensing only. *Shaded regions:* constraints from lensing, dynamics, and photo-z.
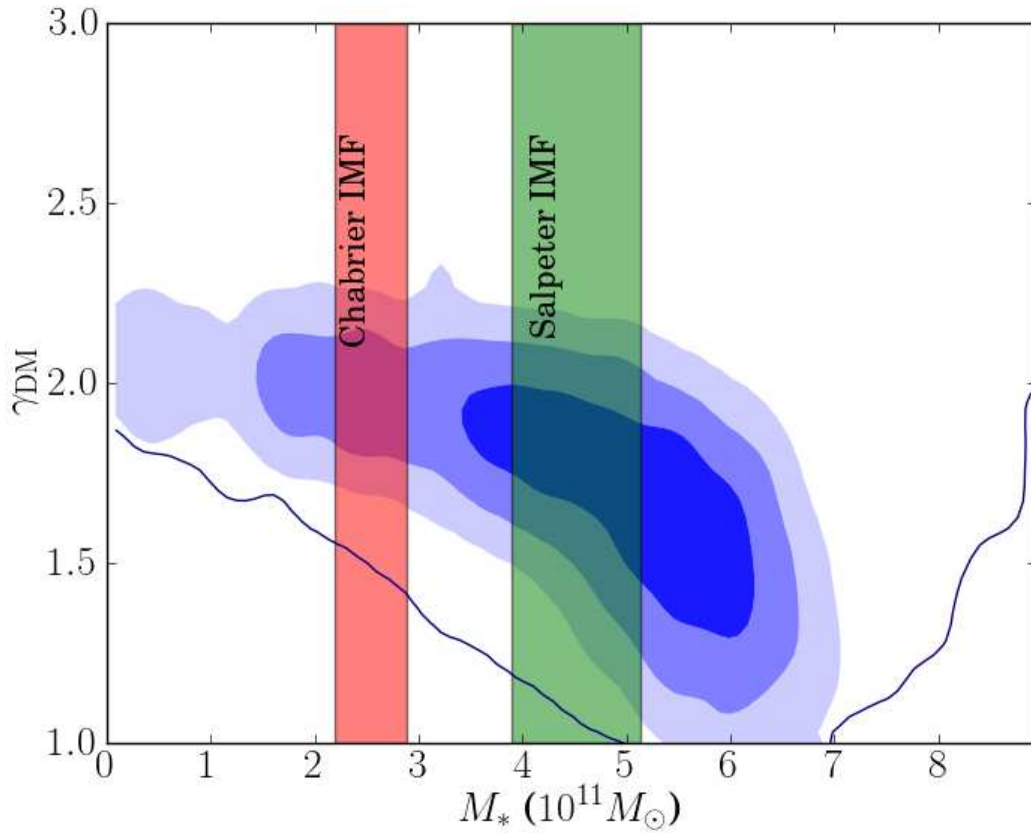
Figure 2.9: Posterior PDF projected in the space $M_* - \gamma_{\mathrm{DM}}$. The vertical shaded regions show independent measurements of the stellar mass from photometry, presented in Section 5.
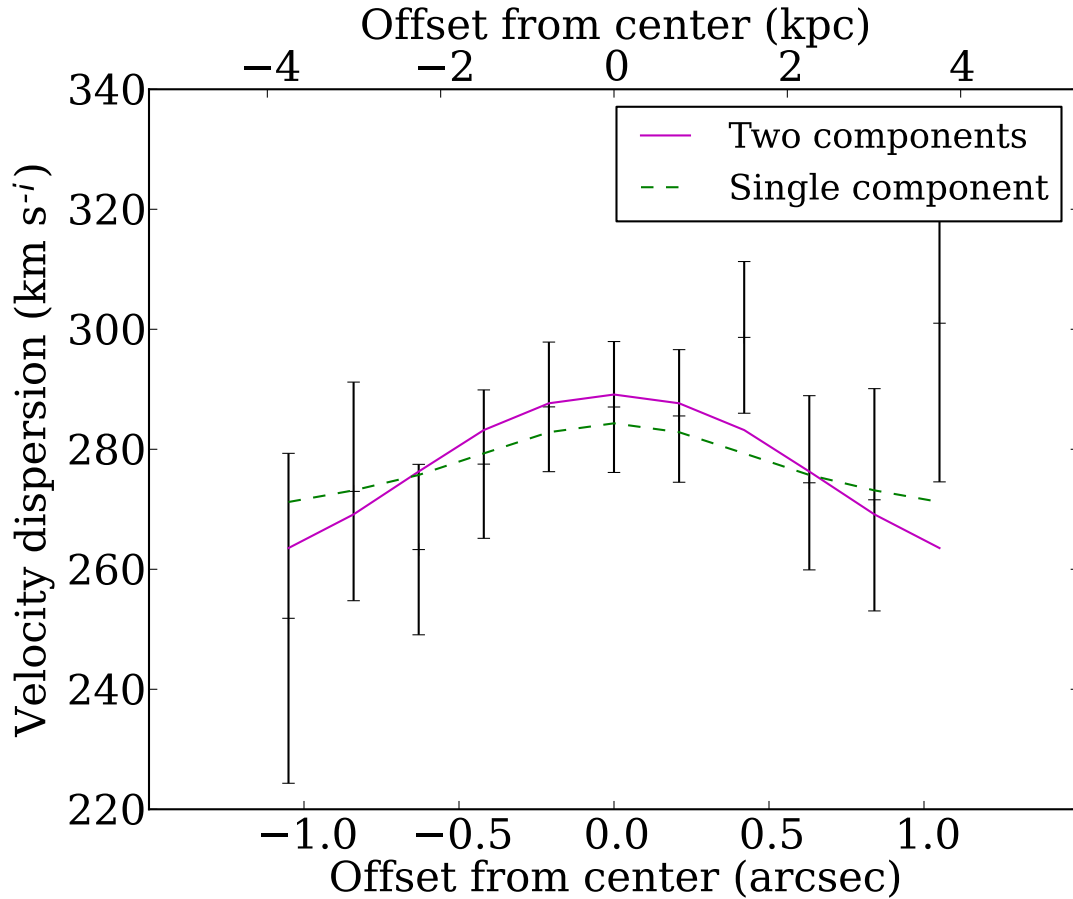
Figure 2.10: Best-fit velocity dispersion profile of the lens. *Solid line:* two components model. *Dashed line:* single power-law model.
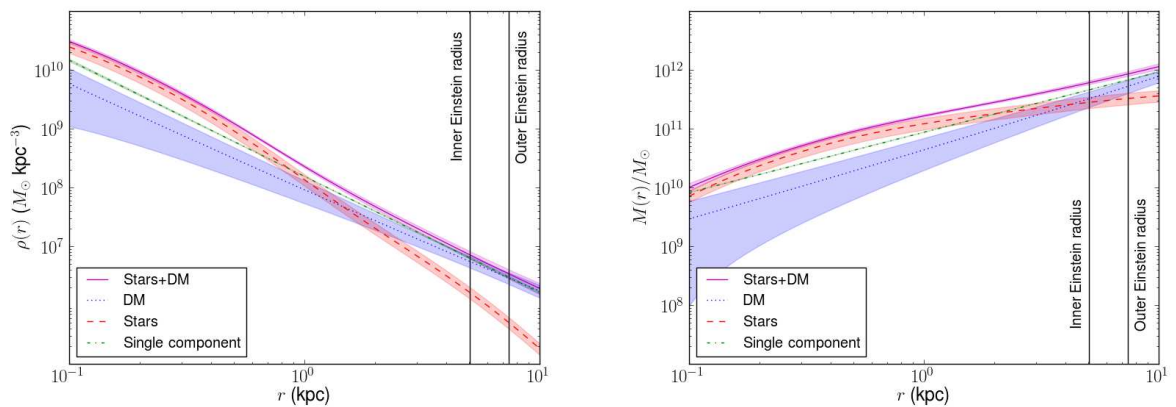
Figure 2.11: Best-fit density (left) and mass (right) profiles. *Solid line:* total mass from bulge-halo decomposition. *Dashed line:* stellar mass. *Dotted line:* dark matter. *Dash-dotted line:* total mass from single component analysis. The shaded regions represent $1 - \sigma$ uncertainties.

work (e.g. Koopmans & Treu 2003; Treu & Koopmans 2004) and expected on theoretical grounds, because strong radial anistropy would lead to instabilities.

In contrast to the power-law model considered in the previous section, this mass model has a density distribution with a slope that changes with radius. It is interesting to compare the local value of the slope at the location of the inner ring with the measurement of Vegetti et al. (2010). Vegetti et al. (2010) modeled the HST F814W image using only lensing information from the inner ring. Lensing is only sensitive to projected masses, therefore, in order for the comparison to be meaningful, we have to consider the logarithmic slope of the total projected mass distribution, evaluated at the inner Einstein radius. We find

$$\frac{d \log \kappa}{d \log r} = -1.1 \pm 0.1. \tag{2.14}$$

This value is consistent with the slope found by Vegetti et al. (2010), which is given by $-(\gamma' - 1) = -1.2$, where γ' is the slope of the 3d mass distribution given in (2.11).

Finally, it is interesting to note how the inference on the stellar mass is rather insensitive to the actual value of the redshift of the second source, z_{s2} (see Figure 2.7). This means that, with the current data quality, a spectroscopic measurement of the redshift of the outer ring would not bring significantly more information.

Table 2.9: Stellar mass of the foreground galaxy

Method	M_* $(M_\odot)$	α
Lensing+dynamics	$5.5^{+0.4}_{-1.3} \times 10^{11}$	
SPS, Chabrier IMF	$(2.5 \pm 0.3) \times 10^{11}$	2.0 ± 0.4
SPS, Salpeter IMF	$(4.5 \pm 0.6) \times 10^{11}$	1.1 ± 0.2

2.7 Discussion

2.7.1 Luminous and dark matter in the lens

The data in our possession allowed us to study the lens galaxy of the system SDSSJ0946+1006 under multiple aspects. Thanks to the high resolution photometry from HST we were able to note now the light distribution is well described with two components, while single component models yield poor fits. These two components appear to be nearly perpendicular (in projection), have significantly different effective radii and surface brightnesses. The colors of the more compact component (component 1 from now on) are also significantly redder (see Table 2.4), indicator of an older or more metal-rich stellar population. As we will discuss below, these characteristics suggest a particular scenario for the past evolution of this object.

In Sections 2.4 and 2.6 we presented two independent measurements of the stellar mass of the foreground galaxy of the system SDSSJ0946+1006 derived with a lensing+dynamics analysis and with a stellar population synthesis study. The measured values of M_*, obtained by marginalizing over the other model parameters, are reported in Table 2.9.

The stellar mass measured from gravitational lensing and dynamics, M_*^{LD}, is larger

than the masses obtained from the SPS study, M_*^{SPS}. This discrepancy can be quantified with the "IMF mismatch" parameter $\alpha \equiv M_*^{\mathrm{LD}}/M_*^{\mathrm{SPS}}$, also reported in Table 2.9. A Salpeter IMF is clearly favored, while the probability of the IMF being heavier than Chabrier ($\alpha_{\mathrm{Chab}} > 1$) is 95%.

This result is in agreement with a general trend observed by Grillo et al. (2009), Treu et al. (2010) and Auger et al. (2010b) for the early-type galaxies of the SLACS sample. They find that, on average, a Salpeter IMF better matches the measurements of stellar masses from lensing and dynamics. A similar result is found by Spiniello et al. (2012) for a very massive early-type galaxy. As discussed extensively by Treu et al. (2010), stellar mass and slope of the dark matter halo are degenerate with respect to typical lensing and dynamics constraints: given a bulge-halo decomposition, steepening the dark matter profile and decreasing the stellar mass can result in fits to the observed velocity dispersion and mass within the Einstein radius as good as the original model. Treu et al. (2010) explained how the observed trend of increasing α with velocity dispersion can either be interpreted as the effect of a correlation between IMF or dark matter inner slope with total mass. Auger et al. (2010b) explored this degeneracy by considering adiabatically contracted DM halos set by an imposed relation between stellar and virial mass, and found preference for a stellar mass-to-light ratio closer to a Salpeter than a Chabrier IMF. Similarly, Napolitano et al. (2010) find that a Kroupa IMF, which has a mass-to-light ratio slightly larger than a Chabrier IMF, fits well adiabatically contracted DM halos. In the present study we allowed the slope of the dark matter halo of our lens galaxy to vary freely. Its measured value, $\gamma_{\mathrm{DM}} = 1.7^{+0.2}_{-0.2}$, is significantly steeper than the inner slope of a NFW halo. Still, we find a stellar mass larger than what can be

accounted for with a Salpeter IMF and not compatible with a Chabrier IMF. Our results imply that a Salpeter IMF provides a far better description of the mass-to-light ratio of the stellar population than a Chabrier IMF even with a steepened dark matter halo. This result is consistent with the recent findings of Cappellari et al. (2012) and van Dokkum & Conroy (2011a).

In contrast, Salpeter-like IMFs are typically ruled out for lower mass systems (Cappellari et al. 2006) or spiral galaxies (Bell & de Jong 2001; Dutton et al. 2011; Suyu et al. 2012; Brewer et al. 2012).

The lensing and dynamics analysis presented in Sect. 2.6 showed evidence for contraction of the dark matter halo with respect to a baryonless NFW profile. A similar result is found by Grillo (2012) for an ensemble measurement of 39 massive elliptical galaxy lenses. This result is in qualitative agreement with many theoretical studies of the evolution of spheroidal galaxies (Blumenthal et al. 1986; Gnedin et al. 2004; Gustafsson et al. 2006; Abadi et al. 2010; Duffy et al. 2010). Duffy et al. (2010) in their simulations of redshift $z = 2$ galaxies find inner dark matter slopes that span the range $1.4 < \gamma_{\mathrm{DM}} < 2.0$ depending on the different prescriptions adopted to model the effect of the baryons. Our measured value of γ_{DM} falls nicely in that range, although our galaxy is at significantly lower redshift. Gnedin et al. (2004) provide a prescription to calculate the dark matter profile of their modified adiabatic contraction (MAC) model. It is interesting to test the MAC model on the measured slope of the dark matter halo of our galaxy. The final dark matter density profile of the MAC model of Gnedin et al. (2004) is determined given the observed light profile, the concentration parameter c of the original (non contracted) NFW halo and the baryon mass fraction within its virial radius, f_b.

Since we do not have information on the initial properties of the dark matter halo of our galaxy, we use a few trial values of the virial mass M_{vir}, spanning a plausible range indicated by a weak lensing study of ellipticals (Gavazzi et al. 2007), and employ a mass-concentration relation from Macciò et al. (2008) based on WMAP5 cosmological parameters. We then calculate the inner slope of the final dark matter distribution with the software Contra (Gnedin et al. 2004). The inferred inner slope for $\log\left(M_{\mathrm{vir}}/M_\odot\right) = 12.0, 13.0, 14.0$ is plotted in Fig. 2.12. Despite the large range of virial mass explored, the slopes of the contracted halos lie around $1.5 < \gamma_{\mathrm{DM}} < 2.0$ over the spatial region covered by our data. The MAC model is therefore able to reproduce our measurement of the dark matter halo slope.

2.7.2 A formation scenario

As our data show, the stellar distribution in the lens galaxy consists of two components that differ in alignment, surface brightness and stellar population. This particular structure suggests different formation histories for the two components. The bright and compact component may have formed first, and later on accreted stellar systems in the outskirts without disrupting the structure of the original bulge. Alternatively, component 2 might have been present originally and component 1 be formed in a star formation event following a wet merger. We point out that in the infrared image we see evidence for tidal distortion in the outskirts of the galaxy (see Figure 2.1), possible indication of an ongoing merger. Part of the faint extended envelope of component 2 could be material accreted relatively recently. The presence of the dust lane in the center of the galaxy
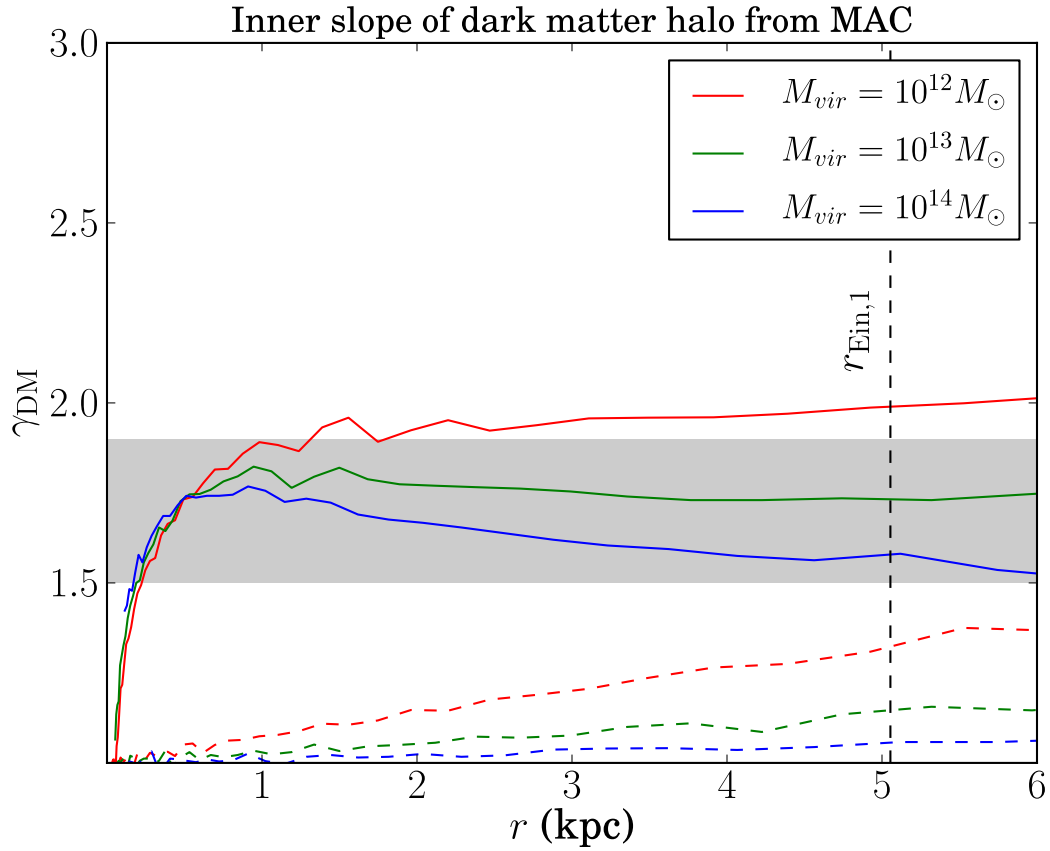
Figure 2.12: *Solid lines:* Inner slope of the dark matter halo for modified adiabatic contraction (MAC; Gnedin et al. 2004) models. *Dashed lines:* Slope of the non-contracted (NFW) dark matter halo. *Shaded region:* 68% confidence interval of the slope measured in this work.

(see § 2.9.1) may also be the result of a recent merger. We also note that Vegetti et al. (2010) detected a compact substructure of mass $\sim 3 \times 10^9 M_\odot$ located in the proximity of the inner ring image, indicating that minor mergers may still be occurring.

Let us consider our first hypothesis: the galaxy consisted initially of the compact component 1. What are the structural parameters of component 1 and how does it relate to other elliptical galaxies? Its effective radius is $r_{\rm eff} = 0.50''$ (see Tables 2.1.2 and 2.1.2), which corresponds to a physical radius of 1.79 kpc. Similar effective radii are found for high redshift ($z > 1.2$) ellipticals (Daddi et al. 2005; Trujillo et al. 2006a; van Dokkum et al. 2008). Its stellar mass as inferred from the SPS analysis is given by $\log\left(M_*^{\rm SPS}/M_\odot\right) = 10.85$ ($\log\left(M_*^{\rm SPS}/M_\odot\right) = 11.13$) for a Chabrier (Salpeter) IMF. Local ellipticals with similar values of the stellar mass have effective radii a factor of a few larger than this object (Shen et al. 2003; Hyde & Bernardi 2009). Analogously, the high redshift objects of Daddi et al. (2005), Trujillo et al. (2006a) and van Dokkum et al. (2008) are also significantly more massive than local galaxies with similar effective radii. Finding objects in the local universe that correspond to these high redshift "red nuggets" is in fact a standing problem in the study of elliptical galaxies. It is not clear how objects initially so compact evolve into the more diffuse galaxies that we observe at recent times.

Recent numerical simulations (Hopkins et al. 2009a; Oser et al. 2012) showed how minor dry mergers can increase the size of elliptical galaxies significantly, with the stars of the accreted objects that grow the outskirts of the galaxy, even though the observed and predicted merger rates are such that this mechanism might not be sufficient (**?**). The observational signature of this process would be the presence of a compact core, the original red nugget, surrounded by a more diffuse distribution of stars from the accreted

systems. The galaxy studied in this paper might be one of these objects.

2.8   Summary

We have presented a new set of photometric and spectroscopic data for the gravitational lens system SDSSJ0946+1006. We used these data to constrain the structural properties of the foreground elliptical galaxy of the system. On the basis of our results, the following statements can be made.

- The redshift of the source corresponding to the outer ring is $z_{s2} = 2.41^{+0.04}_{-0.21}$ at 68% confidence level, as revealed by our photo-z measurement.

- If we describe the total mass distribution with a power-law ellipsoid $\rho \propto r^{-\gamma'}$, lensing and dynamics data give as measured value $\gamma' = 1.98 \pm 0.02 \pm 0.01$. This parameter should be interpreted as an effective slope of the density profile averaged over the region within the outer Einstein ring. The special lensing configuration and the exquisite data quality of our data, allowed us to measure γ' with unprecedented precision. The value obtained is consistent with isothermal ($\gamma' = 2$) and is in agreement with the general trend observed for the massive early-type galaxies of the SLACS sample, $\langle \gamma' \rangle = 2.078 \pm 0.027$ with intrinsic scatter $\sigma_{\gamma'} = 0.16 \pm 0.02$ (Auger et al. 2010a; Koopmans et al. 2009; Barth et al. 2011). See Figure 2.13 for a comparison of our measurement of γ' with measurements of the same parameter for the SLACS sample of early-type galaxies by Auger et al. (2010a).

- We are able to decompose dark and stellar matter with lensing and dynamics data,

assuming a power-law density profile for the dark matter. The derived stellar mass is $5.5^{+0.4}_{-1.3} \times 10^{11} M_{\odot}$, consistent with a Salpeter IMF and inconsistent with a Chabrier IMF. This constraint on the IMF is plotted in Figure 2.13 together with similar measurements for the other SLACS lenses obtained by Treu et al. (2010). Note that we achieve better precision despite using less strict assumptions on the dark matter profile.

- The slope of the dark matter halo is found to be $\gamma_{\mathrm{DM}} = 1.7 \pm 0.2$. This is a strong evidence for contraction relative to the r^{-1} behavior of NFW profile observed in simulations without baryons, and is in agreement with the inner dark matter profiles obtained by Duffy et al. (2010) in their simulations of $z = 2$ galaxies and with the MAC model of Gnedin et al. (2004). Our inferred bulge-halo decomposition has a local projected slope at the inner ring in agreement with the value measured by Vegetti et al. (2010) based on a completely independent technique.

- The particular structure of the stellar distribution, with a compact core and a misaligned faint extended envelope, might be the result of accretion of low mass systems by a compact red nugget.

- A spectroscopic detection of the redshift of the outer ring would still help improve the model, but would not lead to a dramatic change in the results of our analysis.
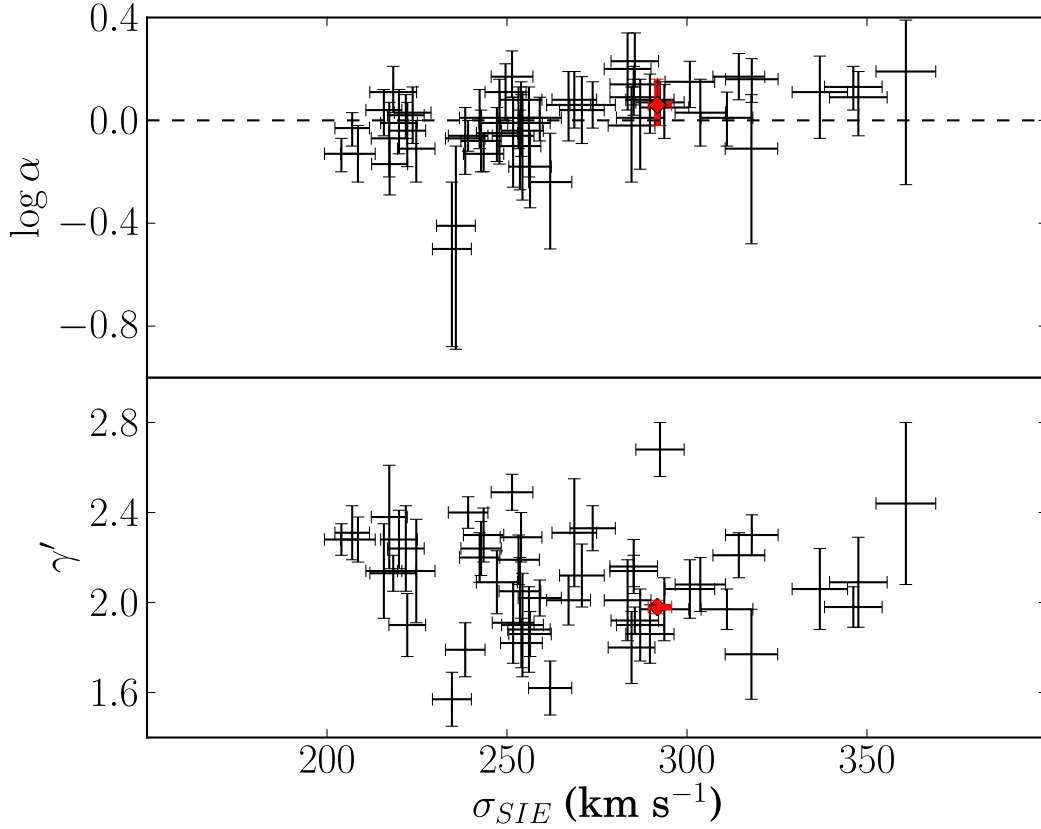
Figure 2.13: *Top panel:* IMF mismatch parameter $\alpha \equiv M_*^{\mathrm{LD}}/M_*^{\mathrm{SPS}}$ relative to a Salpeter IMF vs. lens strength σ_{SIE} for the SLACS lenses of Treu et al. (2010) (black crosses) and for the Jackpot (red cross). Measurements of Treu et al. (2010) are obtained assuming a NFW dark matter halo with fixed scale radius for the lensing and dynamics analysis. *Bottom panel:* average slope of the total density profile γ' vs. lens strength σ_{SIE} for the SLACS lenses of Auger et al. (2010a) (black crosses) and for the Jackpot (red cross).

2.9 Appendix

2.9.1 Dust correction

The presence of dust complicates our analysis. Nevertheless, we deal with it by applying a procedure similar to that adopted by Koopmans et al. (2003) and Suyu et al. (2009) for the system B1608+656. The details of the procedure are the following.

We select a small region in the center of the galaxy for which we want to apply a dust correction. We estimate the intrinsic colors of this central part by measuring them in a region that we think is free of dust.

We assume a dust law from Cardelli et al. (1989), with $R_V = 3.1$. Given the flux in one band and the colors of the object, the fluxes in the remaining bands are determined by the dust law. Therefore, with images in two or more bands we can constrain both the intrinsic flux and the dust content of the object. In our case we determine these two quantities in the central region of the lens on a pixel-by-pixel basis by fitting the F814W, F606W and F438W fluxes. We want to check if we can account for the dark lane observed in the F336W image independently from the data in that band, therefore we do not include that image in our dust analysis. The F160W image is excluded because of its lower spatial resolution. The PSF of the different images is not matched. Our inference on the presence of dust is not affected by this approximation.

The two dust-free colors, F606W - F814W and F438 - F606W, are measured in an annulus around the center and inside of the inner ring. We cannot rule out the presence of a uniform dust screen, but that would not affect our conclusions as the tools that we use for quantitative analyses can account for that. The dust-corrected flux in the lens

Figure 2.14: Dust correction. *Left panel:* Dust map of the central part of the galaxy based on F438W, F606W and F814W images. Dark pixels represent higher column densities of dust. *Middle panel:* Original image in the F336W band. *Right panel:* Dust-corrected F336W band image, showing a single clump of light. The central parts have lower signal-to-noise ratio as a result of the noisy dust map.

center is then calculated with the fitting method described in Sect. 5.4 of Suyu et al. (2009). Figure 2.14 shows the recovered dust map, the F336W image corrected for dust and its original version. It can clearly be seen how the dust map, obtained without using data from the F336W, has largest column density right where we observe the dark lane in the image. In the dust-corrected image, the lens looks indeed more like a single object. The overall amount of dust is relatively small, as the correction to the total magnitude in the F606W band is approximately 0.10 mags.

2.9.2 Ellipticity effects

The mass and light distributions of the lens galaxy are well approximated by ellipses, but we make the assumption of spherical symmetry for the analysis of the kinematics data. How does this assumption affect the results we present? To answer this question we make use of the axisymmetric version of the Jeans equations (Binney & Tremaine

2008)

$$\bar{v_R^2}(R, z) = \bar{v_z^2}(R, z) = \frac{1}{\rho_*(R, z)} \int_z^\infty dz' \rho_*(R, z') \frac{\partial \Phi}{\partial z'} \qquad (2.15)$$

$$\bar{v_\phi^2}(R, z) = \bar{v_R^2} + \frac{R}{\rho_*} \frac{\partial(\rho_8 \bar{v_R^2})}{\partial R} + R \frac{\partial \Phi}{\partial R}, \qquad (2.16)$$

obtained assuming a distribution of stars of the form $f(E, L_z)$.

We take our best-fit single component model from Section 2.5.1 and make it elliptical by assuming that the rotation axis L_z is in the plane of the sky and fixing the projected ellipticities in light and mass to $q_* = 0.95$ and $q = 0.87$ respectively. The first value is the ellipticity of the best single-component fit to the light profile, the latter value is given in Gavazzi et al. (2008). Then we assume isotropy in the velocity dispersion tensor, calculate the line of sight velocity dispersion profile in the two possible cases of oblate or prolate ellipsoid, and compare it to the corresponding spherical case. Results are shown in Fig. 2.9.2. Deviations from spherical symmetry bring differences on the order of a few km s^{-1} on the velocity dispersion profile, well within our uncertainties on the measurements, and therefore is not a concern for possible biases.

More important are the effects of asymmetries along the line of sight. We do not have any direct measurement of the line-of-sight structure of the lens, but from the observed projected flattening we can get information on the intrinsic shape of the galaxy by statistical means. Padilla & Strauss (2008) measured the distribution of intrinsic axis ratios of massive elliptical galaxies. By drawing samples of galaxy shapes from their inferred distribution and assuming random orientations we find that 68% of the objects that produce a projected ellipticity $q_* = 0.95$ have an axis ratio rounder than 0.8. How does the velocity dispersion profile of an oblate (prolate) galaxy with minor (major) axis

along the line of sight and axis ratio of 0.8 differ from that of a spherical galaxy with the same (observed) projected mass within the Einstein radius? We use the axisymmetric Jeans equation to address this question as well. We take our best-fit spherical model and modify it into an oblate (prolate) ellipsoid with the axis ratio of both the light and mass distribution fixed at 0.8, orienting L_z along the line of sight. The line-of-sight velocity dispersion profile for isotropic orbits in the oblate and prolate case is also plotted in Fig. 2.9.2. The spread relative to the spherical case is somewhat larger than the uncertainties. To make sure that our assumption of spherical symmetry does not alter the measurements presented in this Chapter we recalculate the inference of the key model parameters by inflating the error bars on the velocity dispersion measurements by a factor 1.5, matching the scatter introduced by the unknown line-of-sight oblateness or prolateness of the lens. None of the results changes appreciably. The lens modeling does not depend on assumptions on the line-of-sight mass distribution, and so in this regard our results are robust.
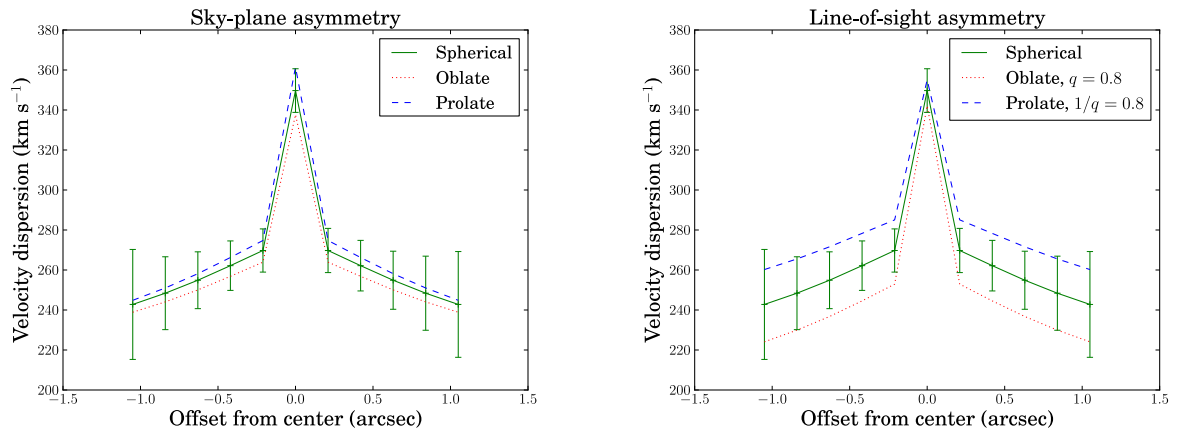
Figure 2.15: *Top:* Line-of-sight velocity dispersion profile for a spherical model and for elliptical models with $q_* = 0.95$ and $q = 0.87$, calculated by solving the axisymmetric Jeans equation. The models have the same projected mass within the inner Einstein radius. PSF smearing is not included, resulting in the high central peak. Overplotted are the error bars on the measured velocity dispersion profile. *Bottom:* Velocity dispersion profile of the spherical model and of an oblate (prolate) ellipsoid with minor (major) axis parallel to the line of sight and axis ratio 0.8.

Chapter 3

The SL2S Galaxy-scale Lens Sample. Lens Models, Photometry and Spectroscopy

Parts of this chapter were published as Sonnenfeld, A.; Gavazzi, R.; Suyu, S. H.; Treu, T.; Marshall, P. J. "The SL2S Galaxy-scale Lens Sample. III. Lens Models, Surface Photometry and Stellar Masses for the final sample" 2013, ApJ, 777, 97, and Sonnenfeld, A.; Treu, T.; Gavazzi, R.; Suyu, S. H.; Marshall, P. J.; Auger, M. W.; Nipoti, C. "The SL2S Galaxy-scale Lens Sample. IV. The dependence of the total mass density profile of early-type galaxies on redshift, stellar mass, and size" 2013, ApJ, 777, 98, and are included here with minor edits.

The current number of known early-type galaxy lenses is avobe two hundred. While some of these lenses were serendipitous findings, most of them were discovered in the context of dedicated surveys. The largest such survey to date is the Sloan Lens ACS (SLACS) survey (Bolton et al. 2004), which provided about 80 lenses. Although this sample has yielded interesting results on the properties of ETGs, there are many astrophysical questions that can be better answered with a larger number of strong lenses spanning a larger volume in the space of relevant physical parameters. For instance, quantities like the dark matter fraction or the density slope of ETGs, measurable with

lensing and stellar kinematics information, might be correlated with other observables such as the stellar mass or the effective radius. Moreover, the mass structure of ETGs could be evolving in time as a result of the mass accretion history. In order to test this scenario, we need a statistically significant number of lenses covering a range of redshift, along with robust measurements of their Einstein radius, stellar mass, size and velocity dispersion. While there are many low-redshift lenses that satisfy this requirement, only a few of the known lenses at $z > 0.3$ have all the data necessary for a reliable study of their mass structure.

One of the goals of the Strong Lensing Legacy Survey (SL2S) collaboration is to extend to higher redshifts the sample of known galaxy-scale gravitational lenses. In Papers I and II (Gavazzi et al. 2012; Ruff et al. 2011) we presented the pilot sample of 16 lenses. Here we extend our study to a sample of 61 objects at redshifts up to $z = 0.8$. In this Chapter we first show the photometric and spectroscopic data of the full SL2S galaxy-scale lens sample. We then present the lensing models of the new systems along with revisited models of the old ones. With respect to Paper I we make more conservative assumptions about the intrinsic shape of the lensed sources by reconstructing them on a pixelized grid (Warren & Dye 2003; Suyu et al. 2006; Koopmans & Treu 2004).

The goal of this work is to present our new sample of lenses, characterize it in terms of Einstein radii and stellar masses, and to compare the effectiveness of ground-based versus space-based images for the purpose of confirming gravitational lens candidates. This Chapter is organized as follows. Section 3.1 summarizes the SL2S and the associated Canada-France-Hawaii-Telescope Legacy Survey (CFHTLS) data, the lens detection method and the sample selection. In Section 3.2 we present all the photometric data set

of the SL2S lenses, either coming from the CFHTLS parent photometry or from additional *Hubble Space Telescope* (*HST*) and Near infrared (IR) follow-up imaging. We show in detail the spectroscopic data set and the measurements of redshifts and velocity dispersions of our lenses in Section 3.3. In Section 3.4 we describe the lens models of the 61 systems. In Section 3.5 we show measurements of the stellar mass of our lenses from stellar population synthesis fitting. In Section 3.6 we discuss the properties of SL2S lenses in relation with lenses from independent surveys. We discuss and summarize our results in Section 3.7.

3.1 The Strong Lensing Legacy Survey

SL2S (Cabanac et al. 2007) is a project dedicated to finding and studying galaxy-scale and group-scale strong gravitational lenses in the Canada France Hawaii Telescope Legacy Survey (CFHTLS). The main targets of this paper are massive red galaxies. The galaxy-scale SL2S lenses are found with a procedure described in detail in Paper I (Gavazzi et al. 2012) that can be summarized as follows. We scan the 170 square degrees of the CFHTLS with the automated software `RingFinder` (**?**). looking for tangentially elongated blue features around red galaxies. The lens candidates are then visually inspected and the most promising systems are followed up with *HST* and/or spectroscopy.

Previous papers have demonstrated the success of this technique. In Paper I (Gavazzi et al. 2012), we obtained lens models for a pilot sample of 16 lenses and in Paper II (Ruff et al. 2011), we combined this information with spectroscopic data to investigate the total mass density profile of the lens galaxies, and its evolution. Here we complete the sample

by presenting all the new systems that have been followed-up with either high-resolution imaging or spectroscopy since the start of the campaign. We also re-analyze the pilot sample to ensure consistency. This paper is focused on the sample's photometric data and lens models, while in Paper IV we present the corresponding spectroscopic observations, model the mass density profile of our lenses, and explore the population's evolution with time.

SL2S is by no means the only systematic survey of massive galaxy lenses: two other large strong-lens samples are those of the SLACS (Bolton et al. 2004) and BELLS (BOSS Emission-Line Lensing Survey; Brownstein et al. 2012) survey. SL2S differs from SLACS and BELLS in the way lenses are found. While we look for lenses in wide-field imaging data, the SLACS and BELLS teams selected candidates by looking for spectroscopic signatures coming from two objects at different redshifts on the same line of sight in the Sloan Digital Sky Survey (SDSS) spectra. These two different techniques correspond to differences in the population of lenses in the respective samples. Given the relatively small fiber used in SDSS spectroscopic observations (1.5″ and 1″ in radius, for SLACS and BELLS respectively), the spectroscopic surveys tend to select preferentially lenses with small Einstein radii, where both the arc from the lensed source and the deflector can be captured within the fiber. SL2S, on the other hand, finds with higher frequency lenses with Einstein radii larger than 1", since they can be more clearly resolved in ground-based images (even after the lensed sources have been deblended from the light of the central deflector). At a given redshift, different values of the Einstein radius correspond to different physical radii at which masses can be measured with lensing. For a quantitative estimate of the range of physical radii probed by the different surveys,
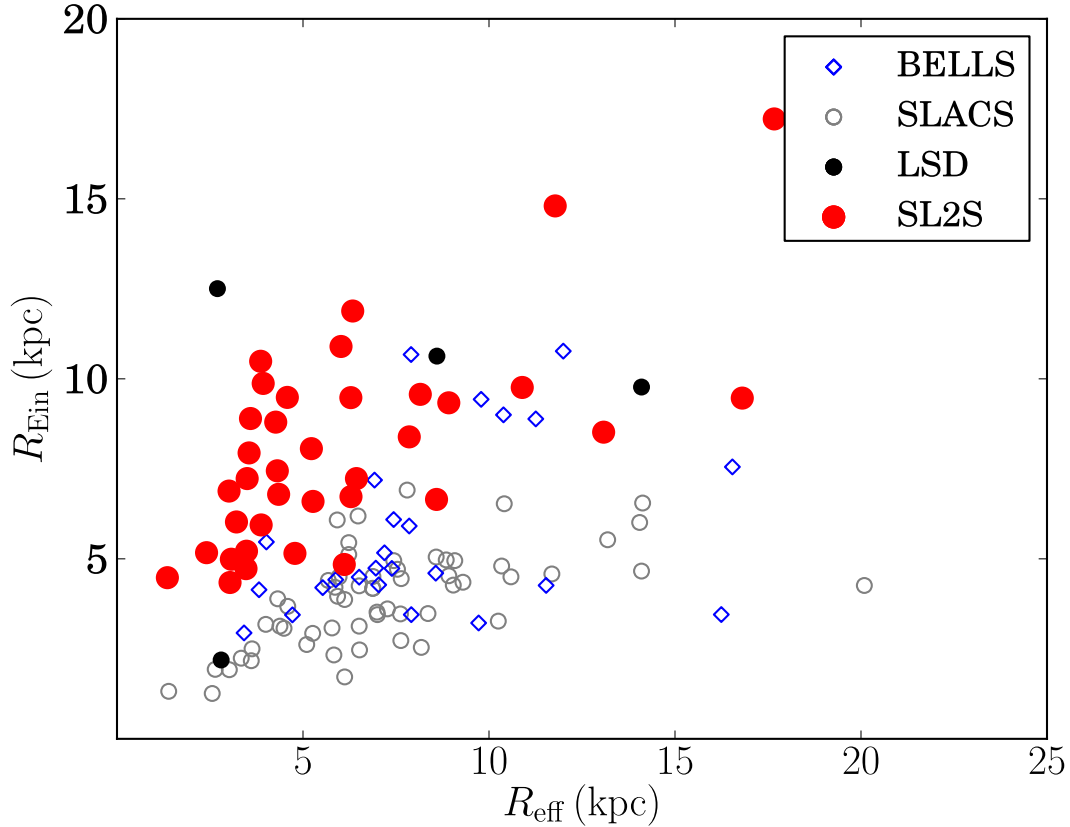
Figure 3.1: Distribution of Einstein radii and effective radii of lenses from SLACS (Auger et al. 2010a), BELLS (Brownstein et al. 2012), LSD (Treu & Koopmans 2004) and grade-A SL2S.

we plot in Figure 3.1 the distribution of Einstein radii and the effective radii for lenses from SL2S (determined in Sections 3.2.1 and 3.4.1), BELLS (Brownstein et al. 2012) and SLACS (Auger et al. 2010a), together with 5 lenses from the LSD study (Treu & Koopmans 2004). The different surveys complement each other nicely, each one providing independent information that cannot be easily gathered from the others.

In Table 3.1 we provide a census of SL2S targets that have been followed up so far. The systems are graded according to their subjective likelihood of being strong lenses: grade A are definite lenses, B are probable lenses, C are possible lenses or, more conservatively,

Grade	A	B	C	X	Total
With high-res imaging	30	3	13	21	67
With spectroscopy	42	**14**	**2**	5	63
High-res imaging and spectroscopy	27	3	0	0	30
Total with follow-up	**45**	14	15	26	100

Table 3.1: Number of SL2S candidates for which we obtained follow-up observations in each quality bin. Grade A: definite lenses, B: probable lenses, C: possible lenses, X: non-lenses. We differentiate between lenses with spectroscopic follow-up, high-resolution imaging follow-up or any of the two. In bold font we give the numbers that add up to our overall sample size of 61.

systems for which the additional data set does not lead to conclusive answers about their actual strong lensing nature, and, grade X are non-lenses. Grades for individual systems are shown in Table 3.4.2 and discussed in Section 3.4.2.

In this paper we show detailed measurements of photometric properties, lens models and stellar masses for all grade A lenses and for all grade B and C systems with spectroscopic follow-up. The same selection criterion is applied in Paper IV.

3.2 Photometric observations

All the SL2S lens candidates are first imaged by the CFHT as part of the CFHT Legacy Survey. CFHT optical images are taken with the instrument Megacam in the u, g, r, i, z filters under excellent seeing conditions. The typical FWHM in the g and i bands is $0''.7$. We refer to Gavazzi et al. (2012) for a more detailed description of ground-based optical observations.

The WIRCam (Puget et al. 2004) mounted on the CFHT was used to get Near IR follow-up photometry for some of the SL2S lens galaxies (Programs 11BF01, PI Gavazzi,

and 07BF15 PI Soucail) or from existing surveys like WIRDS (Bielby et al. 2010, 2012)[1] or from an ongoing one, called Miracles that is gathering a deep Near IR counter-part to a subset of the CFHTLS in the W1 and W4 fields (Arnouts et al., in prep). All these data were kindly reduced by the Terapix team.[2] Ks (and sometimes also J and H) band is used for the systems listed in Table 3.2 to estimate more accurate stellar masses (see 3.5).

In addition to ground-based photometry, 33 of the 61 lens systems presented here have been observed with *HST* as part of programs 10876, 11289 (PI Kneib) and 11588 (PI Gavazzi), over the course of cycles 15, 16 and 17 respectively. A summary of *HST* observations is given in Table 3.3. The standard data reduction described in Paper I was performed.

3.2.1 Properties of lens galaxies

We wish to measure magnitudes, colors, effective radii, ellipticities and orientations of the stellar components of our lenses. This is done first by using the CFHT data, for all systems. We simultaneously fit for all the above parameters to the full set of images in the 5 optical filters, and NIR bands when available, by using the software `spasmoid`, developed by M. W. Auger and described in Bennert et al. (2011). Results are reported in Table 3.2.1. For systems with available *HST* data we repeat the fit using *HST* images alone. The measured parameters are reported in Table 3.2.1. Uncertainties on CFHT lens galaxy magnitudes are dominated by contamination from the background source

---

[1] see also http://terapix.iap.fr/article.php?id_article=832
[2] http://terapix.iap.fr

Table 3.2: Summary of NIR observations

Name	Program	Filter	Exp. time (s)
SL2SJ021325−074355	11BF01	Ks	1050
SL2SJ021411−040502	07BF15	J,Ks	970,2480
SL2SJ021737−051329	07BF15	J,Ks	2470,1810
SL2SJ021902−082934	11BF01	Ks	1020
SL2SJ022357−065142	11BF01	Ks	1000
SL2SJ022511−045433	WIRDS	J,H,Ks	15720,11750,12860
SL2SJ022610−042011	WIRDS	J,H,Ks	13230,10240,11300
SL2SJ022648−040610	WIRDS	J,H,Ks	1800,820,1570
SL2SJ023251−040823	11BF01	Ks	1010
SL2SJ084909−041226	11BF01	Ks	1370
SL2SJ084959−025142	11BF01	Ks	1580
SL2SJ085826−014300	11BF01	Ks	1570
SL2SJ090106−025906	11BF01	Ks	1320
SL2SJ090407−005952	11BF01	Ks	1050
SL2SJ095921+020638	WIRDS	J,H,Ks	7500,16270,2990
SL2SJ220329+020518	11BF01	Ks	1840
SL2SJ220506+014703	MIRACLES	Ks	1140
SL2SJ220629+005728	MIRACLES	Ks	1340
SL2SJ221326−000946	11BF01	Ks	1280
SL2SJ221852+014038	MIRACLES	Ks	970
SL2SJ222012+010606	MIRACLES	Ks	1070
SL2SJ222148+011542	MIRACLES	Ks	250

Table 3.3: Summary of *HST* observations

Set	Program	Instrument	Filter	Exp. time (s)
(a)	10876	ACS	F814W,F606W	800,400
(b)	11689	WFPC2	F606W	1200
(c)	11588	WFC3	F600LP,F475X	720
(d)	11588	WFC3	F475X	360

and are estimated to be 0.3 in u band, 0.2 in g and r, 0.1 in all redder bands, while *HST* magnitudes have an uncertainty of 0.1. Although we used the same data, some of the CFHT magnitudes previously reported for the lenses studied in Paper I and Paper II are slightly inconsistent with the values measured here. This difference is partly due to a different procedure in the masking of the lensed arcs. In Paper I and II, the lensed features were masked out automatically by clipping all the pixels more than 4σ above the best fit de Vaucouleurs profile obtained by fitting the deflector light distribution with `Galfit` (Peng et al. 2002, 2010a), while here the masks are defined manually for every lens. We verified that this different approach is sufficient for causing the observed mismatch. The masking procedure adopted here is more robust and therefore we consider the new magnitudes more reliable. In addition, the measurements reported in Paper I and Paper II were allowing for different effective radii in different bands and the resulting magnitudes depend on the extrapolation of the light profile at large radii where the signal-to-noise ratio is extremely low. Here we fit for a unique effective radius in all bands, resulting in a more robust determination of relative fluxes, i.e. colors, important for the determination of stellar masses from photometry fitting. We note that this corresponds to an assumption of negligible intrinsic color gradient in the lens galaxies. However, asserting an effective radius that is constant across bandpasses mitigates against the much larger contamination from the lensed source. We verified that the quality of fits with a unique effective radius is comparable to that achieved by allowing different values of R_{eff} for different bands, as the difference in the χ^2 values between the two cases is tipically $\sim 10\%$.

Uncertainties on the *HST* effective radii are dominated by the choice of the model

light profile: different models can fit the data equally well but give different estimates of $R_{\rm eff}$. The dispersion is $\sim 10\%$, estimated by repeating the fit with a different surface brightness model, a Hernquist profile, and comparing the newly obtained values of $R_{\rm eff}$ with the de Vaucouleurs ones. Uncertainties on the CFHT effective radii are instead dominated by contamination from the background sources. Effective radii measured from CFHT images are in good agreement with those measured from *HST* data, when present, as shown in Figure 3.2. The scatter on the quantity $R_{\rm eff,CFHT} - R_{\rm eff,HST}$ is $\sim 30\%$; we take this as our uncertainty on CFHT effective radii.

3.3   Spectroscopic observations

The SL2S spectroscopic campaign was started in 2006. The goal of our spectroscopic observations is to measure the lens and source redshifts and lens velocity dispersion for all our systems. Different telescopes (Keck, VLT and Gemini), instruments (LRIS, DEIMOS, X-Shooter, GNIRS) and setups have been used to achieve this goal, reflecting technical advances during the years and the optimization of our strategy. In what follows we describe the procedure used to measure the three key spectroscopic observables. A summary of all measurements is given in Table 3.3.2.

3.3.1   Deflector redshifts and velocity dispersions

The typical brightness of our lenses is around $i \sim 20$. With an 8m class telescope, their redshift can be measured from their optical absorption lines with ~ 10 minutes of exposure time, while a measurement of their velocity dispersion typically takes from 30

Name	$R_{\rm eff}$ (arcsec)	q	PA (degrees)	u	g	r	i	z	J	H	Ks
SL2SJ020457-110309	1.01	0.67	−20.9	22.81	21.93	20.78	19.82	19.27			
SL2SJ020524-093023	0.75	0.64	−75.7	23.69	22.01	20.55	19.50	19.06			
SL2SJ020833-071414	1.06	0.81	61.1	22.71	20.64	18.99	18.22	17.90			
SL2SJ021206-075528	0.78	0.79	−29.2	23.33	21.32	19.75	18.90	18.61			
SL2SJ021247-055552	1.22	1.00	−9.1	23.59	22.73	21.44	20.21	19.77			
SL2SJ021325-074355	1.97	0.60	21.2	24.29	22.28	20.78	19.27	18.82			17.43
SL2SJ021411-040502	1.21	0.88	57.1	23.82	22.39	20.88	19.65	19.23	18.55		17.87
SL2SJ021737-051329	0.73	0.90	87.6	23.21	22.17	20.92	19.70	19.33	18.72		17.97
SL2SJ021801-080247	1.02	1.00	−49.8	23.05	22.07	21.32	20.33	19.64			
SL2SJ021902-082934	0.95	0.74	82.6	23.02	21.37	19.70	18.94	18.55			17.59
SL2SJ022046-094927	0.53	0.71	−68.5	24.17	22.33	20.88	19.88	19.52			
SL2SJ022056-063934	1.42	0.54	−74.8	21.65	19.85	18.47	17.86	17.59			
SL2SJ022346-053418	1.31	0.59	63.4	22.93	21.09	19.56	18.70	18.29			
SL2SJ022357-065142	1.36	0.95	37.2	23.13	21.03	19.42	18.63	18.30			17.45
SL2SJ022511-045433	2.12	0.72	27.5	20.32	18.58	17.36	16.81	16.55	15.99	15.64	15.48
SL2SJ022610-042011	0.84	0.87	52.0	23.30	21.28	19.70	18.80	18.46	18.09	17.70	17.38
SL2SJ022648-040610	0.48	0.30	−47.5	25.12	23.26	21.57	20.12	19.57	18.90	18.52	18.10
SL2SJ022648-090421	1.40	0.81	56.8	22.65	20.46	18.79	18.06	17.69			
SL2SJ022708-065445	0.45	0.28	84.9	23.55	22.49	21.18	20.19	19.76			
SL2SJ023251-040823	1.14	0.70	−72.6	22.28	20.71	19.31	18.72	18.44			17.30
SL2SJ023307-043838	1.31	0.85	45.9	23.44	21.98	20.63	19.41	19.03			
SL2SJ084847-035103	0.45	0.82	−65.4	24.57	23.57	22.16	20.81	20.39			
SL2SJ084909-041226	0.46	0.51	43.7	24.90	23.16	21.70	20.16	19.70			18.60
SL2SJ084934-043352	1.59	0.78	36.4	22.52	20.49	19.01	18.31	18.02			
SL2SJ084959-025142	1.34	0.79	−65.4	21.75	19.85	18.56	17.94	17.68			16.63
SL2SJ085019-034710	0.28	0.22	1.2	23.52	21.48	20.07	19.38	19.14			
SL2SJ085317-020312	0.85	0.61	16.7	24.45	22.81	21.39	20.12	19.67			
SL2SJ085327-023745	1.47	0.81	−24.3	23.07	22.24	21.46	20.29	19.78			
SL2SJ085540-014730	0.69	0.82	−70.8	22.80	21.42	20.05	19.37	19.10			
SL2SJ085559-040917	1.13	0.82	23.1	23.18	21.10	19.48	18.72	18.35			
SL2SJ085826-014300	0.55	0.77	−86.2	24.09	23.15	21.85	20.78	20.38			19.20
SL2SJ090106-025906	0.42	0.82	−67.5	24.53	23.81	22.40	21.16	20.73			19.80
SL2SJ090407-005952	2.00	0.64	71.1	23.59	21.61	20.57	19.47	19.12			17.71
SL2SJ095921+020638	0.46	0.90	42.0	25.28	22.74	21.23	20.23	19.90	19.72	19.38	19.13
SL2SJ135847+545913	0.92	0.79	−72.4	23.93	21.66	20.14	19.16	18.78			
SL2SJ135949+553550	1.13	0.67	35.7	24.40	23.30	21.90	20.69	20.04			
SL2SJ140123+555705	0.86	0.75	−41.9	23.84	21.64	20.05	18.97	18.57			
SL2SJ140156+554446	1.44	0.82	20.2	23.07	20.83	19.28	18.47	18.02			
SL2SJ140221+550534	1.52	0.94	−18.1	22.28	20.47	18.89	18.19	17.82			
SL2SJ140454+520024	2.03	0.79	67.2	22.37	20.17	18.56	17.73	17.37			
SL2SJ140533+550231	0.56	0.67	15.8	24.32	22.48	21.10	20.13	19.62			
	1.11	0.98	−36.03	23.14	22.28	21.11	20.23	19.73			
SL2SJ140546+524311	0.83	0.89	−27.5	23.73	21.62	20.10	19.10	18.74			
SL2SJ140614+520253	2.21	0.50	−60.9	22.67	20.64	19.08	18.22	17.85			
SL2SJ140650+522619	0.80	0.67	87.4	23.84	22.59	21.31	19.96	19.47			

Table 3.4: CFHT photometry. Best fit parameters for de Vaucouleurs models of the surface brightness profile of the lens galaxies, after careful manual masking of the lensed images. Columns 2–4 correspond to the effective radius ($R_{\rm eff}$), the axis ratio of the elliptical isophotes (q), and the position angle measured east of north (PA). The system SL2SJ140533+550231 has two lens galaxies of comparable magnitude, and the parameters of both galaxies are given. The typical uncertainties are a few degrees for the position angle, $\Delta q \sim 0.03$ for the axis ratio, 0.3 for u-band magnitudes, 0.2 for g and r-band magnitudes, 0.1 for magnitudes in the remaining bands, 30% on the effective radii.
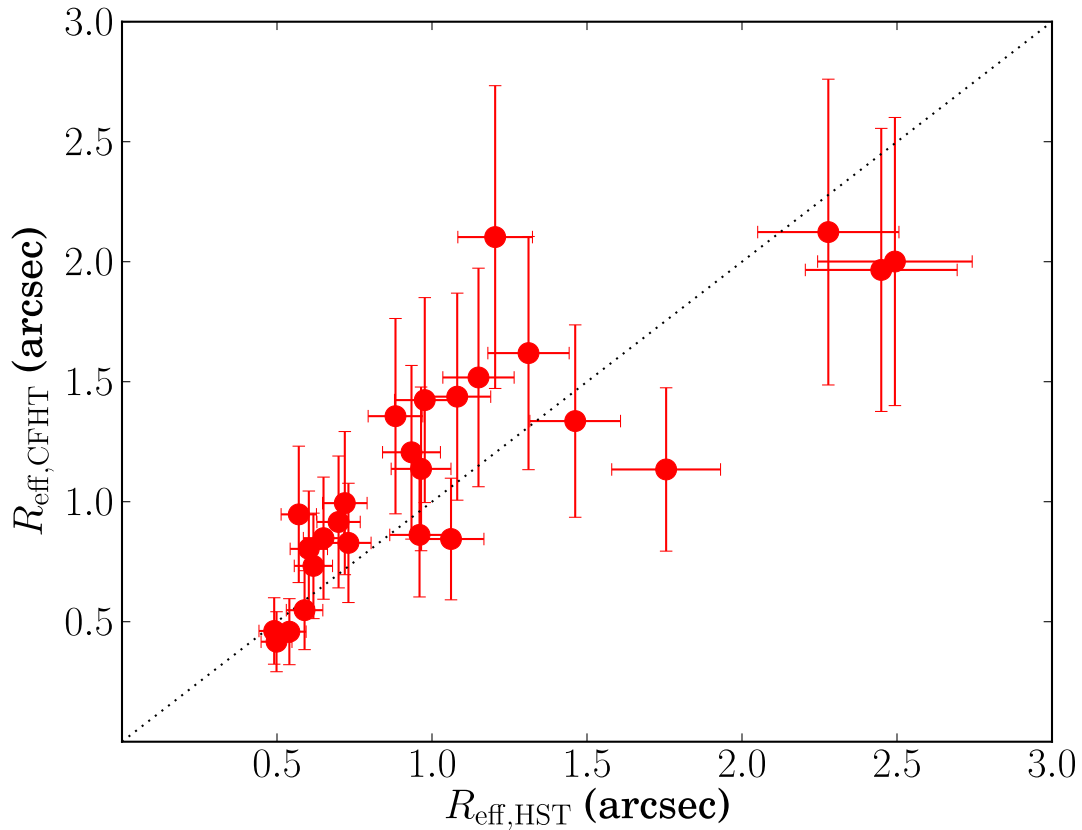
Figure 3.2: Comparison between effective radii measured from ground-based versus space-based photometry. Error bars on *HST* effective radii represent the assigned 10% systematic uncertainty due to fixing the light profile to a de Vaucouleurs model. The relative scatter between the best fit values of the two measurements is 30% and is used to quantify uncertainties in CFHT effective radii.

Name	$R_{\rm eff}$ (arcsec)	q	PA (degrees)	u	g	r	i	z	J	H	Ks
SL2SJ141137+565119	0.85	0.99	2.5	21.68	20.37	19.08	18.55	18.27			
SL2SJ141917+511729	2.10	0.64	47.7	23.33	20.96	19.43	18.56	18.21			
SL2SJ142003+523137	0.72	0.20	71.2	24.69	22.85	21.43	20.70	20.31			
SL2SJ142031+525822	1.11	0.62	-86.0	22.94	20.88	19.36	18.68	18.33			
SL2SJ142059+563007	1.62	0.54	-12.6	22.72	20.73	19.29	18.51	18.16			
SL2SJ142321+572243	1.42	0.82	62.9	23.67	21.65	20.00	18.95	18.64			
SL2SJ142731+551645	0.39	0.31	-63.7	23.33	22.00	20.74	19.85	19.47			
SL2SJ220329+020518	0.99	0.81	-44.7	22.68	21.08	19.80	19.15	18.83			17.85
SL2SJ220506+014703	0.66	0.48	87.2	23.71	21.69	20.09	19.24	18.92			17.73
SL2SJ220629+005728	1.37	0.63	-25.1	23.59	22.31	20.99	19.75	19.24			17.66
SL2SJ221326-000946	0.27	0.34	-29.1	23.60	21.78	20.33	19.74	19.44			18.61
SL2SJ221407-180712	0.68	0.72	57.0	24.81	22.81	21.37	20.15	19.73			
SL2SJ221852+014038	0.90	0.53	-67.1	23.86	21.70	20.19	19.07	18.67			17.54
SL2SJ221929-001743	1.01	0.78	85.1	21.32	19.52	18.31	17.78	17.50			
SL2SJ222012+010606	0.80	0.87	-22.4	22.34	20.47	19.38	18.84	18.56			17.69
SL2SJ222148+011542	1.12	0.81	79.6	22.02	20.15	18.83	18.21	17.91			16.90
SL2SJ222217+001202	1.56	0.66	37.7	22.77	21.03	19.62	18.88	18.53			

Table 3.4: continued.

to 120 minutes. Optical spectroscopy data come from three different instruments.

For most of the systems we have data obtained with the LRIS spectrograph at Keck (Oke et al. 1995). The wavelength coverage of LRIS is typically in the range $3500 - 8000$ Å for data taken before 2009 and extends up to 10000 Å for later data, after the installation of the new detector with much reduced fringing patterns (Rockosi et al. 2010). The spectral resolution is about 140 km s^{-1} FWHM on the red side of the spectrograph. Data reduction for LRIS spectra was performed with a pipeline written by M.W. Auger.

For a set of 13 systems we have VLT observations with the instrument X-Shooter[3]. X-Shooter has both a higher resolution ($\sim 50\,{\rm km\,s^{-1}}$) and a longer wavelength coverage (from 3500 Å up to 25000 Å) than LRIS. X-Shooter spectra were reduced with the default ESO pipeline[4]. The observations were done by nodding along a long slit of width $0\rlap{.}''9$ for

---

[3]ESO/VLT programs 086.B-0407(A), 089.B-0057(A) and 092.B-0663, PI Gavazzi
[4]http://www.eso.org/sci/facilities/paranal/instruments/xshooter/

Name	R_{eff} (arcsec)	q	PA (degrees)	m_{F814W}	m_{F606W}	m_{F600LP}	m_{F475X}	Set
SL2SJ020833-071414	0.94	0.79	70.5	$\cdots$	$\cdots$	18.58	20.69	(c)
SL2SJ021325-074355	2.45	0.67	34.9	$\cdots$	21.08	$\cdots$	$\cdots$	(b)
SL2SJ021411-040502	0.93	0.91	77.8	19.07	20.73	$\cdots$	$\cdots$	(a)
SL2SJ021737-051329	0.61	0.91	71.7	19.13	20.77	$\cdots$	$\cdots$	(a)
SL2SJ021902-082934	0.57	0.73	73.2	$\cdots$	$\cdots$	19.55	21.79	(c)
SL2SJ022357-065142	0.88	0.81	48.0	$\cdots$	$\cdots$	19.21	21.43	(c)
SL2SJ022511-045433	2.28	0.72	25.1	$\cdots$	17.68	$\cdots$	$\cdots$	(b)
SL2SJ022610-042011	1.06	0.81	61.9	$\cdots$	20.00	$\cdots$	$\cdots$	(b)
SL2SJ022648-040610	1.10	0.38	-47.4	$\cdots$	21.45	$\cdots$	$\cdots$	(b)
SL2SJ023251-040823	0.96	0.74	-68.2	$\cdots$	19.91	$\cdots$	$\cdots$	(b)
SL2SJ084909-041226	0.49	0.49	39.1	$\cdots$	$\cdots$	20.62	23.40	(c)
SL2SJ084959-025142	1.46	0.78	-64.1	$\cdots$	18.80	$\cdots$	$\cdots$	(b)
SL2SJ085826-014300	0.59	0.81	82.2	$\cdots$	22.22	$\cdots$	$\cdots$	(b)
SL2SJ090106-025906	0.50	0.80	-20.3	$\cdots$	22.78	$\cdots$	$\cdots$	(b)
SL2SJ090407-005952	2.50	0.79	74.4	$\cdots$	20.89	$\cdots$	$\cdots$	(b)
SL2SJ095921+020638	0.54	0.78	26.0	$\cdots$	21.65	$\cdots$	$\cdots$	(b)
SL2SJ135847+545913	0.70	0.80	-57.1	$\cdots$	$\cdots$	19.65	21.99	(c)
SL2SJ135949+553550	1.76	0.61	30.7	$\cdots$	22.01	$\cdots$	$\cdots$	(b)
SL2SJ140123+555705	0.96	0.78	-43.5	$\cdots$	20.33	$\cdots$	21.66	(b,d)
SL2SJ140156+554446	1.08	0.79	27.2	$\cdots$	$\cdots$	18.90	21.10	(c)
SL2SJ140221+550534	1.15	0.87	-43.9	$\cdots$	$\cdots$	18.59	20.63	(c)
SL2SJ140533+550231	0.91	0.75	-21.3	$\cdots$	21.75	$\cdots$	$\cdots$	(b)
	0.41	0.93	-12.72	$\cdots$	22.02	$\cdots$	$\cdots$	
SL2SJ140546+524311	0.73	0.82	-27.8	$\cdots$	$\cdots$	19.44	21.77	(c)
SL2SJ140650+522619	0.60	0.65	84.3	$\cdots$	21.97	$\cdots$	$\cdots$	(b)
SL2SJ141137+565119	0.65	0.79	8.1	$\cdots$	$\cdots$	18.93	20.65	(c)
SL2SJ141917+511729	1.20	0.69	48.8	$\cdots$	$\cdots$	19.24	21.54	(c)
SL2SJ142031+525822	1.04	0.65	-80.0	$\cdots$	19.86	$\cdots$	$\cdots$	(b)
SL2SJ142059+563007	1.31	0.58	-13.6	$\cdots$	$\cdots$	18.96	21.01	(c)
SL2SJ142321+572243	0.98	0.85	68.2	$\cdots$	$\cdots$	19.48	22.01	(c)
SL2SJ142731+551645	0.50	0.29	-62.1	$\cdots$	21.08	$\cdots$	$\cdots$	(b)
SL2SJ220329+020518	0.72	0.84	-50.6	$\cdots$	$\cdots$	19.79	21.76	(c)
SL2SJ221326-000946	0.50	0.38	-32.5	$\cdots$	20.64	$\cdots$	$\cdots$	(b)
SL2SJ221407-180712	0.77	0.69	49.1	$\cdots$	21.69	$\cdots$	$\cdots$	(b)

Table 3.5: HST photometry. Best fit parameters for de Vaucouleurs models of the surface brightness profile of the lens galaxies, after careful manual masking of the lensed images. Columns 2–4 correspond to the effective radius (R_{eff}), the axis ratio of the elliptical isophotes (q), and the position angle measured east of north (PA). The system SL2SJ140533+550231 has two lens galaxies of comparable magnitude, and the parameters of both galaxies are given. The last column indicates the set of observations used, from the list in Table 3.3.

the UVB and VIS arms and 1″0 for the NIR arm.

Finally, six systems presented here have data obtained with DEIMOS at Keck (Faber et al. 2003). The grating used in all DEIMOS observations is the 600ZD, with a wavelength range between 4500 Å and 9500 Å and a spectral resolution of about $160\,\mathrm{km\,s^{-1}}$. DEIMOS data were reduced with the DEEP2 pipeline (Cooper et al. 2012a; Newman et al. 2012b).

Both redshifts and velocity dispersions are measured by fitting stellar templates, broadened with a velocity kernel, to the observed spectra. This is done in practice with a Monte Carlo Markov Chain adaptation of the velocity dispersion fitting code by van der Marel (1994), written by M. W. Auger and described by Suyu et al. (2010). We used 7 different templates of G and F stars, which should provide an adequate description of the stars in red passive galaxies, taken from the Indo US stellar library. The code also fits for an additive polynomial continuum, to accommodate for template mismatch effects or imperfections in the instrumental response correction. In most cases, a polynomial of order five is used.

The rest-frame wavelength range typically used in our fits is $3850\mathring{A} - 5250\mathring{A}$, which brackets important absorption lines such as Ca K,H at $3934, 3967\mathring{A}$, the G-band absorption complex around $4300\mathring{A}$ and Mgb at $5175\mathring{A}$. Depending on the redshift of the target and the instrument used, this is not always allowed as part of the wavelength region can fall outside the spectral coverage allowed by the detector, or because of Telluric absorption. In those cases the fitted rest-frame region is extended.

Systematic uncertainties in the velocity dispersion measurements are estimated by varying the fitted wavelength region and order of the polynomial continuum. These are

typically on the order of $20\,\mathrm{km\,s^{-1}}$ and are then summed in quadrature to the statistical uncertainty.

All the optical spectra of our systems are shown in Figure 3.3.

3.3.2 Source spectroscopy

Measuring the redshift of a lensed background source is important not only for determining the geometry of the gravitational lens system, but also to confirm that the arc is actually in the background relative to the lens. The arcs of the lensed sources are relatively faint in broad band photometry ($g \sim 24$), implying that their continuum radiation cannot be detected in most cases. However the sources are selected to be blue (Gavazzi et al. 2012) and are often associated with emission lines from star formation and/or nuclear activity. The typical redshifts of our arcs are in the range $1 < z < 3$. This means that optical spectroscopy can effectively detect emission from the [OII] doublet at $3727 - 3729 \mathring{A}$, for the lowest redshift sources, or Ly-α for objects at $z > 2.5$ or so. This is the case for roughly half of the systems observed. The remaining half does not show detectable emission line in the observed optical part of the spectrum, either because the most important lines fall in the near-infrared, or because emission is too weak. Emission lines from the arcs can be easily distinguished by features in the lens because they are spatially offset from the lens light.

X-Shooter observations proved to be remarkably efficient in measuring source redshifts. This is in virtue of its wavelength range that extends through the near infrared up to $25000 \mathring{A}$ and its medium resolution that limits the degrading effect of emission lines

from the atmosphere. Of 13 systems observed with X-Shooter, 12 of them yielded a redshift of the background source, all of which with at least two identified lines.

In addition, for four systems we have near infrared spectroscopic observations with the instrument GNIRS on Gemini North (PI Marshall, GN-2012B-Q-78, PI Sonnenfeld, GN-2013A-Q-91), used in cross-dispersed mode, covering the wavelength range $10000\mathring{A} - 25000\mathring{A}$ at once. Of the four systems observed, two of them show two emission lines from the background source.

In most cases when only optical spectroscopy is available, only one emission line is detected over the whole spectrum. The [OII] doublet can be easily identified even with relatively low resolution spectrographs. The identification of the Ly-α line is less trivial. Ly-α is typically the brightest emission line in the rest frame wavelength range $1000 - 3000\mathring{A}$ when present, but other emission lines like CIV 1546Å, OIII] 1666Åor CIII] 1908Å can sometimes be seen. When we detect an emission line close to the blue end of the spectrum it could in principle be any of those lines. However a detection of one of the above lines and a non-detection of the other ones is quite unlikely, unless CIII] 1908Å falls right at the blue edge of the observed spectrum. In that case though we should expect to observe the [OII] doublet at redder wavelengths. This case is never encountered, therefore in all cases when we detect an unresolved emission line bluer than $6000\mathring{A}$, and no other lines, we can safely assume it is Ly-α. The system SL2SJ022357-065142 is a particular case: we detected an emission line spatially associated with the background source at $9065\mathring{A}$, with a $5 - \sigma$ significance. Given the low S/N the line is both compatible with being the [OII] doublet or an individual line. Possible other lines are [OIII] 5007Åand H-β, which cannot be ruled out. Therefore we do not claim redshift

measurements for that source: deeper data is needed to establish whether the line is the [OII] doublet or not.

The 2d spectra around all the detected emission lines for all the systems are shown in Figure 3.8. Note that for some systems the line emission is multiply imaged on both sides of the foreground object. This provides a decisive clue on the lens nature of those systems, important when ranking our targets by their likelihood of being lenses (Paper III).

Finally, six background sources are bright enough to be visible with continuum radiation and several absorption/emission features can be identified in their spectra. The absorption line spectra of these sources are plotted in Figure 3.7.

Despite our efforts in acquiring spectroscopic data for our lenses, seven of the 36 grade A lenses with spectroscopic follow-up have no measured source redshifts. In Paper II Ruff et al. (2011) made use of photometric data together with lensing cross-section arguments to estimate source redshifts, with a technique called *photogeometric redshift*. Here the fraction of lenses with no source redshift is small compared to the sample size, therefore it is not essential to include them in the analysis through the use of this method.

3.4 Lens models

The main goal is to measure Einstein radii of our lenses. We define the Einstein radius R_{Ein} to be the radius within which the mean surface mass density $\bar{\Sigma}(< R_{\mathrm{Ein}})$ equals the critical density Σ_{cr} of the lensing configuration. While the critical density depends on the lens and source redshifts, the ratio of $\bar{\Sigma}(< R_{\mathrm{Ein}})/\Sigma_{\mathrm{cr}}$ (i.e., the convergence) does not:

Name	obs. date	Instrument	slit (″)	width (″)	seeing (″)	exp. time (s)	z_d	z_s	σ (km/s)	S/N (Å^{-1})	res. (km/s)
SL2SJ020457−110309	11-19-2013	XSHOOTER	0.9	1.60	1.6	4140	0.609	1.89	250 ± 30	9	40
SL2SJ020524−093023	12-03-2013	XSHOOTER	0.9	1.60	1.1	2760	0.557	1.33	276 ± 37	7	40
SL2SJ020833−071414	11-29-2011	LRIS	1.0	1.62	1.0	900	0.428	$\cdots$	295 ± 27	17	150
SL2SJ021206−075528	01-28-2011	LRIS	0.7	1.62	0.6	2700	0.460	$\cdots$	257 ± 25	28	120
SL2SJ021247−055552	10-08-2010	XSHOOTER	0.9	1.60	0.7	2800	0.750	2.74	273 ± 22	22	47
	12-09-2012	DEIMOS	1.0	1.90	1.2	3600			253 ± 28	11	170
SL2SJ021325−074355	09-14-2007	LRIS	1.0	1.68	0.6	1800	0.717	3.48	293 ± 34	5	220
SL2SJ021411−040502	01-28-2011	LRIS	0.7	1.62	0.6	2700	0.609	1.88	264 ± 26	13	120
	10-08-2010	XSHOOTER	0.9	1.60	0.7	2800			209 ± 20	27	49
	12-09-2012	DEIMOS	1.0	1.88	0.8	3600			287 ± 47	10	170
SL2SJ021737−051329	12-23-2006	LRIS	1.5	1.68	0.6	2400	0.646	1.85	239 ± 27	11	160
	09-14-2007	LRIS	1.0	1.68	0.6	3600			292 ± 33	12	120
SL2SJ021801−080247	01-28-2011	LRIS	0.7	1.62	0.6	1800	0.884	2.06	$\cdots$	5	120
	12-09-2012	DEIMOS	1.0	0.81	1.0	1200			$\cdots$	5	170
	11-18-2013	XSHOOTER	0.9	1.60	1.0	2760			246 ± 48	7	40
SL2SJ021902−082934	09-13-2007	LRIS	1.0	1.68	0.7	2700	0.389	2.15	289 ± 23	21	210
SL2SJ022046−094927	12-09-2012	DEIMOS	1.0	1.90	0.8	1800	0.572	2.61	248 ± 27	10	170
	11-20-2013	XSHOOTER	0.9	1.60	1.0	2760			$\cdots$	7	40
SL2SJ022056−063934	09-13-2007	LRIS	1.0	1.68	0.8	1800	0.330	$\cdots$	231 ± 25	23	220
SL2SJ022346−053418	11-30-2011	LRIS	1.0	1.62	0.6	900	0.499	1.44	288 ± 28	20	140
SL2SJ022357−065142	08-06-2010	LRIS	1.0	1.64	1.0	900	0.473	$\cdots$	312 ± 27	23	160
	11-01-2010	LRIS	1.0	1.64	0.9	900			289 ± 28	25	150
SL2SJ022511−045433	09-09-2009	LRIS	1.0	0.81	0.7	1800	0.238	1.20	234 ± 21	54	500
SL2SJ022610−042011	09-14-2007	LRIS	1.0	1.62	0.6	1800	0.494	1.23	263 ± 24	15	230
SL2SJ022648−040610	12-23-2006	LRIS	1.5	1.68	0.6	2700	0.766	$\cdots$	333 ± 24	9	160
	10-08-2010	XSHOOTER	0.9	1.60	0.6	2800			324 ± 21	43	47
	11-20-2013	XSHOOTER	0.9	1.60	1.0	2760			$\cdots$	6	40
SL2SJ022648−090421	09-14-2007	LRIS	1.0	1.68	0.6	1800	0.456	$\cdots$	302 ± 24	23	220
SL2SJ022708−065445	11-23-2013	XSHOOTER	0.9	1.60	0.7	2760	0.561	$\cdots$	$\cdots$	9	40
SL2SJ023251−040823	09-13-2007	LRIS	1.0	1.68	0.7	2700	0.352	2.34	281 ± 26	19	220
	10-06-2010	XSHOOTER	1.0	1.60	0.7	2800			247 ± 32	37	49
SL2SJ023307−043838	11-24-2013	XSHOOTER	0.9	1.60	0.9	2760	0.671	1.87	204 ± 21	9	40
SL2SJ084847−035103	01-03-2011	XSHOOTER	0.9	1.60	1.0	2800	0.682	1.55	197 ± 21	19	49
SL2SJ084909−041226	01-02-2011	XSHOOTER	0.9	1.60	0.9	2800	0.722	1.54	320 ± 24	14	49
	12-09-2012	DEIMOS	1.0	1.88	0.8	6000			275 ± 26	26	160
SL2SJ084934−043352	01-28-2011	LRIS	0.7	1.62	0.6	1800	0.373	$\cdots$	245 ± 24	23	120
SL2SJ084959−025142	01-01-2011	XSHOOTER	0.9	1.60	0.8	2800	0.274	2.09	276 ± 35	67	47
SL2SJ085019−034710	01-28-2011	LRIS	0.7	1.62	0.6	2700	0.337	3.25	290 ± 24	26	120
SL2SJ085317−020312	11-01-2013	DEIMOS	1.0	1.41	0.8	9000	0.698	$\cdots$	213 ± 20	14	160
SL2SJ085327−023745	11-30-2011	LRIS	1.0	1.62	0.9	4800	0.774	2.44	$\cdots$	$\cdots$	150
SL2SJ085540−014730	01-28-2011	LRIS	0.7	1.62	0.6	3600	0.365	3.39	222 ± 25	24	120
	12-09-2012	DEIMOS	1.0	1.88	0.8	2400			209 ± 31	14	160
SL2SJ085559−040917	01-28-2011	LRIS	0.7	1.62	0.6	3600	0.419	2.95	281 ± 22	33	120
SL2SJ085826−014300	11-30-2011	LRIS	1.0	1.62	0.9	3600	0.580	$\cdots$	233 ± 25	$\cdots$	160
SL2SJ090106−025906	01-07-2011	XSHOOTER	0.9	1.60	0.7	2800	0.670	1.19	$\cdots$	7	49
SL2SJ090407−005952	12-30-2010	XSHOOTER	0.9	1.60	0.7	2800	0.611	2.36	183 ± 21	22	52
SL2SJ095921+020638	02-02-2011	XSHOOTER	0.9	1.60	0.7	2800	0.552	3.35	188 ± 22	17	47
SL2SJ135847+545913	04-29-2011	LRIS	1.0	1.62	0.8	2700	0.510	$\cdots$	287 ± 22	28	150
	03-22-2013	GNIRS	0.675	$\cdots$	0.7	7200			$\cdots$	$\cdots$	$\cdots$
SL2SJ135949+553550	03-17-2010	LRIS	1.0	1.62	0.7	5400	0.783	2.77	228 ± 29	9	150
	04-29-2011	LRIS	1.0	1.62	0.9	5400			234 ± 28	12	150
SL2SJ140123+555705	07-20-2006	LRIS	1.5	3.36	0.8	1200	0.527	$\cdots$	332 ± 25	10	210
SL2SJ140156+554446	04-29-2011	LRIS	1.0	1.62	0.8	2700	0.464	$\cdots$	297 ± 22	34	150
SL2SJ140221+550534	xx-xx-2xxx	SDSS	$\cdots$	$\cdots$	$\cdots$	$\cdots$	0.412	$\cdots$	$\cdots$	$\cdots$	$\cdots$
SL2SJ140454+520024	04-30-2011	LRIS	1.0	1.62	0.9	1800	0.456	1.59	342 ± 20	38	140
SL2SJ140546+524311	04-29-2011	LRIS	1.0	1.62	0.8	2700	0.526	3.01	284 ± 21	30	140
	03-26-2013	GNIRS	0.675	$\cdots$	0.5	4800			$\cdots$	$\cdots$	$\cdots$
SL2SJ140614+520253	07-20-2006	LRIS	1.5	3.36	0.8	1200	0.480	$\cdots$	247 ± 29	11	190

Table 3.6: Summary of spectroscopic observations and derived parameters.
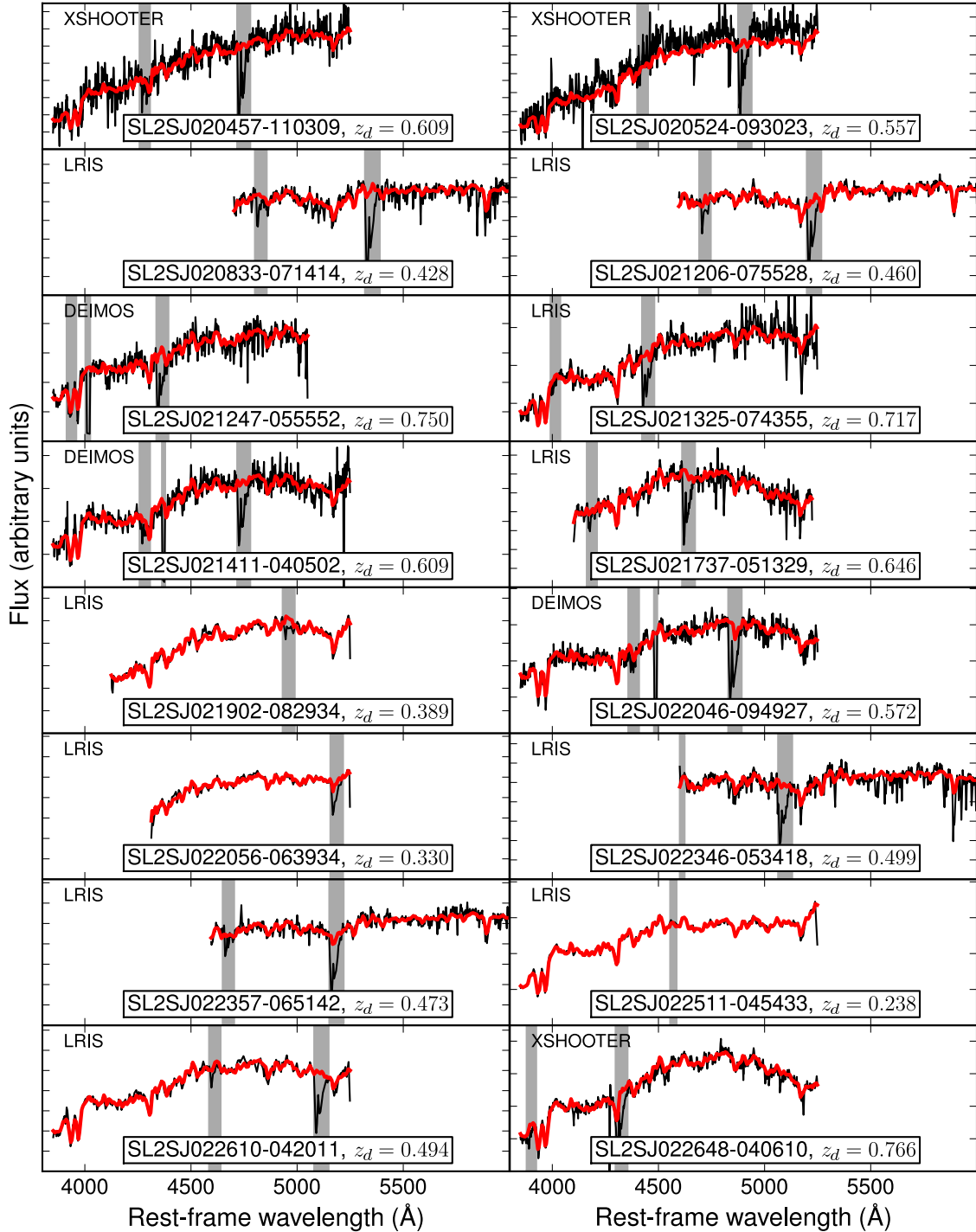
Figure 3.3: 1d spectra of SL2S lenses and lens candidates (in black). Where available, we overplot the best fit spectrum obtained for the velocity dispersion fitting (in red). Only the rest-frame wavelength region used in the fit is shown. Vertical gray bands are regions of the spectrum masked out of the fit and typically correspond to atmospheric absorption features. Each plot indicates the redshift of the galaxy and the instrument used to acquire the data shown.

Figure 3.4: *continued.*

77

Figure 3.5: *continued.*

LRIS

SL2SJ220629+005728, $z_d = 0.704$

XSHOOTER

SL2SJ221326-000946, $z_d = 0.338$

LRIS

SL2SJ221407-180712, $z_d = 0.651$

LRIS

SL2SJ221852+014038, $z_d = 0.564$

LRIS

SL2SJ221929-001743, $z_d = 0.289$

DEIMOS

SL2SJ222012+010606, $z_d = 0.232$

DEIMOS

SL2SJ222148+011542, $z_d = 0.325$

LRIS

SL2SJ222217+001202, $z_d = 0.436$

Rest-frame wavelength (Å)

Rest-frame wavelength (Å)
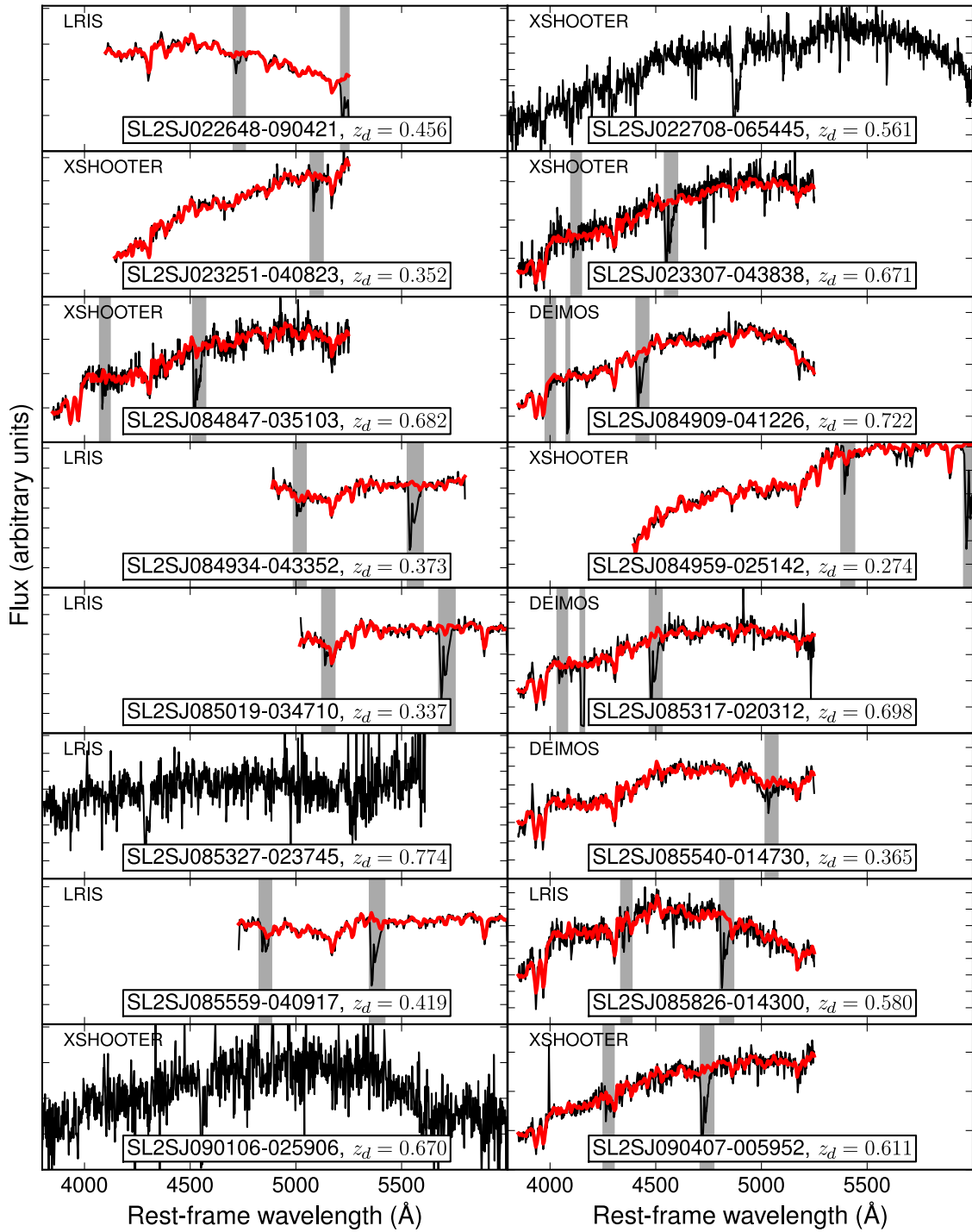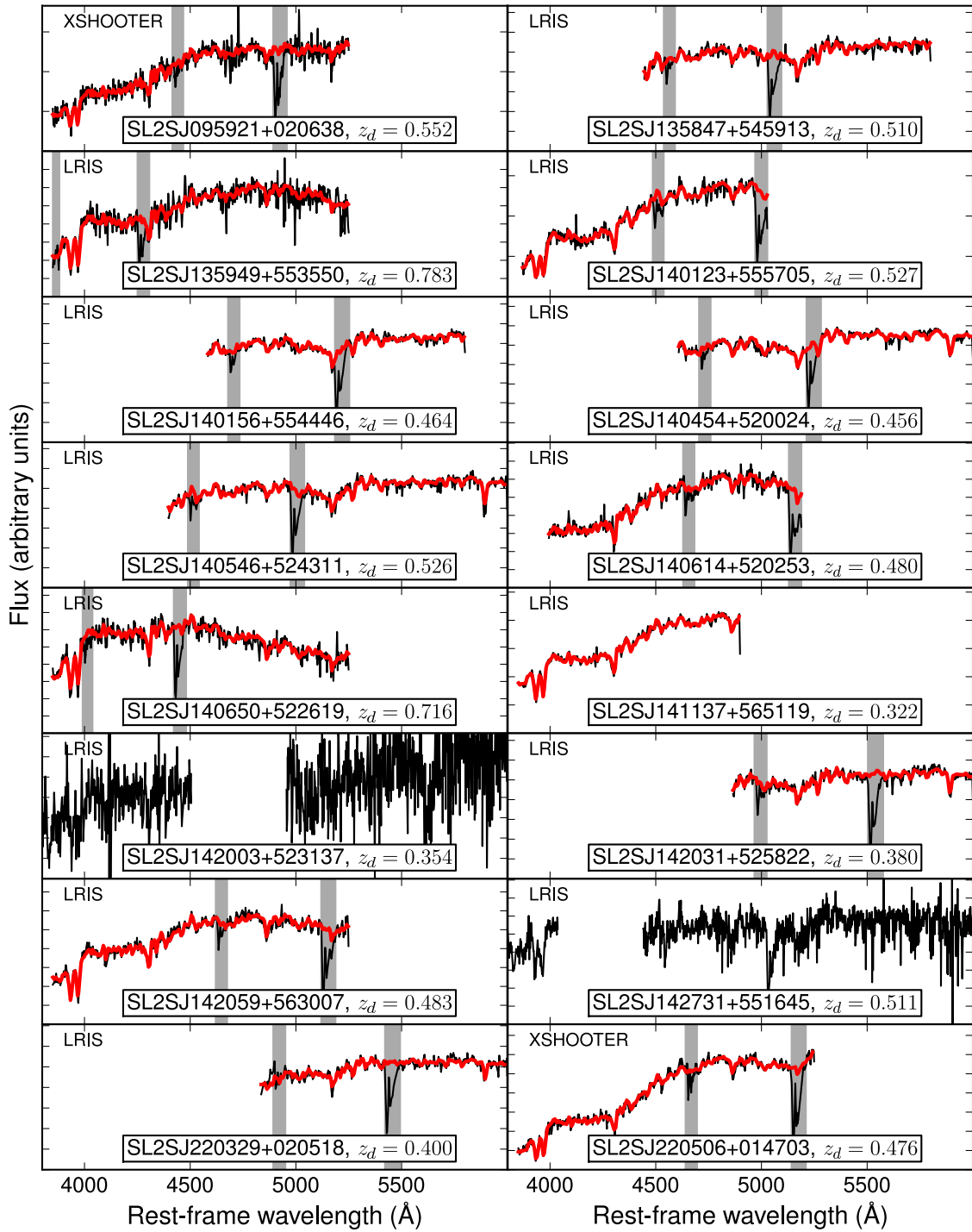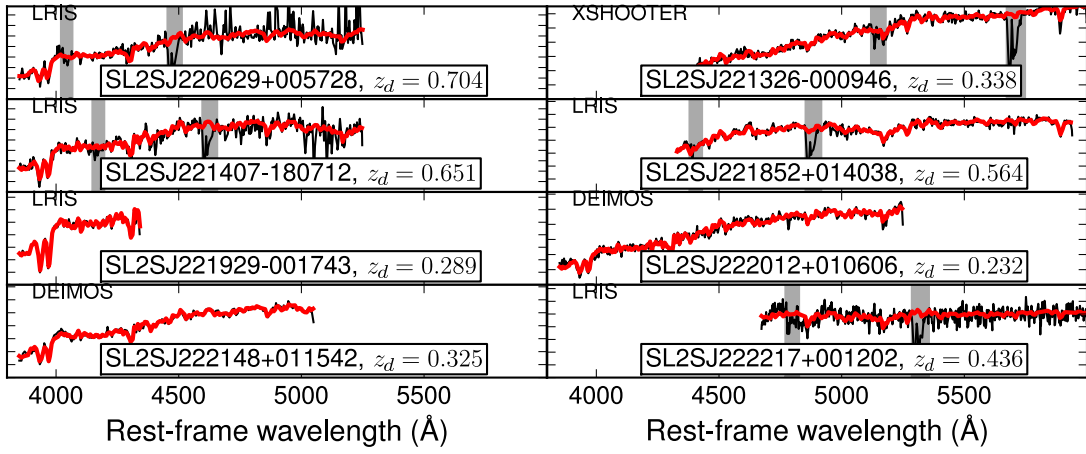
Figure 3.6: *continued.*
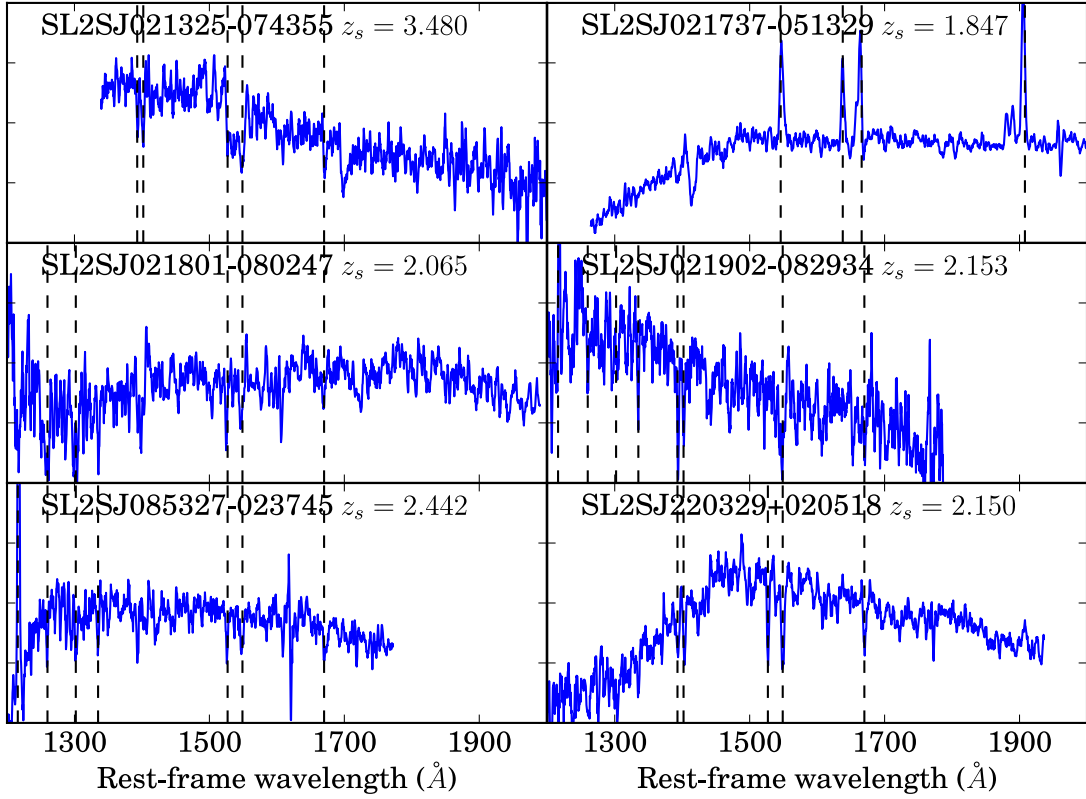
Figure 3.7: Spectra of lensed sources that are bright enough to be detected in the continuum. The vertical dashed lines highlight absorption/emission line features: in order of increasing wavelength Ly-α (1216Å), SiII (1260Å), SiII (1302Å, 1304Å), CII (1335Å), SiIV (1393Å, 1402Å), SiII (1527Å), CIV (1549Å), AlII (1670Å).

Figure 3.8: 2d spectra of SL2S lenses around the identified emission lines from the lensed arcs. Observer frame wavelength in Å is labeled on the horizontal axis.

Name	obs. date	Instrument	slit ($''$)	width ($''$)	seeing ($''$)	exp. time (s)	z_d	z_s	σ (km/s)	S/N (Å^{-1})	res. (km/s)
SL2SJ140650+522619	04-29-2011	LRIS	1.0	1.62	0.9	3600	0.716	1.47	253 ± 19	15	150
	04-30-2011	LRIS	1.0	1.62	0.9	3600			247 ± 20	16	160
SL2SJ141137+565119	01-14-2010	LRIS	1.0	1.62	1.3	2700	0.322	1.42	214 ± 23	35	470
SL2SJ142003+523137	04-30-2011	LRIS	1.0	1.62	0.9	2700	0.354	1.41	$\cdots$	4	150
SL2SJ142031+525822	04-29-2011	LRIS	1.0	1.62	0.8	1800	0.380	0.99	246 ± 23	24	150
SL2SJ142059+563007	04-29-2011	LRIS	1.0	1.62	0.9	1800	0.483	3.12	$\cdots$	20	$\cdots$
	04-30-2011	LRIS	1.0	1.62	0.8	1800			228 ± 19	18	160
SL2SJ142731+551645	04-30-2011	LRIS	1.0	1.62	0.8	3600	0.511	2.58	$\cdots$	12	150
SL2SJ220329+020518	08-06-2010	LRIS	1.0	1.62	0.9	2700	0.400	2.15	213 ± 21	36	170
SL2SJ220506+014703	10-06-2010	XSHOOTER	0.9	1.60	0.8	2800	0.476	2.53	317 ± 30	29	49
SL2SJ220629+005728	09-13-2007	LRIS	1.0	1.68	0.7	2700	0.704	$\cdots$	290 ± 39	6	230
SL2SJ221326−000946	09-09-2009	LRIS	1.0	1.62	1.0	1800	0.338	3.45	165 ± 20	30	150
	07-29-2011	XSHOOTER	0.9	1.60	0.8	2800			177 ± 21	32	56
SL2SJ221407−180712	09-13-2007	LRIS	1.0	1.68	0.7	2700	0.651	$\cdots$	200 ± 24	6	220
SL2SJ221852+014038	08-06-2010	LRIS	1.0	1.62	0.9	2700	0.564	$\cdots$	305 ± 23	28	170
	11-10-2012	GNIRS	0.675	$\cdots$	0.7	3600			$\cdots$	$\cdots$	$\cdots$
SL2SJ221929−001743	09-14-2007	LRIS	0.7	1.68	0.6	1800	0.289	1.02	189 ± 20	23	420
SL2SJ222012+010606	08-18-2012	DEIMOS	1.0	1.88	1.2	3600	0.232	1.07	127 ± 15	14	170
SL2SJ222148+011542	08-18-2012	DEIMOS	1.0	1.88	1.2	3600	0.325	2.35	222 ± 23	25	160
	10-01-2012	XSHOOTER	0.9	1.60	1.0	1400			$\cdots$	$\cdots$	$\cdots$
	11-11-2012	GNIRS	0.675	$\cdots$	0.7	3600			$\cdots$	$\cdots$	$\cdots$
SL2SJ222217+001202	08-06-2010	LRIS	1.0	1.62	0.9	900	0.436	1.36	221 ± 22	13	170
	11-01-2010	LRIS	1.0	1.62	0.9	900			200 ± 29	10	150

Table 3.6: Spectroscopic observations *(continued)*.

in practice then, the deflection angles and lensed image positions can all be predicted given a model with its Einstein radius in angular units. We only consider Einstein radii in angular units throughout this paper.

3.4.1   The method

We measure Einstein radii by fitting model mass distributions to the lensing data. We describe our lenses as singular isothermal ellipsoids (SIE), with convergence κ given by

$$\kappa(x,y) = \frac{R_{\mathrm{Ein}}}{2r}, \tag{3.1}$$

where $r^2 \equiv qx^2 + y^2/q$ and q is the axis ratio of the elliptical isodensity contours. The free parameters of the lens model are therefore R_{Ein}, the axis ratio q, the position angle

(PA) of the major axis, and the x and y positions of the centroid. In principle, more degrees of freedom could be introduced. In some cases, lens models are found to require a constant external shear, with strength γ_{ext} and position angle $\mathrm{PA}_{\mathrm{ext}}$, in order to describe the lensing effect of massive objects (such as groups or clusters) close to the optical axis. However, this external shear is highly degenerate with the mass orientation of the main lens, and our data are not detailed enough to distinguish between the two. For this reason we only include a shear component for the lenses for which we cannot otherwise find a working model.

The fit is performed by generating model lensed images and comparing them to the observed images that have the lens light subtracted. For fixed lens parameters, light from the image plane is mapped back to a grid on the source plane and the source light distribution is then reconstructed following Suyu et al. (2006). This source reconstruction, as well as the entire lensing analysis, follows a Bayesian approach. For a given model lens, the Bayesian evidence of the source reconstruction is computed, which then defines the quality of the lens model. The lens parameter space is then explored with a Monte-Carlo Markov Chain (MCMC) sampler, propagating the source reconstruction evidence as the likelihood of the lens model parameters.

The practical realization of this procedure is done by using the lens modeling software `GLEE`, developed by Suyu & Halkola (2010). This approach differs slightly from the one adopted in Paper I, in that a pixelized source reconstruction is used instead of fitting Sérsic components. To make sure that our analysis is robust, we repeat the fit for the systems previously analyzed in Paper I. This allows us to gauge the importance of systematic effects related to the choice of modeling technique.

For systems with *HST* imaging in more than one band, only the bluest band image is used for the analysis as the signal from the blue star-forming lensed sources is highest. The g band image is used when modeling CFHT data. Typically we only attempt to model a small region of the image around the identified lensed sources, then check that our lens models do not predict detectable lensed sources in areas outside the data region. We assume uniform priors on all the lens parameters except the centroid, for which we use a Gaussian PDF centered on the observed light distribution and with a dispersion of 1 pixel. For systems with only ground-based imaging, for which the lensing signal is diluted by the large PSF, we keep the centroid fixed to that of the optimal light profile. In some cases we also adopt a Gaussian prior on the mass PA, centered on the PA of the light, or we keep the PA fixed. Those cases are individually discussed below.

Our analysis also allows us to determine the brightness of the lensed sources. This is important information as it allows us to constrain their distance in cases where their spectroscopic redshift is unknown (Ruff et al. 2011). The unlensed magnitude of the background object is recovered by fitting Sérsic components to the reconstructed source.

The values of the measured lens parameters with 68% credible intervals ($1 - \sigma$ uncertainties) derived from the posterior probability distribution function marginalized over the remaining parameters are reported in Table 3.4.2. Cutouts of the lens systems with the most-probable image and source reconstruction are shown in Figure 3.9. All images are orientated north up and east left, with the exception of lens models based on WFPC2 data. Those models are performed in the native detector frame in order to avoid degrading further the quality of the WFPC2 images, as they typically have a low S/N. In such situations a compass is displayed to guide the eye.

The formal uncertainties on the Einstein radius given by the MCMC sampling are typically very small: the 1-σ uncertainty is for most lenses smaller than 1%. However, our measurements of the Einstein radius rely partly on the assumption of an SIE profile for the lens mass distribution: in principle, mass models with density slope different from isothermal or isodensity contours different from ellipses can produce different Einstein radii. Perhaps more significantly, some systematic effects can be introduced at various points in our analysis: in particular, the assertions of a specific model PSF, a specific arc mask, and a specific lens light subtraction procedure all induce uncertainty in the final prepared data image (*e.g.* Marshall et al. 2007; Suyu et al. 2009). Bolton et al. (2008a) estimated the systematic uncertainty on typical Einstein radius measurements to be about 2%. We can further verify this result by comparing Einstein radius measurements from paper I with the new values found here. The analysis of Paper I differs from the present one in the lens light subtraction, choice of the arc mask and lens model technique (Sérsic component fitting versus pixelized source reconstruction), so a comparison of the two different measurements should reflect systematics from most of the effects listed above. For a few of the systems already analyzed in Paper I, the current lens models are qualitatively different from the ones presented in Paper I and the measured values of the Einstein radii are correspondingly different. In most cases this is in virtue of the collection of new data with *HST* WFC3 that revealed features on the lensed arcs, previously undetected, that helped improve the lens model. After excluding those systems, the relative scatter between the most probable values of R_{Ein} measured in the two different approaches (current and previous) is 3%. We thus take 3% as our estimate of the systematic uncertainty on the measurement of the Einstein radius

with the technique used here, and convolve the posterior probability distribution for the Einstein radius obtained from the MCMC with a Gaussian with 3% dispersion. All the uncertainties on R_{Ein} quoted in this paper reflect this choice.

3.4.2 The lenses

Although the lens modeling procedure is the same for all lenses, each system has its own peculiarities that need to be taken care of. In what follows we describe briefly and case by case the relevant aspects of those lens models that deserve some discussion.

Lens grades are also discussed in this subsection, when explanation is needed, and are reported in Table 3.4.2. In general we apply the following guidelines. For a system with *HST* imaging we require, in order for it to be a grade A, that at least a pair of multiple images of the same source is visible and that we can describe it with a robust lens mass model compatible with the light distribution of the lens galaxy (i.e. similar centroid, orientation and axis ratio). For systems with only ground-based imaging we impose the additional requirement of having a spectroscopic detection of the background source, in order to be sure that the blue arcs that we observe are not part of the foreground galaxy. Spectroscopic data therefore enters the lens classification process. We refer to our companion paper (Paper IV) when discussing spectroscopic measurements. Furthermore, systems with a reliable ground-based lens model but no source spectroscopy are given grade B, as well as systems with secure spectroscopic detection of the source but no robust lens model. Systems lacking both, or for which we suspect that strong lensing might not be present are instead given grade C. We stress that a grade is not necessarily

a statement on the quality or usefulness of a system as a lens, but rather its likelihood of being a strong lens given the available data. Consequently, grades are subject to change as new data become available.

- SL2SJ020457-110309. The CFHT data reveal an early-type galaxy with a bright blue image, tangentially elongated with respect to it. The blue object is spectroscopically detected to be at higher redshift than the main galaxy. The lens model however does not predict the presence of a counter-image. This is probably because the image of the background source appears to be unusually straight, as opposed to the typical arc-like shape of strongly lensed images. While there is no doubt that the foreground galaxy is lensing the background source, our ground-based data does not allow us to determine whether there is strong lensing or not, therefore we assign a grade B to this system.

- SL2SJ020524-093023. The visible lensed images in this system consist of one arc. The lens model predicts the presence of a counter-image, too faint to be visible in CFHT data.

- SL2SJ020833-071414. The lensed features of this system consist of a double image of a bright compact component and a low surface brightness ring. The model cannot fully reproduce the image of the bright double but this is probably due to the presence of a compact unresolved component, like an AGN. AGNs in the source plane are difficult to model with a pixelized reconstruction technique, because the image regularization process smoothes our model images. This effect is present in other lenses with sharp peaks in the source surface brightness distribution. Since

the signal-to-noise ratio of the *HST* image is low and no additional information comes from spectroscopy, this lens is given a grade B.

- SL2SJ021325-074355. The source lensed by this high redshift galaxy ($z_d = 0.717$) appears to have two separate bright components. Our source reconstruction confirms this picture. There is a massive elliptical galaxy in the foreground that may be providing extra deflection to the light coming from the source, thus perturbing the image. This perturber is very close to the observer ($z = 0.0161$, from SDSS) and therefore its lensing power is greatly reduced with respect to the main deflector. We model the mass distribution from this galaxy with an additional SIE with centroid and PA fixed to the light distribution and R_{Ein} and q as free parameters. To quickly calculate the deflection angles from this perturber we make the approximation that it lies at the same redshift as the main lens. While this is not formally correct, the model still describes qualitatively the presence of an extra source of deflection towards the direction of the foreground galaxy. The impact of this perturber on the lensing model is in any case small.

- SL2SJ021411-040502. The source has two bright components, one of which is lensed into the big arc and its fainter couter-image. The second component forms a double of smaller magnification. This lens was modeled in Paper I where we explained how there are two lens models, with different Einstein radii, that match the image configuration. The pixelized source reconstruction technique adopted here to model the lens favors the solution alternative to the one chosen in Paper I.

- SL2SJ021737-051329. This lens system is in a cusp configuration, meaning that the

88

source lies just within one of the four cusps of the astroid caustic of the lens. Either a mass centroid offset from the light center or a large shear is required to match the curvature of the big arc. This was also needed in Paper I and previously found by Tu et al. (2009). Here, we find the amount of external shear to be $\gamma_{\mathrm{ext}} = 0.11 \pm 0.01$

- SL2SJ022346-053418. The CFHT image shows an extended arc and a bright knot at the opposite side with respect to the lens. Although this latter component might be the counter-image to the arc, its color is different and it is not detected spectroscopically. Therefore only the arc is used for the lensing analysis. The main arc has a higher redshift than the lens, however the lens model is not definitive in assessing whether this system is a strong lens. This is therefore a grade B lens.

- SL2SJ022357-065142. The lensed source appears to have a complex morphology. We identify three distinct components, each of which is doubly imaged.

- SL2SJ022708-065445. An extended blue arc is clearly visible West of a disky early-type galaxy. The reconstructed source appears to consist of two components close to each other. In order to achieve a satisfactory fit, we had to put a Gaussian prior on the position angle of the mass distribution, centered on the PA of the light.

- SL2SJ023307-043838. This double image system allows us to robustly measure the Einstein radius of the lens galaxy.

- SL2SJ084934-043352. Only one arc is visible in the CFHT image. In order to obtain a meaningful lens model we need to fix the PA of the mass profile to that of the light. This system is a grade B due to the lack of spectroscopic detection of

the background source.

- SL2SJ084959-025142 is a double-like lens system. Part of the light close to the smaller arc is masked out in our analysis, as it is probably a contamination from objects not associated with the lensed source.

- SL2SJ085019-034710. The CFHT image shows a bright arc produced by the lensing effect of a disk galaxy. The lens model predicts the presence of a counter-image opposite to the arc, but it is not bright enough to be distinguished from the disk of the lens. In addition, such a counterimage could suffer from substantial extinction.

- SL2SJ085317-020312. One extended arc is visible. We assign a Gaussian prior to the mass position angle in order to obtain a reasonable fit.

- SL2SJ085559-040917. The main blue arc of this system is at redshift 2.95. The other blue features seen in CFHT data however are too faint for us to establish an unambiguous interpretation of the lens configuration. Therefore we conservatively assign grade B to this system. Higher resolution photometry is needed to confirm this lens.

- SL2SJ090106-025906. The WFPC2 image of this system is contaminated with a cosmic ray, which has been masked out in our analysis. Our lens model predicts an image at the position of the cosmic ray, the presence of which cannot be verified with our data. The model however appears to be convincing and the background source is spectroscopically detected, therefore this is a grade A lens.

- SL2SJ095921+020638. This system, belonging to the COSMOS survey had previ-

ously been modeled by Anguita et al. (2009). These authors report a source redshift of 3.14 ± 0.05 whereas we find a slightly greater value of 3.35 ± 0.01 based on our own XSHOOTER data (Paper IV). They report an Einstein radius $R_{\text{Ein}} \sim 0\rlap{.}''71$ in close agreement with our $0\rlap{.}''74 \pm 0\rlap{.}''04$ estimate.

- SL2SJ135847+545913. We identify two distinct bright components in the source: one forms the big arc, the other one is only doubly-imaged.

- SL2SJ140123+555705 is a cusp-like system: three images of a single bright knot can be identified on the arc. The counter-image however is too faint to be detected in the WFC3 snapshot. This lens was already modeled in Paper I. The Einstein radius that we obtain here is not consistent with the value reported then. This is because the current model is obtained by analyzing newly obtained WPC3 data, which reveal more details on the arc. The lack of a counterimage does not prevent an accurate lens modeling because the main arc is very thin, curved and extended.

- SL2SJ140533+550231. This is a particular system, in that there are two lens galaxies of comparable brightness. The lensed image shows four images of a bright knot. We model the system with two SIE components, centered in correspondence with the two light components. Our inference shows a substantial degeneracy between the Einstein radii of the two lenses.

- SL2SJ140546+524311. This system shows a quadruply-imaged bright compact component. Two of the images are almost merged. A relatively large shear is required to match the position and shape of the counter-image opposite to the

arcs.

- SL2SJ140614+520253. A few different blue blobs are visible in the CFHT image, but there is no working lens model that can associate them with the same source. As done in Paper I, we model only the bright extended arc. The resulting Einstein radius differs from the value of Paper I. This reflects the fact that the interpretation of this system as a lens is not straightforward. This is Grade B until future *HST* data shed more light on the actual nature of this system.

- SL2SJ140650+522619 has a cusp configuration. Even though the source appears to have two separate components, the compact structure outside of the main arc is actually a foreground object, as revealed by our spectroscopic observations.

- SL2SJ141137+565119 shows a complete ring. Our lens model cannot account for all the flux in one bright knot on the arc, North of the lens. This could be the result of the presence of substructure close to the highly magnified unresolved knot that requires a minute knowledge of the PSF.

- SL2SJ141917+511729. Only two bright points can be identified on the arc of this system, while no counter-image is visible. The Einstein radius of this lens is rather large (~ 4"), which puts this system in the category of group-scale lenses.

- SL2SJ142003+523137. This disk galaxy is producing a lensed arc. The reconstructed source is compact and difficult to resolve. The predicted counter-image of the arc is too faint to be detected and possibly affected by extinction.

- SL2SJ142059+563007. The WFC3 image of this lens offers a detailed view on the

source structure. We identify three separate bright components, two quads and one double, which allow us to constrain robustly the Einstein radius.

- SL2SJ142731+551645. The source lensed by this disky galaxy is in a typical fold-like configuration, with two of its four images merging into an arc.

- SL2SJ220329+020518. This system shows a bright arc, and a possible counter-image close to the center. However, we are not able to fit both the light from the arc and the candidate counter-image. On the other hand, our spectroscopic analysis reveals [OII] emission at the redshift of the lens (Paper IV), which suggests that the blue bright spot close to the center might be a substructure associated with the lens and not the source. We model the system using light from the arc only. Our model predicts the existence of a faint counter-image that cannot be ruled out by our snapshot observation.

- SL2SJ220506+014703. The spectroscopic follow-up revealed emission from the bright arc at $z = 2.52$. No emission is detected from its counter-image, but since the lens model is robust we give this lens a grade A.

- SL2SJ220629+005728. The image shows a secondary component with a color similar to the main lens, in the proximity of one of the arcs. This component could contribute to the overall lensing effect. We modeled it with a singular isothermal sphere. The fit yielded a small value for its Einstein radius as in Paper I.

- SL2SJ221326-000946 is a disky lens. A merging pair and a third image of the same bright component are identified on the arc. No counter-image is visible in our

images.

- SL2SJ221407-180712. Analogous to other systems with CFHT data only, we need to fix the PA of the mass distribution in order to constrain accurately the Einstein radius. It is a grade B because of the lack of source spectroscopy.

- SL2SJ221929-001743. Only one source component, at a spectroscopic redshift of $z = 1.02$, is visible in the CFHT image. The constraints that this image provides on the lens model are not good enough and we need to fix the position angle of the mass to that of the light. The best-fit model does not predict multiple images. Grade B.

- SL2SJ222012+010606. The CFHT image shows two blue components on opposite sides of the lens. The brighter arc is measured to be at a higher redshift than the lens, while we have no spectroscopic information on the fainter blob. The lens model that we obtain is only partly satisfactory, because it predicts a mass centroid off by ~ 1.5 pixels from the light centroid. Moreover, the stellar mass and velocity dispersion of the foreground galaxy are unusually low in relation to the measured Einstein radius. It seems then plausible that the secondary source component is not a counter-image to the main arc. The foreground galaxy is definitely providing some lensing, but probably not strong. Grade C.

- SL2SJ222148+011542. Two arcs are visible both in photometry and in spectroscopy, making this a grade A lens.

- SL2SJ222217+001202. An arc with no clear counter-image is visible in the ground-

based image of this lens. We put a Gaussian prior on the lens PA, centered on the light PA and with a 10 degree dispersion, in order to obtain a meaningful model of this lens. Grade B.

A few of the systems presented here are also part of the sample studied by More et al. (2012) in their work dedicated to group-scale lenses in the SL2S survey. These are SL2SJ021325−074355, SL2SJ021411−040502, SL2SJ022511−045433, SL2SJ085559−040917, SL2SJ090407−005952, SL2SJ140156+554446, SL2SJ140454+520024, SL2SJ141917+511729, SL2SJ220329+020518 and SL2SJ220506+014703. For easier access, the relevant data of all lenses and candidates studied here can be found on The Master Lens Database online archive (Moustakas, Brownstein et al., in prep.).

3.5   Stellar masses

One of the goals of our study is to better understand the mass assembly of early-type galaxies over cosmic time. While gravitational lensing provides us with a precise measurement of the total mass enclosed within the Einstein radius of our lenses, measurements of the stellar mass are needed to separate the contribution of baryonic and dark matter to the total mass balance. In this paper we estimate stellar masses through stellar population synthesis (SPS) fitting of our photometric measurements: we create stellar populations assuming a simply-parametrized star formation history and stellar initial mass function (IMF), calculate magnitudes in the observed bands and fit to the measurements. The implementation of this procedure is the same as the one in Auger et al. (2009) and is based on a code written by M. W. Auger. We create composite stellar

Name	R_{Ein}	q	PA	m_{s}	Grade	Notes	*HST*?
	(arcsec)		(degrees)	(mag)			
SL2SJ020457-110309	0.57 ± 0.07	0.71 ± 0.14	29.4 ± 32.3	22.61	B		N
SL2SJ020524-093023	0.80 ± 0.10	0.52 ± 0.15	-44.4 ± 22.4	23.74	A		N
SL2SJ020833-071414	2.66 ± 0.08	0.76 ± 0.01	59.4 ± 0.3	24.88	B		Y
SL2SJ021206-075528	1.23 ± 0.04	0.77 ± 0.02	-16.9 ± 4.3	24.72	B		N
SL2SJ021247-055552	1.27 ± 0.04	0.82 ± 0.05	-32.7 ± 4.6	25.11	A		N
SL2SJ021325-074355	2.39 ± 0.07	0.54 ± 0.01	17.9 ± 0.4	23.68	A		Y
comp. 2	0.74 ± 0.12	0.64 ± 0.24	53.6 (fixed)				
SL2SJ021411-040502	1.41 ± 0.04	0.60 ± 0.02	-84.5 ± 1.1	24.61	A		Y
SL2SJ021737-051329	1.27 ± 0.04	0.85 ± 0.03	-73.9 ± 3.1	24.06	A		Y
γ_{ext}	0.11 ± 0.01		1.0 ± 0.1				
SL2SJ021801-080247	1.00 ± 0.03	0.78 ± 0.03	38.8 ± 4.1	24.79	A		N
SL2SJ021902-082934	1.30 ± 0.04	0.78 ± 0.06	-80.3 ± 3.9	26.31	A		Y
SL2SJ022046-094927	1.00 ± 0.03	0.95 ± 0.02	-42.4 ± 12.8	24.15	A		N
SL2SJ022056-063934	1.20 ± 0.04	0.63 ± 0.04	-79.6 ± 2.7	24.57	B		N
SL2SJ022346-053418	1.15 ± 0.10	0.40 ± 0.06	70.7 ± 6.1	24.35	B		N
SL2SJ022357-065142	1.35 ± 0.04	0.79 ± 0.02	66.2 ± 2.7	24.73	A		Y
SL2SJ022511-045433	1.76 ± 0.05	0.58 ± 0.02	24.8 ± 0.5	23.61	A		Y
SL2SJ022610-042011	1.19 ± 0.04	0.77 ± 0.03	-12.7 ± 6.0	25.26	A		Y
SL2SJ022648-040610	1.29 ± 0.05	0.81 ± 0.07	-65.0 ± 7.7	25.93	A	disky	Y
SL2SJ022648-090421	1.56 ± 0.05	0.85 ± 0.03	72.1 ± 4.1	26.16	B		N
SL2SJ022708-065445	0.90 ± 0.05	0.61 ± 0.11	-86.4 ± -85.4	24.51	A	Disky	N
SL2SJ023251-040823	1.04 ± 0.03	0.93 ± 0.03	72.3 ± 22.3	24.36	A		Y
SL2SJ023307-043838	1.77 ± 0.06	0.76 ± 0.04	51.7 ± 2.4	24.40	A		N
SL2SJ084847-035103	0.83 ± 0.08	0.74 ± 0.19	67.4 ± -58.0	23.83	A		N
SL2SJ084909-041226	1.10 ± 0.03	0.73 ± 0.03	40.2 ± 1.8	24.16	A		Y
SL2SJ084934-043352	1.25 ± 0.05	0.66 ± 0.13	36.4 (fixed)	23.87	B		N
SL2SJ084959-025142	1.16 ± 0.04	0.74 ± 0.04	-62.8 ± 2.3	25.85	A		Y
SL2SJ085019-034710	0.93 ± 0.03	0.45 ± 0.04	1.5 ± 3.2	25.59	A	disky	N
SL2SJ085317-020312	0.88 ± 0.12	0.63 ± 0.14	15.7 ± 6.0	24.52	A		N
SL2SJ085327-023745	1.32 ± 0.04	0.71 ± 0.01	0.5 ± 1.7	23.07	A		N
SL2SJ085540-014730	1.02 ± 0.04	0.96 ± 0.03	-48.6 ± 33.9	25.32	A		N
SL2SJ085559-040917	1.34 ± 0.12	0.47 ± 0.14	40.8 ± 25.2	24.14	B		N
SL2SJ085826-014300	0.90 ± 0.03	0.90 ± 0.04	59.5 ± 17.8	26.36	A		Y
SL2SJ090106-025906	1.03 ± 0.03	0.46 ± 0.02	-18.9 ± 1.2	25.68	A		Y
SL2SJ090407-005952	1.41 ± 0.04	0.64 ± 0.01	71.7 ± 0.8	24.32	A		Y
SL2SJ095921+020638	0.74 ± 0.02	0.95 ± 0.01	-72.1 ± 2.5	26.79	A		Y
SL2SJ135847+545913	1.21 ± 0.04	0.76 ± 0.01	-70.7 ± 1.7	24.30	A		Y

Table 3.7: Peak value and 68% confidence interval of the posterior probability distribution of each lens parameter, marginalized over the other parameters. Columns 2–4 correspond to the Einstein radius (R_{Ein}), the axis ratio of the elliptical isodensity contours (q), and the position angle measured east of north (PA) of the SIE lens model. Column 5 shows the magnitude of the de-lensed source in the band used for the lensing analysis: the bluest available band for *HST* data, or g band for CFHT data. The typical uncertainty on the source magnitude is ~ 0.5. Column 6 lists notes on the lens morphology, while column 7 indicates whether the lens has *HST* imaging.

Name	$R_{\rm Ein}$	q	PA	$m_{\rm s}$	Grade	Notes	HST?
	(arcsec)		(degrees)	(mag)			
SL2SJ135949+553550	1.15 ± 0.03	0.60 ± 0.01	55.6 ± 0.5	25.53	A		Y
SL2SJ140123+555705	1.73 ± 0.07	0.49 ± 0.04	-43.8 ± 0.9	26.63	A		Y
SL2SJ140156+554446	2.03 ± 0.06	0.58 ± 0.01	32.0 ± 0.3	24.41	A		Y
SL2SJ140221+550534	1.23 ± 0.04	0.76 ± 0.04	-46.8 ± 3.1	25.41	A		Y
SL2SJ140454+520024	2.55 ± 0.08	0.54 ± 0.03	71.0 ± 0.9	24.79	A		N
SL2SJ140533+550231	1.04 ± 0.07	0.56 ± 0.02	1.4 ± 2.2	24.15	A	double	Y
comp. 2	0.53 ± 0.07	0.81 ± 0.06	45.8 ± 15.4				
SL2SJ140546+524311	1.50 ± 0.05	0.47 ± 0.05	-54.1 ± 1.9	26.44	A		Y
$\gamma_{\rm ext}$	0.04 ± 0.02		-33.1 ± 0.1				
SL2SJ140614+520253	4.36 ± 0.16	0.63 ± 0.03	-53.3 ± 2.0	22.58	C		N
SL2SJ140650+522619	0.94 ± 0.03	1.00 ± 0.01	-27.0 ± 1.2	24.08	A		Y
SL2SJ141137+565119	0.93 ± 0.03	0.85 ± 0.01	62.4 ± 0.3	24.53	A		Y
SL2SJ141917+511729	3.08 ± 0.23	0.62 ± 0.12	47.5 ± 5.1	24.83	A		Y
SL2SJ142003+523137	1.81 ± 0.09	0.35 ± 0.02	66.0 ± 2.0	24.70	A	disky	N
SL2SJ142031+525822	0.96 ± 0.14	0.84 ± 0.14	-79.3 ± 5.9	22.45	B		Y
SL2SJ142059+563007	1.40 ± 0.04	0.67 ± 0.01	-10.3 ± 0.3	25.17	A		Y
SL2SJ142321+572243	1.30 ± 0.10	0.34 ± 0.06	43.9 ± 1.6	31.72	A		Y
SL2SJ142731+551645	0.81 ± 0.03	0.49 ± 0.02	-62.8 ± 1.0	24.73	A	disky	Y
SL2SJ220329+020518	1.95 ± 0.06	0.45 ± 0.02	-31.8 ± 0.2	24.95	A		Y
SL2SJ220506+014703	1.66 ± 0.06	0.73 ± 0.04	80.6 ± 3.7	23.68	A		N
SL2SJ220629+005728	1.56 ± 0.07	0.66 ± 0.04	-29.0 ± 4.2	24.78	B		N
comp. 2	0.16 ± 0.06						
SL2SJ221326-000946	1.07 ± 0.03	0.21 ± 0.01	-41.6 ± 0.5	24.82	A	disky	Y
SL2SJ221407-180712	0.86 ± 0.18	0.89 ± 0.11	57.0 (fixed)	25.01	B		N
SL2SJ221852+014038	1.38 ± 0.08	0.42 ± 0.10	-66.9 ± 5.4	25.54	B		N
SL2SJ221929-001743	0.63 ± 0.11	0.74 ± 0.25	85.1 (fixed)	23.46	B		N
SL2SJ222012+010606	2.15 ± 0.07	0.70 ± 0.04	-25.5 ± 2.7	24.09	C		N
SL2SJ222148+011542	1.40 ± 0.05	0.87 ± 0.03	78.1 ± 4.0	24.48	A		N
SL2SJ222217+001202	1.31 ± 0.25	0.81 ± 0.26	34.8 ± 7.4	24.83	B		N

Table 3.7: continued.
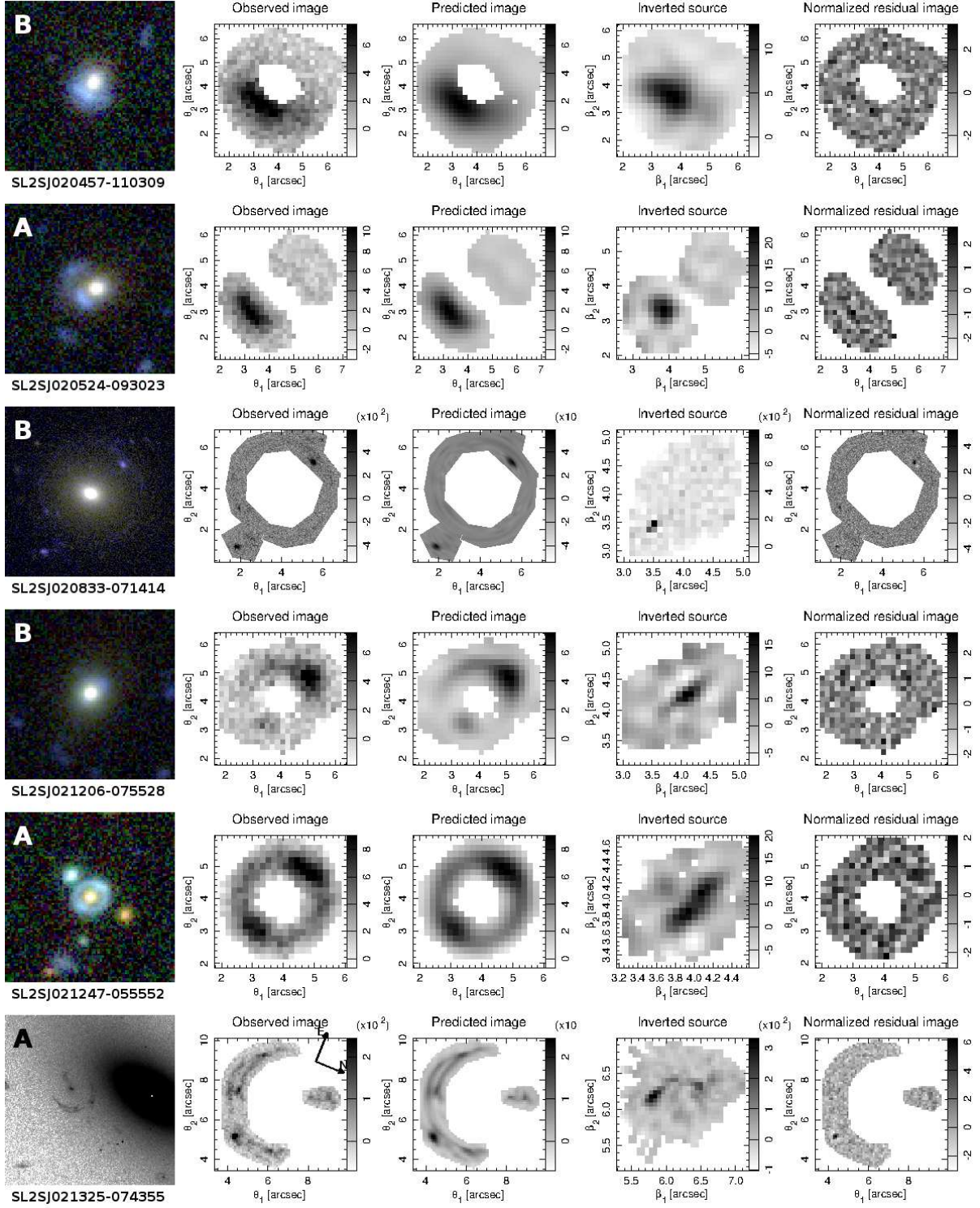
Figure 3.9: Lens modeling results showing, on each row, from left to right, a color cutout image, the input science imaged used for the modeling with uninteresting areas cropped out, the reconstructed lensed image, the reconstructed intrinsic source and the difference image (data−model) normalized in units of the estimated pixel uncertainties.
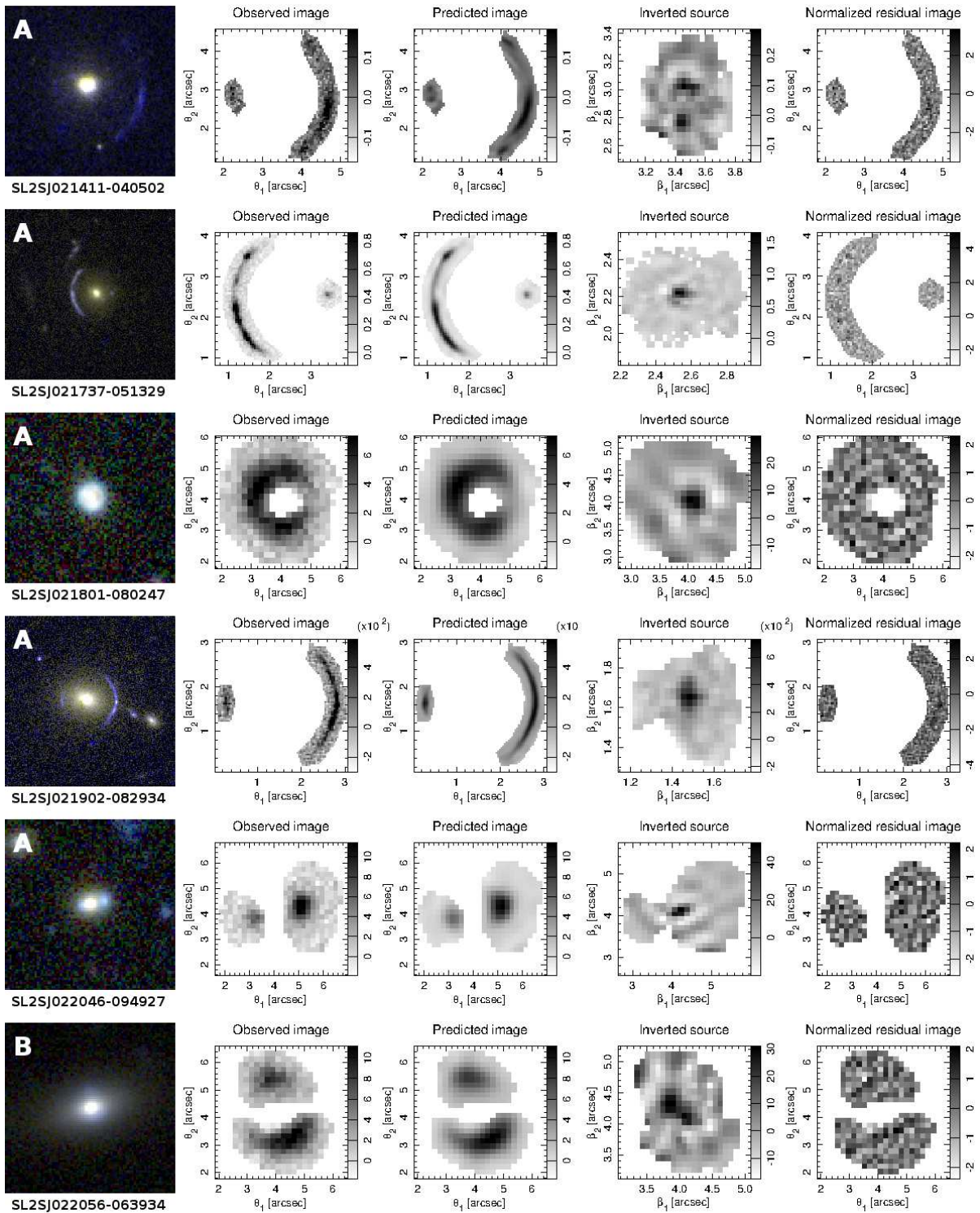
Figure 3.9: continued.
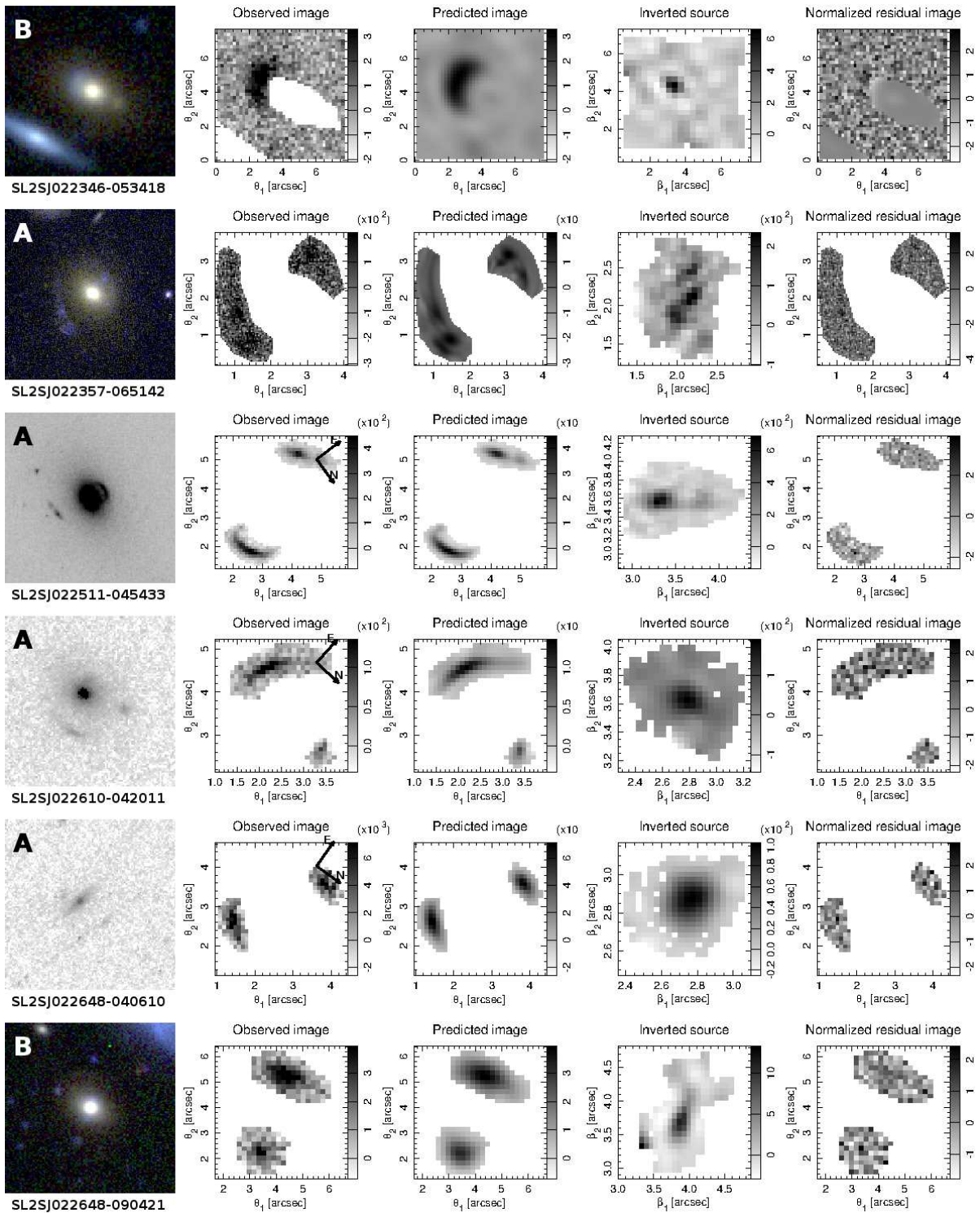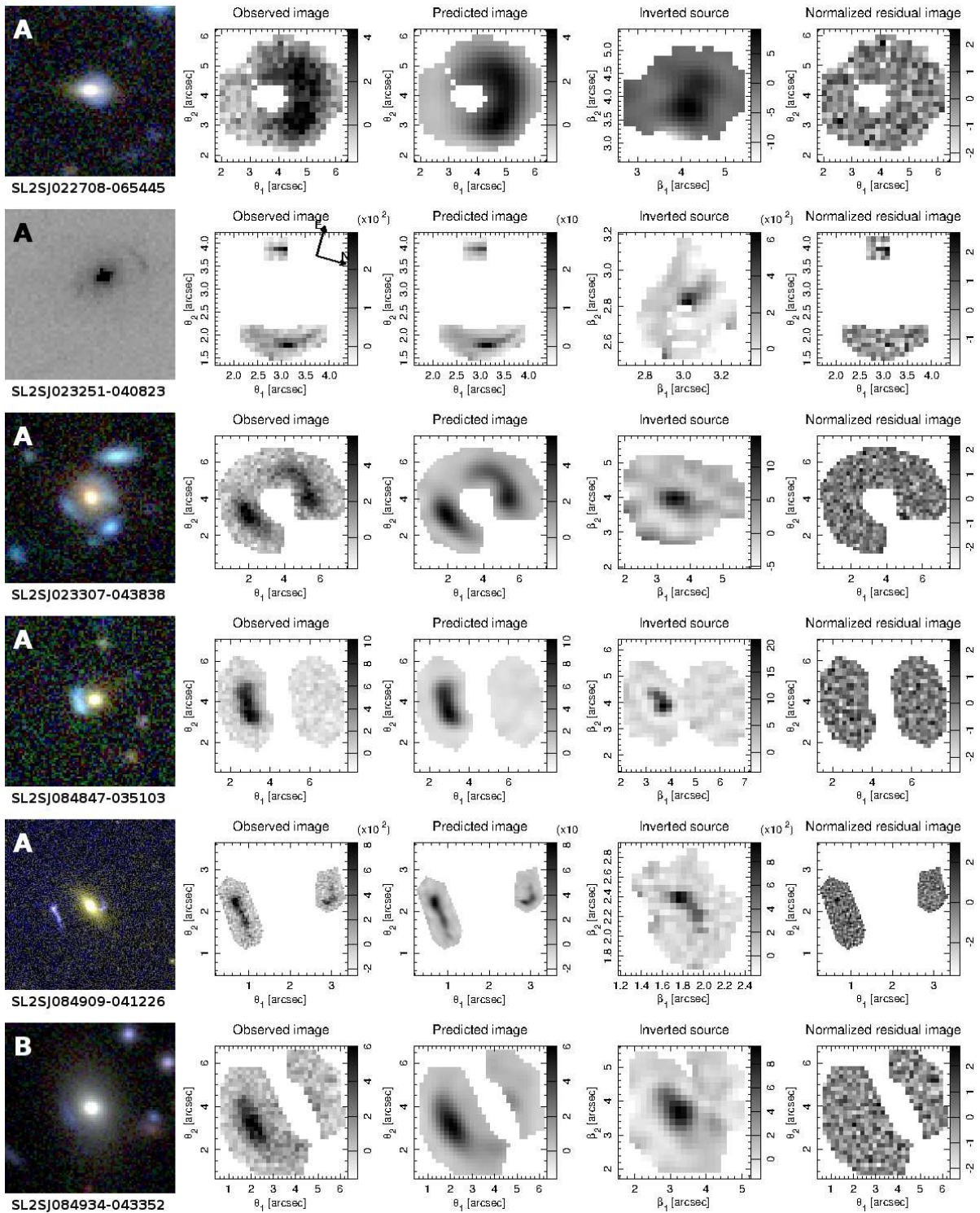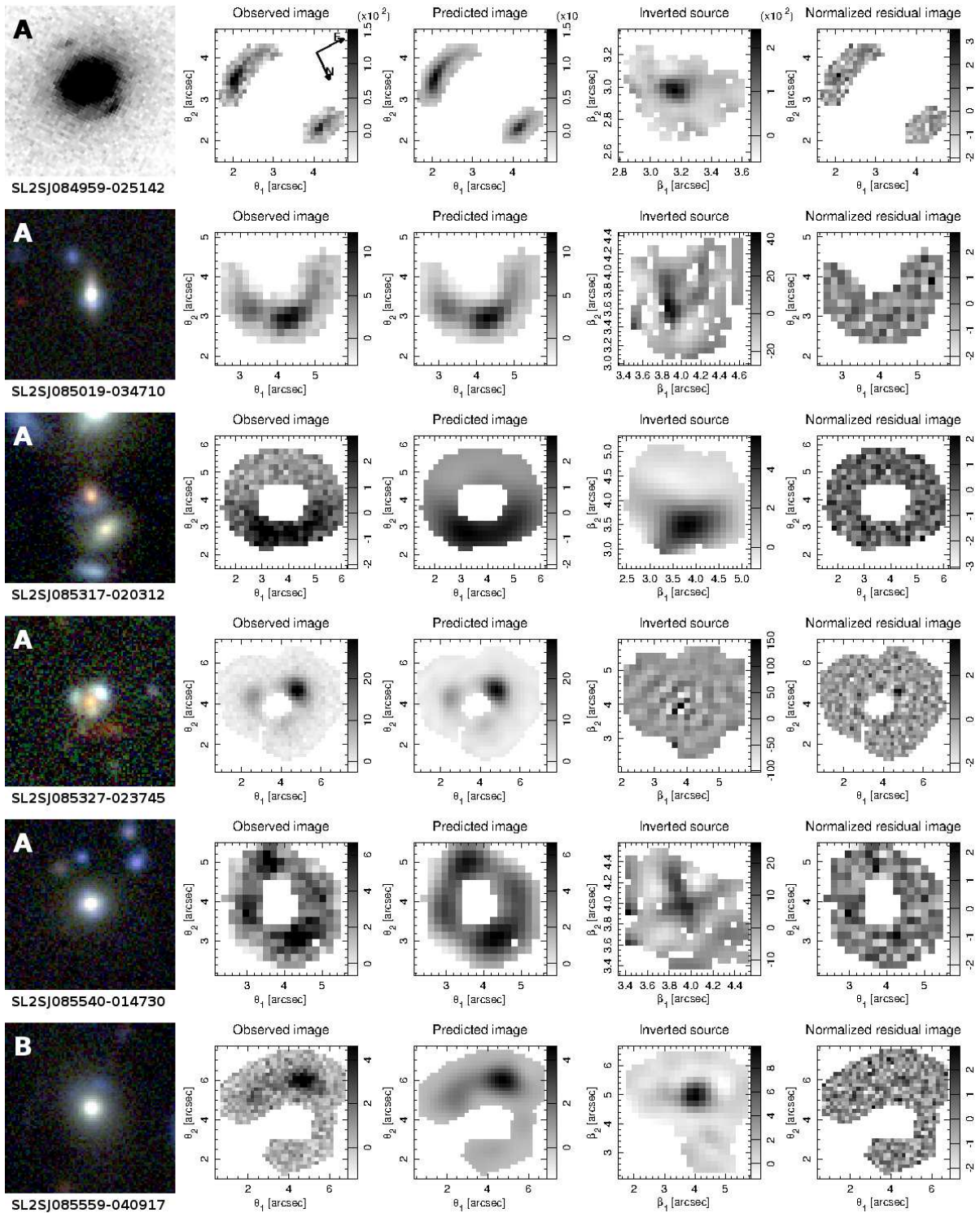
Figure 3.9: continued.

Figure 3.9: continued.

Figure 3.9: continued.

Figure 3.9: continued.

Figure 3.9: continued.
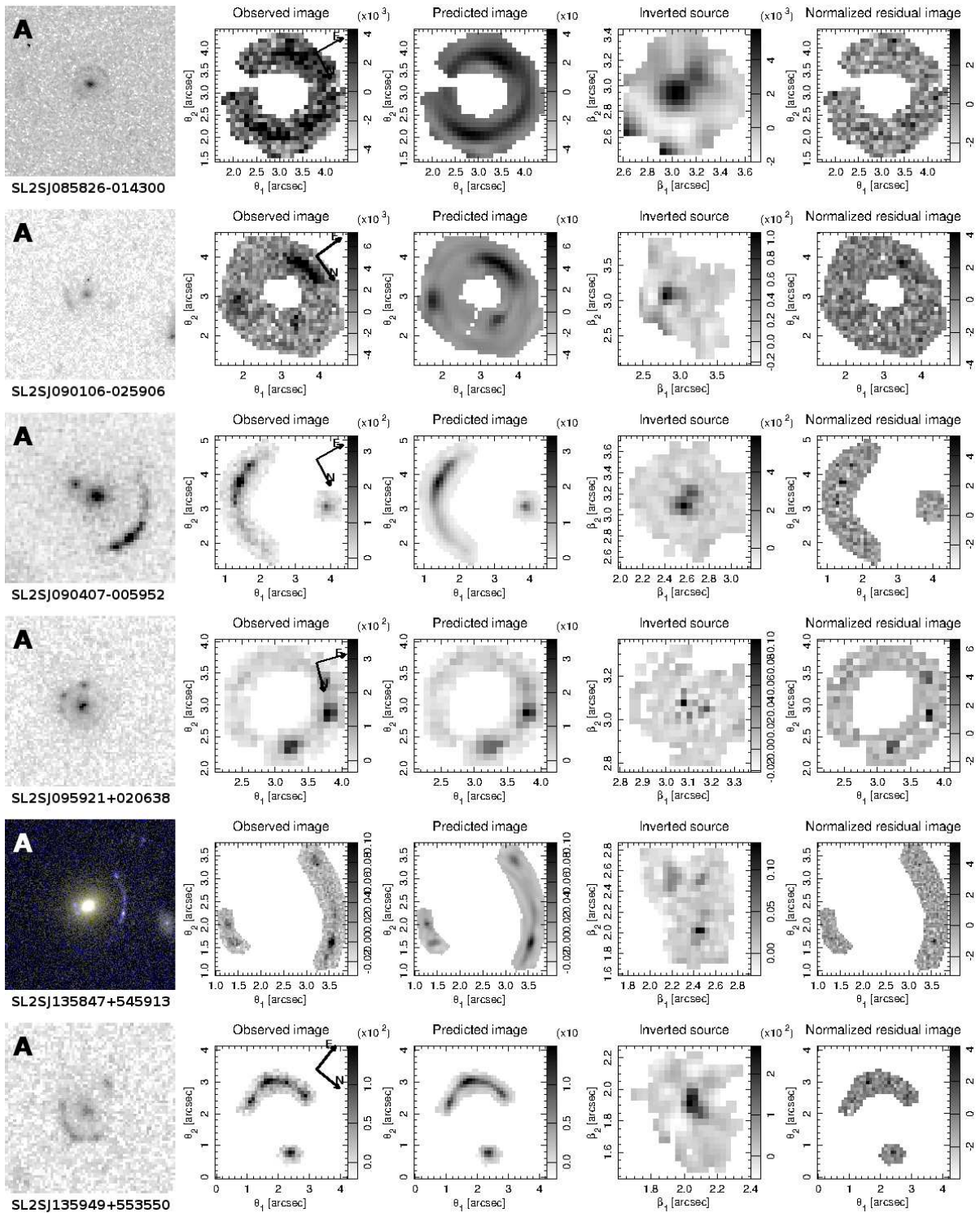
Figure 3.9: continued.
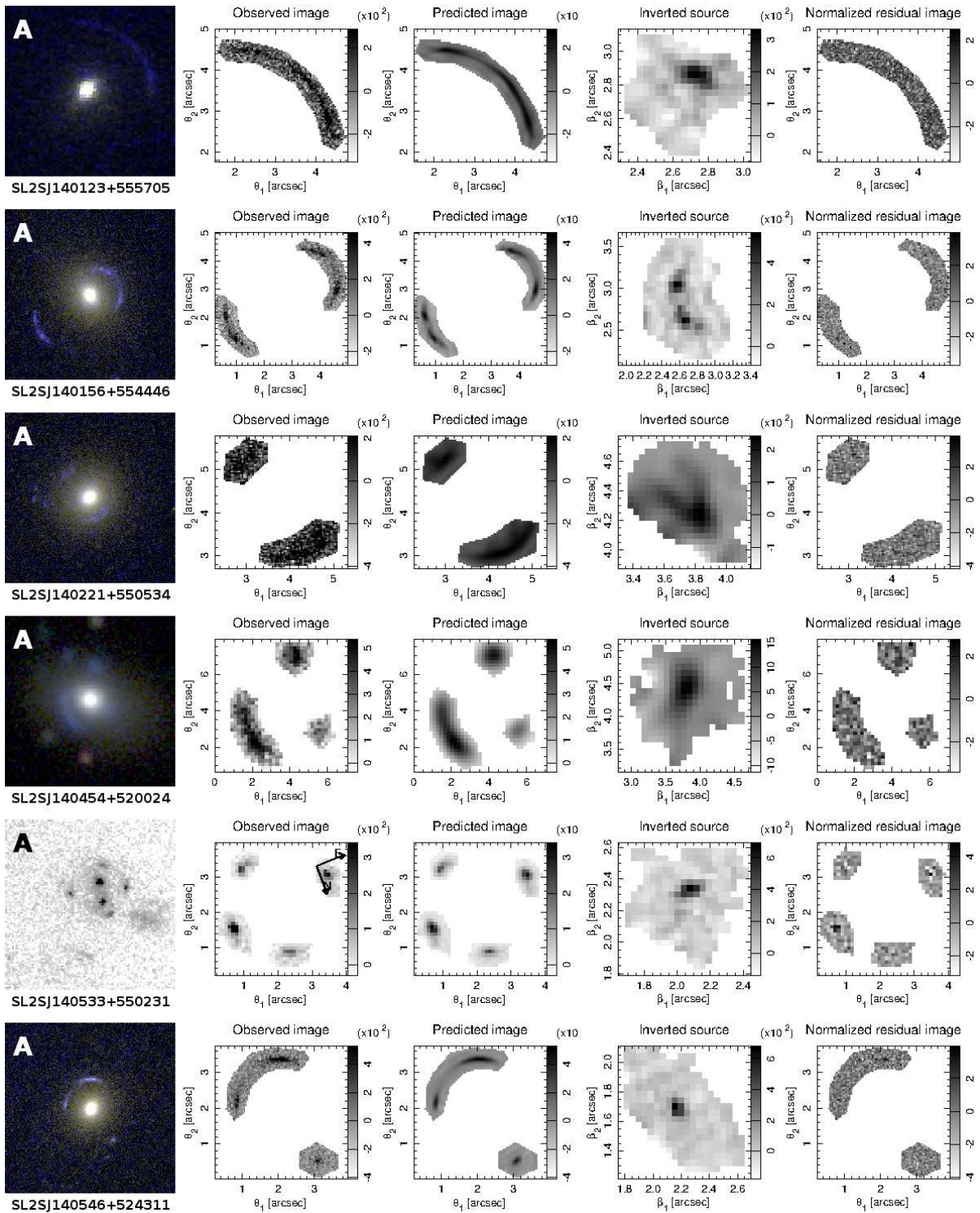
Figure 3.9: continued.
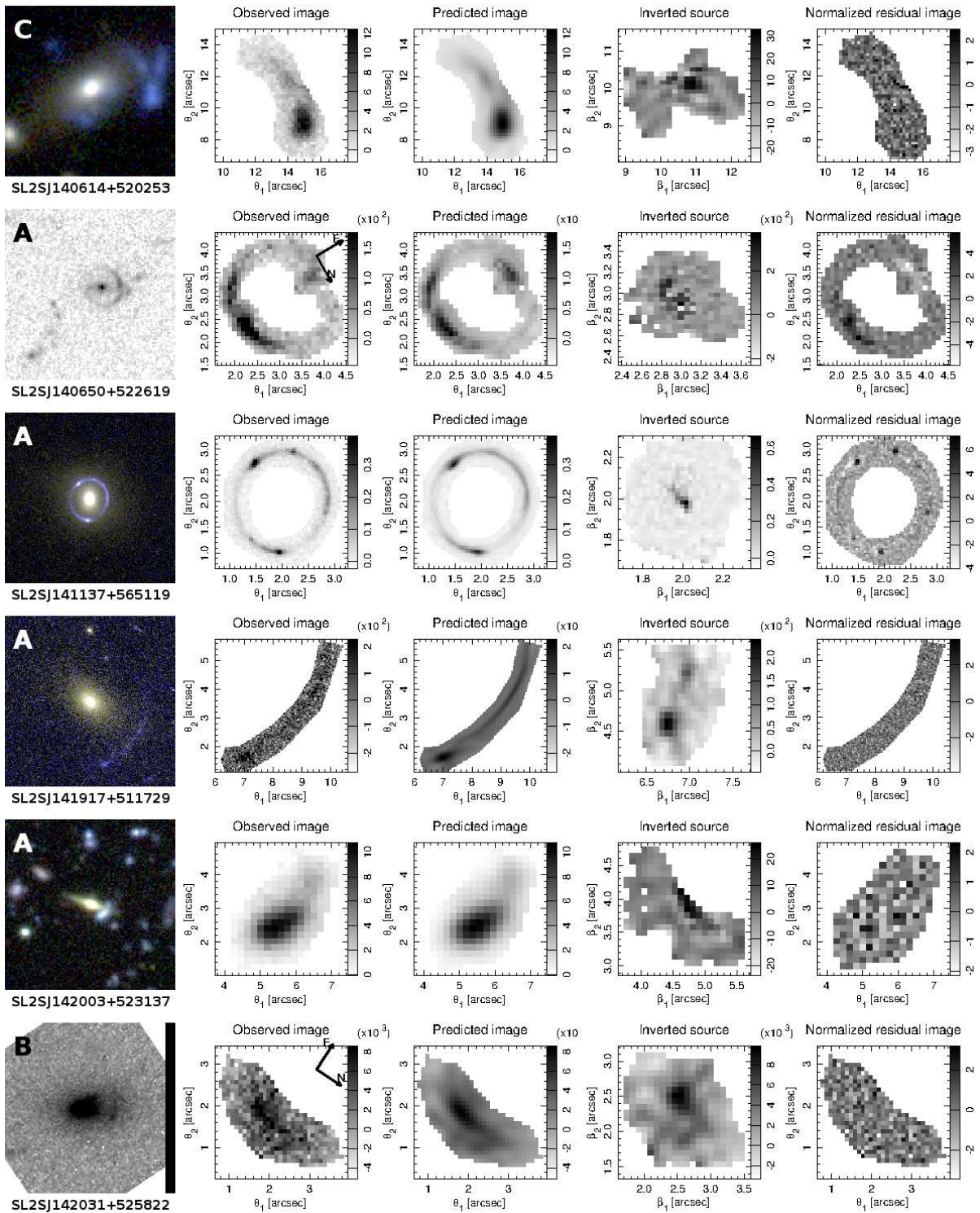
Figure 3.9: continued.
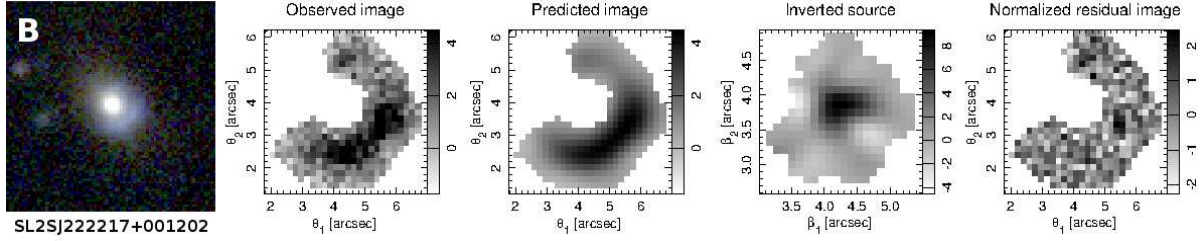
Figure 3.9: continued.

populations from stellar templates by Bruzual & Charlot (2003), with both a Salpeter
and a Chabrier IMF. We assume an exponentially declining star formation history, ap-
propriate given the old age of the red galaxies in our sample. In order to obtain robust
stellar masses, measurements in a few different bands are needed. Although *HST* images
provide better spatial resolution, useful to deblend the lens light from that of the back-
ground source, our objects have *HST* data in at most two bands which are not enough
for the purpose of fitting SPS models. CFHT images on the other hand are deep and
available consistently in five different bands for all of the targets. The inclusion of the
HST photometry to the overall SED fitting would not bring much new information and
we therefore discard it. The fit is based on an MCMC sampling. The measured values
of the stellar masses are reported in Table 3.8. The other model parameters are largely
unconstrained. As a result of the well-known degeneracy between age and metallicity,
our photometric data can only put lower limits on these two quantities.

For the systems with additional NIR observations the fit is repeated including those
data. The addition of NIR fluxes produces stellar masses consistent with the values mea-
sured with optical data only, but with smaller uncertainty (see Figure 3.10). The relative

108

scatter between stellar masses obtained from optical photometry alone and with the addition of NIR data is 0.06 dex in $\log M_*$ and the bias is 0.01. This gives us an estimate of the systematic error coming from the stellar templates being not a perfect description of the data over all photometric bands; in Paper IV, this systematic uncertainty is added to the statistical uncertainty on M_* when dealing with stellar masses. On the one hand the tight agreement between optical and optical+NIR stellar masses should not come as a surprise since the two data sets differ in most cases only by the addition of one band. On the other hand, if the optical data were contaminated with poor subtraction of light from the blue arcs the resulting stellar masses could be biased. The fact that NIR data, with little to no contamination from the background source, does not change the inference is reassuring on the quality of our photometric measurements.

Some of the stellar masses measured here are not consistent with previous measurements from Paper II. This reflects the difference in the measured magnitudes due to the different source masking strategy discussed in Section 3.2.1. The values reported here are to be considered more robust.

The median stellar mass of the sub-sample of grade A SL2S lenses is $10^{11.53} M_\odot$, if a Salpeter IMF is assumed, and the standard deviation of the sample is 0.3 dex in $\log M_*$. The distribution in stellar mass of SL2S galaxies is very similar to that of SLACS galaxies, as shown in Figure 3.10. This is important in view of analyses that combine data from both samples, as we do in Paper IV.

Lens name	z	$\log M_*^{\text{(Chab)}}/M_\odot$	$\log M_*^{\text{(Chab)}}\text{(NIR)}/M_\odot$	$\log M_*^{\text{(Salp)}}/M_\odot$	$\log M_*^{\text{(Salp)}}\text{(NIR)}/M_\odot$
SL2SJ020457-110309	0.609	11.20 ± 0.15	$\cdots$	11.46 ± 0.15	$\cdots$
SL2SJ020524-093023	0.557	11.28 ± 0.12	$\cdots$	11.52 ± 0.12	$\cdots$
SL2SJ020833-071414	0.428	11.59 ± 0.10	$\cdots$	11.84 ± 0.10	$\cdots$
SL2SJ021206-075528	0.460	11.33 ± 0.10	$\cdots$	11.59 ± 0.10	$\cdots$
SL2SJ021247-055552	0.750	11.17 ± 0.17	$\cdots$	11.45 ± 0.17	$\cdots$
SL2SJ021325-074355	0.717	11.71 ± 0.18	11.73 ± 0.15	11.97 ± 0.19	11.97 ± 0.14
SL2SJ021411-040502	0.609	11.34 ± 0.14	11.38 ± 0.10	11.60 ± 0.14	11.63 ± 0.10
SL2SJ021737-051329	0.646	11.29 ± 0.15	11.35 ± 0.11	11.53 ± 0.16	11.60 ± 0.11
SL2SJ021801-080247	0.884	11.27 ± 0.15	$\cdots$	11.54 ± 0.14	$\cdots$
SL2SJ021902-082934	0.389	11.24 ± 0.10	11.20 ± 0.08	11.50 ± 0.10	11.45 ± 0.08
SL2SJ022046-094927	0.572	11.11 ± 0.12	$\cdots$	11.36 ± 0.11	$\cdots$
SL2SJ022056-063934	0.330	11.44 ± 0.10	$\cdots$	11.69 ± 0.09	$\cdots$
SL2SJ022346-053418	0.499	11.51 ± 0.11	$\cdots$	11.76 ± 0.11	$\cdots$
SL2SJ022357-065142	0.473	11.49 ± 0.10	11.44 ± 0.08	11.74 ± 0.10	11.67 ± 0.08
SL2SJ022511-045433	0.238	11.57 ± 0.09	11.59 ± 0.07	11.81 ± 0.09	11.84 ± 0.07
SL2SJ022610-042011	0.494	11.48 ± 0.10	11.41 ± 0.09	11.73 ± 0.11	11.64 ± 0.09
SL2SJ022648-040610	0.766	11.53 ± 0.12	11.46 ± 0.11	11.79 ± 0.12	11.70 ± 0.11
SL2SJ022648-090421	0.456	11.72 ± 0.10	$\cdots$	11.97 ± 0.10	$\cdots$
SL2SJ022708-065445	0.561	10.93 ± 0.14	$\cdots$	11.21 ± 0.14	$\cdots$
SL2SJ023251-040823	0.352	11.11 ± 0.10	11.18 ± 0.08	11.36 ± 0.09	11.43 ± 0.07
SL2SJ023307-043838	0.671	11.44 ± 0.14	$\cdots$	11.71 ± 0.13	$\cdots$
SL2SJ084847-035103	0.682	10.97 ± 0.16	$\cdots$	11.24 ± 0.16	$\cdots$
SL2SJ084909-041226	0.722	11.39 ± 0.14	11.31 ± 0.10	11.63 ± 0.13	11.56 ± 0.11
SL2SJ084934-043352	0.373	11.42 ± 0.10	$\cdots$	11.67 ± 0.10	$\cdots$
SL2SJ084959-025142	0.274	11.27 ± 0.09	11.27 ± 0.07	11.52 ± 0.09	11.51 ± 0.07
SL2SJ085019-034710	0.337	10.89 ± 0.09	$\cdots$	11.14 ± 0.09	$\cdots$
SL2SJ085317-020312	0.698	11.26 ± 0.13	$\cdots$	11.51 ± 0.13	$\cdots$
SL2SJ085327-023745	0.774	11.13 ± 0.16	$\cdots$	11.38 ± 0.16	$\cdots$
SL2SJ085540-014730	0.365	10.86 ± 0.10	$\cdots$	11.11 ± 0.10	$\cdots$
SL2SJ085559-040917	0.419	11.39 ± 0.10	$\cdots$	11.63 ± 0.10	$\cdots$
SL2SJ085826-014300	0.580	10.76 ± 0.14	10.81 ± 0.10	11.01 ± 0.14	11.06 ± 0.10
SL2SJ090106-025906	0.670	10.80 ± 0.17	$\cdots$	11.07 ± 0.16	$\cdots$
SL2SJ090407-005952	0.611	11.30 ± 0.11	11.41 ± 0.11	11.55 ± 0.12	11.66 ± 0.11
SL2SJ095921+020638	0.552	11.03 ± 0.10	10.81 ± 0.09	11.28 ± 0.11	11.04 ± 0.09
SL2SJ135847+545913	0.510	11.39 ± 0.11	$\cdots$	11.66 ± 0.11	$\cdots$
SL2SJ135949+553550	0.783	11.17 ± 0.15	$\cdots$	11.41 ± 0.15	$\cdots$
SL2SJ140123+555705	0.527	11.54 ± 0.11	$\cdots$	11.80 ± 0.11	$\cdots$
SL2SJ140156+554446	0.464	11.59 ± 0.10	$\cdots$	11.85 ± 0.10	$\cdots$
SL2SJ140221+550534	0.412	11.54 ± 0.10	$\cdots$	11.79 ± 0.10	$\cdots$
SL2SJ140454+520024	0.456	11.85 ± 0.10	$\cdots$	12.10 ± 0.10	$\cdots$
SL2SJ140533+550231	$\cdots$	$\cdots$	$\cdots$	$\cdots$	$\cdots$
SL2SJ140546+524311	0.526	11.42 ± 0.11	$\cdots$	11.67 ± 0.11	$\cdots$
SL2SJ140614+520253	0.480	11.68 ± 0.11	$\cdots$	11.93 ± 0.11	$\cdots$
SL2SJ140650+522619	0.716	11.34 ± 0.15	$\cdots$	11.60 ± 0.15	$\cdots$
SL2SJ141137+565119	0.322	11.04 ± 0.09	$\cdots$	11.28 ± 0.09	$\cdots$
SL2SJ141917+511729	$\cdots$	$\cdots$	$\cdots$	$\cdots$	$\cdots$
SL2SJ142003+523137	0.354	10.44 ± 0.10	$\cdots$	10.69 ± 0.10	$\cdots$

Table 3.8: Stellar masses from the fit of stellar population synthesis models to photometric data. The redshift of the lens galaxies is reported in column (2).

Lens name	z	$\log M_*^{\text{(Chab)}}/M_\odot$	$\log M_*^{\text{(Chab)}}(\text{NIR})/M_\odot$	$\log M_*^{\text{(Salp)}}/M_\odot$	$\log M_*^{\text{(Salp)}}(\text{NIR})/M_\odot$
SL2SJ142031+525822	0.380	11.31 ± 0.10	$\cdots$	11.56 ± 0.09	$\cdots$
SL2SJ142059+563007	0.483	11.52 ± 0.10	$\cdots$	11.76 ± 0.10	$\cdots$
SL2SJ142321+572243	$\cdots$	$\cdots$	$\cdots$	$\cdots$	$\cdots$
SL2SJ142731+551645	0.511	10.97 ± 0.12	$\cdots$	11.20 ± 0.12	$\cdots$
SL2SJ220329+020518	0.400	11.00 ± 0.09	11.05 ± 0.08	11.26 ± 0.10	11.31 ± 0.08
SL2SJ220506+014703	0.476	11.26 ± 0.11	11.29 ± 0.09	11.51 ± 0.10	11.53 ± 0.09
SL2SJ220629+005728	0.704	11.40 ± 0.15	11.56 ± 0.12	11.65 ± 0.15	11.81 ± 0.12
SL2SJ221326-000946	0.338	10.73 ± 0.09	10.67 ± 0.06	10.99 ± 0.10	10.92 ± 0.06
SL2SJ221407-180712	0.651	$\cdots$	$\cdots$	$\cdots$	$\cdots$
SL2SJ221852+014038	0.564	11.52 ± 0.11	11.52 ± 0.09	11.79 ± 0.11	11.78 ± 0.09
SL2SJ221929-001743	0.289	11.32 ± 0.09	$\cdots$	11.56 ± 0.09	$\cdots$
SL2SJ222012+010606	0.232	10.73 ± 0.10	10.72 ± 0.07	10.97 ± 0.09	10.96 ± 0.06
SL2SJ222148+011542	0.325	11.30 ± 0.09	11.31 ± 0.07	11.55 ± 0.09	11.56 ± 0.07
SL2SJ222217+001202	0.436	11.26 ± 0.10	$\cdots$	11.50 ± 0.10	$\cdots$

Table 3.8: continued.
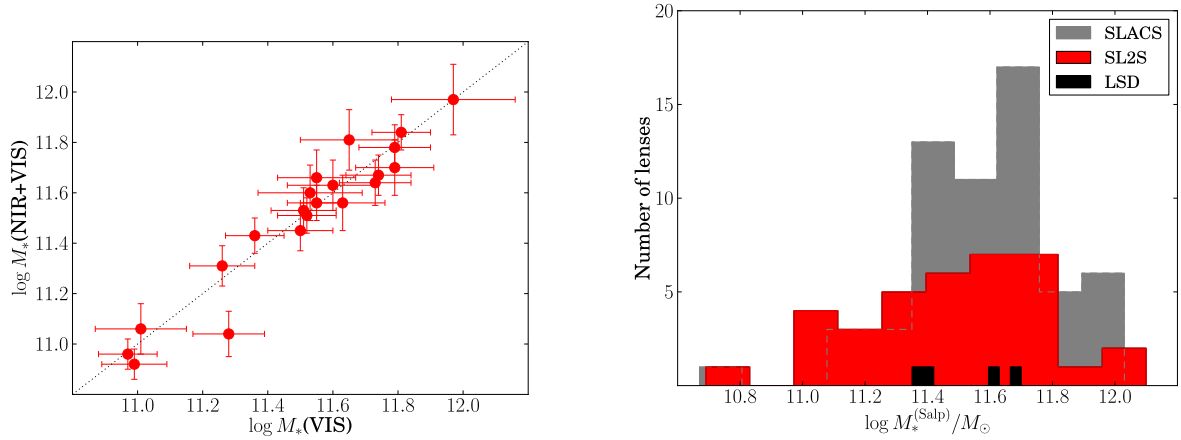
Figure 3.10: . *Left panel:* Comparison of stellar masses obtained with either optical *ugriz* bands only or with optical + near IR bands, for a Salpeter IMF. We observe no significant differences in the recovered masses. *Right panel:* Distribution in stellar mass of the grade A SL2S, SLACS and LSD lenses. SLACS stellar masses are from Auger et al. (2010a) and LSD masses are taken from Ruff et al. (2011). Stellar masses are obtained assuming a Salpeter IMF.

3.6   Sample characterization

We presented effective radii, magnitudes, stellar masses, Einstein radii, lens and source redshifts, and lens velocity dispersions of our lenses. It is possible at this point to look at the distribution of our lenses in the parameter space defined by these quantities. Since our scientific goal is to measure the evolution in the mean density slope with time, it is very important to assess whether other observables appear to evolve in our sample. In Figure 3.11 we plot the effective radii, stellar masses and velocity dispersions as a function of redshift for all our objects, and also for lenses from other surveys. Throughout this paper, when dealing with stellar masses we refer to values measured from stellar population synthesis fitting based on a Salpeter initial mass function (IMF). For a fair comparison, all velocity dispersions, which are measured within rectangular apertures of arbitrary sizes, are transformed into velocity dispersions within a circular aperture, σ_{e2}, with radius $R_{\rm eff}/2$ following the prescription of Jørgensen et al. (1995). The values of σ_{e2} for individual SL2S lenses are reported in Table 4.1.

SL2S lenses do not appear to differ from objects from independent lensing surveys in the average values of $R_{\rm eff}$, M_* and σ_{e2}. As far as trends with redshift within the SL2S sample are concerned, there is a mild increase of the stellar mass with z that will need to be taken into account when discussing the evolution of the mass profile of these objects.

As an additional test, we examine the correlation between mass and effective radius for SL2S, SLACS and LSD lenses and check it against non-lens galaxies. The goal is to make sure that these surveys do not preferentially select lenses with a larger or smaller size than typical ETGs of their mass. The mass-radius relation is seen to evolve with

time (e.g. Damjanov et al. 2011; Newman et al. 2012b; Cimatti et al. 2012). We correct for this evolution by considering effective radii evolved to $z = 0$ assuming the trend measured by Newman et al. (2012b): $\log R_\mathrm{e}(z = 0) = \log R_\mathrm{e} + 0.26z$. Effective radii defined in this way are plotted against measured stellar masses in Figure 3.11, together with the mass-radius relation measured by Newman et al. (2012b) for low-redshift SDSS galaxies. Points in the plot of Figure 3.11 should not be considered as evolutionary tracks of individual objects, as galaxies grow in mass as well as in size. For a given object, its redshift-evolved size $R_\mathrm{e}(z = 0)$ is equivalent to its measured effective radius rescaled by the average size of galaxies at its redshift and at a reference mass. This allows us to promptly display in a single plot how our lenses compare, in terms of size, to other galaxies of the same mass, regardless of redshift. We see from Figure 3.11 that lenses from all surveys lie nicely around the relation found for non-lenses, indicating that our sample of lenses does not appear special when compared to the more general population of galaxies of their redshift.

3.7 Summary

We presented photometric and spectroscopic measurements, lens models and stellar mass measurements for a sample of 61 systems, of which 45 are grade A (definite lenses) and 14 are grade B (probable lenses). We find that *HST* imaging, even in snapshot mode, offers a clear-cut way to determine whether SL2S candidates are actual lenses. Not surprisingly, most grade A lenses are found for systems with *HST* data. 13 of the systems with high-resolution imaging are labeled as grade C lenses, meaning that their
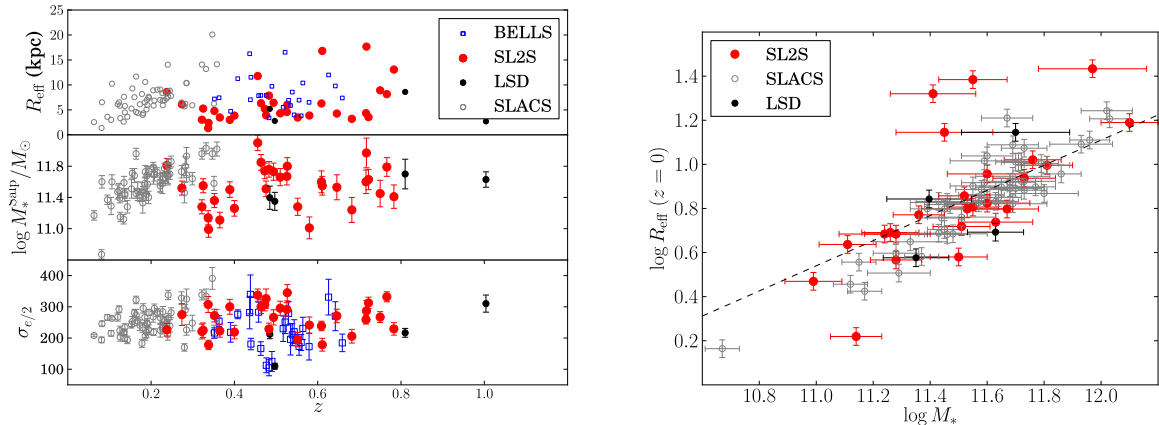
Figure 3.11: *Left panel:* Effective radius, stellar mass and velocity dispersion of lenses as a function of redshift. *Right panel:* Effective radius vs. stellar mass, where R_e values have been corrected for the evolution in the mass-size relation measured by Newman et al. (2012b): $\log R_e(z=0) = \log R_e + 0.26z$. The dashed line indicates the mass-radius relation for SDSS galaxies measured by Newman et al. (2012b).

nature is undetermined. The data for these systems, not shown in this paper, come largely from WFPC2 snapshot observations. The signal-to-noise ratio of these WFPC2 images is low compared to images taken with ACS or WFC3 despite the longer exposure times. Most of the remaining grade C systems are targets observed with NIR photometry and adaptive optics, which proved not to be a very useful technique for the follow-up of our candidates.

We have shown how spectroscopic observations can be used in combination with ground-based imaging with good seeing ($\sim 0.7''$) to confirm gravitational lens candidates by the presence of multiply imaged emission lines from the lensed background source.

Ground-based data can be used in some cases to construct lens models and measure precise Einstein radii: 15 out of 28 lenses with only CFHT photometry are grade A lenses. The uncertainty on $R_{\rm Ein}$ for those lenses is still dominated by the 3% systematic error, meaning that ground based photometry can sometimes be as good as space based imaging

for the purpose of measuring Einstein radii. For most systems however the information is not enough to draw definite conclusions on their nature, and in a few cases the data does not offer enough constraints to measure Einstein radii, mostly because of the difficulty in detecting and exploiting the counterimage as seen from the ground. The range in Einstein radii covered by the grade A lenses in our sample is $5-15$ kpc, typically larger than those of other surveys such as SLACS, probing the mass in regions where the contribution of dark matter is larger.

Stellar masses of lens galaxies can be measured from ground-based data. Measurements of M_* are robust to the inclusion of NIR data. NIR should give more reliable stellar masses, since the blue background sources contribute very little to the infrared flux. Our result suggests that our measurements of the optical photometry of our lenses have little contamination from the background sources, and that we effectively deblended lens and source light. Stellar masses of SL2S lenses cover the range $10^{11}-10^{12}M_\odot$, corresponding to massive ETGs.

We have also shown how SL2S lenses are comparable with lenses from other surveys in terms of their size, mass and velocity dispersion, and lie on the same $M_*-R_{\rm e}$ relation as non-lens galaxies.

In the next Chapter we use all these measurements to put constraints on the mass profile of massive early-type galaxies and its evolution in the redshfit range $0.1 < z < 0.8$.

Chapter 4

The total mass density profile of early-type galaxies

This chapter was published as Sonnenfeld, A.; Treu, T.; Gavazzi, R.; Suyu, S. H.; Marshall, P. J.; Auger, M. W.; Nipoti, C. "The SL2S Galaxy-scale Lens Sample. IV. The dependence of the total mass density profile of early-type galaxies on redshift, stellar mass, and size" 2013, ApJ, 777, 98 and is included here with minor formatting adjustments.

Gravitational lensing, by itself and in combination with other probes, can be used to great effect to measure the mass profiles of early-type galaxies, both in the nearby universe and at cosmological distances (Treu & Koopmans 2002a,b; Rusin et al. 2003; Treu & Koopmans 2004; Rusin & Kochanek 2005; Koopmans et al. 2006; Jiang & Kochanek 2007; Gavazzi et al. 2007; Auger et al. 2010a; Lagattuta et al. 2010). Until recently, however, this approach was severely limited by the small size of the known samples of strong gravitational lenses. This has motivated a number of dedicated searches which have, in the past decade, increased the sample of known strong gravitational lens systems by more than an order of magnitude (e.g., Browne et al. 2003; Bolton et al. 2008b; Faure et al. 2008; Treu et al. 2011).

In spite of all this progress the number of known lenses at $z \sim 0.5$ and above is still a severe limitation. Increasing this sample and using it as a tool to understand the

formation and evolution of massive galaxies is the main goal of our SL2S galaxy-scale lens search (Gavazzi et al. 2012) and other independent searches based on a variety of methods (Brownstein et al. 2012; Marshall et al. 2009; Negrello et al. 2010; Pawase et al. 2014; Inada et al. 2012; González-Nuevo et al. 2012; Wardlow et al. 2013; Vieira et al. 2013).

In our pilot SL2S paper (Ruff et al. 2011) we measured the evolution of the density slope of massive early-type galaxies by combining lensing and dynamics measurements of a sample of just 11 SL2S lenses with similar measurements taken from the literature (Treu & Koopmans 2004; Koopmans et al. 2009; Auger et al. 2010b), finding tentative evidence that the density profile of massive ETGs steepens with cosmic time on average. This trend was later confirmed qualitatively by an independent study of Bolton et al. (2012) and agrees with the theoretical work by Dubois et al. (2013). However, the picture is not clear: the observed trend is tentative at best, while different theoretical studies find contrasting evolutionary trends (Johansson et al. 2012; Remus et al. 2013). More data and better models are needed to make progress.

In order to clarify the observational picture, we have collected a much larger sample of objects, more than tripling the sample of secure lenses with all the necessary measurements, with respect to our pilot study. Photometric, spectroscopic and strong lensing measurements for this expanded sample are presented in the previous Chapter.

The combination of the photometric, lensing, and spectroscopic data is used in this Chapter to study the cosmic evolution of the slope of the average mass density profile of massive early-type galaxies. This is achieved by fitting power law density profiles ($\rho(r) \propto r^{-\gamma'}$; $\gamma' \approx 2$ in the local universe) to the measured Einstein radii and velocity

dispersions of our lenses. Such a measurement of γ' is a good proxy for the mean density slope within the effective radius. The goal of this Chapter is to measure trends of γ' with redshift, in continuity with the work of (Ruff et al. 2011), as well as with other structural properties of massive ETGs, such as stellar mass and size. Such measurements will help us understand the structural evolution of ETGs from $z = 0.8$ to present times.

This Chapter is organized as follows. In Section 4.1 we briefly explain how lensing and kinematics measurements are combined to infer the density slope γ' and discuss the physical meaning of such measurements. In Section 4.2 we combine individual γ' measurements to infer trends of this parameter across the population of ETGs. After a discussion of our results in Section 4.3 we conclude in Section 4.4.

4.1 Power law models

We now proceed to combine lensing measurements with stellar kinematics information to infer the total mass density profile of each lens galaxy. We follow the now standard procedure in lensing and dynamics studies (Treu & Koopmans 2002a), as used by Ruff et al. (2011). We model the total (dark matter + stars) mass profile as a spherical power law $\rho(r) \propto r^{-\gamma'}$ in the kinematic analysis. The free parameters of the model are the slope γ', and the mass normalization. For a given model we calculate the line of sight velocity dispersion within the rectangular aperture of our observation, broadened by the seeing, through the spherical Jeans equation. We assume isotropic orbits and a de Vaucouleurs profile for the distribution of tracers (de Vaucouleurs 1948), with effective radius fixed to the observed one. We then compare the model to the observed velocity dispersion

118

and Einstein radius to derive posterior probability densities for the free parameters. In spite of the clear approximations, the method has been shown to be very robust when compared to results of more sophisticated models (e.g. Barnabè et al. 2011).

The data required for this inference are the Einstein radius of the lens, the redshift of both the deflector galaxy and the lensed source, and the velocity dispersion of the lens. Of the 45 grade A lenses of the SL2S sample, 28 have all the required data. For the analysis presented in this Chapter, only the 25 systems with spectroscopic observations obtained before January 2013 are used. For the few systems with two or more independent measurements of the velocity dispersion, we use the weighted average. The inferred values of γ' are reported in Table 4.1.

4.1.1 The meaning of γ'

Before analyzing the measurements in a statistical sense we need to understand what physical properties the quantity γ' is most sensitive to. Observations (Sonnenfeld et al. 2012) and simple arguments (galaxies have a finite mass) suggest that the true density profile deviates from a pure power law, particularly at large radii. Thus our power law fits to the lensing and kinematics data must be interpreted as an approximation of the average density slope over a radial range explored by our data. Since for a typical lens both the Einstein radius and the velocity dispersion probe the region within the effective radius, we expect that the inferred γ' will be close to the mean density slope within R_{eff}, as suggested by Dutton & Treu (2013a).

However we would like to be more quantitative and explore the two following ques-

119

Name	z_d	$R_{\rm eff}$ (kpc)	$R_{\rm Ein}$ (kpc)	$\sigma_{\rm e2}$ (km s^{-1})	$\log M_*^{\rm Salp}/M_\odot$	γ'	Notes
SL2SJ021247$-$055552	0.750	8.92	9.33	267 ± 17	11.45 ± 0.17	2.05 ± 0.09	
SL2SJ021325$-$074355	0.717	17.67	17.22	287 ± 33	11.97 ± 0.19	1.79 ± 0.12	
SL2SJ021411$-$040502	0.609	6.29	9.48	238 ± 15	11.60 ± 0.14	1.85 ± 0.07	
SL2SJ021737$-$051329	0.646	4.27	8.80	270 ± 21	11.53 ± 0.16	2.02 ± 0.09	
SL2SJ021902$-$082934	0.389	3.01	6.88	300 ± 23	11.50 ± 0.10	2.26 ± 0.08	
SL2SJ022511$-$045433	0.238	8.59	6.65	226 ± 20	11.81 ± 0.09	1.78 ± 0.10	
SL2SJ022610$-$042011	0.494	6.44	7.23	266 ± 24	11.73 ± 0.11	2.01 ± 0.12	
SL2SJ023251$-$040823	0.352	4.78	5.15	271 ± 20	11.36 ± 0.09	2.39 ± 0.10	
SL2SJ084847$-$035103	0.682	3.21	6.02	205 ± 21	11.24 ± 0.16	1.85 ± 0.14	
SL2SJ084909$-$041226	0.722	3.55	7.94	312 ± 18	11.63 ± 0.13	2.14 ± 0.06	
SL2SJ084959$-$025142	0.274	6.11	4.84	275 ± 34	11.52 ± 0.09	2.32 ± 0.17	
SL2SJ085019$-$034710	0.337	1.35	4.48	307 ± 25	11.14 ± 0.09	2.45 ± 0.07	disky
SL2SJ085540$-$014730	0.365	3.48	5.21	222 ± 19	11.11 ± 0.10	2.15 ± 0.11	
SL2SJ090407$-$005952	0.611	16.81	9.47	178 ± 20	11.55 ± 0.12	1.48 ± 0.11	
SL2SJ095921$+$020638	0.552	3.47	4.73	195 ± 22	11.28 ± 0.11	2.11 ± 0.16	
SL2SJ135949$+$553550	0.783	13.08	8.52	229 ± 19	11.41 ± 0.15	1.86 ± 0.14	
SL2SJ140454$+$520024	0.456	11.78	14.80	337 ± 19	12.10 ± 0.10	1.95 ± 0.06	
SL2SJ140546$+$524311	0.526	4.58	9.48	291 ± 21	11.67 ± 0.11	2.14 ± 0.08	
SL2SJ140650$+$522619	0.716	4.35	6.79	258 ± 14	11.60 ± 0.15	2.00 ± 0.07	
SL2SJ141137$+$565119	0.322	3.04	4.34	220 ± 23	11.28 ± 0.09	2.15 ± 0.15	
SL2SJ142059$+$563007	0.483	7.86	8.39	228 ± 19	11.76 ± 0.10	1.93 ± 0.11	
SL2SJ220329$+$020518	0.400	3.86	10.49	218 ± 21	11.26 ± 0.10	1.77 ± 0.09	
SL2SJ220506$+$014703	0.476	3.93	9.87	326 ± 30	11.51 ± 0.10	2.19 ± 0.09	
SL2SJ221326$-$000946	0.338	2.41	5.17	177 ± 15	10.99 ± 0.10	1.89 ± 0.09	disky
SL2SJ222148$+$011542	0.325	5.27	6.59	224 ± 23	11.55 ± 0.09	1.96 ± 0.13	

Table 4.1: Summary of lensing and dynamics measurements.

tions: what kind of average over the true density profile $\rho(r)$ best reproduces the lensing+dynamics γ'? How sensitive to the ratio $R_{\mathrm{Ein}}/R_{\mathrm{e}}$ is the measured γ' for a fixed galaxy mass profile? The former issue is relevant when comparing theoretical models to lensing and dynamics measurements. The latter is important when trying to measure trends of γ' with redshift: the ratio $R_{\mathrm{Ein}}/R_{\mathrm{e}}$ typically increases for purely geometrical reasons, and a dependence of γ' on $R_{\mathrm{Ein}}/R_{\mathrm{e}}$ could in principle bias the inference on the evolution of the slope. In order to answer these questions we simulate γ' measurements on a broad range of model mass profiles and compare these with the true density slopes. We consider a pure de Vaucouleurs profile, a sum of a de Vaucouleurs profile with a Navarro, Frenk & White (Navarro et al. 1997) profile with two values of the dark matter mass fraction f_{DM} within the 3d effective radius, and the most probable total density profile from the bulge + halo decomposition of the gravitational lens SDSSJ0946+1006 by Sonnenfeld et al. (2012). None of these model profiles is a pure power law. We emphasize that the range of models is chosen to be broader than what is likely to be found in real galaxies based on the detailed analysis of SLACS systems by Barnabè et al. (2011).

We again use the spherical Jeans equation to calculate the central velocity dispersion for each of these model galaxies and then fit power law density profiles with fixed total projected mass within different Einstein radii. These simulated measurements of γ' are plotted in Figure 4.1 as a function of $R_{\mathrm{Ein}}/R_{\mathrm{e}}$ for each model profile. In the same plot we show the local logarithmic density slope $-\mathrm{d}\log\rho/\mathrm{d}\log r$ as a function of r, and also the *mass-weighted density slope within radius r*

$$\langle\gamma'(r)\rangle_M = \frac{1}{M(r)}\int_0^r \gamma'(r')4\pi r^2\rho(r')dr', \tag{4.1}$$

121
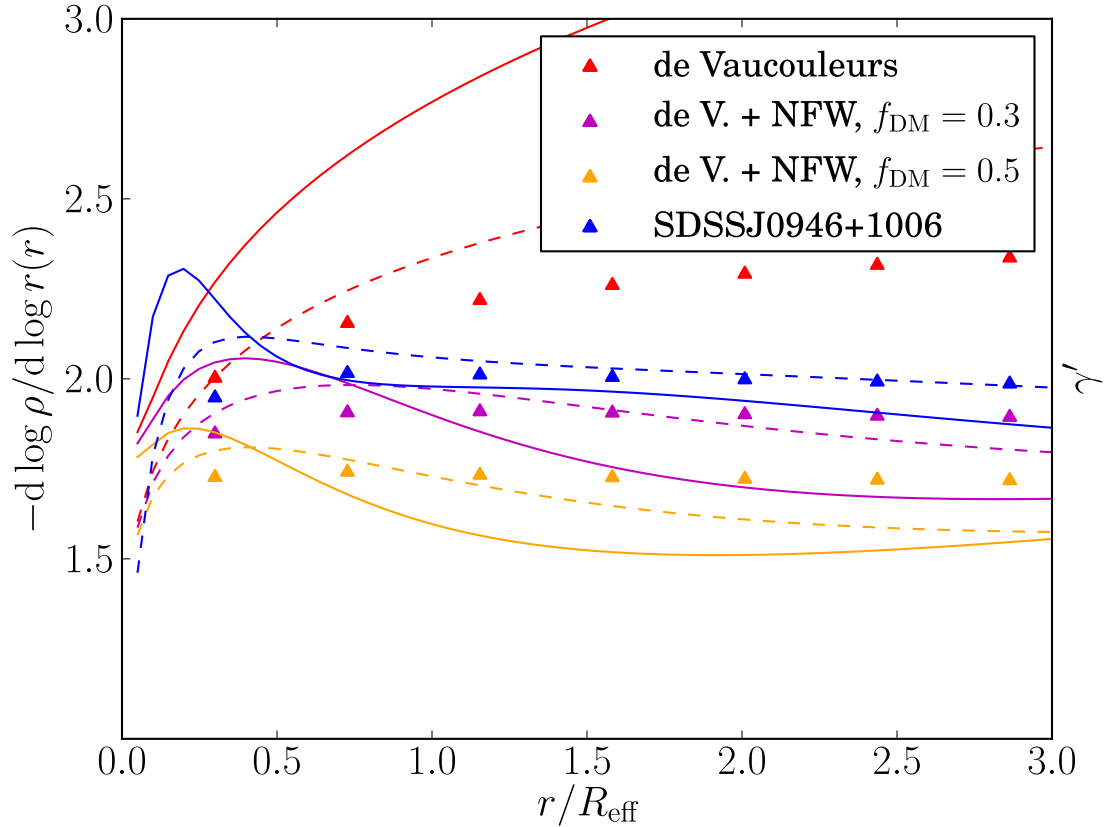
Figure 4.1: *Solid lines:* Local logarithmic density slope as a function of 3d radius, in units of the effective radius. *Dashed lines:* mass-weighted density slope within radius r. *Triangles:* lensing+dynamics γ' for $R_{\mathrm{Ein}} = r$. Different colors indicate the different model mass profiles listed in the body text.

which has been suggested by Dutton & Treu (2013a) to be a good proxy for the lensing + dynamics γ'.

Figure 4.1 shows that measurements of γ' (triangles) are remarkably independent of the ratio of the Einstein radius to the effective radius, for all models. This is an important result: it means that the physical interpretation of γ' measurements will be stable against different lenses having different values of $R_{\mathrm{Ein}}/R_{\mathrm{e}}$. Excluding the pure de Vaucouleurs model, which is ruled out on many grounds (mass-follows light models fail to reproduce lensing and dynamical data, for example Koopmans & Treu 2003),

the difference between the mass-weighted slope and the lensing and dynamics slope is generally smaller than the typical measurement errors on γ' of ~ 0.1, particularly in the region $0.5R_{\mathrm{e}} < r < R_{\mathrm{e}}$. However the radius at which γ' and the mass-weighted slope are closest is slightly different for different mass profiles, and so it is difficult to interpret γ' precisely in terms of a mass-weighted slope within a fixed radius. For very accurate comparisons with lensing and dynamical data, we recommend simulating a lensing and dynamics measurement of the models.

4.2   Dependence of the mass density profile slope γ' on redshift, stellar mass, and effective radius

The main goal of this work is to establish whether, and to what extent, γ' varies with redshift across the population of ETGs. It is useful to first study the trends of γ' on basic parameters (Section 4.2.1) in order to gain insights about the ingredients that will have to be considered in Section 4.2.2 to carry out a rigorous statistical analysis.

4.2.1   Qualitative exploration of the dependency of γ' on other parameters

Figure 4.2 shows the individual lens γ' values as a function of z for SL2S galaxies, as well as lenses from the SLACS (Auger et al. 2010a) and LSD (Treu & Koopmans 2004) surveys. A trend of γ' with z is clearly visible, with lower redshift objects having a systematically steeper slope than higher redshift ones, as previously found by Ruff et al.

(2011) and Bolton et al. (2012). Before making more quantitative statements on the time evolution of γ' we would like to check whether the density slope correlates with quantities other than redshift. Galaxies grow in mass and size during their evolution, and a variation of γ' with time might be the result of a more fundamental dependence of the slope on structural properties of ETGs. Dependences of γ' on the effective radius and the stellar velocity dispersion were explored by Auger et al. (2010a), finding an anticorrelation with the former and no significant correlation with the latter. Here we consider the stellar mass, plotted against γ' in Figure 4.3. A weak trend is visible, with more massive galaxies having a shallower slope. However the stellar mass is a rather steep function of redshift in our sample (see Figure 3.11) and the trend seen in Figure 4.3 might just be the result of this selection function. In fact, if we fit for a linear dependence of γ' on both z and M_* we find that our data are consistent with γ' being independent of M_* at fixed z.

A quantity that is expected to correlate with γ' is the stellar mass density, $\Sigma_* = M_*/(2\pi R_{\mathrm{e}}^2)$: galaxies with a more concentrated stellar distribution should have a steeper overall density profile. This was pointed out by Auger et al. (2010a) and Dutton & Treu (2013a) and is seen in our data, as shown in Figure 4.4. It is therefore important to account for a dependence of γ' on Σ_*, or on the two independent variables on which this quantity depends, R_{e} and M_*, when fitting for the time dependence of the density slope. This is done in the next Section.
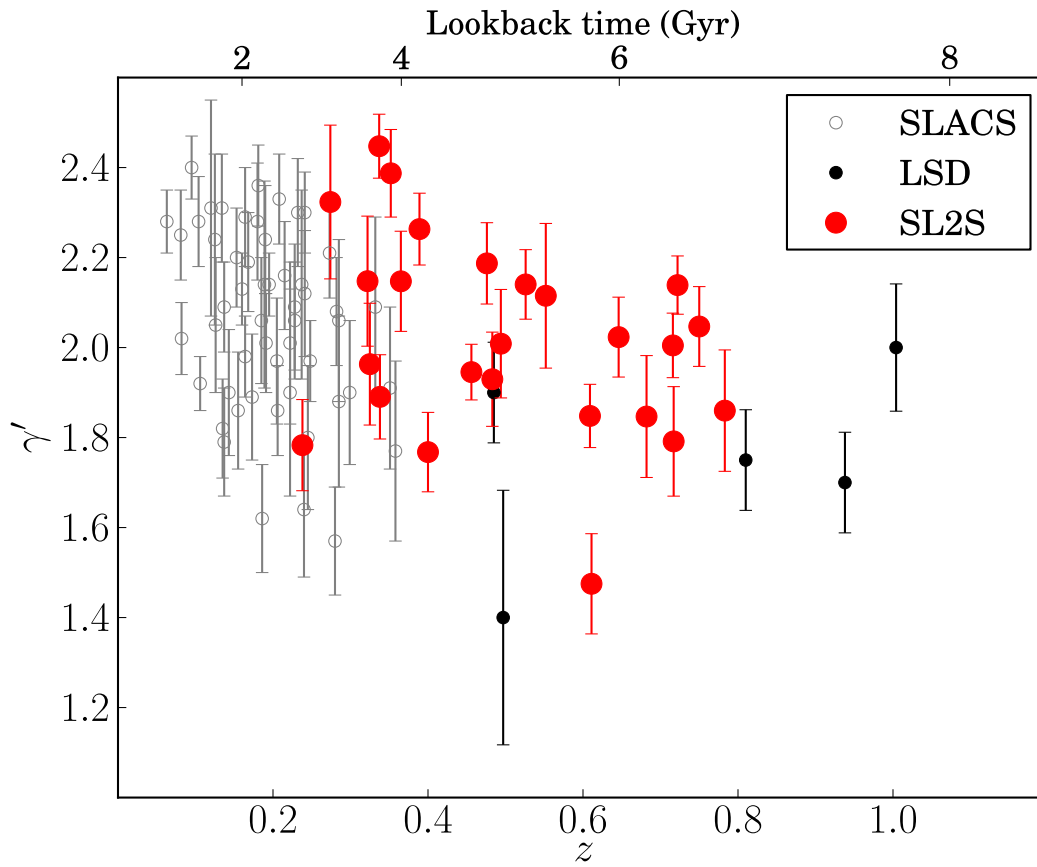
Figure 4.2: Density slope as a function of redshift for SL2S, SLACS and LSD galaxies.
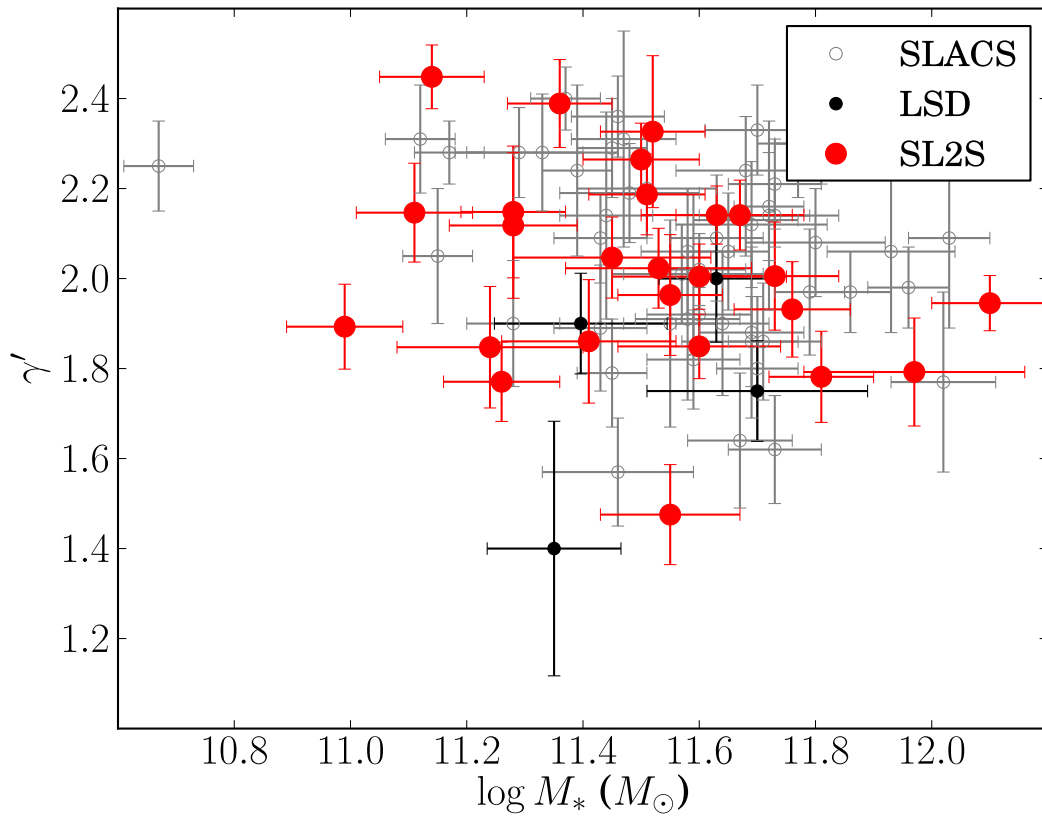
Figure 4.3: Density slope as a function of stellar mass. A Salpeter IMF is assumed.
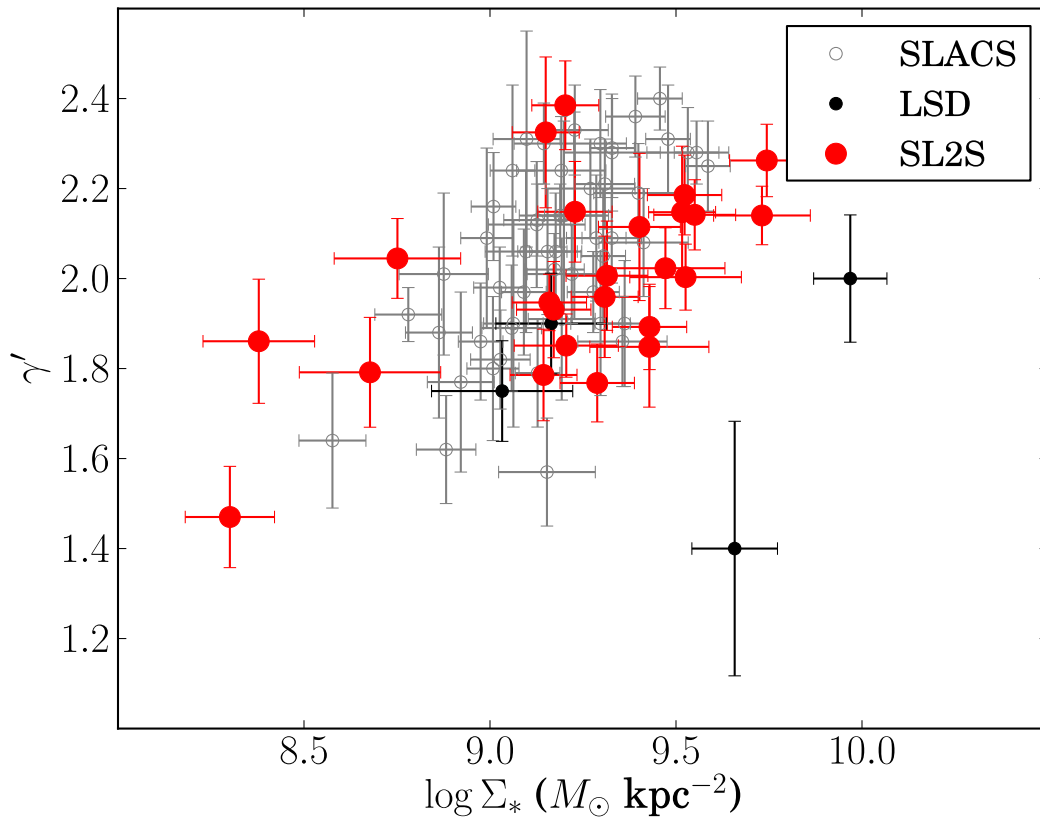
Figure 4.4: Density slope as a function of stellar mass density.

4.2.2 Quantitative Inference

In this Section we aim to quantify how the mean density slope $\langle \gamma' \rangle$ depends on galaxy properties, and on lookback time. The population of ETGs is known to be well-described by two parameters, as revealed by the existence of the Fundamental Plane relation (Djorgovski & Davis 1987; Dressler et al. 1987). Two parameters are then probably sufficient to capture the variation of γ' across the population of ETGs. For our analysis we focus on stellar mass and effective radius (this includes also dependencies on stellar mass density, which is believed to be an important parameter driving γ', as discussed above). Our objective is then to measure the trends in γ' across the three-dimensional space defined by (z, M_*, R_e). This is done with a simple but rigorous Bayesian inference method. We assume that the values of the slope γ' of our lenses are drawn from a Gaussian distribution with mean given by

$$\langle \gamma' \rangle = \gamma_0' + \alpha(z - 0.3) + \beta(\log M_* - 11.5) + \xi \log (R_e/5) \tag{4.2}$$

and dispersion $\sigma_{\gamma'}$. The stellar mass is in solar units and the effective radius in kpc. We also assume that individual stellar masses $M_{*,i}$ are drawn from a parent distribution that we approximate as a Gaussian:

$$\Pr(M_{*,i}) = \frac{1}{\sigma_{M_*}\sqrt{2\pi}} \exp \left[-\frac{\left(\log M_{*,i} - \mu_{M_*}^{\text{(Samp)}}(z_i) \right)}{2\sigma_{M_*}^{2\text{(Samp)}}} \right]. \tag{4.3}$$

To account for selection effects, we allow for a different mean stellar mass and dispersion for lenses of different surveys. We also let the mean stellar mass be a function of redshift. This choice reflects the clear trend of stellar mass with redshift seen in Figure 3.11 for both the SLACS and the SL2S samples, which in turn is determined by SLACS and SL2S

both being magnitude-limited samples. The parameter describing the mean stellar mass is then

$$\mu_{M_*}^{(\text{SLACS})} = \zeta^{(\text{SLACS})}(z_i - 0.2) + \log M_{*,0}{}^{(\text{SLACS})} \tag{4.4}$$

for SLACS galaxies and

$$\mu_{M_*}^{(\text{SL2S})} = \zeta^{(\text{SL2S})}(z_i - 0.5) + \log M_{*,0}{}^{(\text{SL2S})} \tag{4.5}$$

for SL2S and LSD galaxies. We assume flat priors on all the model parameters and fit for them with a Markov chain Monte Carlo following Kelly (2007). The stellar masses considered in this model are those measured in Paper III assuming a Salpeter IMF. The full posterior probability distribution function is shown in Figure 4.5 and the median, 16th and 84th percentile of the probability distribution for the individual parameters, obtained by marginalizing over the remaining parameters, is given in Table 4.2. The fit is done first with SL2S galaxies only and then repeated by adding SLACS and LSD lenses. For six lenses of the SLACS sample Auger et al. (2010a) warn that their velocity dispersions might be significantly incorrect, and we conservatively exclude them from our fit. These are SDSSJ0029$-$0055, SDSSJ0737+3216, SDSSJ0819+4534, SDSSJ0935$-$0003, SDSSJ1213+6708 and SDSSJ1614+4522.

By using only the 25 SL2S lenses for which γ' measurements are possible, we are able to detect a trend of $\langle \gamma' \rangle$ with R_e at the 3-sigma level and a dependence on M_* at the 1-sigma level: at fixed z and M_*, galaxies with a smaller effective radius have a steeper density profile. Similarly, at fixed R_e, galaxies with a larger stellar mass have a marginally larger γ'. If we add 53 lenses from SLACS and 4 lenses from the LSD survey, the trends with M_* and R_e are confirmed at a higher significance, and we detect a dependence of

$$\gamma' = \gamma_0 + \alpha(z - 0.3) + \beta(\log M_* - 11.5) + \xi(\log \Sigma_* - 9.0) + N(0, \sigma_{\gamma'})$$
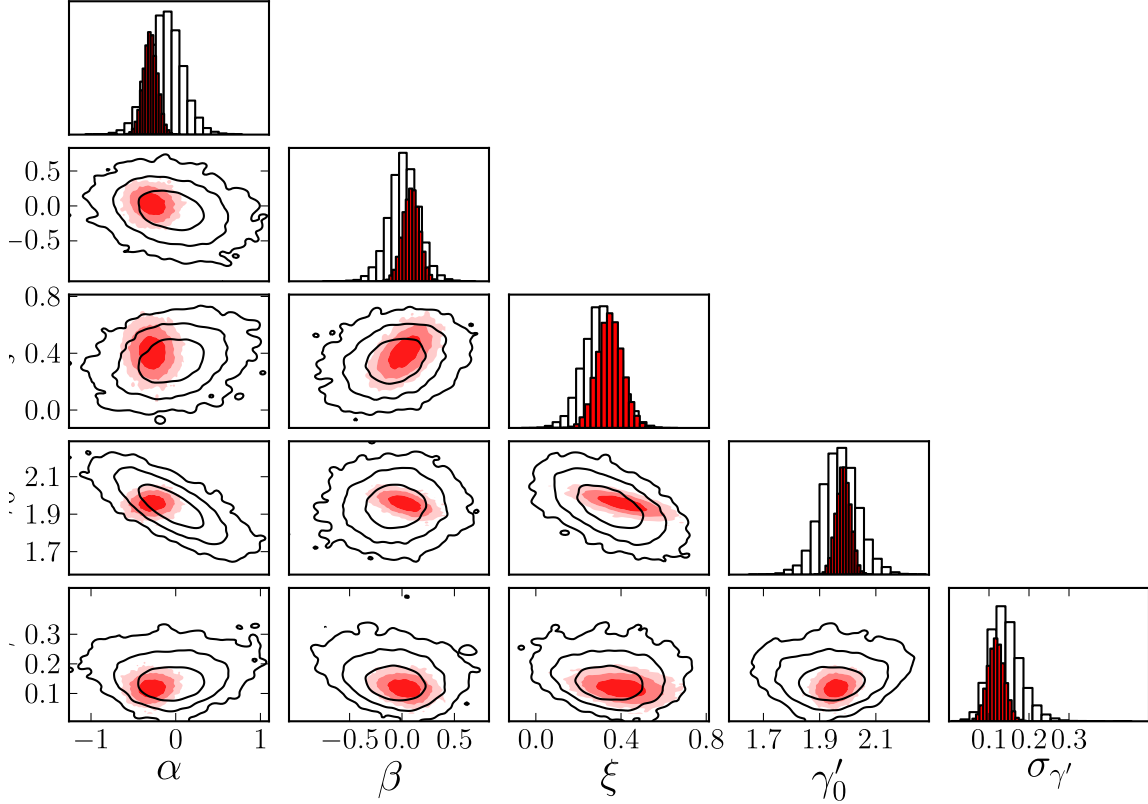
Figure 4.5: Posterior probability distribution function for the model parameters of equation (4.2). *Empty contours:* Inference with SL2S galaxies only. *Filled contours:* SL2S + SLACS + LSD lenses. The different levels represent the 68%, 95% and 99.7% enclosed probability regions.

Table 4.2: Linear model with scatter.

Parameter	SL2S only	SL2S + SLACS + LSD	Notes
$\log M_{*,0}^{\text{(SL2S)}}$	$11.50^{+0.05}_{-0.05}$	$11.49^{+0.05}_{-0.05}$	Mean stellar mass at $z = 0.5$, SL2S sample
$\zeta^{\text{(SL2S)}}$	$0.35^{+0.34}_{-0.33}$	$0.38^{+0.26}_{-0.26}$	Linear dependence of mean stellar mass on redshift, SL2S sample
$\sigma_{M_*}^{\text{(SL2S)}}$	$0.25^{+0.05}_{-0.04}$	$0.23^{+0.04}_{-0.04}$	Scatter in mean stellar mass, SL2S sample
$\log M_{*,0}^{\text{(SLACS)}}$	$\cdots$	$11.59^{+0.03}_{-0.03}$	Mean stellar mass at $z = 0.2$, SLACS sample
$\zeta^{\text{(SLACS)}}$	$\cdots$	$2.35^{+0.39}_{-0.39}$	Linear dependence of mean stellar mass on redshift, SLACS sample
$\sigma_{M_*}^{\text{(SLACS)}}$	$\cdots$	$0.17^{+0.02}_{-0.02}$	Scatter in mean stellar mass, SLACS sample
α	$-0.13^{+0.24}_{-0.24}$	$-0.31^{+0.09}_{-0.10}$	Linear dependence of γ' on redshift.
β	$0.31^{+0.23}_{-0.23}$	$0.40^{+0.16}_{-0.15}$	Linear dependence of γ' on $\log M_*$.
ξ	$-0.67^{+0.20}_{-0.20}$	$-0.76^{+0.15}_{-0.15}$	Linear dependence of γ' on $\log R_{\text{eff}}$.
γ_0	$2.05^{+0.06}_{-0.06}$	$2.08^{+0.02}_{-0.02}$	Mean slope at $z = 0.3$, $\log M_* = 11.5$, $R_{\text{eff}} = 5$ kpc
$\sigma_{\gamma'}$	$0.14^{+0.04}_{-0.03}$	$0.12^{+0.02}_{-0.02}$	Scatter in the γ' distribution

$\langle \gamma' \rangle$ on redshift at the 3-sigma level. Lower redshift objects appear to have a steeper slope than higher redshift counterparts at fixed mass and size. Incidentally, the median value of ξ, the parameter describing the linear dependence of $\langle \gamma' \rangle$ on $\log R_{\rm e}$, is nearly -2 times β, the parameter describing the dependence on $\log M_*$. This suggests that $\langle \gamma' \rangle$ grows roughly as $\beta \log (M_*/R_{\rm e}^2)$, which is equivalent to the stellar mass density. It appears then that the dependence of γ' on the structure of ETGs can be well summarized with a dependence on stellar mass density, leaving little dependence on M_* or $R_{\rm e}$ individually. This confirms and extends the trend with surface mass density seen by Auger et al. (2010a) and Dutton & Treu (2013a).

We then repeated the fit allowing only for a dependence of $\langle \gamma' \rangle$ on redshift and stellar mass density:

$$\langle \gamma' \rangle = \gamma_0 + \alpha(z - 0.3) + \eta(\log \Sigma_* - 9.0). \tag{4.6}$$

This model has one less free parameter with respect to Equation 4.2. Our inference on the parameter describing the dependence on Σ_* is $\eta = 0.38 \pm 0.07$, and the scatter in γ' is $\sigma_{\gamma'} = 0.12 \pm 0.02$, the same value measured for the more general model of Equation 4.2. This is again suggesting that the dependence of γ' on the stellar mass density might be of a more fundamental nature than dependences on mass and size separately.

4.3 Discussion

The main result of the previous section is that the ensemble average total mass density slope of galaxies of a fixed stellar mass increases with cosmic time (i.e. decreases with redshift). This trend with redshift is detected at the $3 - \sigma$ confidence level and is in good

agreement with previous results from Ruff et al. (2011) and Bolton et al. (2012).

Before discussing the physical interpretation of this result, however, it is important to emphasize that what we are measuring is how the population mean density slope changes in the (z, M_*, R_e) space within the population of early-type galaxies, and not how γ' changes along the lifetime of an individual galaxy, $d\gamma'/dz$. In order to infer the latter quantity we need to evaluate the variation of γ' along the evolutionary track of the galaxy as this moves in the (z, M_*, R_e) space. This requires to know how both mass and size of the galaxy change with time, since the slope depends on these parameters. More formally,

$$\frac{d\gamma'(z, \log M_*, \log R_e)}{dz} = \frac{\partial \gamma'}{\partial z} + \frac{\partial \gamma'}{\partial \log M_*} \frac{d \log M_*}{dz} + \frac{\partial \gamma'}{\partial \log R_e} \frac{d \log R_e}{dz}. \tag{4.7}$$

In a parallel with fluid mechanics, our description of the population of galaxies of Section 4.1 is Eulerian, while Equation 6.6 is a Lagrangian specification of the change in time of the mean slope of an individual galaxy, providing a more straightforward way to physically understand the evolution of ETGs.

With all these terms entering Equation 6.6, it is no longer clear if the density slope is indeed getting steeper with time for individual objects. In particular, we have observed that γ' depends significantly on stellar mass density (and thus effective radius). It is then crucial to consider all the terms of the equation before reaching a conclusion. Fortunately this can be done by combining our measurements with results from the literature.

In the context of our model specified in Equation 4.2, the partial derivatives introduced above can be identified and evaluated as follows:

$$\frac{\partial \gamma'}{\partial z} = \alpha = -0.31 \pm 0.10, \tag{4.8}$$

$$\frac{\partial \gamma'}{\partial \log M_*} = \beta = 0.40 \pm 0.16, \tag{4.9}$$

$$\frac{\partial \gamma'}{\partial \log R_{\mathrm{e}}} = \xi = -0.76 \pm 0.15. \tag{4.10}$$

Note that we are not considering the effects of scatter: we are assuming that the change in γ' is the same as that of a galaxy that evolves while staying at the mean γ' as it moves through the (z, M_*, R_{e}) space. By doing so, the evolution in the slope that we derive from Equation 6.6 will be representative of the mean change in γ' over the population, while individual objects can have different evolutionary tracks, within the limits allowed by our constraints on $\sigma_{\gamma'}$.

The remaining quantities to be estimated are the rate of mass and size growth. In the hierarchical merging picture ETGs are expected to grow in stellar mass with time, therefore $\mathrm{d}M_*/\mathrm{d}z < 0$. Observationally, we know massive early-type galaxies grow at most by a factor of two in stellar mass since $z = 1$ (see, e.g., Lin et al. 2013, and references therein). Thus we can conservatively take the mean between zero and 2, even though we will show below that our conclusion are virtually insensitive to this choice:

$$\frac{\mathrm{d}\log M_*}{\mathrm{d}z} = -0.15 \pm 0.15. \tag{4.11}$$

The effective radius grows as a result of the growth in mass, but is itself an evolving quantity at fixed M_* (Damjanov et al. 2011; Newman et al. 2012b; Cimatti et al. 2012; Poggianti et al. 2013): $R_{\mathrm{e}} = R_{\mathrm{e}}(z, M_*(z))$. *We assume that ETGs grow while staying on the observed $M_* - R_{\mathrm{e}}$ relation at all times.* Then we can write

$$\frac{\mathrm{d}\log R_{\mathrm{e}}}{\mathrm{d}z} = \frac{\partial \log R_{\mathrm{e}}}{\partial z} + \frac{\partial \log R_{\mathrm{e}}}{\partial \log M_*}\frac{\mathrm{d}\log M_*}{\mathrm{d}z} \tag{4.12}$$

and use the values measured by Newman et al. (2012b), $\partial \log R_{\mathrm{e}}/\partial z = -0.26 \pm 0.02$ and $\partial \log R_{\mathrm{e}}/\partial \log M_* = 0.59 \pm 0.07$.

Plugging these values into Equation 6.6 we find that

$$\frac{\mathrm{d}\gamma'}{\mathrm{d}z} = (-0.31 \pm 0.10) + (0.40 \pm 0.15)(-0.15 \pm 0.15) + (-0.76 \pm 0.15)[(-0.26 \pm 0.02)$$

$$+ (-0.15 \pm 0.15)(0.59 \pm 0.07)] = -0.10 \pm 0.12$$

$$(4.13)$$

Note that $\mathrm{d}\gamma'/\mathrm{d}z$ has little dependence on the mass growth rate $\mathrm{d}\log M_*/\mathrm{d}z$, which is the most poorly known quantity in this model. To be more quantitative we plot in Figure 4.6 the total derivative $\mathrm{d}\gamma'/\mathrm{d}z$ as a function of $\mathrm{d}\log M_*/\mathrm{d}z$, and show that for any plausible value, spanning over an order of magnitude, the answer is unchanged. Different assumptions on the evolution of the size-mass relation do not change significantly our result. For instance, Damjanov et al. (2011) find a more rapid evolution of R_{e} than Newman et al. (2012b), leading to $\mathrm{d}\gamma'/\mathrm{d}z = 0.06 \pm 0.15$, consistent with no change of the total mass density profile with time.

Thus, the key result is that, when considering all the terms of Equation 6.6, we find that, on average, individual ETGs grow at approximately constant density slope. The observed redshift dependence of γ' *at fixed mass and size* can then be understood as the result of the evolution of the size-mass relation and by the dependency of γ' on the stellar mass density. Qualitatively, in this picture an individual galaxy grows in stellar mass and size so as to decrease its central stellar mass density. During this process, the slope of its total mass density profile does not vary significantly. However the other galaxies that now find themselves to have the original stellar mass and effective radius of this galaxy had originally a steeper mass density profile, thus giving rise to the observed trend in
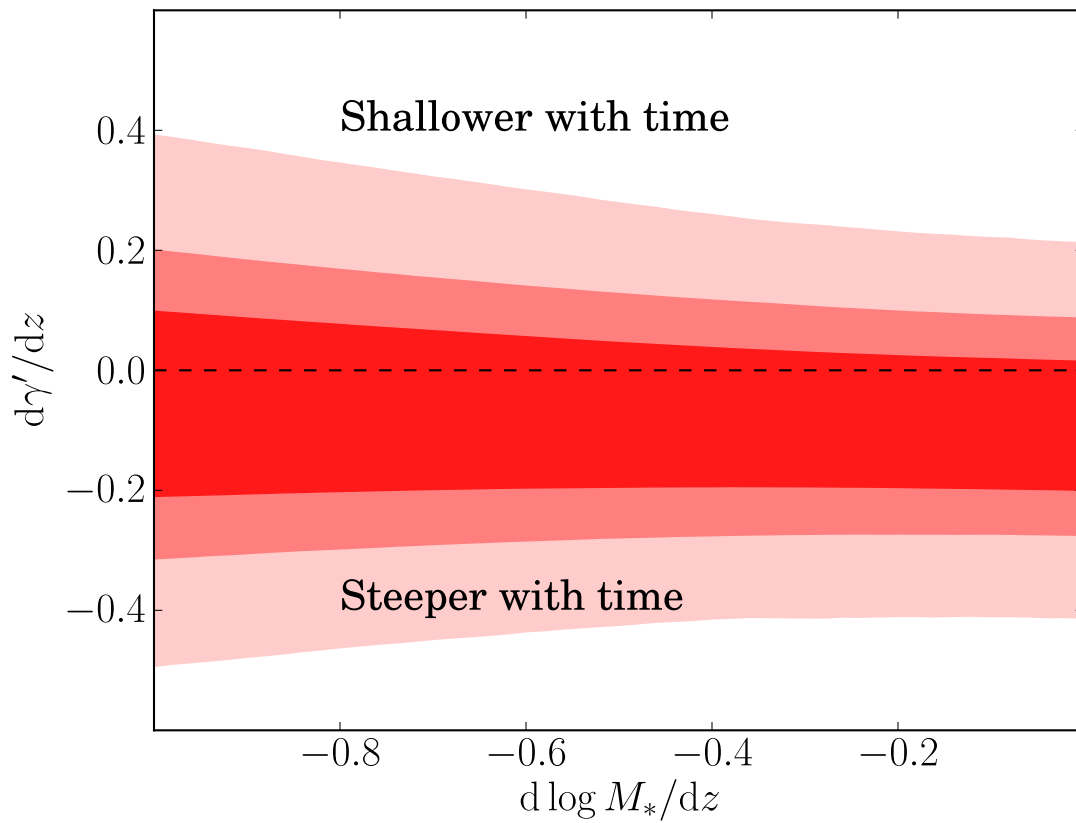
Figure 4.6: Mean intrinsic change of the density slope with redshift of a massive ETG, as a function of its mass growth rate.

$\partial\gamma'/\partial z$.

This is illustrated in Figure 4.7, where we show a possible scenario consistent with the observations. The evolutionary tracks of two representative galaxies between $z = 1$ and $z = 0$ are shown as solid black arrows, in the multi-dimensional parameter space of stellar mass, effective radius, effective density, and slope of the mass density profile γ'. The two galaxies are chosen so that one has at $z = 1$ the same mass and effective radius that the other has at $z = 0$. Mass and size are evolved following Equation 4.11 and Equation 4.12. We then assign γ' at $z = 0$ based on the observed correlation with size and stellar mass (effectively with effective stellar mass density, since $\beta \approx -2\xi$) *and assume it does not evolve for an individual galaxy.* The apparent evolution of γ' at fixed M_* and $R_{\rm e}$ is consistent with the measured value $\partial\gamma'/\partial z = -0.31 \pm 0.10$, and is dictated by a difference in the initial stellar density of their progenitors, being larger for the more massive object.

In the context of simple one-parameter stellar profiles (e.g. de Vaucouleurs), this difference in γ' at fixed mass and size for galaxies at different redshift must be ascribed to corresponding differences in the underlying dark matter distribution. The implications of our results for the dark matter profiles of ETGs will be explored in an upcoming paper (Sonnenfeld et al., in prep.).

An important assumption at the basis of our analysis is that scaling relations of γ' with mass and size measured at low redshift can be used to predict the evolution of the slope for higher redshift objects. This assumption holds well if the evolutionary tracks of higher redshift galaxies stay on parts of the parameter space probed by the lower redshift systems. To first approximation this seems to be the case for the galaxies in our sample.
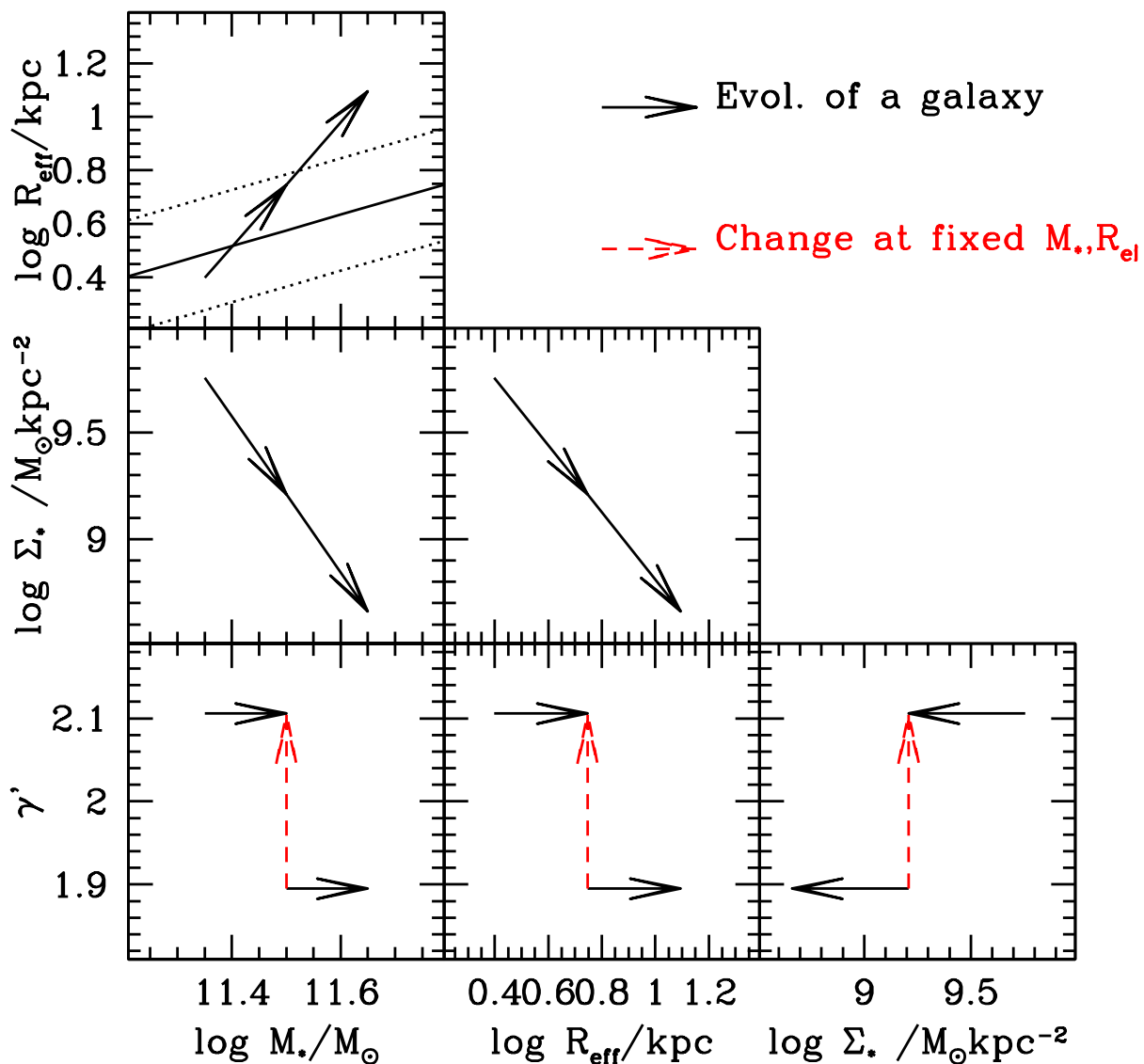
Figure 4.7: Illustration of a scenario consistent with the observed evolution. The evolutionary tracks of two representative galaxies between $z = 1$ and $z = 0$ are shown as solid black arrows, in the multidimensional parameter space of stellar mass, effective radius, effective density, and slope of the mass density profile γ'. Measured correlations with stellar mass are used to assign the other parameters as described in the text. The solid and dotted lines in the top left panel show the mass-size relation at $z = 1$ from Newman et al. (2012b) and the scatter around it. Even if γ' is assumed not to change for an individual galaxy, γ' at fixed stellar mass and size is observed to increase reflecting the difference in their initial ($z = 1$) stellar density, as shown by the red dashed arrows.

Figure **??** shows the positions of our lenses in the $M_* - R_\mathrm{e}$ space, where the effective radius of each object is renormalized by the average R_e of galaxies at its redshift. Under our assumptions, objects evolve along lines parallel to the mass-size relation (dashed line) towards higher masses. There is significant overlap between the high-z SL2S-LSD sample and the lower redshift SLACS sample, implying that SLACS galaxies are informative on the evolution in γ' of SL2S-LSD objects. Differently, one could rely on extrapolations of the scaling relations for γ'.

A more quantitative explanation of our findings would require a detailed comparison with theoretical model and is beyond the scope of this work. However, we can check at least qualitatively how our result compares with published predictions. Nipoti et al. (2009b) studied the impact of dissipationless (dry) mergers on γ' finding that for an individual galaxy the slope tends to get shallower with time. Johansson et al. (2012) looked at the evolution in the slope on nine ETGs in cosmological simulations, finding no clear trend in the redshift range explored by our data. Their simulations include both dry and dissipational (wet) mergers. Remus et al. (2013) examined simulated ETGs in a cosmological framework and in binary mergers. They found slopes that become shallower in time, asymptotically approaching the value $\gamma' \approx 2.1$ as observed in our data. They also detected a correlation between the amount of in-situ star formation and slope, with γ' being larger in systems that experienced more star formation events. Finally, Dubois et al. (2013) produced zoomed cosmological simulations of ETGs with or without AGN feedback. They found that the total density slope becomes steeper with time. They also observed that galaxies with strong AGN feedback have a shallower profile than systems with no AGN feedback and interpreted this result with the AGN shutting off in-situ star

138

formation. Qualitatively, our data is not in stark contrast with any of these models.

A more quantitative comparison is required to find out whether the models work in detail. This is left for future work. The combination of constraints from the evolution of the size stellar mass relation obtained via traditional studies of large samples of ETGs, and our own detailed measurements of the evolution of their internal structure should provide a stringent test for evolutionary models of ETGs, and thus help us improve our understanding of the baryonic and dark matter physics relevant at kpc scales.

4.4   Summary and Conclusions

We have presented a comprehensive analysis of the total density profile of a sample of 25 ETG strong lenses from the SL2S sample. By fitting a power-law density profile $(\rho(r) \propto r^{-\gamma'})$ to the lensing and stellar kinematics data of SL2S, SLACS and LSD lenses we measured the dependence of γ' on redshift, stellar mass and galaxy size, over the ranges $z \approx 0.1 - 1.0$, $\log M_*/M_\odot \approx 11 - 12$, $\mathrm{R}_{\mathrm{eff}} = 1 - 20\mathrm{kpc}$.

Our main results can be summarized as follows:

1. In the context of power-law models for the density profile $\rho_{\mathrm{tot}} \propto r^{-\gamma'}$, the (logarithmic) density slope γ' of the SL2S lenses is approximately – but not exactly – that of a single isothermal sphere ($\gamma' = 2$), consistent with previous studies of lenses in different samples. This can be understood as the result of the combination of a stellar mass density profile that falls off more steeply than the dark matter halo. The relative scaling of the two conspires to produce the power law index close to isothermal ("bulge-halo" conspiracy).

2. At a given redshift, the mass density slope γ' depends on the surface stellar mass density $\Sigma_* = M_*/2R_{\rm e}^2$, in the sense that galaxies with denser stars also have steeper total mass density profiles ($\partial\gamma'/\partial\log\Sigma_* = 0.38 \pm 0.07$).

3. At fixed M_* and $R_{\rm e}$, $\langle\gamma'\rangle$ depends on redshift, in the sense that galaxies at a lower redshifts have on average a steeper average slope ($\partial\gamma'/\partial z = -0.31 \pm 0.10$).

4. Once the dependencies of γ' on redshift and surface stellar mass density are taken into account, less than 6% intrinsic scatter is left ($\sigma'_\gamma = 0.12 \pm 0.02$).

5. The average redshift evolution of γ' for an individual galaxy is consistent with zero: $\mathrm{d}\gamma'/\mathrm{d}z = -0.10 \pm 0.12$. This result is obtained by combining our measured dependencies of $\langle\gamma'\rangle$ on redshift stellar mass and effective radius with the observed evolution of the size stellar mass relation taken from the literature.

The key result of this work is that the dependency of $\langle\gamma'\rangle$ on redshift and stellar mass density does not imply that massive early-type galaxies change their mass density profile over the second half of the lifetime. In fact, at least qualitatively, the observed dependencies can be understood as the results of two effects. Individual galaxies grow in stellar mass and decrease in density over the redshift range 1 to 0, while apparently largely preserving their total mass density profiles. This could be explained by the addition of stellar mass in the outer part of the galaxies in quantities that are sufficient to explain the decrease in stellar mass density but insufficient to alter the total mass density profile, since the regions are already dark matter dominated. As shown by Nipoti et al. (2012), the growth in size during this period is slow enough that it could perhaps be explained

140

by the the infall of dark matter and stars via a drizzle of minor mergers, with material of decreasing density, tracking the decreasing cosmic density. This process needs to happen while substantially preserving the total mass density profile.

Alternatively, the evolution at constant slope can be interpreted as the combined effect of the decrease in stellar mass density and a variation in the dark matter profile (either a steepening or a decrease of the central dark matter distribution). The latter effect would be responsible for the term $\partial \gamma'/\partial z$.

Checking whether these scenarios can work quantitatively requires detailed comparisons with theoretical calculations, which are beyond the scope of this paper.

The second important result of this work is that the total mass density profile of early-type galaxies depends on their stellar mass density, with very little scatter. Qualitatively this makes sense, as we expect that the more concentrated stellar distributions should have been able to contract the overall profile the most. Presumably this difference may trace back to differences in past star formation efficiency or merger history. Therefore, the tightness of the observed correlation should provide interesting constraints on these crucial ingredients of our understanding of early-type galaxies.

Chapter 5

Dark matter halos and stellar IMF of massive ETGs

out to redshift 0.8

This chapter has been submitted to The Astrophysical Journal as Sonnenfeld, A.; Gavazzi, R.; Suyu, S. H.; Treu, T.; Marshall, P. J. "The SL2S Galaxy-scale Lens Sample. III. Lens Models, Surface Photometry and Stellar Masses for the final sample", is available for consultation as arXiv:1410.1881, and is included here with minor edits.

In Chapter 2 we showed how, thanks to data of excellent quality, we can determine the stellar IMF and the density profile of the dark matter halo of a massive galaxy. Here we use strong lensing and stellar velocity dispersion measurements for a set of ~ 80 lenses from the Strong Lensing Legacy Survey (SL2S) and the Sloan ACS Lens Survey (SLACS) to statistically infer the same properties in the population of massive galaxies out to redshift ~ 0.8. Using the same sample of lenses, we showed in Chapter 4 how Sonnenfeld et al. (2013b, hereafter Paper IV) measured the mean density slope γ' of the total density profile $\rho(r) \propto r^{-\gamma'}$ across the population of massive ETGs, finding that ETGs evolve while keeping approximately a constant density slope ($d\gamma'/dz = -0.1 \pm 0.1$). Although intriguing, a trend of the parameter γ' is not of easy interpretation. It is not clear how dark matter and baryons conspire to mantain a constant density slope while the

stellar component becomes less concentrated. Here we address this question by fitting a two-component model, consisting of a stellar spheroid and a dark matter halo, to the same data. We characterize simultaneously the distribution of dark matter halo and stellar IMF properties with a hierarchical Bayesian inference method: a robust statistical tool that allows us to properly take into account scatter in the population. We *explicitly* take into account the selection function of our lensing surveys, allowing us to learn about the general population of galaxies rather than just characterizing the population of strong lenses.

This Chapter is organized as follows. In Section 5.1 we describe the model adopted to describe the density profile of the lenses in our sample. In Section 5.2 we introduce the statistical framework used for the analysis of the population of ETGs. In Section 5.3 we explain how the selection function of lensing surveys is taken into account. In Section 5.4 we assume a Navarro Frenk and White (NFW Navarro et al. 1997) model for the dark matter halo of all lenses and combine individual measurements to infer the properties of the population of massive ETGs. In Section 5.5 we generalize the analysis to the case of halos with free inner slope. After a discussion of our results in Section 5.6 we conclude in Section 5.7.

The number of SL2S lenses with a complete set of data necessary for a lensing and dynamics analysis is now 28, with the addition of systems SL2SJ020524-093023, SL2SJ021801-080247 and SL2SJ022046-094927 to the sample analyzed in Paper IV.

5.1 Two component mass models

The analysis presented in Paper IV is based on power-law model density profiles for the total (stellar and dark) mass. Though very instructive, studying the total density profile leaves open questions on what the detailed structure of the mass profile is. Different mass profiles could give rise to the same value of γ' when fitted with a power-law model. Massive ETGs have a slope close to $\gamma' \approx 2$. Models in which the mass follows the light correspond to steeper slopes ($\gamma' \approx 2.3$). In order to get $\gamma' = 2$ there must be a non-stellar (dark) component with a mean slope shallower than isothermal. We want to disentangle the contribution of the dark component to the mass distribution of our lenses from that of the stars. For this purpose, we consider mass models with two components: a stellar spheroid and a dark matter halo. We model the stellar spheroid with a de Vaucouleurs profile with effective radius fixed to the observed one, and a uniform prior on the stellar mass-to-light ratio. The dark matter halo is modeled with a generalized Navarro, Frenk & White (gNFW) profile (Zhao 1996):

$$\rho_{\mathrm{DM}}(r) \propto \frac{1}{r^{\gamma_{\mathrm{DM}}}(1 + r/r_s)^{3-\gamma_{\mathrm{DM}}}}. \tag{5.1}$$

Both components are spherical. We fix the effective radius of the stellar component to the observed one, and the scale radius of the dark matter is fixed to $r_s = 10R_{\mathrm{e}}$, which is a typical value seen in numerical simulations (e.g. Kravtsov 2013). The impact of this choice on our inference will be discussed at the end of this Section. This mass model has three degrees of freedom, which we describe in terms of the stellar mass M_*, the projected dark matter mass within a cylinder of $5\,\mathrm{kpc}$ radius M_{DM5}, and the inner slope of the dark matter halo γ_{DM}. We fit this model to the observed Einstein radius and central velocity
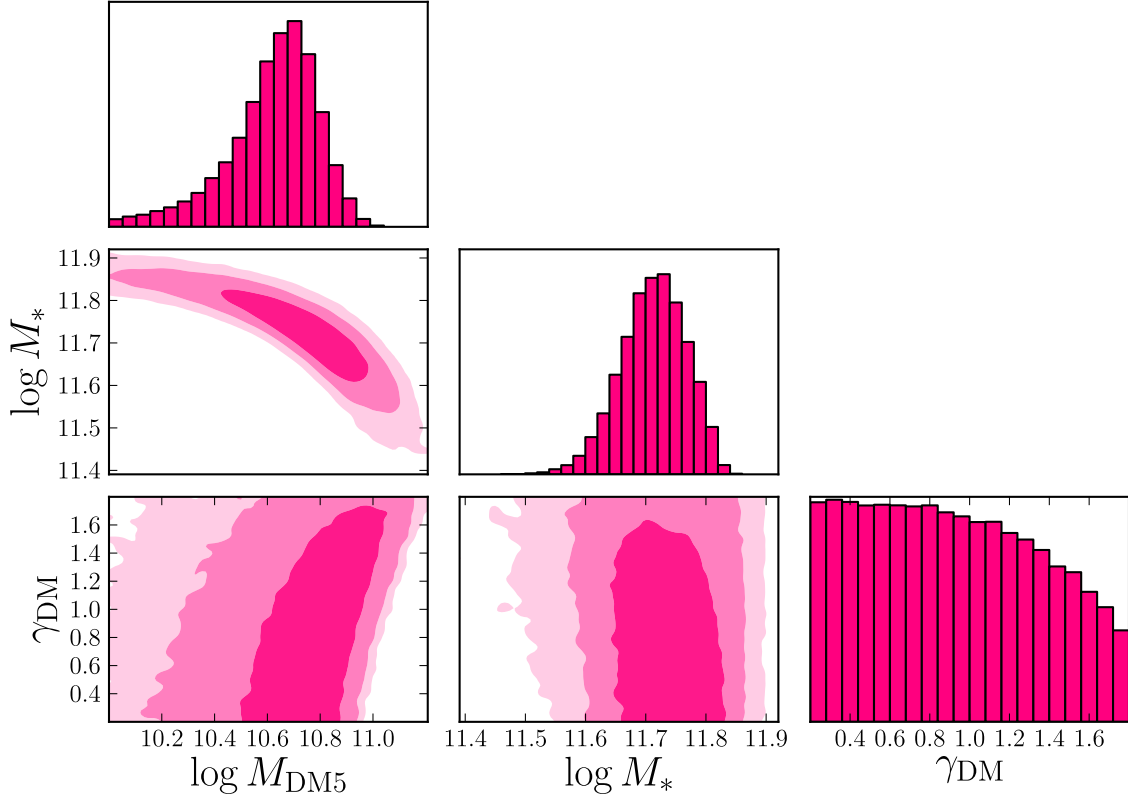
Figure 5.1: Posterior probability distribution for a de Vaucouleurs + gNFW mass model of the gravitational lens SL2SJ142059+563007. The model parameters are the total stellar mass M_*, the inner slope of the dark matter halo $\gamma_{\rm DM}$ and the projected dark matter mass $M_{\rm DM5}$ enclosed within a cylinder of 5 kpc radius.

dispersion with the same procedure used in Paper IV. Model Einstein radii are calculated given M_*, $M_{\rm DM5}$ and $\gamma_{\rm DM}$ assuming spherical profiles, and model velocity dispersions are calculated through the spherical Jeans equation assuming isotropic orbits. The fit is done in a Bayesian framework, assuming a uniform prior on $\log M_*$, $\log M_{\rm DM5}$ and $\gamma_{\rm DM}$, and restricting the range of possible values for the latter quantity to $0.2 < \gamma_{\rm DM} < 1.8$. Note that this is very similar to the "free" model adopted by (Cappellari et al. 2012).

As an example, we show in Figure 5.1 the posterior probability distribution function of the model parameters for the lens SL2SJ142059+563007. The model is largely un-

constrained, since it consists of three free parameters that are fit to only two pieces of data: the Einstein radius and the central velocity dispersion. As expected and observed by previous authors (e.g. Treu & Koopmans 2002a,b), there is a strong degeneracy between the inner slope and normalization of the dark matter component. The tilt of this degeneracy is determined in part by our choice of parametrizing the dark matter halo in terms of the mass enclosed within 5 kpc. This is not directly observable, while the mass enclosed within the Einstein radius is better constrained by the data. For the lens in this example, the Einstein radius is larger than 5 kpc, therefore for fixed dark matter mass within R_{Ein}, the inferred mass at 5 kpc will depend on the assumed value of the dark matter slope. Nevertheless, 5 kpc is close in value to the median Einstein radius of the lenses considered in this work and the choice of M_{DM5} to parametrize the dark matter mass will prove useful later in this work, when analyzing the entire set of lenses statistically.

For systems with data of exceptional quality, the degeneracy between dark matter mass and slope can be broken without having to make additional assumptions (e.g. Sonnenfeld et al. 2012). In our work, we do not wish to constrain γ_{DM} and M_{DM5} for individual systems, but we measure their *population average* values by statistically combining measurements over a large number of lenses. This will be the subject of Sections 5.2, 5.4 and 5.5. Nevertheless, it is interesting to constrain the dark matter content and the stellar mass of individual lenses. This can be done, provided we make a more restrictive assumption on the shape of the dark matter halo. We do this by fixing the inner slope of the dark matter halo to $\gamma_{\mathrm{DM}} = 1$ and hence restrict ourselves to NFW density profiles for the rest of this section. The free parameters of the model are now

the stellar mass M_* and the normalization of the dark matter halo, M_{DM5}. The model is very similar to the one used by Treu et al. (2010). The only difference lies in the choice of the scale radius of the NFW component, r_s. In Treu et al. (2010) this was fixed to 30 kpc, while here we fix it to ten times the effective radius of the stellar component.

We fit this model to the lensing and stellar kinematics data of each one of the SL2S lenses, as well as lenses from the SLACS survey. Our two component model, with a de Vaucouleurs spheroid and an NFW dark matter halo, provides excellent fits to most of our lenses. The only exceptions are a few SLACS lenses with very steep density slope $\gamma' > 2.2$, i.e. with relatively large velocity dispersions for their Einstein radius (similar to PG1115+080 Treu & Koopmans 2002b). In the context of our model, a steep density slope corresponds to a larger ratio between stellar and dark matter mass, since the NFW halo has a much shallower density profile than a de Vaucouleurs profile at the scale relevant for our measurements, i.e. at the effective radius. The steepest density profile we can construct with such a two component model is a galaxy with no dark matter. For these few SLACS lenses, even if we assign the entire mass enclosed within the Einstein radius to the spheroid, the model velocity dispersion is still smaller than the measured one, although consistent within the uncertainty. A perfect match with the data would require $\gamma_{\mathrm{DM}} > 2$, excluded by our prior. The inference then favors small dark matter masses for those systems. Adopting a more flexible model for the stellar density profile does not help in this case: Posacki et al. (2014) did a similar spheroid and halo decomposition to the same SLACS lenses considered here using a multigaussian fit to the photometry, and still found very small dark matter fractions for some of the objects.

The derived model parameters for the SL2S lenses are reported in Table 5.1. The

147

parameters considered are the stellar mass, M_*, the projected dark matter mass enclosed within 5 kpc, M_{DM5}, the projected dark matter mass enclosed within R_{e}, M_{DMe}, the fraction of dark matter mass projected within a cylinder of radius R_{e}, f_{DMe}, and finally the *IMF mismatch parameter* (Treu et al. 2010), defined as the ratio between the true stellar mass and its estimate based on stellar population synthesis models assuming a Salpeter IMF, $M_*^{\mathrm{(SPS)}}$:

$$\alpha_{\mathrm{IMF}} \equiv \frac{M_*}{M_*^{\mathrm{(SPS)}}}. \tag{5.2}$$

In this parametrization, a Chabrier IMF corresponds to $\log \alpha_{\mathrm{IMF}} \approx -0.25$. Individual measurements of the IMF mismatch parameter and the dark matter fraction are plotted as a function of redshift in Figures 5.2 and 5.3. Under the above assumptions and with typical data quality, we are able to determine dark matter masses with a $\sim 50\%$ precision on individual objects. We recall that the values reported are obtained by assuming a fixed ratio between scale radius of the dark matter halo and effective radius of the light distribution, $r_s = 10 R_{\mathrm{e}}$. Decreasing the value of the proportionality constant to $r_s = 5 R_{\mathrm{e}}$ results in dark matter masses smaller by ~ 0.10 dex and stellar masses larger by ~ 0.05 dex. We use these values as an estimate of the systematic uncertainty introduced by fixing the value of the dark matter scale radius. The systematic uncertainty introduced by fixing the dark matter slope is only moderately larger, as can be deduced from Figure 5.1.

Most of the individual measurements of the IMF normalization are consistent with a Salpeter IMF. There are however a few outliers in the measurements shown in Figure 5.2. This is because the values of α_{IMF} plotted in Figure 5.2 are obtained by marginalizing over the dark matter mass. The actual probability distributions in the $\alpha_{\mathrm{IMF}} - M_{\mathrm{DM5}}$
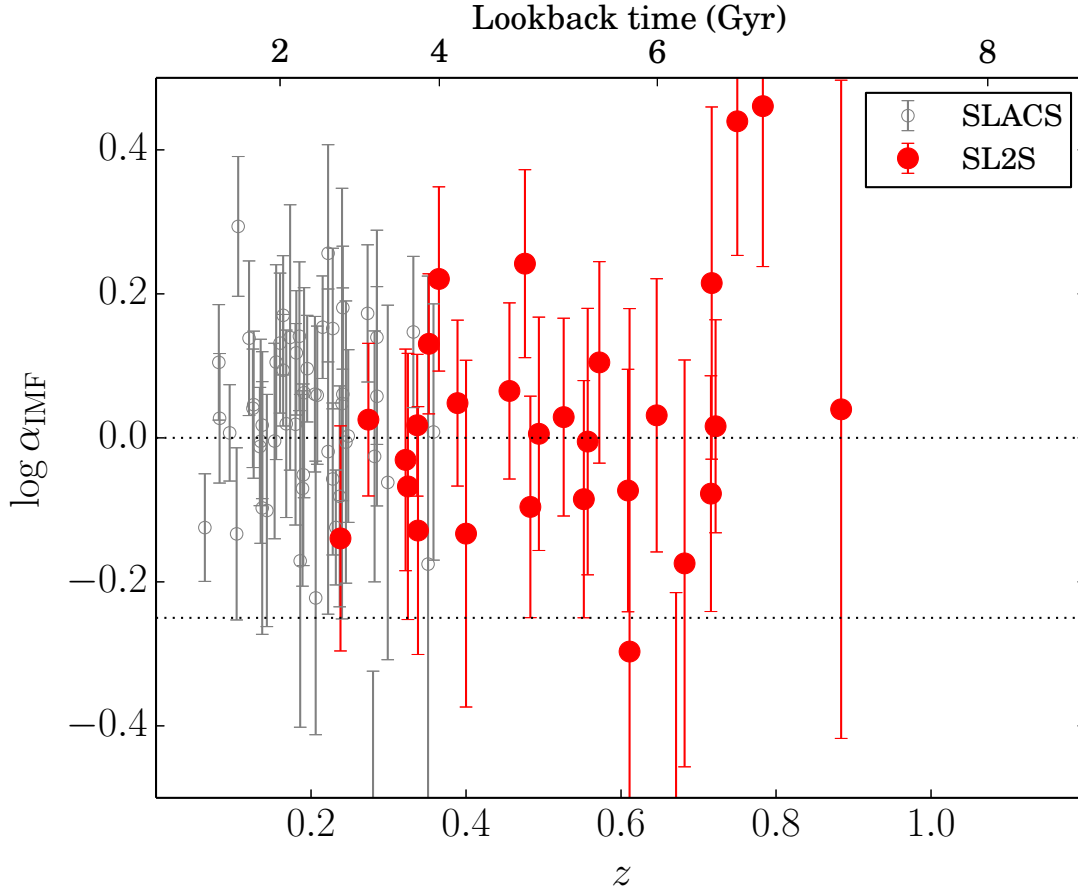
Figure 5.2: IMF mismatch parameter $\alpha_{\mathrm{IMF}} = M_*/M_*^{(\mathrm{Salp})}$, referred to a Salpeter IMF, as a function of redshift for galaxies of the SL2S, SLACS and LSD samples.

space are very elongated and extend closer to the value $\log \alpha_{\mathrm{IMF}} = 0$ than the marginalized posterior would suggest. The strong degeneracy between stellar and dark matter mass is taken fully into account in the population analysis described in the next Section.

5.2 Hierarchical Bayesian Inference

As shown above, the lensing and stellar kinematics data available for typical strong lenses are not sufficient to constrain both the slope and the normalization of the dark

Name	z	$R_{\rm e}$ (kpc)	$\log M_*^{\rm Salp}$ $M_\odot$	$\log M_*^{\rm LD}$ $M_\odot$	$\log \alpha_{\rm IMF}$	$\log M_{\rm DM5}$ $M_\odot$	$\log M_{\rm DMe}$ $M_\odot$	$f_{\rm DMe}$
SL2SJ020524$-$093023	0.56	4.82	11.52 ± 0.12	$11.54^{+0.08}_{-0.11}$	-0.01 ± 0.18	$10.41^{+0.37}_{-0.29}$	$10.38^{+0.37}_{-0.29}$	$0.12^{+0.17}_{-0.06}$
SL2SJ021247$-$055552	0.75	8.92	11.45 ± 0.17	$11.90^{+0.06}_{-0.09}$	0.44 ± 0.19	$10.63^{+0.23}_{-0.37}$	$11.05^{+0.23}_{-0.37}$	$0.22^{+0.15}_{-0.12}$
SL2SJ021325$-$074355	0.72	17.67	11.97 ± 0.19	$12.21^{+0.12}_{-0.18}$	0.21 ± 0.25	$11.04^{+0.11}_{-0.17}$	$11.96^{+0.11}_{-0.17}$	$0.54^{+0.16}_{-0.17}$
SL2SJ021411$-$040502	0.61	6.29	11.60 ± 0.14	$11.54^{+0.08}_{-0.10}$	-0.07 ± 0.17	$11.16^{+0.05}_{-0.06}$	$11.32^{+0.05}_{-0.06}$	$0.55^{+0.08}_{-0.08}$
SL2SJ021737$-$051329	0.65	4.27	11.53 ± 0.16	$11.57^{+0.09}_{-0.12}$	0.03 ± 0.19	$11.06^{+0.09}_{-0.11}$	$10.95^{+0.09}_{-0.11}$	$0.33^{+0.12}_{-0.09}$
SL2SJ021801$-$080247	0.88	7.90	11.54 ± 0.14	$11.75^{+0.16}_{-0.53}$	0.04 ± 0.46	$10.93^{+0.33}_{-0.52}$	$11.26^{+0.33}_{-0.52}$	$0.39^{+0.43}_{-0.28}$
SL2SJ021902$-$082934	0.39	3.01	11.50 ± 0.10	$11.56^{+0.04}_{-0.07}$	0.05 ± 0.12	$10.48^{+0.29}_{-0.30}$	$10.13^{+0.29}_{-0.30}$	$0.07^{+0.08}_{-0.03}$
SL2SJ022046$-$094927	0.57	3.45	11.36 ± 0.11	$11.49^{+0.05}_{-0.10}$	0.11 ± 0.14	$10.48^{+0.30}_{-0.30}$	$10.23^{+0.30}_{-0.30}$	$0.10^{+0.12}_{-0.05}$
SL2SJ022511$-$045433	0.24	8.59	11.81 ± 0.09	$11.67^{+0.12}_{-0.13}$	-0.14 ± 0.15	$11.08^{+0.11}_{-0.20}$	$11.47^{+0.11}_{-0.20}$	$0.55^{+0.13}_{-0.18}$
SL2SJ022610$-$042011	0.49	6.44	11.73 ± 0.11	$11.76^{+0.09}_{-0.13}$	0.01 ± 0.16	$10.82^{+0.23}_{-0.48}$	$10.99^{+0.23}_{-0.48}$	$0.25^{+0.18}_{-0.17}$
SL2SJ023251$-$040823	0.35	4.78	11.36 ± 0.09	$11.50^{+0.03}_{-0.04}$	0.13 ± 0.10	$10.22^{+0.25}_{-0.15}$	$10.19^{+0.25}_{-0.15}$	$0.09^{+0.07}_{-0.03}$
SL2SJ023307$-$043838	0.67	9.21	11.71 ± 0.13	$11.17^{+0.28}_{-0.51}$	-0.63 ± 0.41	$11.35^{+0.02}_{-0.04}$	$11.79^{+0.02}_{-0.04}$	$0.89^{+0.07}_{-0.09}$
SL2SJ084847$-$035103	0.68	3.21	11.24 ± 0.16	$11.09^{+0.19}_{-0.23}$	-0.18 ± 0.28	$11.18^{+0.09}_{-0.15}$	$10.87^{+0.09}_{-0.15}$	$0.55^{+0.16}_{-0.19}$
SL2SJ084909$-$041226	0.72	3.55	11.63 ± 0.13	$11.65^{+0.07}_{-0.08}$	0.02 ± 0.15	$11.00^{+0.11}_{-0.16}$	$10.76^{+0.11}_{-0.16}$	$0.20^{+0.08}_{-0.07}$
SL2SJ084959$-$025142	0.27	6.11	11.52 ± 0.09	$11.56^{+0.03}_{-0.06}$	0.03 ± 0.10	$10.33^{+0.31}_{-0.22}$	$10.47^{+0.31}_{-0.22}$	$0.14^{+0.14}_{-0.05}$
SL2SJ085019$-$034710	0.34	1.35	11.14 ± 0.09	$11.16^{+0.03}_{-0.04}$	0.02 ± 0.10	$10.25^{+0.23}_{-0.18}$	$9.39^{+0.23}_{-0.18}$	$0.03^{+0.03}_{-0.01}$
SL2SJ085540$-$014730	0.36	3.48	11.11 ± 0.10	$11.35^{+0.05}_{-0.10}$	0.22 ± 0.13	$10.50^{+0.27}_{-0.34}$	$10.25^{+0.27}_{-0.34}$	$0.14^{+0.13}_{-0.08}$
SL2SJ090407$-$005952	0.61	16.81	11.55 ± 0.12	$11.35^{+0.33}_{-0.61}$	-0.30 ± 0.48	$11.21^{+0.05}_{-0.09}$	$12.09^{+0.05}_{-0.09}$	$0.92^{+0.06}_{-0.11}$
SL2SJ095921$+$020638	0.55	3.47	11.28 ± 0.11	$11.24^{+0.05}_{-0.14}$	-0.09 ± 0.16	$10.45^{+0.33}_{-0.31}$	$10.20^{+0.33}_{-0.31}$	$0.15^{+0.19}_{-0.08}$
SL2SJ135949$+$553550	0.78	13.08	11.41 ± 0.15	$11.91^{+0.09}_{-0.13}$	0.46 ± 0.22	$10.74^{+0.21}_{-0.36}$	$11.44^{+0.21}_{-0.36}$	$0.41^{+0.19}_{-0.22}$
SL2SJ140454$+$520024	0.46	11.78	12.10 ± 0.10	$12.17^{+0.07}_{-0.07}$	0.07 ± 0.12	$11.08^{+0.08}_{-0.11}$	$11.69^{+0.08}_{-0.11}$	$0.40^{+0.09}_{-0.09}$
SL2SJ140546$+$524311	0.53	4.58	11.67 ± 0.11	$11.71^{+0.08}_{-0.09}$	0.03 ± 0.14	$10.80^{+0.15}_{-0.27}$	$10.74^{+0.15}_{-0.27}$	$0.18^{+0.09}_{-0.09}$
SL2SJ140650$+$522619	0.72	4.35	11.60 ± 0.15	$11.52^{+0.07}_{-0.07}$	-0.08 ± 0.17	$11.06^{+0.08}_{-0.10}$	$10.96^{+0.08}_{-0.10}$	$0.35^{+0.08}_{-0.08}$
SL2SJ141137$+$565119	0.32	3.04	11.28 ± 0.09	$11.29^{+0.05}_{-0.13}$	-0.03 ± 0.16	$10.56^{+0.32}_{-0.35}$	$10.21^{+0.32}_{-0.35}$	$0.14^{+0.18}_{-0.08}$
SL2SJ142059$+$563007	0.48	7.86	11.76 ± 0.10	$11.68^{+0.11}_{-0.14}$	-0.10 ± 0.16	$10.85^{+0.16}_{-0.25}$	$11.17^{+0.16}_{-0.25}$	$0.38^{+0.17}_{-0.16}$
SL2SJ220329$+$020518	0.40	3.86	11.26 ± 0.10	$11.17^{+0.14}_{-0.21}$	-0.13 ± 0.24	$11.30^{+0.03}_{-0.04}$	$11.12^{+0.03}_{-0.04}$	$0.64^{+0.11}_{-0.10}$
SL2SJ220506$+$014703	0.48	3.93	11.51 ± 0.10	$11.76^{+0.07}_{-0.09}$	0.24 ± 0.13	$10.76^{+0.19}_{-0.38}$	$10.60^{+0.19}_{-0.38}$	$0.12^{+0.09}_{-0.07}$
SL2SJ221326$-$000946	0.34	2.41	10.99 ± 0.10	$10.88^{+0.11}_{-0.15}$	-0.13 ± 0.17	$11.06^{+0.06}_{-0.07}$	$10.57^{+0.06}_{-0.07}$	$0.49^{+0.12}_{-0.10}$
SL2SJ222148$+$011542	0.33	5.27	11.55 ± 0.09	$11.51^{+0.13}_{-0.18}$	-0.07 ± 0.19	$10.88^{+0.19}_{-0.34}$	$10.92^{+0.19}_{-0.34}$	$0.34^{+0.20}_{-0.19}$

Table 5.1: Redshifts, effective radii, stellar masses from SPS fitting (from Paper III) and from lensing and dynamics, projected dark matter masses within 5 kpc and within the effective radius, projected dark matter fractions within the effective radius of SL2S lenses.
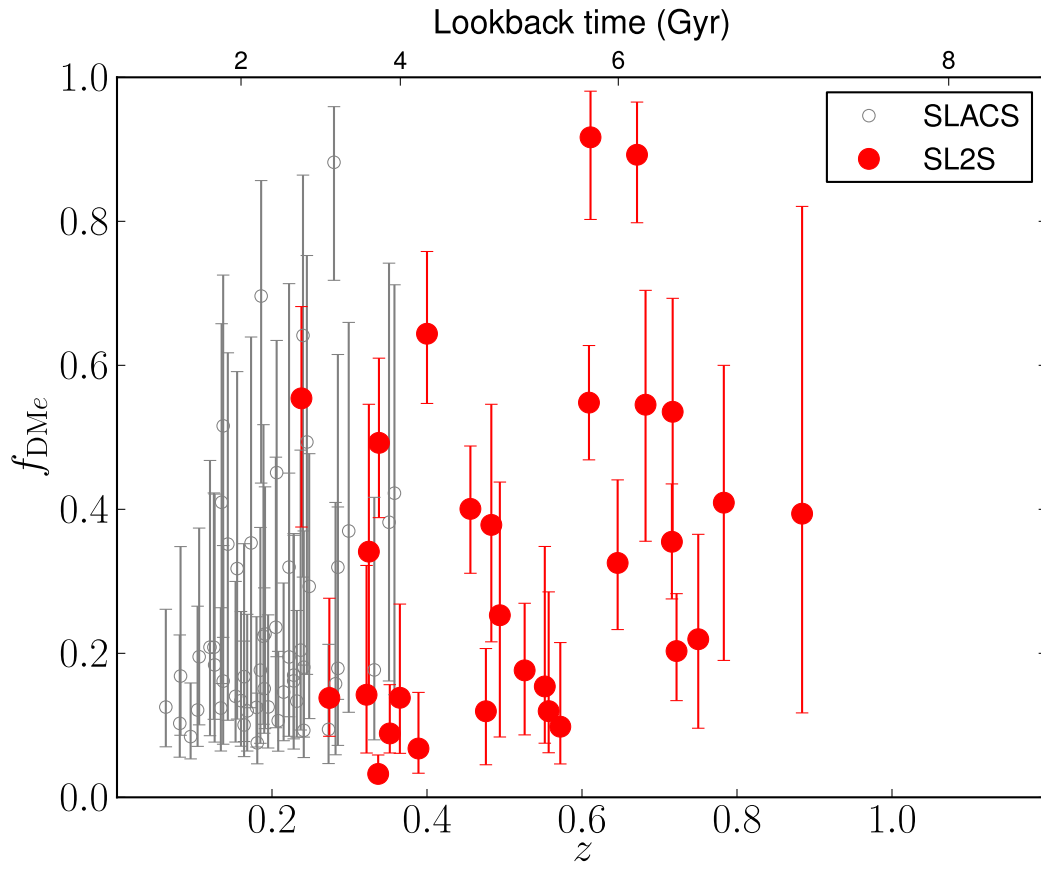
Figure 5.3: Fraction of mass in dark matter projected within a cylinder of radius equal to the effective radius, as a function of redshift.

matter halo of individual objects. An important question is whether the IMF normalization or the dark matter fraction evolve with time within the population of ETGs. One possible way of addressing this question is performing a linear fit for $\alpha_{\mathrm{IMF}}(z)$ and $f_{\mathrm{DM}e}(z)$. However, the analysis of Paper IV revealed that the density slope γ' of ETGs is a function of mass and size as well as redshift. This dependency of γ' on M_* and R_{e} will presumably be reflected on α_{IMF} or $f_{\mathrm{DM}e}$. It is then important to take all dependencies into account when addressing the time evolution of these two parameters.

We want to characterize the population of early-type galaxies which our strong lenses are drawn from. The focus is on the stellar mass, the IMF normalization, the dark matter mass within 5 kpc and the inner dark matter slope. Our lenses span a range of redshifts, stellar masses and sizes and we are interested to measure whether there are structural variations with these quantities. In analogy to the work of Paper IV, the strategy we adopt is a hierarchical Bayesian inference method. We assume that the values of the parameters describing individual galaxies, $\boldsymbol{\omega}_i$, are drawn from a parent distribution described by a set of hyper-parameters $\boldsymbol{\tau}$ to be determined from the data $\mathbf{d}$. From Bayes theorem,

$$\mathrm{Pr}(\boldsymbol{\tau}|\mathbf{d}) \propto \mathrm{Pr}(\mathbf{d}|\boldsymbol{\tau})\mathrm{Pr}(\boldsymbol{\tau}). \tag{5.3}$$

In turn, the probability of observing the data $\mathbf{d}$ given the population model $\boldsymbol{\tau}$ can be written as the following product over the individual objects' marginal distributions:

$$\mathrm{Pr}(\mathbf{d}|\boldsymbol{\tau}) = \prod_i^N \int d\boldsymbol{\omega}_i \mathrm{Pr}(\mathbf{d}_i|\boldsymbol{\omega}_i)\mathrm{Pr}(\boldsymbol{\omega}_i|\boldsymbol{\tau}). \tag{5.4}$$

The integrals run over all the parameters of individual galaxies $\boldsymbol{\omega}_i$. The first term in the product of Equation 5.4 is the likelihood function for an individual galaxy's model

152

parameters $\boldsymbol{\omega}_i$ given the data $\mathbf{d}_i$. The set of model parameters for an individual galaxy is $\boldsymbol{\omega}_i = (M_{*,i}, M_{\mathrm{DM5},i}, \gamma_{\mathrm{DM},i}, \alpha_{\mathrm{IMF},i}, z_i, R_{\mathrm{e},i})$, where M_{DM5} is the dark matter mass within the effective radius. The data consist of the measured Einstein radius $R_{\mathrm{Ein},i}$, effective radius, redshift, velocity dispersion within the aperture used for spectroscopic observations $\sigma_{\mathrm{ap},i}$ and the stellar mass measured with the stellar population synthesis analysis, $M_{*,i}^{(\mathrm{SPS})}$. In order to speed up computations, redshifts and effective radii of all lenses are assumed to be known exactly. This approximation does not introduce any significant uncertainty since the typical precision on effective radii measurements is 10% (Sonnenfeld et al. 2013a), which corresponds to a small uncertainty on the key model parameters, and the uncertainty on redshifts is $\delta z = 0.001$. The likelihood of observing data $\mathbf{d}_i$ for lens i, given its parameters $\boldsymbol{\omega}_i$ can be factorized as follows:

$$
\begin{aligned}
\Pr(\mathbf{d}_i|\boldsymbol{\omega}_i) = \quad & \Pr(R_{\mathrm{Ein},i}|\boldsymbol{\omega}_i)\Pr(\sigma_{\mathrm{ap},i}|\boldsymbol{\omega}_i) \times \\
& \Pr(M_{*,i}^{(\mathrm{SPS})}|\boldsymbol{\omega}_i)\delta(R_{\mathrm{eff},i}^{(\mathrm{obs})} - R_{\mathrm{e},i})\delta(z_i^{(\mathrm{obs})} - z_i) \quad (5.5)
\end{aligned}
$$

This is possible because the observational uncertainties on the measured Einstein radius, velocity dispersion and SPS stellar mass are independent of each other. For some lenses in the SL2S sample, more than one velocity dispersion measurements is available (Sonnenfeld et al. 2013b). In those cases, the velocity dispersion term in Equation 5.5 becomes a product over the multiple measurements.

The second term in the integrand of (5.4) is the probability for the galaxy's individual stellar mass and halo mass given the set of hyper-parameters $\boldsymbol{\tau}$. The hyper-parameters must describe the population of galaxies from which our strong lenses are drawn. Similarly to Paper IV, we assume that the structural properties of ETGs, in this case the

153

dark matter mass and the IMF normalization, are a function of redshift, stellar mass and effective radius. In the formalism of Kelly (2007),

$$\boldsymbol{\xi}_i = \{z_i, M_{*,i}, R_{\mathrm{e},i}\} \tag{5.6}$$

are the independent variables, while

$$\boldsymbol{\eta}_i = \{M_{\mathrm{DM5},i}, \gamma_{\mathrm{DM},i}, \alpha_{\mathrm{IMF},i}\} \tag{5.7}$$

are the dependent variables. It is useful to distinguish among the hyper-parameters the ones that describe the distribution in the independent variables, $\boldsymbol{\psi}$, and those describing the distribution of dependent variables, which we label as $\boldsymbol{\theta}$, following the notation of Kelly (2007). The quantity $\mathrm{Pr}(\boldsymbol{\omega}_i|\boldsymbol{\tau})$ has then the following form:

$$\mathrm{Pr}(\boldsymbol{\omega}_i|\boldsymbol{\tau}) = \mathrm{Pr}(\boldsymbol{\xi}_i|\boldsymbol{\psi})\mathrm{Pr}(\boldsymbol{\eta}_i|\boldsymbol{\xi}_i, \boldsymbol{\theta}), \tag{5.8}$$

where $\boldsymbol{\omega}_i = \boldsymbol{\xi}_i \cup \boldsymbol{\eta}_i$ and $\boldsymbol{\tau} = \boldsymbol{\psi} \cup \boldsymbol{\theta}$. The probability distribution of the independent variables describes how galaxies in our sample are distributed in the $\{z, M_*, R_{\mathrm{e}}\}$ space. It encodes both information on the distribution of galaxies in the Universe and the way lens candidates are targeted in our lensing surveys, in terms of selections in stellar mass (or similarly, luminosity), redshift and size. We assume that the distribution in the independent variables can be written as the product of two Gaussians in $\log M_*$ and $\log R_{\mathrm{e}}$:

$$\mathrm{Pr}(\boldsymbol{\xi}_i|\boldsymbol{\psi}) =$$
$$\frac{1}{\sigma_*\sqrt{2\pi}} \exp\left[-\frac{(\log M_{*,i} - \mu_*(\boldsymbol{\omega}_i))^2}{2\sigma_*^2}\right] \times$$
$$\frac{1}{\sigma_R\sqrt{2\pi}} \exp\left[-\frac{(\log R_{\mathrm{e},i} - \mu_R(\boldsymbol{\omega}_i))^2}{2\sigma_R^2}\right]. \tag{5.9}$$

The mean of these Gaussians is assumed to be different for lenses of different surveys:

$$\mu_*^{(\text{SL2S})} = \zeta_*^{(\text{SL2S})}(z_i - 0.5) + \log \mu_{*,0}^{(\text{SL2S})}, \tag{5.10}$$

$$\mu_*^{(\text{SLACS})} = \zeta_*^{(\text{SLACS})}(z_i - 0.2) + \log \mu_{*,0}^{(\text{SLACS})}, \tag{5.11}$$

$$\mu_R^{(\text{SL2S})} = \zeta_R^{(\text{SL2S})}(z_i - 0.5) + \beta_R^{(\text{SL2S})}(\log M_* - 11.5) +$$
$$\log \mu_{R,0}^{(\text{SL2S})}, \tag{5.12}$$

$$\mu_R^{(\text{SLACS})} = \zeta_R^{(\text{SLACS})}(z_i - 0.2) + \beta_R^{(\text{SLACS})}(\log M_* - 11.5)$$
$$+ \log \mu_{R,0}^{(\text{SLACS})}. \tag{5.13}$$

We also assume different values of the dispersion σ_*, σ_R for SL2S and SLACS lenses. Note that there's no explicit term for the distribution in z in Equation 5.9. This is equivalent to assuming a uniform distribution in redshift. The more physically relevant quantity is the second term in Equation 5.8, which describes the properties of the dark matter halos and stellar IMF for galaxies of given z, M_* and R_{e}. The goal of this work is to understand the properties of massive galaxies, irrespective of their lens nature. However, some galaxies are more likely to be strong lenses than others, because the lensing probability depends in part on the density profile (Mandelbaum et al. 2009). Moreover, some strong lenses are more easily detectable than others, as discussed for example by Arneson et al. (2012); Smith & Lucey (2013); Gavazzi et al. (2014). Then, in order to make accurate statements on the evolution on galaxies based on strong lensing measurements, we must take into account these selection effects. It is important to verify whether the selection of lenses in the SLACS or SL2S surveys introduce a significant bias with respect to the general

population of ETGs, and to quantify it. The term $\Pr(\boldsymbol{\eta}_i|\boldsymbol{\xi}_i, \boldsymbol{\theta})$ should then include a term taking into account the probability for a galaxy described by parameters $\boldsymbol{\eta}_i$ of being a strong lens detected in a survey. We describe such probability with a set of hyper-parameters $\boldsymbol{\lambda}$. The term relative to the dependent variables is then also assumed to be product of Gaussians, multiplied by a selection function term $\mathcal{S}(\boldsymbol{\eta}_i|\boldsymbol{\xi}_i, \boldsymbol{\lambda})$:

$$
\begin{aligned}
\Pr(\boldsymbol{\eta}_i|\boldsymbol{\xi}_i, \boldsymbol{\theta}, \boldsymbol{\lambda}) = \mathcal{S}(\boldsymbol{\eta}_i|\boldsymbol{\xi}_i, \boldsymbol{\lambda}) \times \\
\frac{1}{\sigma_{\mathrm{DM}}\sqrt{2\pi}} \exp\left[-\frac{(\log M_{\mathrm{DM5},i} - \mu_{\mathrm{DM}}(\boldsymbol{\xi}_i))^2}{2\sigma_{\mathrm{DM}}^2}\right] \times \\
\frac{1}{\sigma_{\gamma}\sqrt{2\pi}} \exp\left[-\frac{(\gamma_{\mathrm{DM},i} - \mu_{\gamma}(\boldsymbol{\xi}_i))^2}{2\sigma_{\gamma}^2}\right] \times \\
\frac{1}{\sigma_{\mathrm{IMF}}\sqrt{2\pi}} \exp\left[-\frac{(\log \alpha_{\mathrm{IMF},i} - \mu_{\mathrm{IMF}}(\boldsymbol{\xi}_i))^2}{2\sigma_{\mathrm{IMF}}^2}\right] \times \\
\mathcal{S}(\boldsymbol{\eta}_i|\boldsymbol{\xi}_i, \boldsymbol{\lambda}).
\end{aligned}
\tag{5.14}
$$

The term $\mathcal{S}(\boldsymbol{\eta}_i|\boldsymbol{\xi}_i, \boldsymbol{\lambda})$, which will be discussed in Section 5.3, represents the lensing selection function. This term multiplies the intrinsic distribution of galaxy parameters, which we assumed to be described by a product of Gaussians, to give the distribution observed in strong lenses. Note that a similar decomposition could in principle be written for the distribution in the independent variables, $\Pr(\boldsymbol{\xi}_i|\boldsymbol{\psi})$. In practice, we are interested in recovering the true distribution for the dependent variables only. The means of the Gaussians in Equation 5.14 are in general functions of galaxy redshift, stellar mass and effective radius. In particular, we expect the dark matter mass to grow with the stellar mass. We also expect the ratio between stellar and dark mass and the dark matter slope to vary with projected stellar mass density, $\Sigma_* = M_*/(2\pi R_{\mathrm{e}}^2)$, as the results of Paper IV highlighted how the density profile of ETGs at fixed redshift depends to first order on Σ_*, with systems with more compact stellar distributions having steeper density slopes.

We then choose to parametrize the scaling relations of dark matter halo and stellar IMF normalization in terms of M_* and Σ_*, as follows:

$$\mu_{\mathrm{DM}} = \quad \zeta_{\mathrm{DM}}(z_i - 0.3) + \beta_{\mathrm{DM}}(\log M_{*,i} - 11.5) +$$

$$\xi_{\mathrm{DM}} \log \Sigma_*/\Sigma_0 + \log M_{\mathrm{DM},0} \tag{5.15}$$

$$\mu_\gamma = \quad \gamma_0 \tag{5.16}$$

$$\mu_{\mathrm{IMF}} = \quad \zeta_{\mathrm{IMF}}(z_i - 0.3) + \beta_{\mathrm{IMF}}(\log M_* - 11.5) +$$

$$\xi_{\mathrm{IMF}} \log \Sigma_*/\Sigma_0 + \log \alpha_{\mathrm{IMF},0} \tag{5.17}$$

Although it might seem more natural to assume a scaling in M_* and R_{e}, which would isolate the dependence on stellar mass to only one parameter, M_* and R_{e} are highly correlated because of the observed tight mass-size relation. As a result, dependences on M_* or R_{e} are highly interchangeable and it is difficult to isolate the two with our data. A parameterization in terms of M_* and Σ_* mitigates this effect. For the average dark matter slope we do not allow for any scaling with any independent variable. This choice is driven by the little information available from our data on the slope for an individual galaxy (see Figure 5.1). Allowing for too much freedom would result in the average slope of the population of galaxies being undetermined. As always, when the likelihood is not very informative, it is important to choose very carefully the model parameters and priors. To summarize, the set of hyper-parameters describing the distribution of independent variables is

$$\boldsymbol{\psi} = \{\zeta_*, \mu_{*,0}, \sigma_*, \zeta_R, \beta_R, \mu_{R,0}, \sigma_R\}, \tag{5.18}$$

157

with each parameter defined separately for the distribution of SL2S and SLACS lenses, while the hyper-parameters describing the dependent variables distribution is

$$\boldsymbol{\theta} = \quad \{\zeta_{\mathrm{DM}}, \beta_{\mathrm{DM}}, \xi_{\mathrm{DM}}, M_{\mathrm{DM},0}, \sigma_{\mathrm{DM}}, \gamma_0, \sigma_\gamma,$$

$$\zeta_{\mathrm{IMF}}, \beta_{\mathrm{IMF}}, \xi_{\mathrm{IMF}}, \alpha_{\mathrm{IMF},0}, \sigma_{\mathrm{IMF}}, \boldsymbol{\lambda}\}. \tag{5.19}$$

Finally, we need to specify the form of the selection function correction $\mathcal{S}(\boldsymbol{\eta}_i|\boldsymbol{\xi}_i, \boldsymbol{\lambda})$ in Equation 5.14. The following section is devoted to it.

5.3   The selection function

With the term "selection function" we define the mapping between the global population of ETGs and the subset of the population sampled by our lens catalogs. The goal of this section is to characterize this selection function in a both accurate and computationally tractable way. SL2S and SLACS, from which our lenses are chosen, are different lensing surveys and are in general subject to different selection effects. Nevertheless, selection effects for the SL2S and SLACS surveys are qualitatively similar, and will be treated within the same framework.

We can identify three main sources of selection. The first one is the brightness of the lens. Both SLACS and SL2S samples were assembled by following-up massive ETGs, brighter than a threshold. For the subset of SLACS galaxies we are considering, the lower limit to the brightness was implicitly set by the requirement of the lens galaxy being targeted in the SDSS spectroscopic survey and having sufficient S/N to allow for a velocity dispersion measurement (citation needed). For SL2S, only ETGs brighter than 21.5 in i-band were followed-up (Gavazzi et al. 2014). While the luminosity function of

ETGs is well described by a one or two Schechter functions (Ilbert et al. 2013), selection in brightness results in a different luminosity function for strong lenses, with a cut at low luminosities. Luminosity is not directly parametrized in the model described in Section 5.2, but it is tightly related to the stellar mass. This selection effect can then be captured by the parameters describing the distribution in stellar mass in equations (5.10) and (5.11).

The second selection effect is due to different lenses having different strong lensing cross-sections, X_{lens}, i.e. different probability of producing systems of multiple images of background sources. Mandelbaum et al. (2009) studied in detail how lensing cross-section depends on lens properties. As expected from general lensing theory, their main finding is that galaxy mass and density profile are the most important parameters determining X_{lens}: more massive galaxies have larger lensing cross-section, and so do galaxies with a steeper density profile, at fixed mass. Quantitatively, the probability of a galaxy described by parameters $\boldsymbol{\omega}_i$ of being a strong lens is proportional to $X_{\mathrm{lens}}(\boldsymbol{\omega}_i)$. Therefore, the term $\mathcal{S}(\boldsymbol{\eta}_i|\boldsymbol{\xi}_i, \boldsymbol{\lambda})$ in Equation 5.14, which is proportional to the probability of detecting a lens of parameters $\boldsymbol{\omega}_i$ given a selection function described by $\boldsymbol{\lambda}$, should also be proportional to X_{lens}. The strong lensing cross-section of a lens with a smooth density profile monotonically decreasing with radius is given by the area enclosed by the radial caustic, i.e. the points in the source plane mapped to points of infinite magnification in the radial direction. For simplicity, we calculate $X_{\mathrm{lens}}(\boldsymbol{\omega}_i)$ assuming spherical symmetry, as the area enclosed within the radial critical curve, unlike the tangential critical curve, is not very sensitive to the ellipticity of the lens. Formally, the term X_{lens} has units of solid angle. In practice, X_{lens} is rescaled so that the probability $\mathrm{Pr}(\boldsymbol{\eta}_i|\boldsymbol{\xi}_i, \boldsymbol{\theta}, \boldsymbol{\lambda})$ defined

in Equation 5.14 integrated over $\boldsymbol{\eta}_i$ is normalized to unity. The third selection effect that we consider is the different detectability of strong lenses of different properties in the two surveys considered, i.e. the probability, given a strong lens, of detecting it in a given lensing survey. The detection probability in the SL2S was studied by Gavazzi et al. (2014), while that in SLACS-like surveys was studied by Arneson et al. (2012). The most obvious parameter determining the detection probability is the brightness of the lensed background source: brighter arcs are easier to detect for both the SL2S and SLACS surveys. In addition to the source brightness, another important parameter determining the detection probability in both SL2S and SLACS is the Einstein radius. Gavazzi et al. (2014) have shown how the selection function for SL2S lenses is mostly a function of R_{Ein}, with a peak in the range $1'' < R_{\mathrm{Ein}} < 3''$. SL2S lenses are selected photometrically by looking for blue arcs around red galaxy in ground based observations (Gavazzi et al. 2012). This technique works best for lenses with Einstein radius larger than $\sim 1''$, since arcs with R_{Ein} smaller than that are difficult to resolve in ground based photometry. The upper limit is due to the fact that lenses with radius smaller than $3''$ were preferentially targeted in the lens-finding algorithm, to favor galaxy-scale lenses over group-scale ones. For SLACS, lens candidates were selected by looking for emission lines from lensed star-forming galaxies, and then confirmed by HST imaging. Lenses with too small Einstein radii are more difficult to confirm with this method, because of confusion between the source and the deflector light. At the opposite end, lenses with too large Einstein radii can escape the selection because the lensed features contribute little to the flux deposited within the $1''\!.5$-radius fiber used by SDSS spectroscopic observations. This description matches qualitatively the findings of Arneson et al. (2012). The results of Arneson et al.

(2012) cannot be directly applied to our analysis though, because the lens models considered by them have power-law density profiles, different from the two-component profiles adopted here. We summarize these properties instead by approximating the detection probability with a Gaussian function in R_{Ein}, which multiplies the previously discussed lensing cross-section term in the selection correction:

$$\mathcal{S}(\boldsymbol{\eta}_i|\boldsymbol{\xi}_i, \boldsymbol{\lambda}) = \frac{A X_{\mathrm{lens}}}{\sqrt{2\pi}\sigma_{\mathrm{sel}}} \exp\left\{ -\frac{(R_{\mathrm{Ein}}(\boldsymbol{\omega}_i) - R_{\mathrm{sel}})^2}{2\sigma_{\mathrm{sel}}} \right\} \tag{5.20}$$

where R_{Ein} is a function of the lens parameters $\boldsymbol{\omega}_i$ and A is a normalization constant. Here $\boldsymbol{\lambda} = \{R_{\mathrm{sel}}, \sigma_{\mathrm{sel}}\}$ are hyper-parameters describing the selection function, which can be different for SL2S and SLACS surveys. Note that there is no source brightness term in Equation 5.20, which we anticipated being important in determining the detection probability of a strong lens. This is because the source brightness is not directly modeled in the hierarchical Bayesian inference framework introduced in the previous section. The term Equation 5.20 should then be considered as the effective selection function, obtained by marginalizing over all possible values of the source brightness. To illustrate what a selection function of the form given by Equation 5.20 corresponds to in terms of stellar and dark matter mass, we show in Figure 5.4 how the Einstein radius of a typical lens changes as a function of M_* and M_{DM5}, the other parameters being fixed. A Gaussian selection function in the Einstein radius implies that only lenses that occupy a band in the $\log M_* - \log M_{\mathrm{DM5}}$ plane can be observed. In the same plot we show the lensing cross-section depends on M_* and M_{DM5}. As expected, larger masses correspond to larger lensing cross-sections.
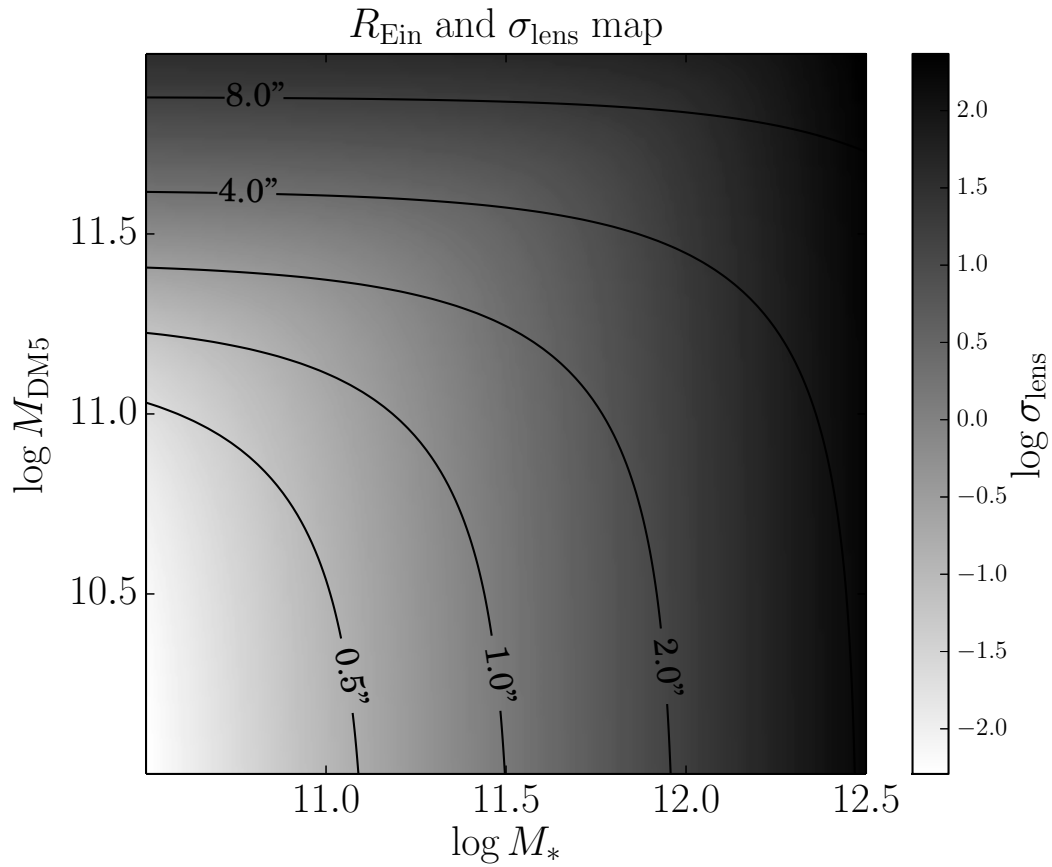
Figure 5.4: *Solid lines:* levels of constant angular Einstein radius (in arcsec) as a function of $\log M_*$ and $\log M_{\mathrm{DM5}}$ for a lens at redshift $z_d = 0.3$, with source redshift $z_s = 1.5$, effective radius $R_{\mathrm{e}} = 5\mathrm{kpc}$ and $\gamma_{\mathrm{DM}} = 1$. *Intensity map:* logarithm of the strong lensing cross section, X_{lens} in arcsec^2.

5.4 Results, NFW halos

Before proceeding to analyze the most general case, we focus in this section on models with a fixed dark matter slope $\gamma_{\rm DM} = 1$, corresponding to an NFW profile. This will indicate whether we can get an adequate description of the evolution of the structure of massive galaxies with a simple dark matter model. We need to explore the posterior probability distribution $\Pr(\boldsymbol{\tau}|\mathbf{d})$ via Markov Chain Monte Carlo (MCMC). This requires evaluating, for each lens and at each step of the chain, the likelihood term $\Pr(\mathbf{d}_i|\boldsymbol{\omega}_i)$ given by Equation 5.5 and integrating over all possible values of the lens parameters $\boldsymbol{\omega}_i$, as given by Equation 5.4. The integration over $\log \alpha_{\rm IMF}$ can be performed analytically, because both the likelihood Equation 5.5 and the parent distribution Equation 5.14 are Gaussian in $\log \alpha_{\rm IMF}$. Integrals over z and $\log R_{\rm e}$ are trivial, because lens redshift and effective radius are assumed to be known exactly. We are left with two-dimensional integrals over $\log M_*$ and $\log M_{\rm DM5}$. This is a computationally expensive operation, because M_* and $M_{\rm DM5}$ enter the likelihood and the selection function term $\mathcal{S}(\boldsymbol{\eta}_i|\boldsymbol{\xi}_i, \boldsymbol{\lambda})$ through the Einstein radius and the velocity dispersion, which are in general non-analytic functions of these parameters. In order to speed up the computation, we sample the likelihood term beforehand for each galaxy and then perform the integrals in Equation 5.4 via Monte Carlo integration at each step of the chain, evaluating the integrand by importance sampling (see e.g. Suyu et al. 2010; Busha et al. 2011, and references therein). For both computational and physical reasons (our lenses have a finite amount of stars and dark matter), we truncate the distribution Equation 5.14 between 10.5 and 12.5 in $\log M_*$ and between 10.0 and 12.0 in $\log M_{\rm DM5}$. In order to be self-consistent, at each step of the

chain all probability terms must be normalized to unity. The term $\Pr(\boldsymbol{\eta}_i|\boldsymbol{\xi}_i, \boldsymbol{\theta})$ requires particular care, as it contains a term, $\mathcal{S}$, that is non-analytic in the model parameters. The following equality should hold

$$\int d\boldsymbol{\eta}_i \Pr(\boldsymbol{\eta}_i|\boldsymbol{\xi}_i, \boldsymbol{\theta}) = 1 \tag{5.21}$$

for each set of values of $\boldsymbol{\xi}_i$ and $\boldsymbol{\theta}$. This is an implicit equation for the normalization constant in Equation 5.14, which we solve via Monte Carlo integration.

We assume a uniform prior on all model hyper-parameters. We sample the posterior probability distribution with an MCMC with 100000 points, using PyMC (Patil et al. 2010). The median, 16th and 84th percentile of the posterior probability distribution function (PDF) of each parameter, marginalized over the other parameters, are listed in Table 5.2. The inference on the hyper-parameters describing the dependent variables ($M_{\rm DM5}$ and $\alpha_{\rm IMF}$), $\boldsymbol{\xi}$, is plotted in Figures 5.5 and 5.6.

The parameters explored by this model are numerous. Among the results of this analysis we highlight the following. *Under the assumption that dark matter halos of all ETGs have an NFW profile:*

- The average projected dark matter mass within 5 kpc in massive ETGs is $\log M_0 = 10.80^{+0.14}_{-0.11}$.

- We find marginal evidence for an anticorrelation between dark matter mass enclosed within 5 kpc ($M_{\rm DM5}$) and stellar mass density Σ_* (parameter $\xi_{\rm DM} < 0$), as well as a correlation between $M_{\rm DM5}$ and redshift (parameter $\zeta_{\rm DM} < 0$). No strong correlations between central dark matter mass and stellar mass is detected (parameter $\beta_{\rm DM}$ is consistent with zero).

	With $\mathcal{S}$	No $\mathcal{S}$	Parameter description
$\mu_{*,0}^{(\mathrm{SL2S})}$	$11.53^{+0.06}_{-0.06}$	$11.54^{+0.06}_{-0.06}$	Mean stellar mass at $z = 0.5$, SL2S sample
$\zeta_{*}^{(\mathrm{SL2S})}$	$0.46^{+0.32}_{-0.29}$	$0.42^{+0.31}_{-0.30}$	Linear dependence of mean stellar mass on redshift, SL2S sample
$\sigma_{*}^{(\mathrm{SL2S})}$	$0.27^{+0.05}_{-0.04}$	$0.27^{+0.05}_{-0.04}$	Scatter in mean stellar mass, SL2S sample
$\mu_{*,0}^{(\mathrm{SLACS})}$	$11.66^{+0.03}_{-0.04}$	$11.67^{+0.03}_{-0.03}$	Mean stellar mass at $z = 0.2$, SLACS sample
$\zeta_{*}^{(\mathrm{SLACS})}$	$2.40^{+0.39}_{-0.41}$	$2.42^{+0.36}_{-0.41}$	Linear dependence of mean stellar mass on redshift, SLACS sample
$\sigma_{*}^{(\mathrm{SLACS})}$	$0.24^{+0.03}_{-0.02}$	$0.23^{+0.03}_{-0.02}$	Scatter in mean stellar mass, SLACS sample
$\mu_{R,0}^{(\mathrm{SL2S})}$	$0.69^{+0.04}_{-0.03}$	$0.68^{+0.04}_{-0.03}$	Mean effective radius at $z = 0.5$, $\log M_* = 11.5$, SL2S sample
$\zeta_{R}^{(\mathrm{SL2S})}$	$0.26^{+0.21}_{-0.18}$	$0.25^{+0.22}_{-0.16}$	Linear dependence of mean effective radius on redshift, SL2S sample
$\beta_{R}^{(\mathrm{SL2S})}$	$0.65^{+0.13}_{-0.14}$	$0.70^{+0.13}_{-0.13}$	Linear dependence of mean effective radius on stellar mass, SL2S sample
$\sigma_{R}^{(\mathrm{SL2S})}$	$0.17^{+0.03}_{-0.03}$	$0.16^{+0.03}_{-0.02}$	Scatter in mean effective radius, SL2S sample
$\mu_{R,0}^{(\mathrm{SLACS})}$	$0.71^{+0.01}_{-0.01}$	$0.70^{+0.01}_{-0.01}$	Mean effective radius at $z = 0.2$, $\log M_* = 11.5$, SLACS sample
$\zeta_{R}^{(\mathrm{SLACS})}$	$0.09^{+0.16}_{-0.18}$	$0.02^{+0.16}_{-0.19}$	Linear dependence of mean effective radius on redshift, SLACS sample
$\beta_{R}^{(\mathrm{SLACS})}$	$0.61^{+0.04}_{-0.05}$	$0.65^{+0.05}_{-0.04}$	Linear dependence of mean effective radius on stellar mass, SLACS sample
$\sigma_{R}^{(\mathrm{SLACS})}$	$0.07^{+0.01}_{-0.01}$	$0.07^{+0.01}_{-0.01}$	Scatter in mean effective radius, SLACS sample
ζ_{DM}	$0.57^{+0.44}_{-0.43}$	$0.94^{+0.25}_{-0.24}$	Linear dependence of $\log M_{\mathrm{DM5}}$ on redshift.
β_{DM}	$0.10^{+0.27}_{-0.24}$	$-0.10^{+0.19}_{-0.19}$	Linear dependence of $\log M_{\mathrm{DM5}}$ on $\log M_*$.
ξ_{DM}	$-0.57^{+0.27}_{-0.24}$	$-0.27^{+0.18}_{-0.19}$	Linear dependence of $\log M_{\mathrm{DM5}}$ on $\log \Sigma_*$
$\log M_{\mathrm{DM,0}}$	$10.78^{+0.14}_{-0.11}$	$10.63^{+0.06}_{-0.07}$	Mean M_{DM5} at $z = 0.3$, $\log M_* = 11.5$, $R_{\mathrm{eff}} = 5$ kpc
σ_{DM}	$0.29^{+0.08}_{-0.06}$	$0.23^{+0.04}_{-0.04}$	Scatter in the M_{DM5} distribution
ζ_{IMF}	$-0.05^{+0.06}_{-0.09}$	$-0.06^{+0.06}_{-0.09}$	Linear dependence of IMF normalization on redshift.
β_{IMF}	$0.22^{+0.04}_{-0.05}$	$0.18^{+0.05}_{-0.05}$	Linear dependence of IMF normalization on $\log M_*$.
ξ_{IMF}	$0.08^{+0.06}_{-0.06}$	$0.04^{+0.07}_{-0.06}$	Linear dependence of IMF normalization on $\log \Sigma_*$
$\log \alpha_{\mathrm{IMF,0}}$	$0.04^{+0.01}_{-0.01}$	$0.05^{+0.02}_{-0.01}$	Mean IMF normalization at $z = 0.3$, $\log M_* = 11.5$, $R_{\mathrm{eff}} = 5$ kpc
σ_{IMF}	$0.01^{+0.02}_{-0.01}$	$0.02^{+0.02}_{-0.01}$	Scatter in the IMF normalization distribution
$R_{\mathrm{sel}}^{(\mathrm{SL2S})}$	$1.28^{+0.28}_{-0.20}$	$\cdots$	Mean observable Einstein radius, SL2S sample
$\sigma_{\mathrm{sel}}^{(\mathrm{SL2S})}$	$0.61^{+0.18}_{-0.13}$	$\cdots$	Dispersion in observable Einstein radius, SL2S sample
$R_{\mathrm{sel}}^{(\mathrm{SLACS})}$	$0.95^{+0.16}_{-0.24}$	$\cdots$	Mean observable Einstein radius, SLACS sample
$\sigma_{\mathrm{sel}}^{(\mathrm{SLACS})}$	$0.20^{+0.10}_{-0.06}$	$\cdots$	Dispersion in observable Einstein radius, SLACS sample

Table 5.2: NFW model. Median, 16th and 84th percentile of the posterior probability distribution function of each model hyper-parameter, marginalized over the other parameters. Results are reported for the full case and ignoring the selection function.

$$\log M_{\text{DM5}} = \zeta_{\text{DM}}(z - 0.3) + \beta_{\text{DM}}(\log M_* - 11.5) + \xi_{\text{DM}} \log \Sigma_*/\Sigma_0 + \log M_0 + N(0, \sigma_{M_{\text{DM}}})$$
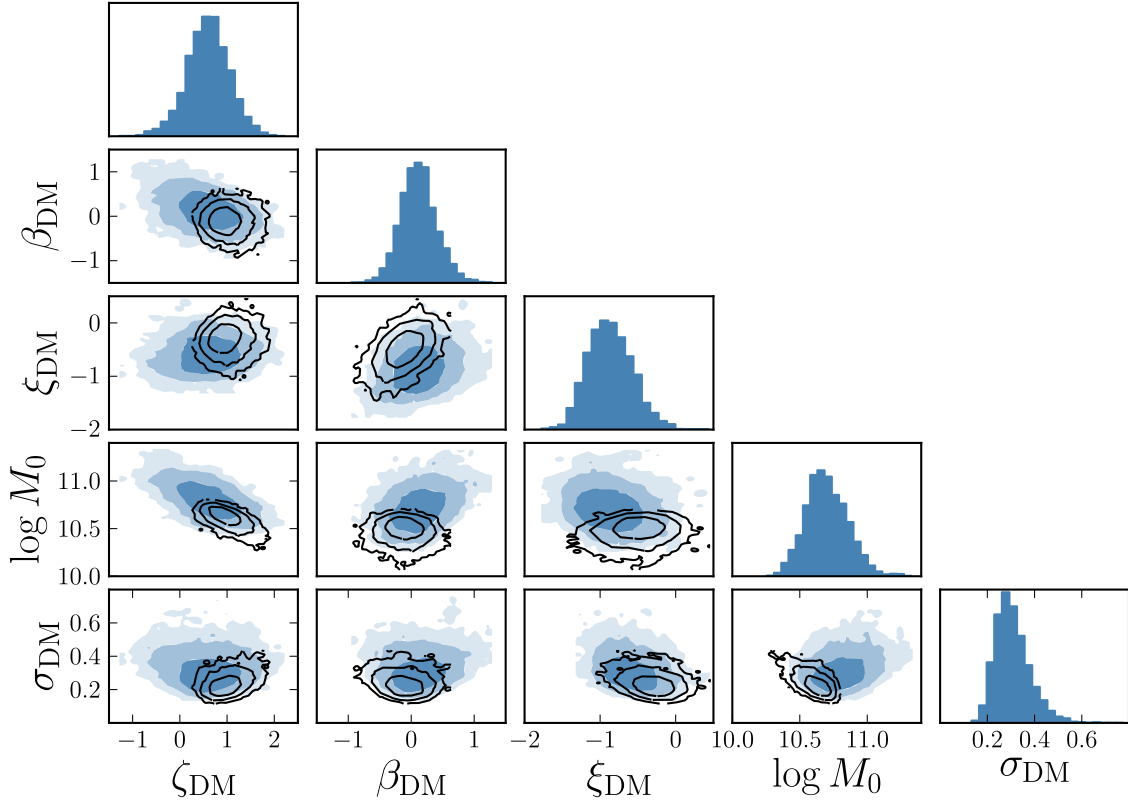
Figure 5.5: Model hyper-parameters describing the dark matter mass within a shell of radius r_{eff}. *Empty contours:* inference with no selection function term. *Filled contours:* including the selection function term. The different levels represent the 68%, 95% and 99.7% enclosed probability regions.

$$\log \alpha_{\mathrm{IMF}} = \zeta_{\mathrm{IMF}}(z - 0.3) + \beta_{\mathrm{IMF}}(\log M_* - 11.5) + \xi_{\mathrm{IMF}} \log \Sigma_* / \Sigma_0 + \log \alpha_{\mathrm{IMF},0} + N(0, \sigma_{\mathrm{IMF}})$$
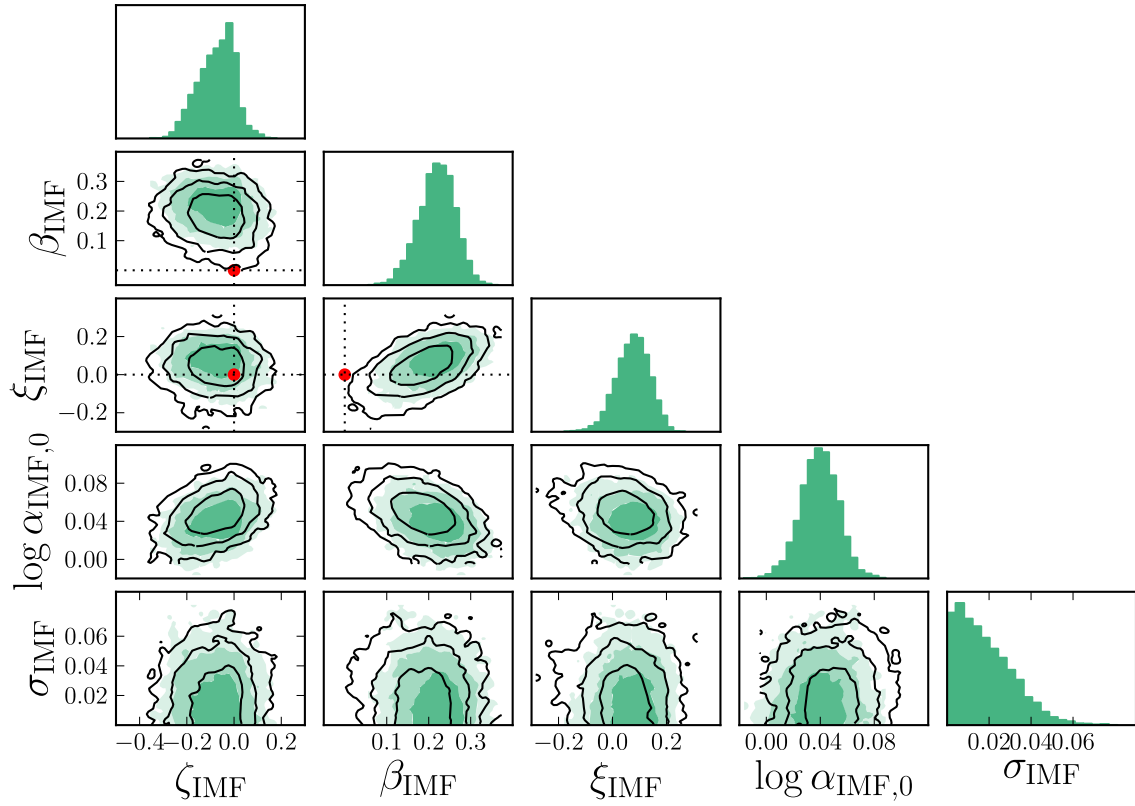
Figure 5.6: IMF parameters. The red dots indicate the parameter values corresponding to a universal IMF. *Empty contours:* inference with no selection function term. *Filled contours:* including the selection function term.

- The IMF normalization is consistent with an IMF slightly heavier than Salpeter: $\log \alpha_{\mathrm{IMF},0} = 0.04 \pm 0.02$.

- The IMF normalization correlates positively with stellar mass ($\beta_{\mathrm{IMF}} = 0.21 \pm 0.05$). No correlation with redshift or stellar mass density is detected.

In order to illustrate the effect of the selection function term $\Pr(\boldsymbol{\omega}_i|\boldsymbol{\lambda})$, we also show the posterior PDF obtained excluding it from our analysis. Such model without the selection function correction strictly describes the population of strong lenses used in our analysis, as opposed to the general population of massive ETGs. The posterior PDF of the model without the selection function term is consistent with the more sophisticated model taking into account selection effects. Nevertheless, the inferred properties of the dark matter halos are slightly different in the two cases. By not accounting for the selection function we detect a strong dependence of the dark matter mass with redshift, as the parameter ζ_{DM} is larger than zero with more than $3-\sigma$ significance for this model (empty contours in Figure 5.5). A positive value of ζ_{DM} means that lenses at lower redshift have preferentially smaller dark matter masses than lenses at higher redshift. At the same time, the average dark matter mass at the reference point $z = 0.3$, $\log M_* = 11.5$, $\Sigma_* = \Sigma_0$ is smaller with respect to the full analysis: $\log M_0 = 10.62^{+0.08}_{-0.10}$. Given the nature of our strong lens sample, with lenses from the SLACS survey dominating the low-redshift part of the sample and SL2S lenses populating the high-redshift end, this result implies that SLACS lenses have on average smaller dark matter masses than similar lenses at higher redshift. Since the trend in redshift of M_{DM5} is greatly reduced when selection effects are taken into account, this suggests that the lower dark matter masses

measured for SLACS lenses is not necessarily related to an intrinsic difference between ETGs at low and intermediate redshift, but might just be the result of the SLACS survey selecting preferentially lenses in smaller dark matter halos. We further investigated this aspect by repeating the analysis for SLACS and SL2S lenses separately, with and without the selection function term. We confirmed that the SLACS sample is more sensitive to selection effects. In particular it is the Einstein radius selection term of Equation 5.20 that drives the offset between the model with $\Pr(\boldsymbol{\omega}_i|\boldsymbol{\lambda})$ and the one without. According to our model, the detection efficiency in the SLACS survey, which we fit directly for, is a Gaussian in R_{Ein} with mean $R_{\mathrm{sel}} = 0.96^{+0.15}_{-0.21}$ and dispersion $\sigma_{\mathrm{sel}} = 0.20^{+0.10}_{-0.06}$. This is a peaked function in R_{Ein} that favors the detection of lenses with smaller Einstein radii and therefore smaller dark matter masses.

We chose to parametrize the dark matter content with the dark matter mass projected within 5 kpc. Many studies, both observational and theoretical, focus instead on the mass enclosed within the effective radius, $M_{\mathrm{DM}e}$. For a better comparison with the literature it is then useful to check what our results imply for this quantity. As we show in Appendix 5.8.1, $M_{\mathrm{DM}e}$ increases with M_* with a power smaller than unity and has a strong anti-correlation with stellar mass density, meaning that ETGs are not homologous systems.

5.4.1 Evolution of individual objects

The above analysis reveals how key quantities of massive ETGs scale with redshift, stellar mass and stellar mass density. In order to gain a better understanding of the evolution of ETGs, it is useful to consider the evolution of individual objects along their

evolutionary tracks. In a fluid kinematics analogy, we would like to transition from an Eulerian description of the fields M_{DM5} and α_{IMF} at fixed M_*, z and R_{e}, which is given by the analysis presented above, to a Lagrangian description of the evolution of these quantities along the history of individual galaxies. While the latter quantity is not directly observable, it can be inferred with the formalism introduced in Paper IV, which connects the observed scaling relations with external constraints on the evolution of size and stellar mass. We denote with d/dz the derivative with respect to redshift along the evolutionary track of an individual galaxy. Then we can write

$$
\begin{aligned}
\frac{d \log M_{\mathrm{DM5}}}{dz} = {} & \frac{\partial \log M_{\mathrm{DM5}}}{\partial z} + \frac{\partial \log M_{\mathrm{DM5}}}{\partial \log M_*} \frac{d \log M_*}{dz} + \\
& \frac{\partial \log M_{\mathrm{DM5}}}{\partial \log \Sigma_*} \frac{d \log \Sigma_*}{dz}
\end{aligned}
\tag{5.22}
$$

and

$$
\begin{aligned}
\frac{d \log \alpha_{\mathrm{IMF}}}{dz} = {} & \frac{\partial \log M_{\mathrm{DM5}}}{\partial z} + \frac{\partial \log M_{\mathrm{DM5}}}{\partial \log M_*} \frac{d \log M_*}{dz} + \\
& \frac{\partial \log \alpha_{\mathrm{IMF}}}{\partial \log \Sigma_*} \frac{d \log \Sigma_*}{dz}.
\end{aligned}
\tag{5.23}
$$

This is the evolution in M_{DM5} and α_{IMF} of a galaxy for which these quantities scale with z, M_* and Σ_* in the same way as the population averages μ_{DM} and μ_{IMF}. The presence of scatter will in general modify the picture, but we expect the above expressions to be correct to first order. Equations 5.22 and 5.23 hold as long as the population of ETGs is not significantly polluted by the formation of new objects that enter the sample in the redshift range that we consider. Current estimates show that the number density of massive galaxies evolves very modestly below redshift 1 (Cassata et al. 2013; Ilbert et al. 2013; Muzzin et al. 2013).

The partial derivatives in Equation 5.22 can be identified with the parameters ζ_{DM}, β_{DM} and ξ_{DM} measured in our analysis, while those in Equation 5.23 are matched to ζ_{IMF}, β_{IMF} and ξ_{IMF}. The two total derivatives, $d\log M_*/dz$ and $d\log\Sigma_*/dz$ are the rate of change in stellar mass and stellar mass density of an individual galaxy. The latter depends on the former, and on the evolution of the effective radius as well:

$$\frac{d\log\Sigma_*}{dz} = \frac{d\log M_*}{dz} - 2\frac{d\log R_{\mathrm{e}}}{dz}. \qquad (5.24)$$

As in Paper IV, we can evaluated $d\log R_{\mathrm{e}}/dz$ by combining constraints from the redshift and mass dependence of R_{e}, assuming again that individual galaxies evolve in the same way as the average:

$$\frac{d\log R_{\mathrm{e}}}{dz} = \frac{\partial\log R_{\mathrm{e}}}{\partial z} + \frac{\partial\log R_{\mathrm{e}}}{\partial\log M_*}\frac{d\log M_*}{dz}. \qquad (5.25)$$

For the scaling of effective radius with mass, we take the value measured by Newman et al. (2012a): $\partial\log R_{\mathrm{e}}/\partial\log M_* = 0.59\pm0.07$. The redshift dependence has been measured by a number of authors (e.g. Damjanov et al. 2011; Newman et al. 2012a; Cimatti et al. 2012; Huertas-Company et al. 2013), with significant scatter between the measurements. Here we take $\partial\log R_{\mathrm{e}}/\partial z$ to be the mean between these measurements, and use the standard deviation as an estimate of its uncertainty: $\partial\log R_{\mathrm{e}}/\partial z = -0.37\pm0.08$. With this prescription we evaluate the derivatives Equation 5.22 and Equation 5.23, which we plot in Figure 5.7 as a function of the, unknown, mass growth rate $d\log M_*/dz$. The uncertainties on the derived evolution of enclosed dark matter and IMF normalization are relatively large, in part due to the uncertainty on the mass-size relation and its evolution. We expect the dark matter enclosed within 5 kpc to exhibit little change over time, since most of the matter accreted in the later phases of the evolution of an ETGs will likely
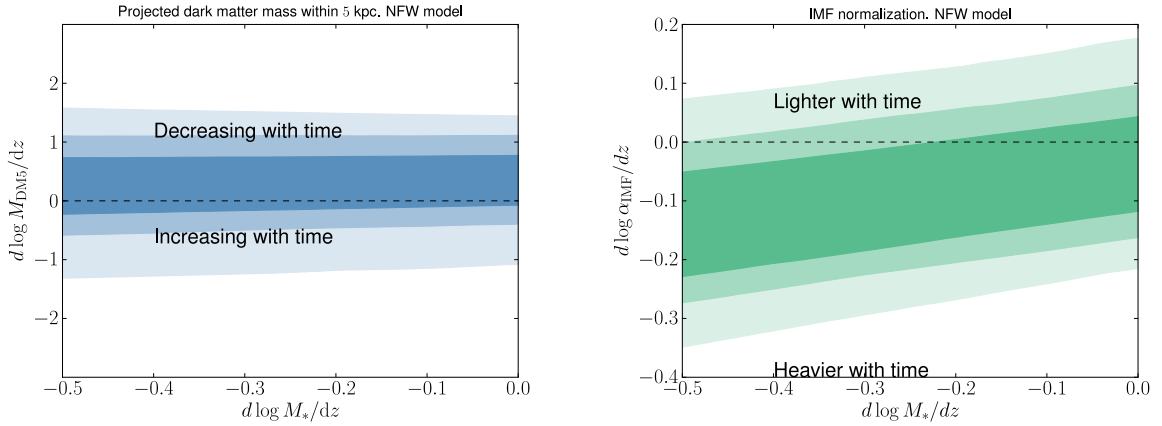
Figure 5.7: *Left panel:* Rate of change in projected dark matter enclosed within a cylinder of radius 5 kpc along the evolutionary track of an individual galaxy, calculated from Equation 5.22, as a function of the growth rate in stellar mass. *Right panel:* Rate of change in the IMF normalization along the evolutionary track of an individual galaxy, calculated from Equation 5.23, as a function of the growth rate in stellar mass. An NFW profile for the dark matter halo is assumed. The different colors represent the 68%, 95% and 99% probability regions.
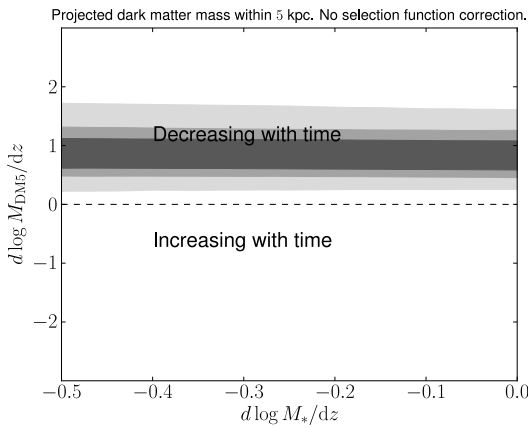
Figure 5.8: Rate of change in projected dark matter enclosed within a cylinder of radius 5 kpc along the evolutionary track of an individual galaxy, calculated from Equation 5.22, as a function of the growth rate in stellar mass, inferred ignoring the selection function term. An NFW profile for the dark matter halo is assumed. The different colors represent the 68%, 95% and 99% probability regions.

grow the outskirts of the galaxy. We also expect the IMF normalization to show little change over time, because a significant change of the IMF would require the accretion or formation of stars with an extremely different IMF from the preexisting population, a scenario at odds with our current knowledge of stellar populations in the Universe. Our measurements are consistent with these expectations, though with the current data we are unable to make precise statements in this regard.

In Figure 5.8 we plot the evolution in dark matter mass inferred from the population model without the selection function term – that is to say, assuming that the strong lenses from both the SL2S and SLACS survey are an unbiased sample of the general population of early-type galaxies. Under this assumption, the data require dark matter masses to *decrease with time* at a significant rate, with more than 3-σ confidence, in sharp contrast with the result plotted in Figure 5.7, which does take the selection function into account. It is difficult to imagine a physical scenario in which the stellar mass increases by a modest amount while at the same time a comparable, or larger, amount of dark matter is ejected from the inner 5 kpc of a galaxy. We believe that the implausible scenario of Figure 5.8 is an indication that the selection function does indeed need to be included in the modeling. (However, as we will show below, the lack of selection function modeling in our previous work does not actually affect the conclusions of papers I-IV.)

5.5 Results, free inner slope

The results of the analysis presented in Section 5.4 depend on the assumption of a fixed NFW shape for the dark matter profile of all ETGs. Here we relax that assumption and

consider gNFW profiles instead, with density profile given by Equation 5.1. We impose that individual values of the inner dark matter slope lie in the range $0.2 < \gamma_{\rm DM} < 1.8$, as we expect the dark matter density profile to be shallower than the total density profile, which is measured to be close to isothermal ($\gamma' \approx 2$ Koopmans et al. 2006). As pointed out in Section 5.1, allowing for one extra degree of freedom in the dark matter halo model results in a significant degeneracy in the determination of the properties of individual galaxies. However, we know that ETGs constitute a family of objects with rather homogeneous characteristics. The large number of available lenses therefore can help us break the degeneracy and pin down the population average properties of the luminous and dark matter distributions. In particular, the tilt of the degeneracy contour between the dark matter mass within 5 kpc and the inner slope, plotted in Figure 5.1 for one of the SL2S lenses, depends on the value of the Einstein radius: the data constrain the projected mass enclosed within $R_{\rm Ein}$ and the value of $M_{\rm DM5}$ is obtained by extrapolating the Einstein mass to 5 kpc assuming a value of $\gamma_{\rm DM}$. Different lenses have different values of $R_{\rm Ein}$, therefore the direction of the degeneracy contour between $M_{\rm DM5}$ and $\gamma_{\rm DM}$ will be different for each lens, depending on the amount of extrapolation required to match the mass at 5 kpc from the mass at $R_{\rm Ein}$. If the scatter in $M_{\rm DM5}$ across the population of massive ETGs is small, then it is possible to rule out extreme values of the dark matter slope by simply multiplying the probability distribution for individual lenses, which is what our hierarchical Bayesian model effectively does.

The posterior PDF for the parameters describing the population distribution of dark matter halos and IMF normalizations is plotted in Figure 5.9 and Figure 5.10, while the median and 68% confidence interval is listed in Table 5.3 for all the inferred parameters.

174

$$\gamma_{DM} = \gamma_0 + N(0, \sigma_\gamma) \quad ; \quad \log M_{DM} = \zeta_{DM}(z - 0.3) + \beta_{DM}(\log M_* - 11.5) + \xi_{DM} \log \Sigma_*/\Sigma_0 + \log M_0 + N(0, \sigma_{M_{DM}})$$
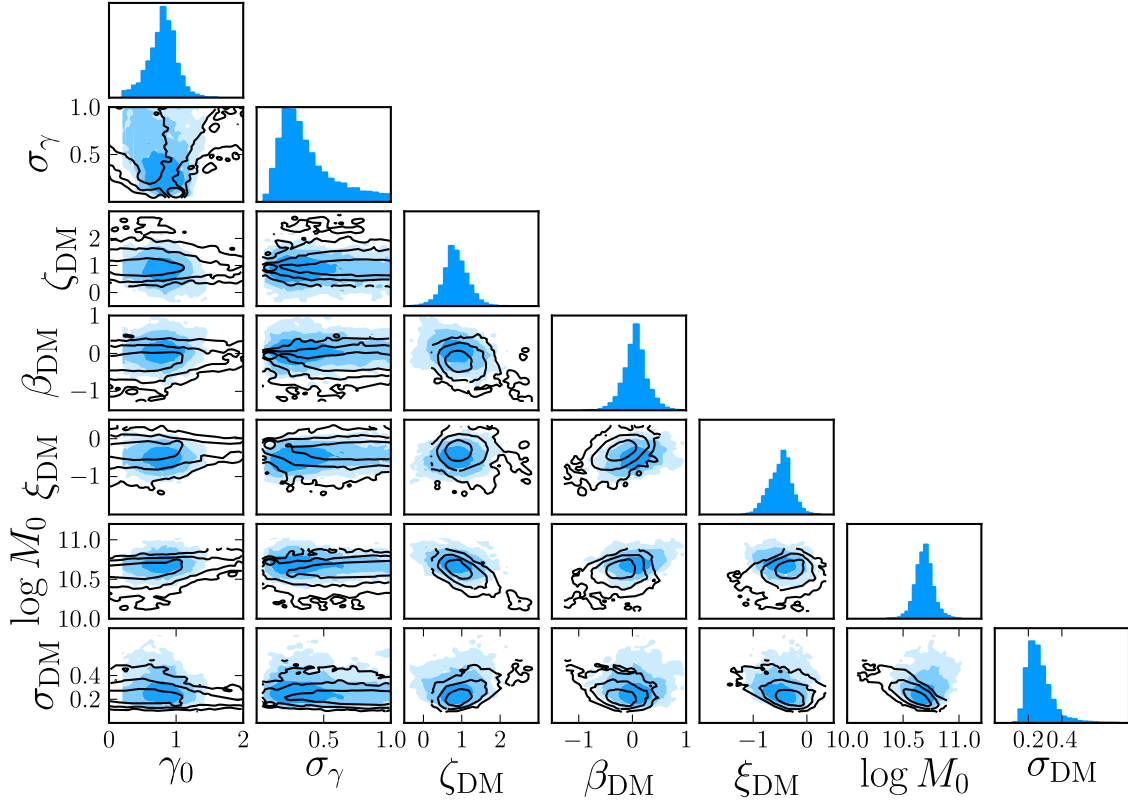
Figure 5.9: Model hyper-parameters describing the dark matter mass within a shell of radius $r_{\rm eff}$ and inner slope, for a gNFW dark matter halo. *Empty contours:* inference with no selection function term. *Filled contours:* including the selection function term. The different levels represent the 68%, 95% and 99.7% enclosed probability regions.

$$\log \alpha_{\text{IMF}} = \zeta_{\text{IMF}}(z - 0.3) + \beta_{\text{IMF}}(\log M_* - 11.5) + \xi_{\text{IMF}} \log \Sigma_*/\Sigma_0 + \alpha_{\text{IMF},0} + N(0, \sigma_{\text{IMF}})$$
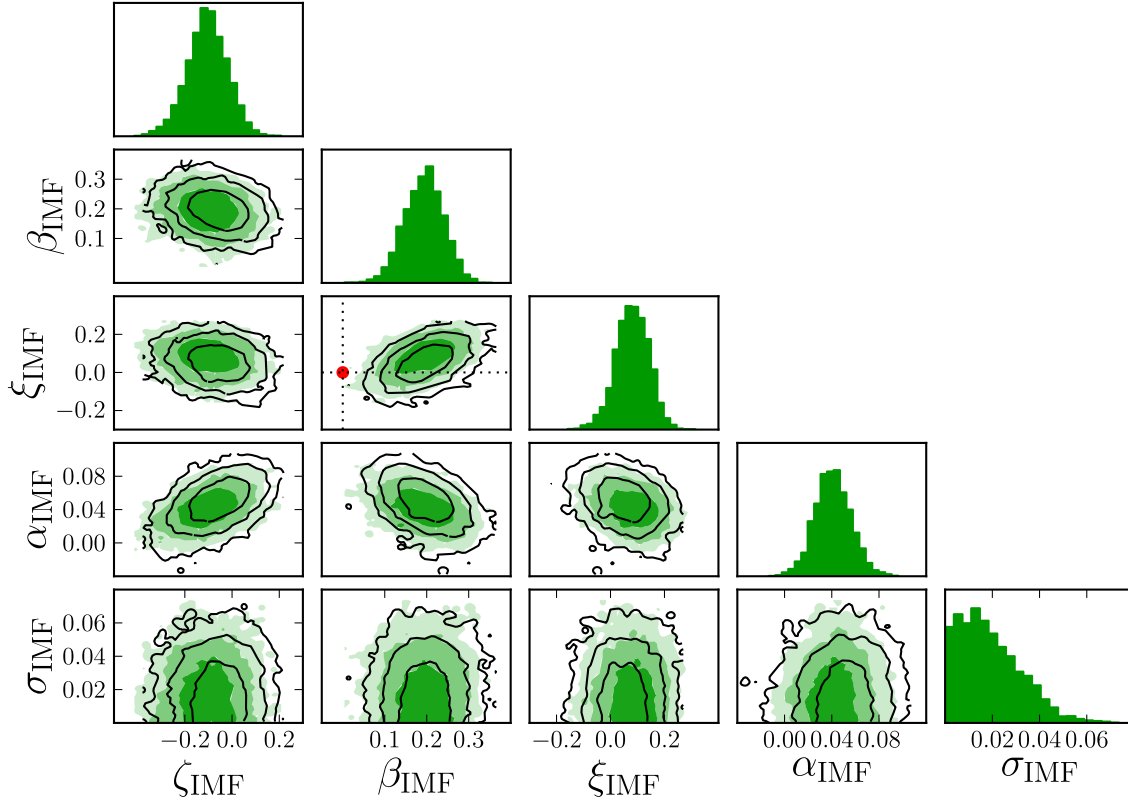
Figure 5.10: IMF normalization hyper-parameters, for a gNFW dark matter halo. The red dot indicates the parameter values corresponding to a universal IMF. *Empty contours:* inference with no selection function term. *Filled contours:* including the selection function term.
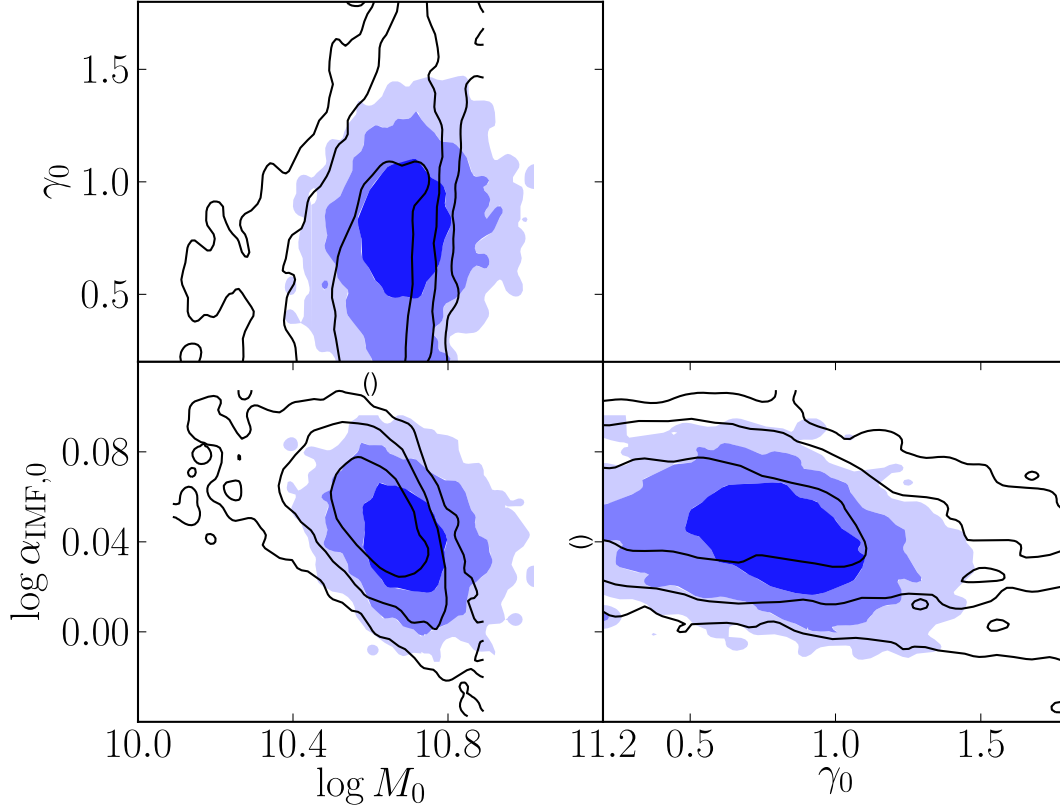
Figure 5.11: Model hyper-parameters describing the average dark matter mass within 5 kpc, average dark matter slope and average IMF normalization, for galaxies at $z = 0.3$, $\log M_* = 11.5$, $R_{\mathrm{e}} = 5\mathrm{kpc}$. *Empty contours:* inference with no selection function term. *Filled contours:* including the selection function term.

 The average inner dark matter slope inferred in our analysis is consistent with $\gamma_{\mathrm{DM}} = 1$ corresponding to an NFW profile, though with a significant uncertainty: $\gamma_0 = 0.85^{+0.16}_{-0.18}$. The scatter in the slope is not well constrained and can be as large as $\sigma_\gamma \sim 0.5$. The inference on the parameters describing the dark matter mass and IMF normalization is very similar to the NFW case: mild anticorrelation between M_{DM5} and stellar mass density and a positive correlation with redshift, no strong correlation of M_{DM5} with stellar mass, strong correlation between α_{IMF} and stellar mass. The main difference is a smaller scatter in M_{DM5} in the gNFW case.

	With $\mathcal{S}$	No $\mathcal{S}$	Parameter description
$\log \mu_{*,0}^{(\mathrm{SL2S})}$	$11.53^{+0.06}_{-0.06}$	$11.55^{+0.06}_{-0.06}$	Mean stellar mass at $z = 0.5$, SL2S sample
$\zeta_{*}^{(\mathrm{SL2S})}$	$0.32^{+0.35}_{-0.31}$	$0.45^{+0.33}_{-0.32}$	Linear dependence of mean stellar mass on redshift, SL2S sample
$\sigma_{*}^{(\mathrm{SL2S})}$	$0.27^{+0.05}_{-0.04}$	$0.28^{+0.05}_{-0.04}$	Scatter in mean stellar mass, SL2S sample
$\log \mu_{*,0}^{(\mathrm{SLACS})}$	$11.66^{+0.03}_{-0.03}$	$11.67^{+0.03}_{-0.03}$	Mean stellar mass at $z = 0.2$, SLACS sample
$\zeta_{*}^{(\mathrm{SLACS})}$	$2.36^{+0.36}_{-0.43}$	$2.44^{+0.35}_{-0.43}$	Linear dependence of mean stellar mass on redshift, SLACS sample
$\sigma_{*}^{(\mathrm{SLACS})}$	$0.23^{+0.03}_{-0.02}$	$0.23^{+0.03}_{-0.02}$	Scatter in mean stellar mass, SLACS sample
$\log \mu_{R,0}^{(\mathrm{SL2S})}$	$0.69^{+0.04}_{-0.04}$	$0.67^{+0.04}_{-0.04}$	Mean effective radius at $z = 0.5$, $\log M_* = 11.5$, SL2S sample
$\zeta_{R}^{(\mathrm{SL2S})}$	$0.36^{+0.22}_{-0.24}$	$0.28^{+0.22}_{-0.20}$	Linear dependence of mean effective radius on redshift, SL2S sample
$\beta_{R}^{(\mathrm{SL2S})}$	$0.65^{+0.16}_{-0.15}$	$0.69^{+0.14}_{-0.14}$	Linear dependence of mean effective radius on stellar mass, SL2S sample
$\sigma_{R}^{(\mathrm{SL2S})}$	$0.18^{+0.04}_{-0.03}$	$0.16^{+0.03}_{-0.02}$	Scatter in mean effective radius, SL2S sample
$\log \mu_{R,0}^{(\mathrm{SLACS})}$	$0.70^{+0.01}_{-0.01}$	$0.70^{+0.01}_{-0.01}$	Mean effective radius at $z = 0.2$, $\log M_* = 11.5$, SLACS sample
$\zeta_{R}^{(\mathrm{SLACS})}$	$0.07^{+0.18}_{-0.17}$	$0.03^{+0.18}_{-0.19}$	Linear dependence of mean effective radius on redshift, SLACS sample
$\beta_{R}^{(\mathrm{SLACS})}$	$0.64^{+0.05}_{-0.05}$	$0.63^{+0.05}_{-0.05}$	Linear dependence of mean effective radius on stellar mass, SLACS sample
$\sigma_{R}^{(\mathrm{SLACS})}$	$0.07^{+0.01}_{-0.01}$	$0.07^{+0.01}_{-0.01}$	Scatter in mean effective radius, SLACS sample
γ_0	$0.80^{+0.18}_{-0.22}$	$0.57^{+0.41}_{-0.35}$	Mean γ_{DM} at $z = 0.3$, $\log M_* = 11.5$, $R_{\mathrm{eff}} = 5$ kpc
σ_γ	$0.34^{+0.27}_{-0.14}$	$0.69^{+0.21}_{-0.25}$	Scatter in the γ_{DM} distribution
ζ_{DM}	$0.86^{+0.31}_{-0.30}$	$0.94^{+0.27}_{-0.21}$	Linear dependence of M_{DM5} on redshift.
β_{DM}	$0.05^{+0.22}_{-0.21}$	$-0.22^{+0.18}_{-0.19}$	Linear dependence of M_{DM5} on $\log M_*$.
ξ_{DM}	$-0.49^{+0.20}_{-0.22}$	$-0.33^{+0.17}_{-0.18}$	Linear dependence of M_{DM5} on $\log \Sigma_*$
$\log M_{\mathrm{DM,0}}$	$10.69^{+0.08}_{-0.07}$	$10.62^{+0.07}_{-0.09}$	Mean M_{DM5} at $z = 0.3$, $\log M_* = 11.5$, $R_{\mathrm{eff}} = 5$ kpc
σ_{DM}	$0.26^{+0.08}_{-0.05}$	$0.22^{+0.05}_{-0.04}$	Scatter in the M_{DM5} distribution
ζ_{IMF}	$-0.11^{+0.09}_{-0.09}$	$-0.06^{+0.08}_{-0.09}$	Linear dependence of IMF normalization on redshift.
β_{IMF}	$0.19^{+0.05}_{-0.05}$	$0.20^{+0.04}_{-0.04}$	Linear dependence of IMF normalization on $\log M_*$.
ξ_{IMF}	$0.09^{+0.06}_{-0.07}$	$0.06^{+0.06}_{-0.07}$	Linear dependence of IMF normalization on $\log \Sigma_*$
$\log \alpha_{\mathrm{IMF,0}}$	$0.04^{+0.02}_{-0.02}$	$0.05^{+0.02}_{-0.02}$	Mean IMF normalization at $z = 0.3$, $\log M_* = 11.5$, $R_{\mathrm{eff}} = 5$ kpc
σ_{IMF}	$0.02^{+0.02}_{-0.01}$	$0.02^{+0.02}_{-0.01}$	Scatter in the IMF normalization distribution
$R_{\mathrm{sel}}^{(\mathrm{SL2S})}$	$1.34^{+0.31}_{-0.23}$	$\cdots$	Mean observable Einstein radius, SL2S sample
$\sigma_{\mathrm{sel}}^{(\mathrm{SL2S})}$	$0.68^{+0.18}_{-0.16}$	$\cdots$	Dispersion in observable Einstein radius, SL2S sample
$R_{\mathrm{sel}}^{(\mathrm{SLACS})}$	$0.96^{+0.24}_{-0.27}$	$\cdots$	Mean observable Einstein radius, SLACS sample
$\sigma_{\mathrm{sel}}^{(\mathrm{SLACS})}$	$0.30^{+0.13}_{-0.07}$	$\cdots$	Dispersion in observable Einstein radius, SLACS sample

Table 5.3: gNFW model. Median, 16th and 84th percentile of the posterior probability distribution function of each model hyper-parameter, marginalized over the other parameters. Results are reported for the full case and ignoring the selection function.
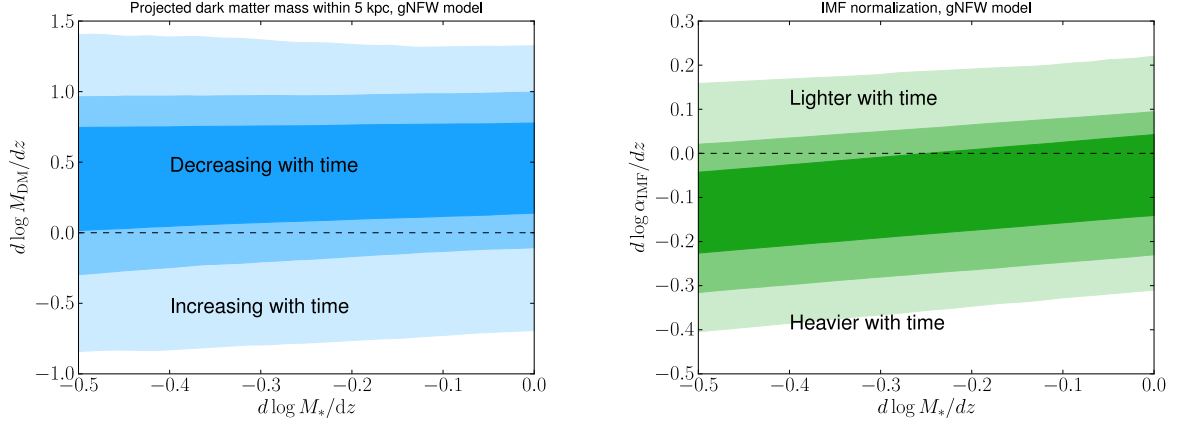
Figure 5.12: *Left panel:* Rate of change in projected dark matter mass within a cylinder of radius 5 kpc along the evolutionary track of an individual galaxy, calculated from Equation 5.22, as a function of the growth rate in stellar mass. *Right panel:* Rate of change in the IMF normalization along the evolutionary track of an individual galaxy, calculated from Equation 5.23, as a function of the growth rate in stellar mass. The dark matter halo is described with a gNFW profile.

To better illustrate the degeneracies in the model we plot in Figure 5.11 the projection of the posterior PDF on the parameters describing the average dark matter mass, slope and IMF normalization for galaxies at $z = 0.3$, $\log M_*$ and $R_e = 5$kpc. We can see a significant degeneracy between the IMF normalization and both the dark matter mass and density slope. As discussed by Auger et al. (2010a) these degeneracies are expected in a study of this nature and illustrate how independent constraints on the stellar IMF can help determine the properties of the dark matter halos of ETGs.

In continuity with the work of Section 5.4.1, we can calculate the rate of change of M_{DM5} and α_{IMF} along the evolutionary tracks of individual galaxies in the gNFW case. These are plotted in Figure 5.12. The same operation is trivial for the dark matter slope, since we are assuming that the average slope is constant across the whole population of massive galaxies. The measurements on the dark matter mass and IMF normalization are consistent with no evolution, similarly to the simpler NFW case.

5.6 Discussion

In Paper IV we studied the evolution of the total density profile of massive ETGs. We found that the population average slope of the density profile, γ', increases with decreasing redshift, at fixed M_* and $R_{\rm e}$, and increases with Σ_*. We also showed how γ' stays more or less constant along the evolution of individual galaxies between $z = 1$ and $z = 0$. The goal of the present paper is to understand what changes in the internal structure are responsible for the observed correlations of γ' with z, M_* and $R_{\rm e}$. The main steps forward in this work compared to Paper IV are 1) the use of a more physically realistic density profile, composed of a spheroid and halo instead of a single power-law component, and 2) a treatment of the lensing selection function, explicitly accounted for when deriving our results. The latter is an important point, as it allows us to make accurate statements on the general population of massive galaxies, and not only on the population of lenses.

The analysis carried out in this paper is split into two parts: first we fix the inner slope of the dark matter halo to $\gamma_{\rm DM} = 1$, then we relax this assumption. The inference on the population distribution of dark matter masses and stellar IMF normalization is consistent in the two cases, as the average dark matter slope inferred in Section 5.5 is very close to that of an NFW profile. We found that the dark matter mass enclosed within 5 kpc anticorrelates with the stellar mass density and positively correlates with redshift. These correlations mirror the trends of the slope of the total density profile γ' with Σ_* and z measured in Paper IV. At fixed redshift, galaxies with a more compact stellar distribution (larger Σ_*) tend to have smaller dark matter masses. Stellar mass

density is in turn related to the formation and evolution history. We know for example that minor dry mergers tend to decrease the concentration of stars by building up an extended envelope of accreted stars (Naab et al. 2009). Galaxies with a more extended stellar component then might be systems that have gone through more merger events than the average. It would then be interesting to test whether in simulations such systems are found to have larger central dark matter masses, at fixed radius, as suggested by our data.

One important point is that the inference on the evolution of the dark matter mass within 5 kpc depends significantly on the selection function. In particular, our analysis reveals how SLACS lenses have preferentially smaller dark matter masses with respect to the population average. Our work is the first to explicitly fit for the selection function in deriving the properties of early-type galaxies from strong lensing measurements. The way the selection function correction is implemented is by describing the distribution function of lenses as a product between the general distribution of massive galaxies and the probability of detecting them in lensing surveys. The latter term is in turn the product between the lensing cross-section and an Einstein radius selection term, which describes the different probability of detecting strong lenses of different Einstein radii. According to the works of Arneson et al. (2012) and Gavazzi et al. (2014), dedicated to the selection function of SLACS-like surveys and SL2S respectively, the Einstein radius seems to be the main quantity determining the detection probability. Of the two terms in the selection function, the Einstein radius selection is the dominant one while the lensing cross section correction has little effect on the results of our analysis. Strong lenses are drawn from the high mass end of the population of galaxies. At fixed stellar

mass, the difference between the distribution of strong lenses and the general distribution of galaxies is small compared to the scatter in the population. Even though lenses with radically different density profiles can have significantly different cross-sections, as shown by Mandelbaum et al. (2009), the lensing cross-section bias is in practice small because of the small intrinsic scatter in density profile across the population of ETGs (consistent with the small scatter of the mass plane, Auger et al. 2010a; Nipoti et al. 2008).

In light of this result it is important to verify the impact of the selection function on the measurement of the redshift evolution of the slope of the density profile carried out in Paper IV, which was based on the same sample of lenses used here. As we show in Appendix 5.8.2, the results of Paper IV are robust to selection function effects. As a further test, we checked whether the galaxies described in our population model lie on the Fundamental Plane relation. As shown in Appendix 5.8.3, that is the case.

The results presented in this work are all based on the assumption of a fixed de Vaucouleurs profile with a spatially constant mass-to-light ratio for the stellar distribution and an isotropic velocity dispersion tensor. If any of these assumptions break down, for example with an evolving stellar profile or orbital anisotropy, then the inference might suffer from biases. Studies of ETGs with more complex dynamical models that fit for orbital anisotropy have found no evidence for significant anisotropies (e.g. Cappellari et al. 2013b). It seems unlikely that allowing for anisotropy would bring significant changes to our results. We tested for the effect of fixing the light profile to a de Vaucouleurs model by repeating the analysis of SL2S lenses with both a Hernquist (Hernquist 1990) and a Jaffe (Jaffe 1983) profile for the stars, and found no difference in the results. The effect of assuming a spatially constant mass-to-light ratio can be more subtle. In particular, if

the stars accreted in merger events, which are thought to be the main drivers of the size growth of ETGs, have a lighter IMF or even a smaller mass-to-light ratio with respect to the pre-existing stellar population, then the light distribution of the stellar component will have a shallower profile than its mass distribution. Indeed some observations suggest that the mass-to-light ratio decreases with increasing radius in early-type galaxies (e.g. Szomoru et al. 2013; Martín-Navarro et al. 2014). In particular, Szomoru et al. (2013) estimate the half-mass radius to be $\sim 25\%$ smaller than the half-light radius. At fixed light profile, a galaxy with a negative gradient in the mass-to-light ratio has a steeper density profile than a model with constant M/L, and thus requires less stellar mass and more dark matter to produce the slope of the total density profile measured with lensing and dynamics. If not taken into account, such a gradient in the mass-to-light ratio would then lead to an overestimate the IMF normalization and an underestimate of the dark matter mass. More detailed data is necessary to rule out this possibility. Nevertheless, if we repeat the analysis assuming a stellar half-mass radius 25% smaller than the half-light radius for each lens, as suggested by the observations of Szomoru et al. (2013), we find results consistent with the original analysis.

In this work we explored correlations between the dark matter mass and stellar IMF with redshift, stellar mass and size. We know a more significant correlation must exist between dark matter mass and the environment of the lens, since ETGs at the center of clusters and large groups have larger projected dark matter masses than our lenses.

We leave the exploration of correlations with the environment to future work, when better data and a more extended sample of lenses will be available, covering a broader range of environments.

5.6.1 Comparison with previous works

The inner dark matter slope of ETGs has been measured in a limited number of cases. Sonnenfeld et al. (2012) measured $\gamma_{\rm DM} = 1.7 \pm 0.2$ for the gravitational lens SDSSJ0946+1006, a $z = 0.222$ ETG from the SLACS sample. This value is slightly larger than the average inferred here, but is not implausible given the large scatter in $\gamma_{\rm DM}$ of the population allowed by our data.

Grillo (2012) found $\gamma_{\rm DM} = 1.7 \pm 0.5$ for the average of the SLACS lenses assuming a Salpeter IMF, which should however be corrected to $1.40^{+0.15}_{-0.26}$ as described by Dutton & Treu (2013a). In our work we let the IMF normalization be a free parameter and find a marginally shallower average dark matter slope and an IMF slightly heavier than Salpeter. Given that most mass enclosed within the Einstein radius is stellar, a small change in the IMF can result in a significant change in the dark matter. Indeed, if we repeat our analysis imposing a Salpeter IMF, we find much steeper dark matter slopes, consistent with the result of Grillo (2012). Oguri et al. (2014) fitted for an average mass profile of ETG lenses in a similar way to the analysis of Grillo (2012) but using a larger sample of lenses and including constraints from gravitational microlensing data for a few of them. They measured the dark matter slope to be $\gamma_{\rm DM} = 1.60^{+0.18}_{-0.13}$, the dark matter fraction to be around 30% and find an IMF normalization slightly smaller than a Salpeter IMF. While dark matter fraction and IMF normalization are in good agreement with our findings, the slope of the dark matter halo measured by Oguri et al. (2014) is significantly larger. Even though the lenses used in the analysis of Oguri et al. (2014) are for the most part the same ones used here, there are two important differences between

the two works. The first difference is that Oguri et al. (2014) used microlensing data for a few system and no stellar kinematics information. The second difference is that we allowed for scatter in the population of galaxies, while Oguri et al. (2014) assumed a fixed inner slope and scaling with stellar mass of the dark matter halo, and fixed stellar IMF for all systems. It is possible that by allowing for scatter the inference on the dark matter slope would be consistent with our results. Dutton & Treu (2013b) and Dutton et al. (2013) find that ETGs of the mass range $\log M_* \sim 11.5$ favor a slightly heavier than Salpeter IMF and standard NFW halos for the dark matter, in perfect agreement with our results. Barnabè et al. (2013) successfully constrained the inner dark matter slope for two galaxies of the SLACS sample, thanks to a more sophisticated stellar dynamics analysis based on spatially resolved spectroscopic data. They measured $\gamma_{\mathrm{DM}} = 0.92^{+0.72}_{-0.64}$ for SDSSJ0936+0913 and $\gamma_{\mathrm{DM}} = 0.46^{+0.41}_{-0.30}$ for SDSSJ0912+0029. Cappellari et al. (2013a) put constraints on the dark matter fractions of a large number of local ETGs from the ATLAS 3D sample finding an average fraction of 13% within a sphere of radius R_{e}, corresponding to $f_{\mathrm{DM}e} \sim 25\%$ for an NFW profile, consistent with our results.

Concerning the IMF of ETGs and its variations with galaxy mass, a large number of works have been published in recent years. Robust constraints on the IMF of individual systems are only available for a very limited number of objects. Sonnenfeld et al. (2012) showed that a Chabrier IMF is ruled out at 95% confidence level in SDSSJ0946+1006, a much more massive ($\log M_* \sim 11.6$) ETG. Spiniello et al. (2012) found preference for a Salpeter IMF over a Chabrier IMF for a very massive lens galaxy in a group-scale halo. Barnabè et al. (2013) find an IMF close to Salpeter for two SLACS lenses. These results are consistent with our work. Microlensing provides an independent way

to determine the absolute value of the stellar mass-to-light ratio and therefore the IMF mismatch parameter and the dark matter fraction. Recent works by Oguri et al. (2014) and Schechter et al. (2014) find an IMF consistent with Salpeter and Jiménez-Vicente et al. (2014) find a projected dark matter fraction consistent with our results. A Salpeter IMF appears to be preferred over Chabrier even at $z \sim 0.8$ (Shetty & Cappellari 2014), in agreement with our results.

Smith & Lucey (2013) constrain the IMF normalization of a massive low redshift lens to be close to that of a Kroupa IMF and inconsistent with a Salpeter IMF. While their result appears to be in tension with our model, our data allows for a certain degree of scatter in the IMF normalization and it is possible that this galaxy is just an outlier in the IMF distribution of massive ETGs, especially considering uncertainties and intrinsic scatter in the correlation between the IMF normalization and galaxy global parameters like stellar velocity dispersion.

A series of studies based on lensing and dynamics (Treu et al. 2010; Auger et al. 2010b; Posacki et al. 2014), on the analysis of stellar absorption features (van Dokkum & Conroy 2010, 2011b, 2012; Conroy & van Dokkum 2012; Ferreras et al. 2013; La Barbera et al. 2013) and on spatially resolved stellar dynamics (Cappellari et al. 2012; Tortora et al. 2013) have found indications for a systematic variation of the IMF with galaxy mass or velocity dispersion, with the more massive systems requiring a heavier IMF. Our result of an increasing IMF normalization with stellar mass further confirm the trend. Finally, Brewer et al. (2014) constrained the IMF normalization of the population of spiral galaxy bulges, with a hierarchical Bayesian inference technique similar to the one adopted in this paper, finding that the average IMF normalization must be smaller than

that of a Salpeter IMF. If we extrapolate our results down to the typical masses of spiral bulges, we find IMFs consistent with their results.

5.7   Summary and Conclusions

We re-examined the SL2S sample of ETG lenses, extending the sample of grade A lenses and lenses usable for a joint lensing and stellar dynamics analysis with the use of key spectroscopic data recently acquired. We then used SL2S and SLACS lenses to explore two component mass models describing the stellar spheroid and dark matter halo of massive ETGs. We fit for the distribution function of dark matter masses, dark matter inner slopes and stellar IMF normalization across the population of massive ETGs with a Bayesian hierarchical inference method that allows for scatter in the population and takes into account the selection function, i.e. the mapping between the general population of massive galaxies and our sample of lenses. This is the most statistically robust attempt at describing the population of ETGs with gravitational lensing data. We found the following.

- The projected dark matter mass within 5 kpc, M_{DM5}, correlates with redshift and anti-correlates with stellar mass density. The average dark matter mass for galaxies at $z = 0.3$, stellar mass of $\log M_* = 11.5$ and effective radius $R_{\mathrm{e}} = 5$ kpc is $\langle \log M_{\mathrm{DM5}} \rangle = 10.7 \pm 0.1^{(\mathrm{stat})} \pm 0.1^{(\mathrm{syst})}$.

- SLACS lenses appear to have slightly smaller dark matter masses than the population average for galaxies of similar mass, size and redshift.

- The time evolution of the dark matter mass for individual objects, inferred by tracing the dark matter mass for galaxies of average mass and size at each redshift, is consistent with a mass within the inner 5 kpc that is constant with time. Correcting for the selection function is critical for recovering this result.

- The average inner slope of the dark matter halos of our lenses is consistent with that of an NFW profile. We were unable to test for correlations of the slope with redshift, stellar mass or size because the uncertainties are too large with the current data. Spatially extended stellar kinematics data would help better constrain the dark matter slope.

- The IMF normalization is close to that of a Salpeter IMF and is heavier for galaxies with larger stellar mass, in agreement with previous studies.

Our finding of central dark matter content anti-correlating with stellar mass density can be interpreted as the result of more compact galaxies living in dark matter halos of smaller mass. Stellar mass density is believed to be closely related to the assembly history of a galaxy: mergers that are predominantly dry contribute to create an extended envelope of stars, therefore galaxies with larger size might have undergone significantly more mergers with respect to more compact objects of similar mass. Our result then seems to agree with the notion that mergers are more frequent in larger halos (Fakhouri & Ma 2009), as well as with recent claims of correlation between environmental density and size of massive ETGs (Cooper et al. 2012b; Lani et al. 2013).

Current and future surveys such as the Dark Energy Survey, the Large Synoptic Survey Telescope, and Euclid will provide tens of thousands of new lenses (Oguri &

Marshall 2010). Hierarchical Bayesian inference will allow to optimally combine the information from such a large number of systems and enable us to probe further the interplay between dark matter and baryons.

5.8 Appendix

5.8.1 Dark matter enclosed within R_{e}

We want to derive what our findings on the variation of M_{DM5} across the population of ETGs correspond to in terms of the projected dark matter enclosed within the effective radius, $M_{\mathrm{DM}e}$. Let us derive how $M_{\mathrm{DM}e}$ scales with redshift, stellar mass and stellar mass density. For simplicity we restrict ourselves to the NFW case. For galaxies with $R_{\mathrm{e}} = 5\mathrm{kpc}$, $M_{\mathrm{DM5}} = M_{\mathrm{DM}e}$ by definition. Therefore for these galaxies the variation with z of the dark matter mass projected within the effective radius, at fixed stellar mass and stellar mass density, is described exactly by ζ_{DM}:

$$\frac{\partial \log M_{\mathrm{DM}e}}{\partial z} = \zeta_{\mathrm{DM}} = 1.02^{+0.32}_{-0.26}. \qquad (5.26)$$

Let us consider the variation of $M_{\mathrm{DM}e}$ with stellar mass, at fixed redshift and stellar mass density. In order for the stellar mass density to be fixed, at a variation in stellar mass $\delta \log M_*$ must correspond a variation in effective radius $\delta \log R_{\mathrm{e}} = 0.5\delta \log M_*$. At fixed dark matter content, a variation in effective radius introduces a change in $M_{\mathrm{DM}e}$. In particular for a galaxy with $R_{\mathrm{e}} = 5\mathrm{kpc}$ and an NFW dark matter halo with $r_s = 10R_{\mathrm{e}}$,

$$\delta \log M_{\mathrm{DM}e} \approx 1.61\delta \log R_{\mathrm{e}}. \qquad (5.27)$$

Then, at fixed stellar mass density and redshift, the variation in $M_{\mathrm{DM}e}$ with stellar mass is given by the sum of a term describing the increase in halo mass, captured by the hyper-parameter β_{DM}, and a term due to the increase in effective radius:

$$\frac{\partial \log M_{\mathrm{DM}e}}{\partial \log M_*} = \beta_{\mathrm{DM}} + 0.80 = 0.56 \pm 0.20. \tag{5.28}$$

Finally a similar argument shows that, at fixed redshift and stellar mass, a variation in stellar mass density corresponds to a change in $M_{\mathrm{DM}e}$ given by

$$\frac{\partial \log M_{\mathrm{DM}e}}{\partial \log M_*} = \xi_{\mathrm{DM}} - 0.80 = -1.26^{+0.31}_{-0.33}. \tag{5.29}$$

For homologous systems, $\partial \log M_{\mathrm{DM}e}/\partial \log M_* = 1$ and $\partial \log M_{\mathrm{DM}e}/\partial \log \Sigma_* = 0$. The fact that the values we measure are inconsistent with these implies that ETGs are not homologous systems.

5.8.2   Relation to power-law models

In Paper IV we measured the slope of the density profile and its variation across the population of strong lenses, assuming a power-law form for the density profile. Here we are fitting a model consisting of a stellar spheroid and a dark matter halo to the same exact set of lenses. Are the results from the two analyses consistent? Additionally, in this work we take into account the lensing selection function. What would be the effect of the selection function on the analysis of Paper IV? We can answer both these questions by generating mock samples of lenses from the population distribution inferred here, and then analyzing them with the same method of assuming power-law density profiles that we used in Paper IV. We generated mock ensembles of 80 lenses, uniformly

distributed in redshift between $z = 0.1$ and $z = 0.8$, with a Gaussian distribution in stellar mass centered at $\mu_* = 11.6$ and with dispersion $\sigma_* = 0.3$, values similar to the distribution of SL2S and SLACS lenses. Effective radii were drawn from a Gaussian with mean given by Equation 5.12 and dispersion $\sigma_R^{(\mathrm{SL2S})}$, and dark matter masses were drawn from a Gaussian with mean given by Equation 5.15 and dispersion σ_{DM}. For simplicity we assumed NFW profiles for the dark matter halos, since the inference with free inner slope is consistent with that assuming NFW profiles. The values of the hyper-parameters describing effective radius and dark matter distributions were drawn from the posterior PDF obtained from the fit described in Section 5.4. For each ensemble we drew one set of hyper-parameters, and then drew the individual values of effective radii and dark matter masses. We then simulated measurements of the density slope γ' and added noise. This was done in Paper IV by fitting a power-law density profile to the measured central velocity dispersion and Einstein radius. In our case we can calculate the model velocity dispersion while the Einstein radius is simply set equal to the effective radius. We have shown in Paper IV that the ratio between the Einstein radius and the effective radius has little impact on the measurement of γ'. Each mock sample is then fit with the same model for the population distribution of γ' used in Paper IV, which consists of a Gaussian distribution with mean given by

$$\langle \gamma' \rangle = \gamma_0' + \alpha'(z - 0.3) + \beta'(\log M_* - 11.5) + \xi' \log R_{\mathrm{e}}/5\,\mathrm{kpc} \qquad (5.30)$$

and dispersion σ_γ'. For each mock realization, we fit for the parameters of this distribution with MCMC, to give the posterior PDF for the Paper IV model parameters given the mock data. This allows us to perform the posterior predictive checks we need. For our

	With $\Pr(\boldsymbol{\omega}_i|\boldsymbol{\lambda})$	No $\Pr(\boldsymbol{\omega}_i|\boldsymbol{\lambda})$	Paper IV
α	$-0.30^{+0.26}_{-0.24}$	$-0.40^{+0.15}_{-0.18}$	$-0.31^{+0.09}_{-0.10}$
β	$0.35^{+0.18}_{-0.20}$	$0.40^{+0.15}_{-0.14}$	$0.40^{+0.16}_{-0.15}$
ξ	$-0.64^{+0.19}_{-0.19}$	$-0.51^{+0.17}_{-0.16}$	$-0.76^{+0.15}_{-0.15}$
γ_0	$1.88^{+0.05}_{-0.08}$	$1.95^{+0.04}_{-0.04}$	$2.08^{+0.02}_{-0.02}$
σ_γ	$0.15^{+0.04}_{-0.04}$	$0.11^{+0.03}_{-0.03}$	$0.12^{+0.02}_{-0.02}$

Table 5.4: Fit of a Gaussian distribution in density slope with mean given by Equation 5.30 and dispersion σ'_γ to mock populations of lenses drawn from the two component model of Section 5.4.

test statistic, we predict the marginalized PDFs for the Paper IV model parameters, by considering the average of these quantities over the ensemble. Results from this exercise are reported in Table 5.8.2. The parameters recovered in this way are well consistent with the values measured in Paper IV, with the exception of the mean density slope, γ_0. The slope measured for mocks generated from our two component model is systematically shallower than the value measured directly on the lenses of our sample. This discrepancy reflects the inability of reproducing relatively large values of the density slope ($\gamma' > 2.2$) with sums of de Vaucouleurs and NFW profiles, as discussed in Section 5.1. However, the key trends with z, M_* and $R_{\rm e}$ are recovered, meaning that the conclusions of Paper IV, namely that γ' correlates with Σ_* and anticorrelates with z, are perfectly consistent with the present work. Furthermore, there is little difference between the values of the power-law parameters obtained by fitting mocks created by taking the selection function into account or not. This is an important result, as it implies that the results of Paper IV are robust with respect to selection effects.

5.8.3 A Posterior Predictive Test

Our hierarchical Bayesian model provides us with the the posterior probability distribution in the hyper-parameters describing the population of massive galaxies. One way to verify whether the inferred model is a realistic one is to draw mock observations from the posterior probability distribution and compare them with real galaxies. In particular it is interesting to check if mock galaxies drawn from our model lie on the Fundamental Plane. For simplicity, we consider the stellar mass Fundamental Plane (Hyde & Bernardi 2009):

$$\log \left(\frac{R_\mathrm{e}}{\mathrm{kpc}} \right) = a \log \left(\frac{\sigma_0}{\mathrm{km\,s^{-1}}} \right) - 2.5b \log \left(\frac{M_*}{2\pi R_\mathrm{e}^2} \right) + c, \tag{5.31}$$

where σ_0 is the central velocity dispersion. Hyde & Bernardi (2009) measured $a = 1.3989$, $b = 0.3164$, $c = 4.4858$ from a sample of ~ 50000 ETGs in the SDSS. Stellar masses were obtained by Gallazzi et al. (2005) assuming a Chabrier IMF. The observed scatter around Equation 5.31 is 0.11.

In order to compare our model with the Fundamental Plane measurements we drew 1000 samples from the posterior PDF, then generated one SL2S-like galaxy for each sample and calculated the observables that enter Equation 5.31. Differently from the test of Appendix 5.8.2, we fix the galaxy redshift to $z = 0.3$ for a better match with the Hyde & Bernardi (2009) sample. Stellar population synthesis stellar masses are corrected to a Chabrier IMF for consistency. In Figure 5.13 we plot the stellar mass Fundamental Plane observed by Hyde & Bernardi (2009) together with the mock observations generated from our model. The scatter in the mock observations is the result of both intrinsic scatter in the distribution of the parameters describing the individual galaxies and the uncertainty
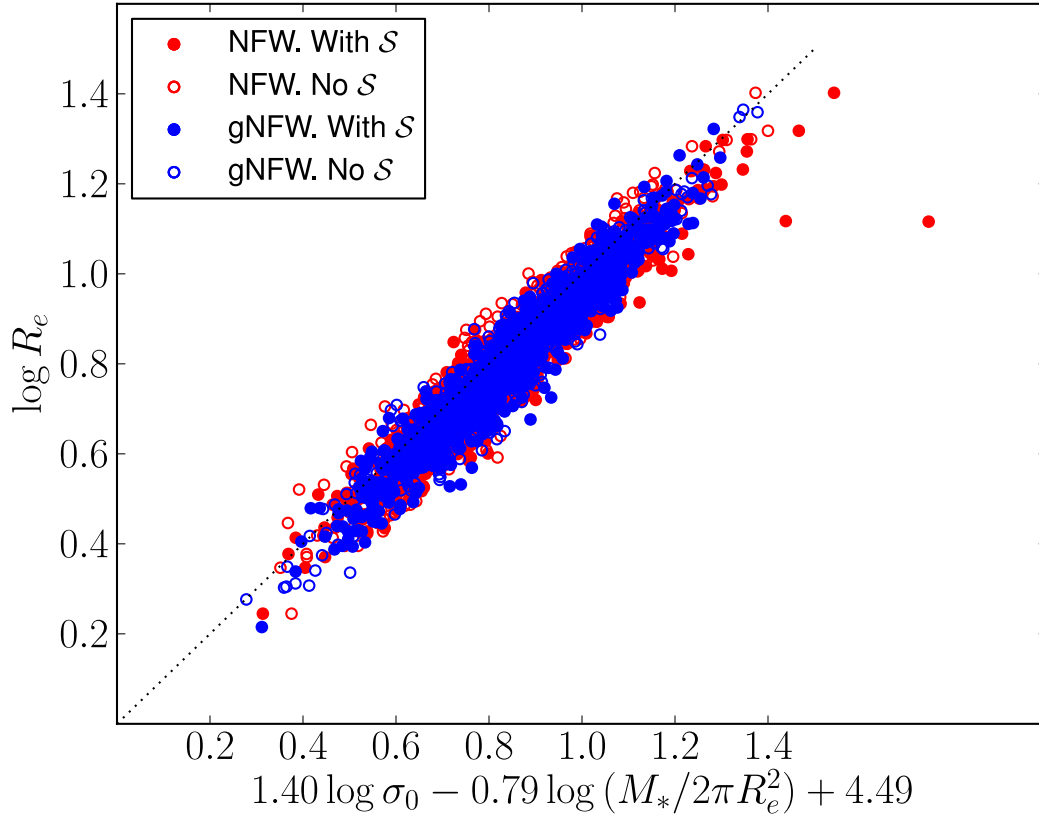
Figure 5.13: Stellar mass Fundamental Plane from mock observations generated from the posterior probability distribution function of sections 6 and 7. The coefficient of the Fundamental Plane relation are *not* fitted to the mock observations but are taken from the work of Hyde & Bernardi (2009).

in the hyper-parameters. The mock observations lie on the Fundamental Plane Even though Fundamental Plane constraints were not explicitly used in our inference, this result shows that our model provides a correct description of the distribution in size, stellar mass and velocity dispersion.

Chapter 6

Testing a dry merger evolution scenario

This chapter was published as Sonnenfeld, A.; Nipoti, C.; Treu, T.; "Purely Dry Mergers do not Explain the Observed Evolution of Massive Early-type Galaxies" 2014, ApJ, 786, 89, and is included here with minor formatting adjustments.

ETGs are generally believed to grow as a result of dissipational (dry) mergers. As discussed in § 1.1.1, dry mergers appear to be able to account for the size evolution of ETGs at $z < 1$ and are compatible with the low star formation rates measured in these objects.

In this Chapter we test the dry merger scenario by adding to the size-evolution constraints the recent measurement of the evolution of the slope γ' of the total density profile of massive ($M_* > 10^{11} M_\odot$) ETGs in the range $0 < z < 1$. Sonnenfeld et al. (2013b) show that ETGs increase in mass and size while keeping their density slope approximately constant and close to isothermal ($\gamma' \approx 2$). By combining these two observational constraints we show that an evolution driven by purely dry mergers is ruled out, and some amount of dissipation is needed.

The Chapter is organized as follows. In Section 6.1 we construct a dry-merger evolutionary model and we compare with observations the evolution of γ' for a sample of mock

galaxies. In Section 6.2 we extend the model by including dissipation in the mergers and compare the predictions of this new model with observations. In Section 6.3 we quantify the amount of dissipation needed to fit both observational constraints and compare. We then discuss our results in Section 6.4 and conclude in Section 6.5.

6.1 Dry mergers

6.1.1 Evolution in mass, size, and density slope

In the dry-merger scenario, galaxies increase their stellar and dark mass by accreting material from other galaxies. No new stars are generated during or after the merging process. Nipoti et al. (2012) presented an analytic model, based on both cosmological and galaxy-merger N-body simulations, which allows to compute the dry-merging driven evolution of halo mass M_{h}, stellar mass M_*, effective radius R_{e} and velocity dispersion, expected for spheroidal galaxies in ΛCDM cosmology. We refer the reader to Nipoti et al. (2012) for a detailed description of the model: here we just recall that the merger rate, as a function of z, M_{h} and merger mass ratio ξ, is the one measured in the Millennium simulations (Fakhouri et al. 2010) and that the variations in R_{e} and M_* are related by

$$\frac{\mathrm{d}\ln R_{\mathrm{e}}}{\mathrm{d}\ln M_*}(\xi) = \left[2 - \frac{\ln\left(1 + \xi^{2-\beta_R}\right)}{\ln\left(1 + \xi\right)}\right], \qquad (6.1)$$

where β_R is the logarithmic slope of the stellar mass-size relation ($R_{\mathrm{e}} \propto M_*^{\beta_R}$). The model depends on few parameters (essentially β_R and the minimum merger mass ratio ξ_{min}) and on the stellar-to-halo mass relation (SHMR) used to associate halo and stellar masses. Here we adopt the model of Nipoti et al. (2012) with $\xi_{\mathrm{min}} = 0.03$, $\beta_R = 0.6$

and Leauthaud et al. (2012) SHMR, but we verified that our results do not depend significantly on these choices.

In this paper we extend the model by computing the change in the slope γ' of the total density profile to be compared with measurements of the same quantity from the lensing and stellar kinematics study of Sonnenfeld et al. (2013b). In practice, we need a formula analogous to equation (6.1), which gives $\mathrm{d}\gamma'/\mathrm{d}\ln M_*$ expected for dry mergers as a function of the merger mass ratio of ξ. For this purpose, we use a set of dissipationless binary-merger N-body simulations, which are described in Section 6.1.2. The analysis of these N-body calculations leads us to parameterize the change in γ' resulting from mergers of mass ratio ξ as

$$\frac{\mathrm{d}\gamma'}{\mathrm{d}\ln M_*}(\xi) = a\xi + b, \tag{6.2}$$

with $a = 0.6$ and $b = -0.73$ (dashed line in Figure 6.1). In practice, dry mergers make the density profile shallower and, for the same amount of total accreted mass, minor mergers are more effective at changing the density slope than major mergers.

We note that throughout the paper ξ indicates the *dark matter mass ratio* between the satellite and the main galaxy. The corresponding *stellar mass ratio* is in general different from ξ, because M_*/M_h depends on M_h. In our model when a halo of mass M_h undergoes a merger with mass ratio ξ the increase in dark matter mass is ξM_h, and the increase in stellar mass is $\mathcal{R}_{*\mathrm{h}}\xi M_\mathrm{h}$, where $\mathcal{R}_{*\mathrm{h}}$ is the ratio of stellar to dark matter mass of the satellite. For given increase in stellar mass, the variation of R_e and γ' depends on ξ, but not on $\mathcal{R}_{*\mathrm{h}}$: this is justified because our N-body simulations indicate that the effect of varying $\mathcal{R}_{*\mathrm{h}}$ is small (see Section 6.1.2).

6.1.2 N-body simulations of binary dissipationless mergers

In order to estimate $\mathrm{d}\gamma'/\mathrm{d}\ln M_*$ as a function of the merger mass ratio ξ (see Section 6.1.1), we collect a set of dissipationless binary-merger N-body simulations by combining new simulations and simulations from previous works. In particular we take four simulations with $\xi = 1$ and $M_{\mathrm{h}}/M_* = 49$ of Nipoti et al. (2009b, runs named 2D1ph, 2D1po, 4D1ph, 4D1po in table 2 of that paper) and two simulations with $\xi = 0.2$ and $M_{\mathrm{h}}/M_* = 49$ of Nipoti et al. (2012, see section 3.3.2 in that paper). Our reference set of binary-merger simulations (named set D in Table 6.1 and Figure 6.1) is supplemented by two new simulations with $\xi = 0.5$ and $M_{\mathrm{h}}/M_* = 49$ (in all runs of this set the main galaxy and satellite have the same M_{h}/M_*). In these simulations (except runs 4D1ph and 4D1po, which are re-mergers of runs 2D1ph and 2D1po; see Nipoti et al. 2009b) both the progenitor galaxies are represented by the two-component galaxy model D of Nipoti et al. (2009b, see table 1 of that paper). In all the runs of this set the ratio between the effective radius of the satellite and of the main galaxy is $\xi^{0.6}$ and the orbits are parabolic: some encounters are head-on ($r_{\mathrm{peri}} = 0$), others are off-axis ($r_{\mathrm{peri}}/r_{\mathrm{vir}} \simeq 0.2$ for $\xi = 0.2$ and $\xi = 0.5$; see Nipoti et al. (2009b) for the orbital parameters of the $\xi = 1$ runs). Here r_{peri} is the pericentric radius and r_{vir} is the virial radius of the main halo.

In order to minimize systematic errors, we measure γ' in simulated galaxies with the same method used in observations. In particular, the density slope γ' measured by Sonnenfeld et al. (2013b) is obtained by fitting a power-law $\rho \propto r^{-\gamma'}$ to the luminosity-weighted line-of-sight velocity dispersion within a circular aperture of radius $R_{\mathrm{e}}/2$ and to the total projected mass within a cylinder of radius R_{Ein}. For a given lens the value

198
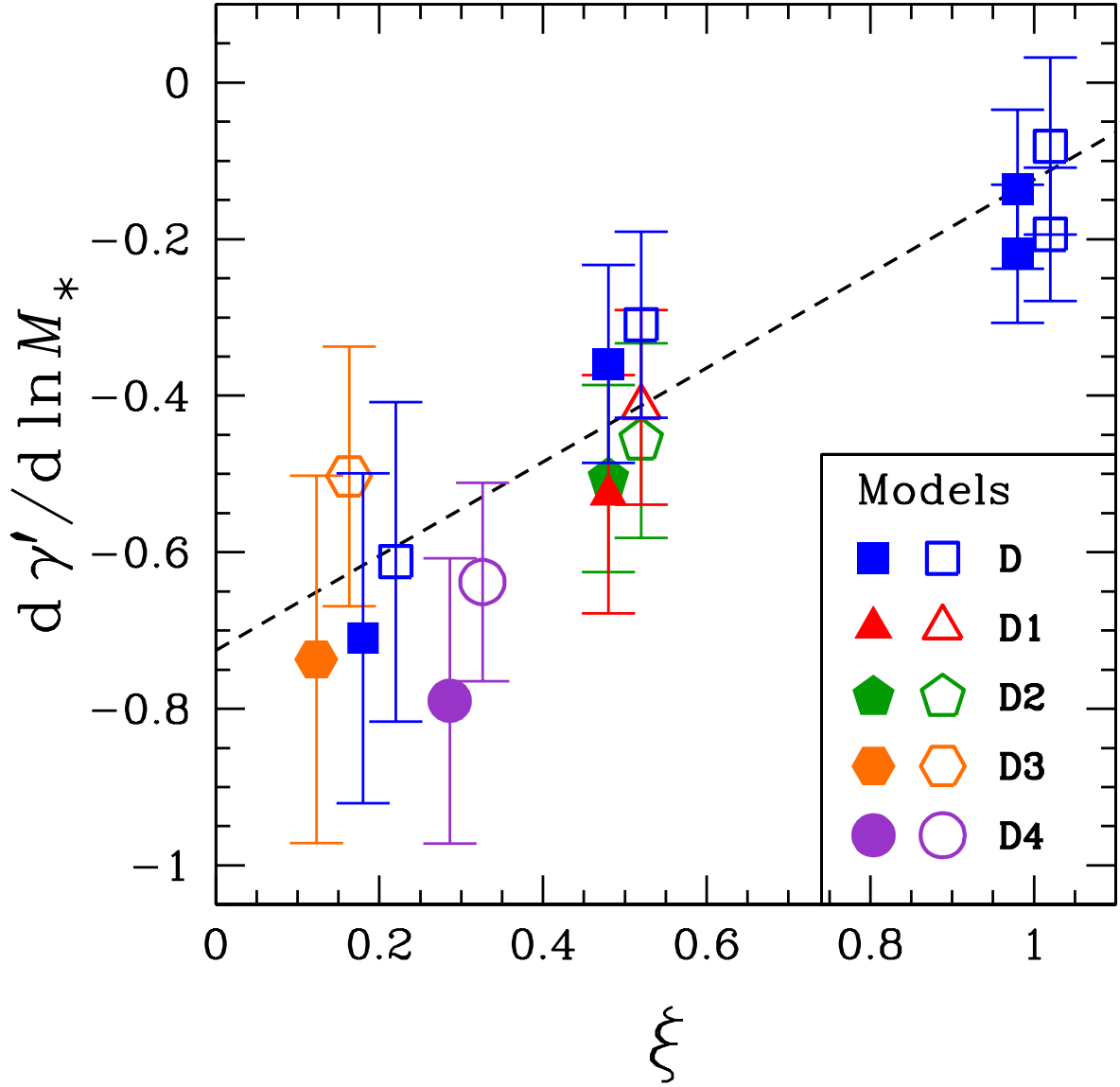
Figure 6.1: Change in the density slope γ' per logarithmic unit of accreted stellar mass as a function of merger mass ratio ξ in dissipationless binary-merger N-body simulations. The different models are described in Table 6.1. Filled symbols indicate head-on mergers while empty symbols refer to off-axis mergers (for the sake of clarity, the filled and empty points are shifted horizontally by -0.02 and 0.02, respectively). The error bars account for projection effects. The dashed line is the linear best-fit to the set of models D. In the case $\xi = 1$ we consider two successive steps of a merger hierarchy: mergers of two D models (step 1; lower points the plot) and re-mergers of the remnant of step 1 with an identical system (upper points in the plot).

Set	$(M_h/M_*)_1$	C_1	$(r_s/R_e)_1$	$(M_h/M_*)_2$	C_2	$(r_s/R_e)_2$
D	49	8.0	11.6	49	8.0	11.6
D1	49	5.0	11.6	49	5.0	11.6
D2	49	8.0	6.0	49	8.0	6.0
D3	49	8.0	11.6	35	8.5	8.8
D4	49	8.0	11.6	75	8.5	15.0

Table 6.1: Paramaters of galaxy models in dissipationless binary-merger N-body simulations. Set: name of the simulation set. C: NFW concentration. r_s: NFW scale radius. R_e: effective radius. M_h: total dark-matter mass. M_*: total stellar mass. Subscript 1 is for the main galaxy, subscript 2 for the satellite.

of the Einstein radius R_{Ein} depends on the distance of the lensed background source: R_{Ein} increases for increasing source redshift z_s. Typical strong lenses such as those of the SLACS (?) or SL2S (?) surveys have Einstein radii not too different from their effective radii. Sonnenfeld et al. (2013b) showed that measurements of γ' with lensing and stellar dynamics are very stable against variations of the ratio R_{Ein}/R_e. When measuring γ' in simulated galaxies we will always assume $R_{Ein} = R_e$, as varying the ratio R_{Ein}/R_e has little impact on the measured γ'.

For our reference set of N-body simulations (set D) $d\gamma'/d\ln M_*$ as a function of the merger mass ratio ξ is fitted by Equation 6.2 with $a = 0.60 \pm 0.19$ and $b = -0.73 \pm 0.13$. The evolution in γ' is obtained by fixing the parameters a and b in Equation 6.2 to their best-fit values. We verified that our results are robust against variations of a and b within the measured uncertainties. Of course, it is important to verify whether the adopted formula for $d\gamma'/d\ln M_*(\xi)$ is also robust against variation of the parameters characterizing the galaxy models. For this purpose we ran eight additional simulations with the same orbital and galaxy parameters as the corresponding simulations of set D, but changing the concentration $C \equiv r_{vir}/r_s$, where r_s is the Navarro Frenk and White

(NFW Navarro et al. 1997) scale radius, the stellar-to-halo mass ratio $M_*/M_{\rm h}$ and the ratio $r_{\rm s}/R_{\rm e}$ of the progenitor galaxies. The values of the parameters of these additional sets of simulations (named D1, D2, D3 and D4) are reported in Table 6.1 and are chosen to span the range of values expected for real galaxies. We note that in all cases the progenitors have γ' in the range $1.97 \lesssim \gamma' \lesssim 2.03$. The results of the runs D1, D2, D3 and D4 are very similar to those of the corresponding runs D (see Figure 6.1). Thus we conclude that our adopted formula is robust with respect to variations in the properties of the host galaxy and its satellite within realistic ranges.

All the binary-merger N-body simulations were run with the parallel N-body code FVFPS (Fortran Version of a Fast Poisson Solver; Londrillo et al. 2003; Nipoti et al. 2003). The parameters of the simulations with $\xi = 1$ are given in Nipoti et al. (2009b). In the runs with $\xi < 1$ we adopted the following values of the code parameters: minimum value of the opening parameter $\theta_{\rm min} = 0.5$ and softening parameter $\varepsilon = 0.04 R_{\rm e}$, where $R_{\rm e}$ is the initial effective radius of the main galaxy. The time-step Δt, which is the same for all particles, is allowed to vary adaptively in time as a function of the maximum particle density $\rho_{\rm max}$: in particular, we adopted $\Delta t = 0.3/(4\pi G \rho_{\rm max})^{1/2}$. The initial conditions of the new simulations are realized as in Nipoti et al. (2009b), but with dark matter particles twice as massive as the stellar particles. The total number of particles used in each simulation is in the range $1.6 - 3.4 \times 10^6$.

In all the simulations used in this work the galaxy collision is followed up to the virialization of the resulting stellar system. We define the merger remnant as the systems composed by the bound stellar and dark matter particles at the end of the simulation. The intrinsic and projected properties of the progenitors and of the merger remnants are

determined as in Nipoti et al. (2009b), with the exception of γ', which, as pointed out above, is computed with the same procedure used for observed lenses by Sonnenfeld et al. (2013b).

6.1.3 The model sample

Our goal is to follow the evolution of a sample of model galaxies between $z = 1$ and $z = 0$, matching the characteristic of the sample observed by Sonnenfeld et al. (2013b). We thus consider $N_{\mathrm{gal}} = 1000$ objects with $\log M_*$ drawn from a Gaussian with mean $\mu_* = 11.5$ and dispersion $\sigma_* = 0.3$. The starting point of the evolutionary tracks of all galaxies is fixed at $z = 0.3$, which is the redshift for which observations of γ' are most robust. Effective radii are drawn from the mass-size relation measured by Newman et al. (2012a). Halo masses are assigned with the same SHMR used in the galaxy evolution model described in Section 6.1.1. For fixed M_*, M_{h} and R_{e}, the value of γ' is not uniquely determined as this depends on additional parameters, such as the orbital anisotropy and the concentration of the dark matter halo. The initial values of γ' are then drawn from the distribution measured by Sonnenfeld et al. (2013b). Once the initial values are set, M_*, M_{h}, R_{e} and γ' are evolved according to our model as described in Section 6.1.1.

Roughly half of the accreted stellar mass and the corresponding change in γ' is due to mergers with $\xi < 0.2$. Since $\xi = 0.2$ is the smallest mass ratio we consider in our N-body simulations, our predictions on the evolution of γ' for the sample of mock galaxies relies in part on an extrapolation of Equation 6.2. We verified that even in the extreme case in which the function $d\gamma'/d\ln M_*(\xi)$ flattens abruptly below $\xi = 0.2$ the conclusions of

our analysis do not change.

6.1.4 Comparison with observations

The measurements by Sonnenfeld et al. (2013b) constrain the parameter γ' in ETGs as a function of their redshift, stellar mass and half-light radius. The mean change of γ' with one of these parameters and others fixed is measured to be

$$\frac{\partial \gamma'}{\partial z} = -0.31 \pm 0.10, \tag{6.3}$$

$$\frac{\partial \gamma'}{\partial \log M_*} = 0.40 \pm 0.16, \tag{6.4}$$

$$\frac{\partial \gamma'}{\partial \log R_{\mathrm{e}}} = -0.76 \pm 0.15. \tag{6.5}$$

According to the formalism introduced in Sonnenfeld et al. (2013b), the observed change of γ' with redshift for a galaxy with a mass growth rate $\mathrm{d}\log M_*/\mathrm{d}z$ and a size growth rate of $\mathrm{d}\log R_{\mathrm{e}}/\mathrm{d}z$ is

$$\frac{\mathrm{d}\gamma'}{\mathrm{d}z} = \frac{\partial \gamma'}{\partial z} + \frac{\partial \gamma'}{\partial \log M_*}\frac{\mathrm{d}\log M_*}{\mathrm{d}z} + \frac{\partial \gamma'}{\partial \log R_{\mathrm{e}}}\frac{\mathrm{d}\log R_{\mathrm{e}}}{\mathrm{d}z}. \tag{6.6}$$

The quantities $\mathrm{d}\log M_*/\mathrm{d}z$ and $\mathrm{d}\log R_{\mathrm{e}}/\mathrm{d}z$ are not constrained by the observations, but are directly provided by our model for the dry merger evolution of galaxies.

An implicit assumption of Equation 6.6 is that the observed trends of γ' with stellar mass and size are determined uniquely by the intrinsic evolution of galaxies, and not by the appearance of new objects with time. This is a reasonable approximation, given that the total number density of quiescent galaxies has little evolution since $z \sim 1$ (Cassata et al. 2013), particularly at the large masses of our sample (Ilbert et al. 2013).

Figure 6.2 shows the model evolution of the density slope averaged over the sample of 1000 galaxies, $\langle\gamma'\rangle$. The mean change in γ' with redshift for the sample average is $d\gamma'/dz = 0.33$, and the scatter over the sample is $\sigma_{d\gamma'/dz} = 0.15$. The average mass and size growth rates are $d\log M_*/dz = -0.27$ (galaxies roughly double in stellar mass from $z = 1$ to $z = 0$) and $d\log R_e/dz = -0.36$ respectively. The figure also shows the observed mean change in γ' calculated following Equation 6.6. This is $d\gamma'/dz = -0.13 \pm 0.12$. The key result is that predicted and observed evolution in γ' differ significantly.

Equation 6.6 provides an efficient way to quickly compare model predictions with observations. However, in this context the "observed" evolution of γ' is really a combination of observed quantities (the partial derivatives) and model predictions ($d\log M_*/dz$ and $d\log R_e/dz$). A more direct evaluation of the goodness of the model is obtained by comparing models to the observables, i.e. the partial derivatives. Such a comparison is done in Section 6.3. Here we simply point out a discrepancy between the predicted evolution of γ' and observed data, the significance of which will be discussed later.

6.2   Wet mergers

The above analysis is based on the assumption that the growth of galaxies is a result of purely dry mergers. In practice, mergers between galaxies are expected to involve the accretion of gas, which can radiate away energy and sink to the central parts of the main galaxy, eventually leading to star formation episodes. This infall of gas can alter the density profile of the accreting galaxy, making it steeper. Thus introducing dissipation in our model should help reproduce the observed evolution of γ'.
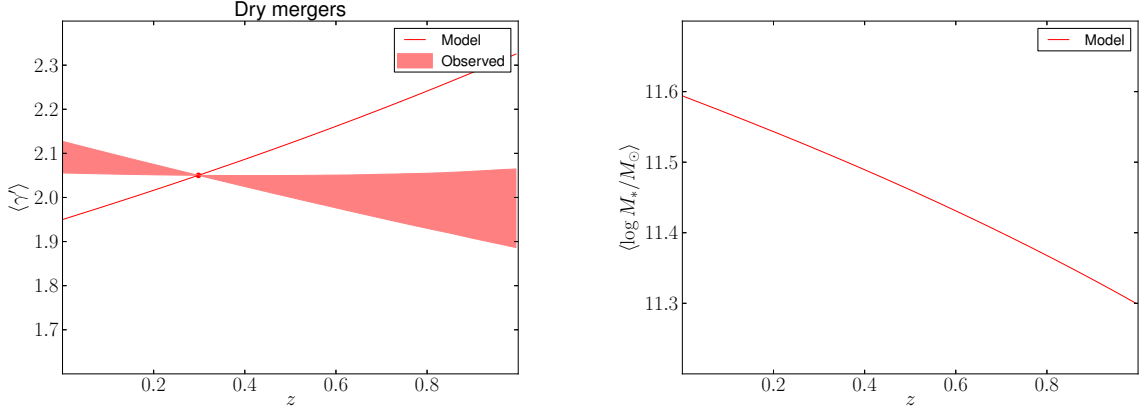
Figure 6.2: *Left panel. Solid line:* Density slope γ', averaged over the mock galaxy population described in Section 6.1.3, as a function of redshift. *Shaded region:* 68% confidence region for the observed change in γ' for a population of galaxies with the same mass and size growth rate as the model one. *Right panel.* Average stellar mass of the mock galaxy sample as a function of redshift.

Following the spirit of our approach we introduce dissipation using a simple toy model. In spite of its simplicity this approach allows us to isolate cleanly the effect of dissipation and estimate whether this solution can work at all. Thus it should provide a very good complement to hydrodynamic cosmological simulations which are just starting to achieve the resolution to model the internal structure of ETGs (Feldmann et al. 2010; Oser et al. 2012; Johansson et al. 2012; Remus et al. 2013; Dubois et al. 2013).

We wish to test whether dissipation *can* work and therefore we consider a plausible yet somewhat extreme model which maximizes the effects on the mass profile. In practice, we assume that a small fraction of the baryonic mass of the merging satellite is cold gas, which, in the merging process, falls exactly to the center of the galaxy and forms stars. We calculate the response of the mass distribution of the galaxy to the infall of cold gas following the adiabatic contraction recipe of Blumenthal et al. (1986), which is stronger than more recent ones based on numerical simulations (e.g. Gnedin et al. 2004).

The galaxies are modeled as spherical de Vaucouleurs stellar bulges and a dark matter halo with an NFW profile. The ratio between halo mass and stellar mass is $M_h/M_* = 50$, and the ratio between the scale radius of the NFW profile and the effective radius of the stellar component is $r_s/R_{\text{eff}} = 10$. For given infalling mass we first calculate the new distribution of stellar and dark matter mass following adiabatic contraction. Then we calculate the stellar half-light radius. Finally we calculate γ' consistently with lensing and dynamics measurements.

The change in R_e and γ' is caused by both the addition of new material at $r = 0$ and by the subsequent contraction of the preexisting mass. The two effects have a comparable impact on γ'. Figure 6.3 shows the original mass distribution as well as the one following gas infall and adiabatic contraction for a typical system. The relation between the change in γ' due to and the accreted gas mass dM_g can be fitted with a linear relation

$$\frac{\mathrm{d}\gamma'}{\mathrm{d}M_g} = \frac{c}{M_*},\tag{6.7}$$

with $c = 7.9$ (see Figure 6.3). The exact value of c depends on the properties of the main galaxy. However, for the same parameters explored in Section 6.1.1 and summarized in Table 6.1 the variation of c is smaller than 10%.

This ingredient is then added to the model describing the evolution of γ' in the dry merger case. The accreted gas mass is assumed to be a fraction f_g of the accreted stellar mass, so $dM_g = f_g dM_*$: for simplicity we assume that f_g is independent of redshift, stellar and halo mass. Then Equation 6.2 is modified to

$$\frac{\mathrm{d}\gamma'}{\mathrm{d}M_*}(\xi) = \frac{1}{M_*}\left[a\xi + b + cf_g\right].\tag{6.8}$$
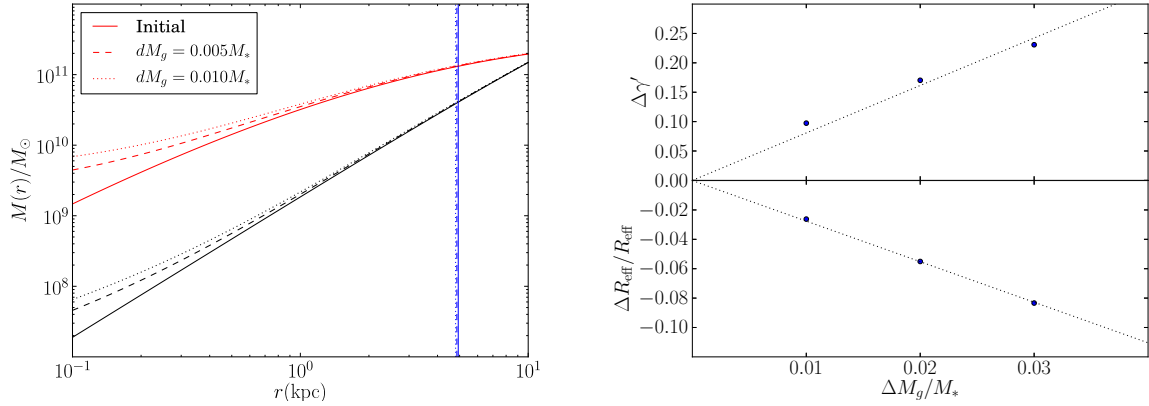
Figure 6.3: *Left panel:* Stellar (red) and dark matter (black) mass profiles for a model galaxy, before and after the infall of gas at the center and the subsequent adiabatic contraction. The blue vertical lines indicate $r = R_{\text{eff}}$. *Right panel: Top:* Change in the density slope as a function of infalling gas (blue dots), and its best linear fit of Equation 6.7 (dashed line). *Bottom:* Logarithmic change in the effective radius as a function of infalling gas (blue dots), and its best linear fit of Equation 6.9 (dashed line).

The effect of the infall of gas on the effective radius is quantified as

$$\frac{\mathrm{d}\log R_{\text{e}}}{\mathrm{d}\log M_*} = -2.8 f_g, \tag{6.9}$$

which is a measure of the reduced increase of R_{e} due to dissipation (see also Ciotti et al. 2007). This term will be added to Equation 6.1 when calculating the size evolution in the model with wet mergers.

We set $f_g = 0.1$ and calculate the evolution of the population average of γ' analogously to Section 6.1.4. Results are plotted in Figure 6.4, together with the observed evolution calculated with Equation 6.6. The average change in γ' is now $\mathrm{d}\gamma'/\mathrm{d}z = -0.15$ with a scatter of $\sigma_{d\gamma'/dz} = 0.03$. Note that this new model modifies also the interpretation of the observational results owing to the slightly smaller theoretical size growth entering Equation 6.6. The key result is that, by introducing a reasonable amount of dissipation, model predictions and observations are now in good agreement.
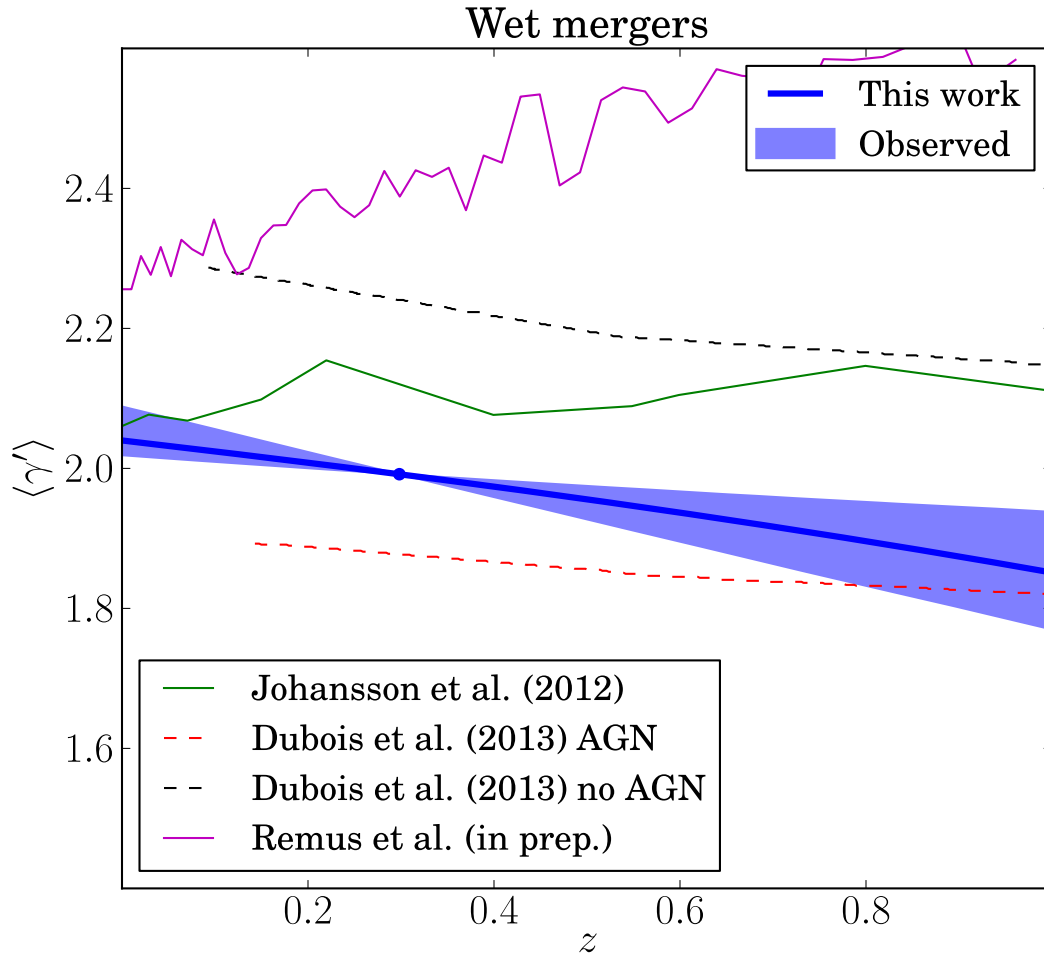
Figure 6.4: *Solid line:* Density slope γ', averaged over the mock galaxy population described in Section 6.1.3 and evolved taking into account the effects of wet mergers assuming $f_g = 0.1$. *Shaded region:* 68% confidence region for the observed change in γ' for a population of galaxies with the same mass and size growth rate as the model one. For comparison, we plot the average γ' of galaxies from cosmological simulations of Johansson et al. (2012), Dubois et al. (2013) and Remus et al. (in prep.).

So far we have focused our attention to the evolution of the density slope γ'. There is another important piece of observations that a successful model of galaxy evolution needs to reproduce: the size evolution. We want to verify whether the two models considered so far predict a size growth consistent with observations. This is done in Figure 6.5, where we plot R_{e} as a function of z for the sample average in both the dry and wet merger model, together with the observed average size evolution of galaxies with the same mass as the model average, for various literature measurements and assuming no progenitor bias. Most measurements imply a stronger size evolution than our model predictions for both the dry and wet merger case, the discrepancy being worse for the wet merger model. Adding dissipational effects then helps matching γ' observations, but increases the tension with size evolution data. Our knowledge of the size distribution of massive ETGs at $z < 1$ therefore should rule out models with too much dissipation. In the following section we determine how much disspation is needed, if at all, to best match both sets of observables. This inference will also allow us to perform model selection, i.e to compare how well the purely dry merger scenario compares with the wet merger one.

6.3 Constraining the amount of dissipation

As shown in Section 6.2, the infall of cold gas and the subsequent adiabatic contraction help reconcile the predicted evolution of the density profile with observations. At the same time however adiabatic contraction leads to a decrease of the effective radius, such that models with too much dissipation are in tension with size evolution measurements. The importance of these two effects increases with increasing gas fraction, which we
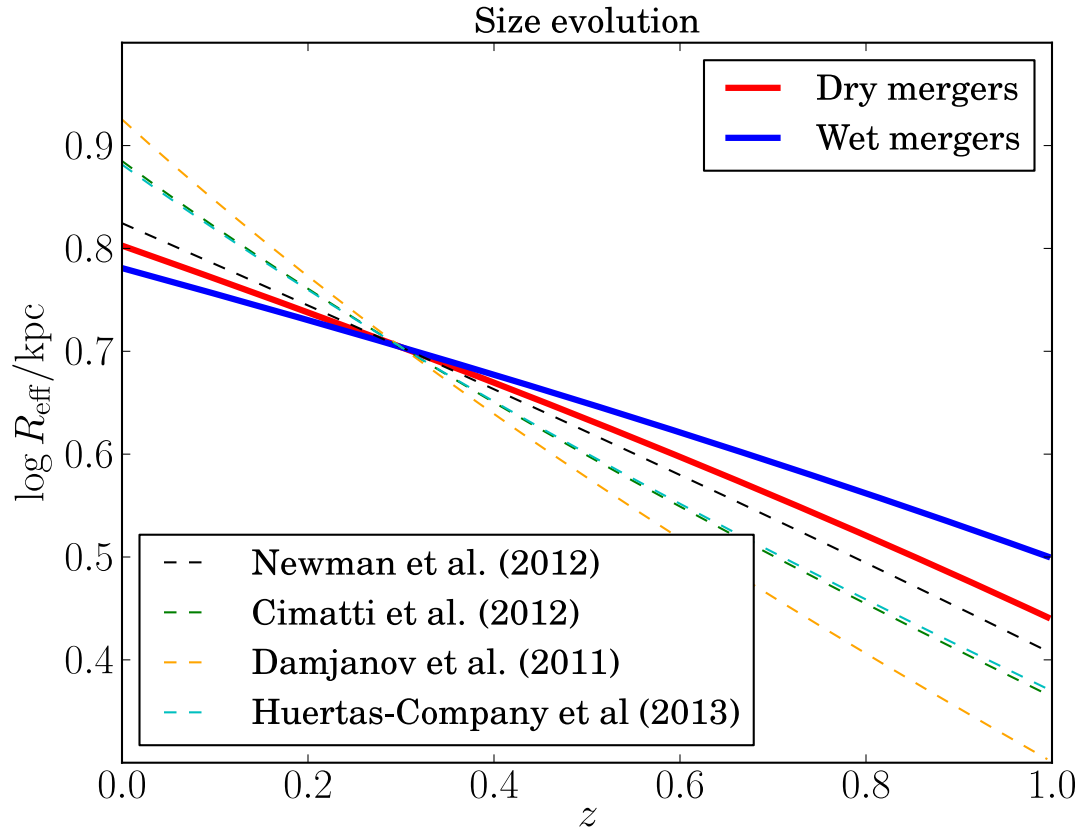
Figure 6.5: *Solid lines:* redshift evolution of the mock sample average of the effective radius in the dry (red) and wet (blue) merger case. A gas fraction $f_g = 0.1$ is assumed in the latter case. *Dashed lines:* observed size growth we infer from the best-fit size evolution measurements by Damjanov et al. (2011), Newman et al. (2012a), Cimatti et al. (2012), Huertas-Company et al. (2013) assuming no progenitor bias.

parameterize with f_g. We wish to estabilish which values of f_g provide the best match to the data, including both density slope and size measurements. We do this by generating mock populations of ETGs, evolved with different values of f_g, and by comparing scaling relations of γ' and R_e with observations. Our mock population is built by picking, for each one of the $N_{\text{gal}} = 1000$ mock galaxies described in Section 6.1.3, a random snapshot on its evolutionary track. This results in a set of galaxies uniformly distributed in redshift in the interval $0 < z < 1$. Sizes and density slopes of these mock galaxies will depend on the amount of dissipation allowed by the model, parameterized by f_g. For fixed f_g, we can infer how the average density slope of the mock population scales with redshift, stellar mass and effective radius by measuring $\partial\gamma'/\partial z$, $\partial\gamma'/\partial\log M_*$, $\partial\gamma'/\partial\log R_e$ with the same method used by Sonnenfeld et al. (2013b). Similarly, we can measure how the average effective radius scales with redshift and stellar mass. We assume the following relation:

$$
\begin{aligned}
\langle\log R_e\rangle = \quad & \log R_0 + \frac{\partial\log R_e}{\partial z}(z - 0.3) + \\
& +\frac{\partial\log R_e}{\partial\log M_*}(\log M_* - 11).
\end{aligned}
\tag{6.10}
$$

We then fit for f_g by comparing the model partial derivatives of γ' and R_e with the values measured by Sonnenfeld et al. (2013b) (Equation 6.3, Equation 6.4, Equation 6.5) and in size evolution studies. The redshift dependence of the average effective radius, $\partial\log R_e/\partial z$, has been measured by different authors. As Figure 6.5 shows, there is some scatter between the reported values, possibly indicative of an underlying systematic uncertainty in the determination of the size evolution, of differences in the selection function. In order to take this uncertainty into account, we assume as the observed

value of $\partial \log R_{\mathrm{e}}/\partial z$ the mean between the values measured by Newman et al. (2012a), Damjanov et al. (2011), Cimatti et al. (2012), Huertas-Company et al. (2013), and we take their standard deviation as the uncertainty:

$$\frac{\partial \log R_{\mathrm{e}}}{\partial z} = -0.37 \pm 0.08. \tag{6.11}$$

The mass dependence of R_{e} is measured by Newman et al. (2012a) to be $\partial \log R_{\mathrm{e}}/\partial \log M_* = 0.59 \pm 0.07$. The fit is done in a Bayesian framework. The posterior probability distribution for the gas fraction, as well as the redshift evolution of γ' and R_{e}, is shown in Figure 6.6.

The data prefer non-zero values of the gas fraction, with a median and $1 - \sigma$ interval of $f_g = 0.08 \pm 0.01$. Purely dry merger models ($f_g = 0$) are disfavored at more than 99% CL (formally at 8-σ). The redshift dependence of γ' is well matched by the model, and the z-dependence of R_{e} is consistent with observations at the $2 - \sigma$ level. Although not plotted in Figure 6.6, we verified that the dependences of γ' on R_{e} and M_*, as well as the dependence of R_{e} on M_*, are well consistent with observations. This is expected, since the same observed scaling relations were used to initialize the mock sample at $z = 0.3$.

6.4 Discussion

In Section 6.1.4 we evaluated the mean evolution in the slope of the density profile γ' of a mock sample of massive ETGs, under the assumption of growth by purely dry mergers. We found that purely dry mergers produce a strong decrease in γ', $d\gamma'/dz = 0.33$ on average, inconsistent with observations. This result is robust against different choices for the SHMR and against variations in the values of the model parameters. We then
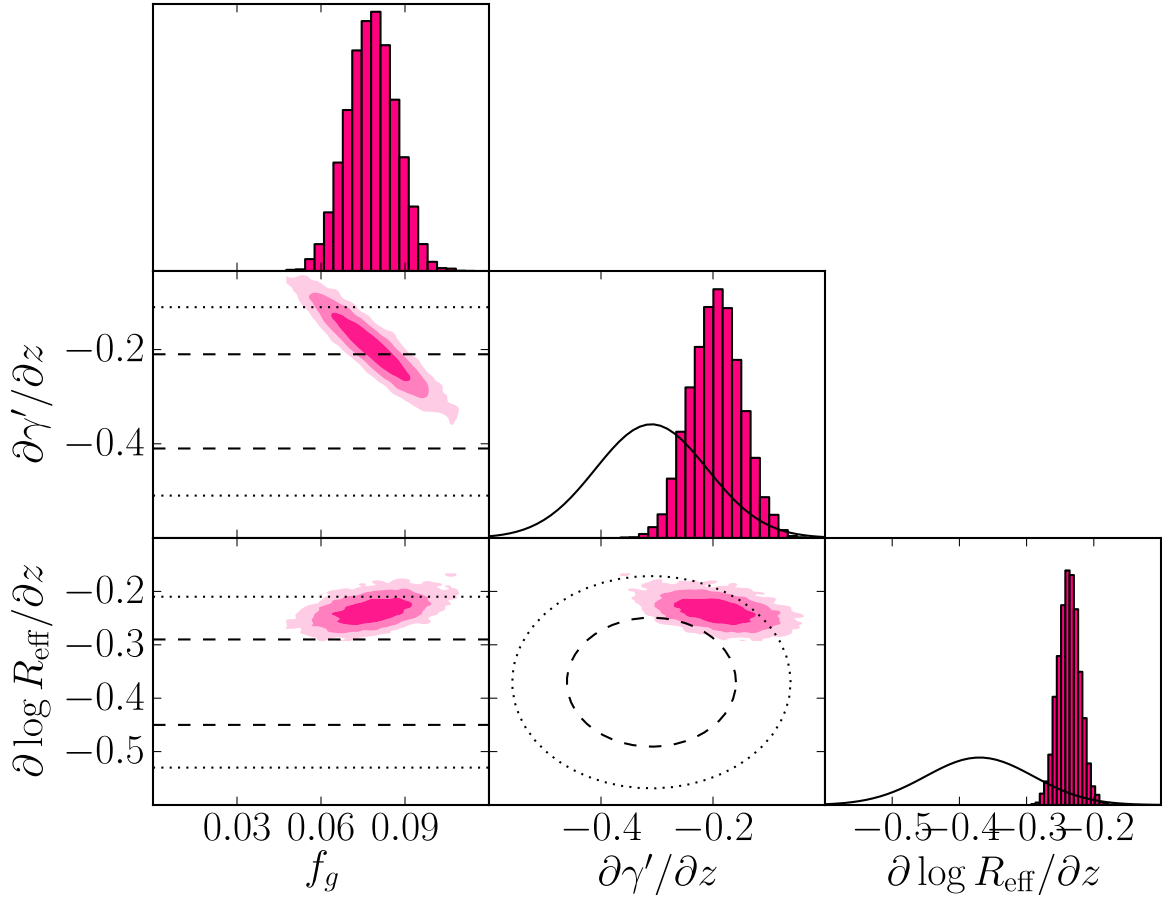
Figure 6.6: *Filled contours:* Posterior probabiliy distribution of the parameters describing the mock population of ETGs, projected on the space defined by the gas fraction, the dependence of γ' on redshift, and the dependence of $R_{\rm e}$ on redshift. *Dashed and dotted lines:* 68% and 95% enclosed probability of the observed redshift dependence of γ', from Sonnenfeld et al. (2013b), and of the effective radius, obtained by combining measurements by Newman et al. (2012a), Damjanov et al. (2011), Cimatti et al. (2012) and Huertas-Company et al. (2013), as explained in the text.

extended our model allowing for a modest amount of star formation in the mergers, and quantified the resulting effect on γ'.

When considering simultaneously the evolution in density slope and size, we find that models with dissipation are strongly favored over purely dry merger models. The most probable model has $f_g = 0.08$, which according to our assumptions means that 8% of the accreted baryonic mass consists of gas that falls to the center of the galaxy and forms stars. The mock galaxies in our sample double their stellar mass between $z = 1$ and $z = 0$, on average. This would imply that 4% of the final stellar mass of our galaxies being the result of in-situ star formation at $z < 1$, or a specific star formation rate (sSFR) of $\sim 0.01 \mathrm{Gyr}^{-1}$. These numbers are consistent with the largest amount of recent star formation allowed by observations of ETGs, including spectral properties (Trager et al. 2000; Treu et al. 2002; ?; Thomas et al. 2010), the evolution of the Fundamental Plane (Treu et al. 2005), UV (Kaviraj et al. 2011) and mid-IR fluxes (Fumagalli et al. 2013) and spectral energy distribution fitting (van Dokkum et al. 2010; Tonini et al. 2012). Thus we conclude that our model is as wet as it can be without violating known observational constraints. The other extreme assumption of our model is that this cold gas falls all the way to the center before forming stars. Although this is clearly a toy-picture, it is at least qualitatively consistent with the "blue cores" seen in the center of massive ETGs at these redshifts (Menanteau et al. 2001; Treu et al. 2005; Pipino et al. 2009). Observations of color gradients and their evolution (e.g. Szomoru et al. 2013) provide additional tests for the plausibility of the proposed scenario. Preliminary calculations show the predicted change in colors due to wet mergers to be relatively small, and consistent with observations. However a more detailed comparison requires a careful

assessment of the observational selection function as well as additional assumptions on the star formation history and stellar populations. This is beyond the scope of this paper and left for future work.

Purely dry mergers maximize the size growth of ETGs for a given increase in mass, and thus introducing some dissipation makes it harder to explain this observation. Even though the tension with the size-growth data is much less than that between purely dry mergers and the evolution of the mass density profiles, it illustrates the challenges of achieving a fully self consistent and quantitative description of the evolution of massive early-type galaxies. The discrepancy might be the result of progenitor bias (e.g. van der Wel et al. 2009; Cassata et al. 2013), which we have not accounted for. López-Sanjuan et al. (2012) estimate that progenitor bias contributes $\sim 20\%$ to the observed size evolution at $z < 1$. This however raises the question of whether the observed evolution in the density slope might also be strongly influenced by progenitor bias effects. Can the observation of $\langle \gamma' \rangle \approx 2$ between $z = 1$ and $z = 0$ still be consistent with the dry merger model if we allow for the continuous emergence of new systems pushing the population average $\langle \gamma' \rangle$ towards the measured value? This is very unlikely. Our model shows that dry mergers decrease the average density slope of a population of galaxies by ~ 0.3 between $z = 1$ and $z = 0$. On the other hand, the scatter in γ' over the population of massive ETGs is as small as 0.12 (Sonnenfeld et al. 2013b). In order to reproduce both the observed $\langle \gamma' \rangle$ and scatter at $z = 0$, the descendants of $z = 1$ ETGs must be strongly outnumbered by newly born systems, at odds with observations (Ilbert et al. 2013; Cassata et al. 2013).

The toy model developed in Section 6.2 is far from perfect, given the many simplifying

assumptions it is based on. The effect of wet mergers on the density profile of ETGs is probably less pronounced in reality than in the idealized case considered here, and must be studied with dedicated numerical simulations in order to make quantitative statements. Nevertheless, our work shows with great clarity that i) dry mergers cannot be the *only* mechanism driving the evolution of massive ETGs; ii) a small amount of dissipation, consistent with observations, can bring the predicted evolution of γ' in agreement with lensing measurements, as previously proposed by Ruff et al. (2011). This finding is consistent with results from cosmological simulations that include dissipative effects, which predict trends in γ' in qualitative agreement with the data (Johansson et al. 2012; Remus et al. 2013; Dubois et al. 2013, see Figure 6.4).

As an alternative to the wet merger scenario, Bolton et al. (2012), based on the results of simulations by Nipoti et al. (2009b), suggested off axis major dry mergers as a way to increase the density slope. However, among the off-axis simulations of Nipoti et al. (2009b), only those with $M_*/M_{\rm h} \sim 0.1$ produce remnants with γ' higher than in the progenitor, while γ' decreases sharply in those with the more cosmologically motivated stellar-to-dark mass ratio $M_*/M_{\rm h} \sim 0.02$. Moreover, we stress that a crucial point in connecting models with observations is defining γ' in a consistent way. Theoretical works (e.g. Nipoti et al. 2009b; Johansson et al. 2012; Dubois et al. 2013) often define γ' by fitting $\rho(r)$ with a power law $\rho(r) \propto r^{-\gamma'}$ over a range of radii. The two methods give different values of the slope (see Figure 6.7) and we verified that, by measuring γ' as described in Section 6.1.1, the higher values of γ' predicted by the simulations of Nipoti et al. (2009b) get revised downward by an appreciable amount. The net effect, and one of the core result of our work, is that dry mergers decrease the density slope γ', as defined

216

in lensing and dynamics measurements.

Finally, while our results suggest that dissipation plays a role in the evolution of ETGs, the origin of the cold gas involved in the process can still be subject of debate. Gas can for example be produced as a result of stellar mass loss. If internal sources of gas are the dominant ones, then wet mergers might not be necessary to keep the density profile from getting shallower, provided that the gas can effectively cool down and reach the central parts of the galaxy. Mergers might still play a role by inducing starbursts in the pre-existing gas.

6.5 Conclusions

We studied the effect of dry mergers on the slope of the density profile of massive ETGs. Both minor and major mergers produce a decrease in the density slope γ', the effect being stronger for minor mergers, at fixed accreted mass. However, purely dry mergers produce a strong decrease in γ' with time, inconsistent with lensing observations at more than 99% significance. We thus developed a toy model to account for the infall of cold gas and star formation following wet mergers. We found that it is sufficient to accrete 4% of total mass in the form of cold gas to match the observed evolution in γ' since $z \sim 1$, while still be consistent with the observed size evolution. We suggest a scenario where the outer regions of massive ETGs grow by accretion of stars and dark matter, while small amounts of dissipation and nuclear star formation conspire to keep the mass density profile constant and approximately isothermal.
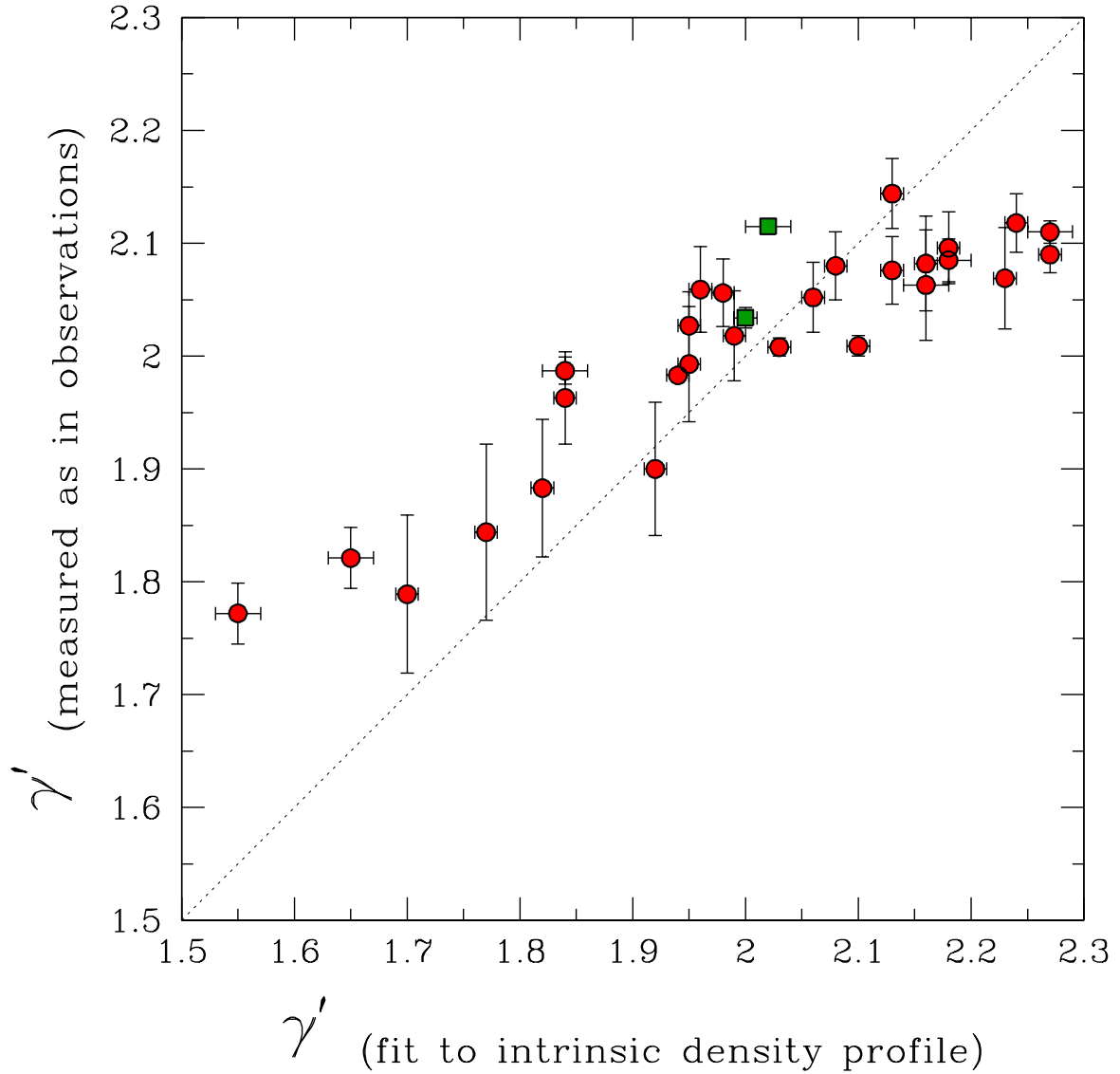
Figure 6.7: Total density slope γ' as defined in lensing and dynamics studies vs. γ' obtained by a direct fit to the angle-averaged density profile $\rho(r)$ for the merger remnants (circles) and progenitors (squares) of the N-body simulations of Nipoti et al. (2009b). Vertical error bars account for projection effects.

Chapter 7

Future directions

This Thesis explores the structure of early-type galaxies with different strong lensing-based observational approaches. We can identify two strategies that can improve measurements of this kind in both *precision* and *accuracy*. These are 1) including information about the *environment* of lenses and 2) increasing the number of known lenses, taking advantage of current and upcoming surveys. In this Chapter we discuss these two strategies.

7.1 The environment of lenses

One limitation of strong lensing is that it is only sensitive to projected masses. This complicates the interpretation of some of the results obtained so far. For instance, one of the main results of Chapter 5 is that galaxies with a more compact stellar distribution have a smaller amount of *projected* dark matter within a fixed physical aperture. We do not know if these differences in the projected dark matter mass arise because of differences in the mass in the inner few kpcs or at large radii. These two scenarios would have very different implications on our understanding of the evolution of ETGs. In the former case, a reduced amount of dark matter in the center of more compact galaxies

would point towards feedback mechanisms that, being stronger for systems with a larger concentration of baryons, pushed dark matter out from the inner regions. In the latter case instead a smaller projected dark matter mass would reflect a smaller halo mass. As discussed in Chapter 5, such a relation between halo mass and stellar mass density could be the result of mergers being more frequent in halos of larger mass, a result that would have important implications for galaxy assembly models.

Measurements of the environment of our strong lenses could help discriminate between these two scenarios. The mass of a halo correlates with the abundance of member galaxies. Counting the number of galaxies associated with the same halos as our lenses would then give us an independent constraint on the halo mass, breaking the degeneracy between total mass and mass in the center. Although there have been a few studies of the environment of strong lenses (Fassnacht et al. 2007; Auger et al. 2008; Treu et al. 2009), these have been limited by the lack of spectroscopic information and/or by low statistics. Photometric data allows only for very noisy measurements of the environment of a galaxy. Spectroscopic redshifts of neighboring galaxies are necessary in order to obtain an accurate description of the environment of a lens. We started a spectroscopic campaign in which we collected data on the environment of a few SL2S lenses using the instrument DEIMOS on Keck and we will continue gathering data of this kind in the upcoming months, possibly using the Gemini Telescopes.

Additional information on both the mass of the halo and on its geometry could be gathered by using weak lensing measurements, in continuity with the work by Gavazzi et al. (2007), or X-ray emission by the intragroup medium, at least for the most massive systems. Future X-ray surveys such as eROSITA could provide us with X-ray measure-

ments on a statistically significant number of strong lens ETGs in groups, allowing for accurate assessment of their environment.

7.2   Strong lensing in the LSST era

Ongoing surveys such as the Dark Energy Survey (DES) and the Hyper Suprime-Cam (HSC) survey will allow for the discovery of hundreds of new lenses, and upcoming surveys such as the Large Synoptic Survey Telescope (LSST) and Euclid will push the number of known lenses to tens of thusdands (Oguri & Marshall 2010). The work presented in this Thesis is based for the first part on a detalied study of one strong lens system characterized by a rare double ring configuration, the "Jackpot", and for the second part on the analysis of a relatively large ($N \sim 80$) number of regular strong lenses. It is easy to see how increasing the number of known lenses would help with the second strategy, although this would pose new challenges such as carrying out follow-up observations for large numbers of lenses and reducing the sources of systematic errors, currently comparable to the statistical uncertainties. At the same time, as new lenses are discovered a non-negligible fraction of these (roughly one in a thousand Gavazzi et al. 2008) will be double lens plane systems, allowing for studies like the one described in Chapter 2 to be possible for a statistically significant number of systems. Moreover, it will be possible to discover systems with even more exotic congiurations. Double lenses such as the "Jackpot" could, if the two lenses have comparable strength, produce *three rings instead of two* (Werner et al. 2008). The additional ring would appear closer to the center with respect to the "Jackpot" case and corresponds to light rays coming from

221
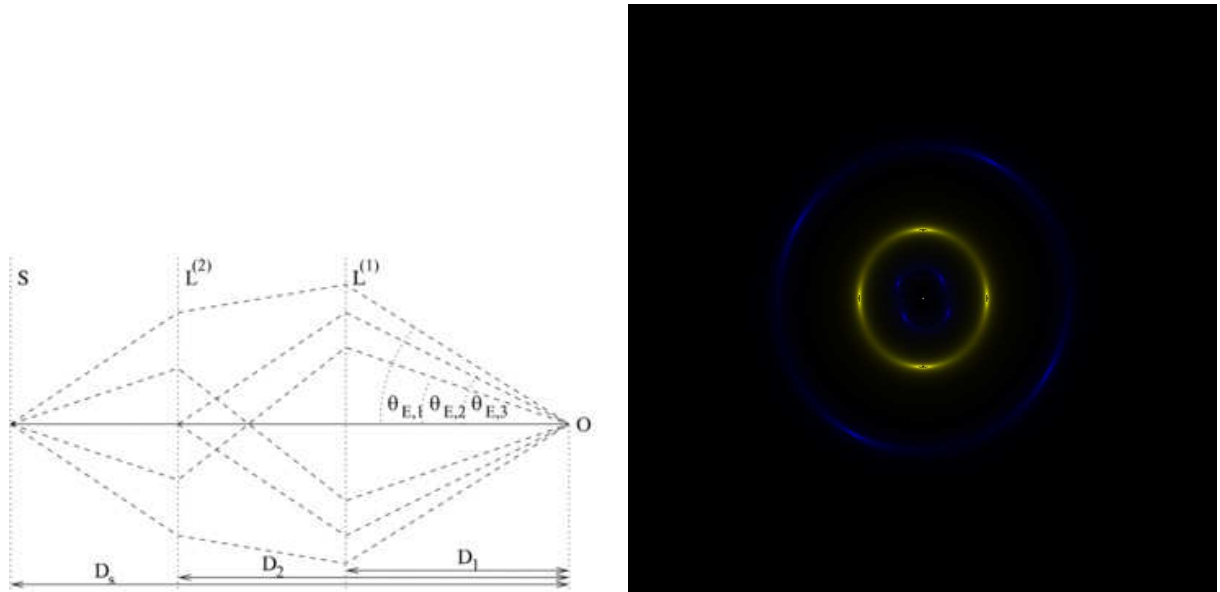
Figure 7.1: *Left panel:* Sketch of the lensing optical bench for a system of two lenses at two different redshifts generating a total of three Einstein rings. With respect to the case of SDSSJ0946+1006, the additional ring is formed from ligh rays coming from the background source (S) and crossing the optical axis (from Werner et al. 2008). *Right panel.* Simulation of a double lens system with a triple ring configuration. Light from the foreground lens galaxy has been subtracted. Blue images correspond to the farthest source, while yellow images correspond to the first source/second lens.

the background source and crossing the optical axis before reaching the observer (see

Figure 7.1). Such systems would provide more constraints with respect and would allow

to reconstruct the density profile of their lenses in greater detail.

With the two-order-of-magnitude increase in the number of lenses granted by LSST

and Euclid, strong lensing will likely continue to be an excellent tool for the study of

early-type galaxies in the next decade.

Bibliography

Abadi, M. G., Navarro, J. F., Fardal, M., Babul, A., & Steinmetz, M. 2010, MNRAS, 407, 435

Agnello, A., Evans, N. W., Romanowsky, A. J., & Brodie, J. P. 2014, MNRAS, 442, 3299

Anguita, T., Faure, C., Kneib, J.-P., et al. 2009, A&A, 507, 35

Arneson, R. A., Brownstein, J. R., & Bolton, A. S. 2012, ApJ, 753, 4

Auger, M. W., Becker, R. H., & Fassnacht, C. D. 2008, AJ, 135, 1311

Auger, M. W., Treu, T., Bolton, A. S., et al. 2009, ApJ, 705, 1099

—. 2010a, ApJ, 724, 511

Auger, M. W., Treu, T., Gavazzi, R., et al. 2010b, ApJ, 721, L163

Barnabè, M., Czoske, O., Koopmans, L. V. E., Treu, T., & Bolton, A. S. 2011, MNRAS, 415, 2215

Barnabè, M., Spiniello, C., Koopmans, L. V. E., et al. 2013, MNRAS, 436, 253

Bartelmann, M., & Schneider, P. 2001, Phys. Rep., 340, 291

Barth, A. J., Ho, L. C., & Sargent, W. L. W. 2002, AJ, 124, 2607

Barth, A. J., Nguyen, M. L., Malkan, M. A., et al. 2011, ApJ, 732, 121

Bell, E. F., & de Jong, R. S. 2001, ApJ, 550, 212

Belli, S., Newman, A. B., & Ellis, R. S. 2013, ArXiv e-prints, arXiv:1311.3317

Benítez, N. 2000, ApJ, 536, 571

Bennert, V. N., Auger, M. W., Treu, T., Woo, J.-H., & Malkan, M. A. 2011, ApJ, 726, 59

Bertin, E., Mellier, Y., Radovich, M., et al. 2002, in Astronomical Society of the Pacific Conference Series, Vol. 281, Astronomical Data Analysis Software and Systems XI, ed. D. A. Bohlender, D. Durand, & T. H. Handley, 228

Bielby, R., Hudelot, P., McCracken, H. J., et al. 2012, A&A, 545, A23

Bielby, R. M., Finoguenov, A., Tanaka, M., et al. 2010, A&A, 523, A66

Binney, J., & Tremaine, S. 2008, Galactic Dynamics: Second Edition, ed. Binney, J. & Tremaine, S. (Princeton University Press)

Blumenthal, G. R., Faber, S. M., Flores, R., & Primack, J. R. 1986, ApJ, 301, 27

Bolton, A. S., Burles, S., Koopmans, L. V. E., et al. 2008a, ApJ, 682, 964

—. 2008b, ApJ, submitted

Bolton, A. S., Burles, S., Schlegel, D. J., Eisenstein, D. J., & Brinkmann, J. 2004, AJ, 127, 1860

Bolton, A. S., Brownstein, J. R., Kochanek, C. S., et al. 2012, ArXiv e-prints, arXiv:1201.2988

Brewer, B. J., Marshall, P. J., Auger, M. W., et al. 2014, MNRAS, 437, 1950

Brewer, B. J., Dutton, A. A., Treu, T., et al. 2012, MNRAS, 422, 3574

Browne, I. W. A., et al. 2003, MNRAS, 341, 13

Brownstein, J. R., Bolton, A. S., Schlegel, D. J., et al. 2012, ApJ, 744, 41

Bruzual, G., & Charlot, S. 2003, MNRAS, 344, 1000

Busha, M. T., Marshall, P. J., Wechsler, R. H., Klypin, A., & Primack, J. 2011, ApJ, 743, 40

Cabanac, R. A., Alard, C., Dantel-Fort, M., et al. 2007, A&A, 461, 813

Cappellari, M., Bacon, R., Bureau, M., et al. 2006, MNRAS, 366, 1126

Cappellari, M., McDermid, R. M., Alatalo, K., et al. 2012, Nature, 484, 485

Cappellari, M., Scott, N., Alatalo, K., et al. 2013a, MNRAS, 432, 1709

Cappellari, M., McDermid, R. M., Alatalo, K., et al. 2013b, MNRAS, arXiv:1208.3523

Cardelli, J. A., Clayton, G. C., & Mathis, J. S. 1989, ApJ, 345, 245

Carollo, C. M., Bschorr, T. J., Renzini, A., et al. 2013, ApJ, 773, 112

Cassata, P., Giavalisco, M., Guo, Y., et al. 2011, ApJ, 743, 96

Cassata, P., Giavalisco, M., Williams, C. C., et al. 2013, ApJ, 775, 106

Chabrier, G. 2003, PASP, 115, 763

Choi, J., Conroy, C., Moustakas, J., et al. 2014, ApJ, 792, 95

Cimatti, A., Daddi, E., & Renzini, A. 2006, A&A, 453, L29

Cimatti, A., Nipoti, C., & Cassata, P. 2012, MNRAS, 422, L62

Ciotti, L., Lanzoni, B., & Volonteri, M. 2007, ApJ, 658, 65

Coe, D., Benítez, N., Sánchez, S. F., et al. 2006, AJ, 132, 926

Conroy, C., & van Dokkum, P. G. 2012, ApJ, 760, 71

Cooper, M. C., Newman, J. A., Davis, M., Finkbeiner, D. P., & Gerke, B. F. 2012a, spec2d: DEEP2 DEIMOS Spectral Pipeline, astrophysics Source Code Library, ascl:1203.003

Cooper, M. C., Griffith, R. L., Newman, J. A., et al. 2012b, MNRAS, 419, 3018

Daddi, E., Renzini, A., Pirzkal, N., et al. 2005, ApJ, 626, 680

Damjanov, I., Abraham, R. G., Glazebrook, K., et al. 2011, ApJ, 739, L44

de Vaucouleurs, G. 1948, Annales d'Astrophysique, 11, 247

Djorgovski, S., & Davis, M. 1987, ApJ, 313, 59

Dressler, A., Lynden-Bell, D., Burstein, D., et al. 1987, ApJ, 313, 42

Dubois, Y., Gavazzi, R., Peirani, S., & Silk, J. 2013, MNRAS, 433, 3297

Duffy, A. R., Schaye, J., Kay, S. T., et al. 2010, MNRAS, 405, 2161

Dutton, A. A., & Treu, T. 2013a, ArXiv e-prints, arXiv:1303.4389

—. 2013b, ArXiv e-prints, arXiv:1303.4389

Dutton, A. A., Brewer, B. J., Marshall, P. J., et al. 2011, MNRAS, 417, 1621

Dutton, A. A., Treu, T., Brewer, B. J., et al. 2013, MNRAS, 428, 3183

Faber, S. M., Phillips, A. C., Kibrick, R. I., et al. 2003, in Society of Photo-Optical Instrumentation Engineers (SPIE) Conference Series, Vol. 4841, Society of Photo-Optical Instrumentation Engineers (SPIE) Conference Series, ed. M. Iye & A. F. M. Moorwood, 1657–1669

Fakhouri, O., & Ma, C.-P. 2009, MNRAS, 394, 1825

Fakhouri, O., Ma, C.-P., & Boylan-Kolchin, M. 2010, MNRAS, 406, 2267

Fassnacht, C. D., Kocevski, D. D., Auger, M. W., et al. 2007, ApJ, submitted,, 711, arXiv:astro-ph/07112066

Faure, C., Kneib, J.-P., Covone, G., et al. 2008, ApJS, 176, 19

Feldmann, R., Carollo, C. M., Mayer, L., et al. 2010, ApJ, 709, 218

Feldmann, R., & Mayer, L. 2014, ArXiv e-prints, arXiv:1404.3212

Ferrarese, L., & Merritt, D. 2000, ApJ, 539, L9

Ferreras, I., La Barbera, F., de la Rosa, I. G., et al. 2013, MNRAS, 429, L15

Fontana, A., Pozzetti, L., Donnarumma, I., et al. 2004, A&A, 424, 23

Fruchter, A., Sosey, M., Hack, W., et al. 2009, The MultiDrizzle Handbook, version 3.0

Fumagalli, M., Labbe, I., Patel, S. G., et al. 2013, ArXiv e-prints, arXiv:1308.4132

Gallazzi, A., Charlot, S., Brinchmann, J., White, S. D. M., & Tremonti, C. A. 2005, MNRAS, 362, 41

Gavazzi, R., Marshall, P. J., Treu, T., & Sonnenfeld, A. 2014, ApJ, 785, 144

Gavazzi, R., Treu, T., Koopmans, L. V. E., et al. 2008, ApJ, 677, 1046

Gavazzi, R., Treu, T., Marshall, P. J., Brault, F., & Ruff, A. 2012, ApJ, 761, 170

Gavazzi, R., Treu, T., Rhodes, J. D., et al. 2007, ApJ, 667, 176

Gebhardt, K., Bender, R., Bower, G., et al. 2000, ApJ, 539, L13

Gnedin, O. Y., Ceverino, D., Gnedin, N. Y., et al. 2011, ArXiv e-prints, arXiv:1108.5736

Gnedin, O. Y., Kravtsov, A. V., Klypin, A. A., & Nagai, D. 2004, ApJ, 616, 16

González-Nuevo, J., Lapi, A., Fleuren, S., et al. 2012, ApJ, 749, 65

Grillo, C. 2012, ApJ, 747, L15

Grillo, C., Gobat, R., Lombardi, M., & Rosati, P. 2009, A&A, 501, 461

Gustafsson, M., Fairbairn, M., & Sommer-Larsen, J. 2006, Phys. Rev. D, 74, 123522

Häring, N., & Rix, H.-W. 2004, ApJ, 604, L89

Hennebelle, P., & Chabrier, G. 2008, ApJ, 684, 395

Hernquist, L. 1990, ApJ, 356, 359

Hilbert, S., White, S. D. M., Hartlap, J., & Schneider, P. 2007, MNRAS, 382, 121

Hilz, M., Naab, T., & Ostriker, J. P. 2013, MNRAS, 429, 2924

Hopkins, P. F. 2012, MNRAS, 423, 2037

—. 2013, MNRAS, 430, 1653

Hopkins, P. F., Bundy, K., Hernquist, L., Wuyts, S., & Cox, T. J. 2010, MNRAS, 401, 1099

Hopkins, P. F., Bundy, K., Murray, N., et al. 2009a, MNRAS, 398, 898

Hopkins, P. F., Hernquist, L., Cox, T. J., Keres, D., & Wuyts, S. 2009b, ApJ, 691, 1424

Huertas-Company, M., Mei, S., Shankar, F., et al. 2013, MNRAS, 428, 1715

Hyde, J. B., & Bernardi, M. 2009, MNRAS, 396, 1171

Ilbert, O., McCracken, H. J., Le Fèvre, O., et al. 2013, A&A, 556, A55

Inada, N., Oguri, M., Shin, M.-S., et al. 2012, AJ, 143, 119

Jaffe, W. 1983, MNRAS, 202, 995

Jiang, G., & Kochanek, C. S. 2007, ApJ, 671, 1568

Jiménez-Vicente, J., Mediavilla, E., Kochanek, C. S., & Muñoz, J. A. 2014, ArXiv 1407.3955, arXiv:1407.3955

Johansson, P. H., Naab, T., & Ostriker, J. P. 2012, ApJ, 754, 115

Jørgensen, I., Franx, M., & Kjaergaard, P. 1995, MNRAS, 276, 1341

Kaviraj, S., Tan, K.-M., Ellis, R. S., & Silk, J. 2011, MNRAS, 411, 2148

Kelly, B. C. 2007, ApJ, 665, 1489

Koopmans, L. V. E., & Treu, T. 2003, ApJ, 583, 606

Koopmans, L. V. E., & Treu, T. 2004, in Astrophysics and Space Science Library, Vol. 301, Astrophysics and Space Science Library, ed. M. Plionis, 23

Koopmans, L. V. E., Treu, T., Bolton, A. S., Burles, S., & Moustakas, L. A. 2006, ApJ, 649, 599

Koopmans, L. V. E., Treu, T., Fassnacht, C. D., Blandford, R. D., & Surpi, G. 2003, ApJ, 599, 70

Koopmans, L. V. E., Bolton, A., Treu, T., et al. 2009, ApJ, 703, L51

Kravtsov, A. V. 2013, ApJ, 764, L31

Kroupa, P. 2001, MNRAS, 322, 231

La Barbera, F., Ferreras, I., Vazdekis, A., et al. 2013, MNRAS, 433, 3017

Lagattuta, D. J., Fassnacht, C. D., Auger, M. W., et al. 2010, ApJ, 716, 1579

Lani, C., Almaini, O., Hartley, W. G., et al. 2013, MNRAS, 435, 207

Leauthaud, A., Tinker, J., Bundy, K., et al. 2012, ApJ, 744, 159

Lin, Y.-T., Brodwin, M., Gonzalez, A. H., et al. 2013, ApJ, 771, 61

Londrillo, P., Nipoti, C., & Ciotti, L. 2003, Memorie della Societa Astronomica Italiana Supplementi, 1, 18

López-Sanjuan, C., Le Fèvre, O., Ilbert, O., et al. 2012, A&A, 548, A7

Macciò, A. V., Dutton, A. A., & van den Bosch, F. C. 2008, MNRAS, 391, 1940

Mandelbaum, R., van de Ven, G., & Keeton, C. R. 2009, MNRAS, 1066

Marconi, A., & Hunt, L. K. 2003, ApJ, 589, L21

Marshall, P. J., Hogg, D. W., Moustakas, L. A., et al. 2009, ApJ, 694, 924

Marshall, P. J., et al. 2007, ApJ, 671, 1196

Martín-Navarro, I., La Barbera, F., Vazdekis, A., Falcón-Barroso, J., & Ferreras, I. 2014, ArXiv e-prints, arXiv:1404.6533

Menanteau, F., Abraham, R. G., & Ellis, R. S. 2001, MNRAS, 322, 1

Merritt, D. 1985, AJ, 90, 1027

More, A., Cabanac, R., More, S., et al. 2012, ApJ, 749, 38

Muzzin, A., Marchesini, D., Stefanon, M., et al. 2013, ApJ, 777, 18

Naab, T., Johansson, P. H., & Ostriker, J. P. 2009, ApJ, 699, L178

Napolitano, N. R., Romanowsky, A. J., & Tortora, C. 2010, MNRAS, 405, 2351

Navarro, J. F., Frenk, C. S., & White, S. D. M. 1997, ApJ, 490, 493

Negrello, M., Hopwood, R., De Zotti, G., et al. 2010, Science, 330, 800

Newman, A. B., Ellis, R. S., Bundy, K., & Treu, T. 2012a, ApJ, 746, 162

Newman, A. B., Treu, T., Ellis, R. S., & Sand, D. J. 2013, ApJ, 765, 25

Newman, J. A., Cooper, M. C., Davis, M., et al. 2012b, ArXiv e-prints, arXiv:1203.3192

Nipoti, C., Londrillo, P., & Ciotti, L. 2003, MNRAS, 342, 501

Nipoti, C., Treu, T., Auger, M. W., & Bolton, A. S. 2009a, ApJ, 706, L86

Nipoti, C., Treu, T., & Bolton, A. S. 2008, MNRAS, 390, 349

—. 2009b, ApJ, 703, 1531

Nipoti, C., Treu, T., Leauthaud, A., et al. 2012, MNRAS, 422, 1714

Oguri, M., & Marshall, P. J. 2010, MNRAS, 405, 2579

Oguri, M., Rusu, C. E., & Falco, E. E. 2014, MNRAS, 439, 2494

Oh, S.-H., de Blok, W. J. G., Brinks, E., Walter, F., & Kennicutt, Jr., R. C. 2011, AJ, 141, 193

Oke, J. B., Cohen, J. G., Carr, M., et al. 1995, PASP, 107, 375

Oser, L., Naab, T., Ostriker, J. P., & Johansson, P. H. 2012, ApJ, 744, 63

Osipkov, L. P. 1979, Soviet Astronomy Letters, 5, 42

Padilla, N. D., & Strauss, M. A. 2008, MNRAS, 388, 1321

Padoan, P., & Nordlund, Å. 2002, ApJ, 576, 870

Padoan, P., Nordlund, A., & Jones, B. J. T. 1997, MNRAS, 288, 145

Patil, A., Huard, D., & Fonnesbeck, C. J. 2010, Journal of Statistical Software, 35, 1

Pawase, R. S., Courbin, F., Faure, C., Kokotanekova, R., & Meylan, G. 2014, MNRAS, doi:10.1093/mnras/stu179

Peng, C. Y., Ho, L. C., Impey, C. D., & Rix, H.-W. 2002, AJ, 124, 266

—. 2010a, AJ, 139, 2097

Peng, Y.-j., Lilly, S. J., Kovač, K., et al. 2010b, ApJ, 721, 193

Pipino, A., Kaviraj, S., Bildfell, C., et al. 2009, MNRAS, 395, 462

Poggianti, B. M., Calvi, R., Bindoni, D., et al. 2013, ApJ, 762, 77

Pontzen, A., & Governato, F. 2012, MNRAS, 421, 3464

Posacki, S., Cappellari, M., Treu, T., Pellegrini, S., & Ciotti, L. 2014, ArXiv e-prints, arXiv:1407.5633

Posti, L., Nipoti, C., Stiavelli, M., & Ciotti, L. 2013, ArXiv e-prints, arXiv:1310.2255

Pozzetti, L., Bolzonella, M., Zucca, E., et al. 2010, A&A, 523, A13

Puget, P., Stadler, E., Doyon, R., et al. 2004, in Society of Photo-Optical Instrumentation Engineers (SPIE) Conference Series, Vol. 5492, Society of Photo-Optical Instrumentation Engineers (SPIE) Conference Series, ed. A. F. M. Moorwood & M. Iye, 978–987

Remus, R.-S., Burkert, A., Dolag, K., et al. 2013, ApJ, 766, 71

Rockosi, C., Stover, R., Kibrick, R., et al. 2010, in Society of Photo-Optical Instrumentation Engineers (SPIE) Conference Series, Vol. 7735, Society of Photo-Optical Instrumentation Engineers (SPIE) Conference Series

Ruff, A. J., Gavazzi, R., Marshall, P. J., et al. 2011, ApJ, 727, 96

Rusin, D., & Kochanek, C. S. 2005, ApJ, 623, 666

Rusin, D., Kochanek, C. S., & Keeton, C. R. 2003, ApJ, 595, 29

Salpeter, E. E. 1955, ApJ, 121, 161

Schechter, P. L., Pooley, D., Blackburne, J. A., & Wambsganss, J. 2014, ApJ, 793, 96

Schneider, P., Ehlers, J., & Falco, E. E. 1992, Gravitational Lenses (Springer-Verlag Berlin Heidelberg New York)

Shankar, F., Marulli, F., Bernardi, M., et al. 2013, MNRAS, 428, 109

Shen, S., Mo, H. J., White, S. D. M., et al. 2003, MNRAS, 343, 978

Shetty, S., & Cappellari, M. 2014, ApJ, 786, L10

Smith, R. J., & Lucey, J. R. 2013, MNRAS, 434, 1964

Sonnenfeld, A., Gavazzi, R., Suyu, S. H., Treu, T., & Marshall, P. J. 2013a, ApJ, 777, 97

Sonnenfeld, A., Treu, T., Gavazzi, R., et al. 2012, ApJ, 752, 163

—. 2013b, ApJ, 777, 98

Sonnenfeld, A., Treu, T., Marshall, P. J., et al. 2014, ArXiv e-prints, arXiv:1410.1881

Spiniello, C., Trager, S., Koopmans, L. V. E., & Conroy, C. 2014, MNRAS, 438, 1483

Spiniello, C., Trager, S. C., Koopmans, L. V. E., & Chen, Y. P. 2012, ApJ, 753, L32

Suyu, S. H., & Halkola, A. 2010, A&A, 524, A94

Suyu, S. H., Marshall, P. J., Auger, M. W., et al. 2010, ApJ, 711, 201

Suyu, S. H., Marshall, P. J., Blandford, R. D., et al. 2009, ApJ, 691, 277

Suyu, S. H., Marshall, P. J., Hobson, M. P., & Blandford, R. D. 2006, MNRAS, 371, 983

Suyu, S. H., Hensel, S. W., McKean, J. P., et al. 2012, ApJ, 750, 10

Suyu, S. H., Treu, T., Hilbert, S., et al. 2014, ApJ, 788, L35

Szomoru, D., Franx, M., van Dokkum, P. G., et al. 2013, ApJ, 763, 73

Thomas, D., Maraston, C., Schawinski, K., Sarzi, M., & Silk, J. 2010, MNRAS, 404, 1775

Tonini, C., Bernyk, M., Croton, D., Maraston, C., & Thomas, D. 2012, ApJ, 759, 43

Tortora, C., Romanowsky, A. J., & Napolitano, N. R. 2013, ApJ, 765, 8

Trager, S. C., Faber, S. M., Worthey, G., & González, J. J. 2000, AJ, 120, 165

Treu, T. 2010, ARA&A, 48, 87

Treu, T., Auger, M. W., Koopmans, L. V. E., et al. 2010, ApJ, 709, 1195

Treu, T., Dutton, A. A., Auger, M. W., et al. 2011, MNRAS, 417, 1601

Treu, T., Gavazzi, R., Gorecki, A., et al. 2009, ApJ, 690, 670

Treu, T., & Koopmans, L. V. E. 2002a, ApJ, 575, 87

—. 2002b, MNRAS, 337, L6

—. 2004, ApJ, 611, 739

Treu, T., Stiavelli, M., Casertano, S., Møller, P., & Bertin, G. 2002, ApJ, 564, L13

Treu, T., et al. 2005, ApJ, 633, 174

Trujillo, I., Feulner, G., Goranova, Y., et al. 2006a, MNRAS, 373, L36

Trujillo, I., Förster Schreiber, N. M., Rudnick, G., et al. 2006b, ApJ, 650, 18

Tu, H., Gavazzi, R., Limousin, M., et al. 2009, A&A, 501, 475

van der Marel, R. P. 1994, MNRAS, 270, 271

van der Wel, A., Bell, E. F., van den Bosch, F. C., Gallazzi, A., & Rix, H.-W. 2009, ApJ,
  698, 1232

van Dokkum, P. G., & Conroy, C. 2010, Nature, 468, 940

—. 2011a, ApJ, 735, L13

—. 2011b, ApJ, 735, L13

—. 2012, ApJ, 760, 70

van Dokkum, P. G., Franx, M., Kriek, M., et al. 2008, ApJ, 677, L5

van Dokkum, P. G., Whitaker, K. E., Brammer, G., et al. 2010, ApJ, 709, 1018

Vegetti, S., Koopmans, L. V. E., Bolton, A., Treu, T., & Gavazzi, R. 2010, MNRAS,
  408, 1969

Vieira, J. D., Marrone, D. P., Chapman, S. C., et al. 2013, Nature, 495, 344

Wardlow, J. L., Cooray, A., De Bernardis, F., et al. 2013, ApJ, 762, 59

Warren, S. J., & Dye, S. 2003, ApJ, 590, 673

Werner, M. C., An, J., & Evans, N. W. 2008, MNRAS, 391, 668

Zhao, H. 1996, MNRAS, 278, 488